Cyclotron Resonance-induced Photoelectric Phenomena in Two-dimensional Electron Systems excited by Terahertz Radiation

Dissertation

zur Erlangung des Doktorgrades
der Naturwissenschaften (Dr. rer. nat.)
der Fakultät für Physik
der Universität Regensburg

vorgelegt von

Erwin Mönch

aus Astana, Kasachstan

im Jahr 2024

Promotionsgesuch eingereicht am: 11.01.2024

Die Arbeit wurde angeleitet von: Prof. Dr. Sergey D. Ganichev

Prüfungsausschuss

Vorsitzender: Prof. Dr. Klaus Richter

1. Gutachter: Prof. Dr. Sergey D. Ganichev

2. Gutachter: Prof. Dr. Christian Schüller

weiterer Prüfer: Prof. Dr. Dieter Weiss

Contents

1 Introduction

Cyclotron resonance is a well-known phenomenon that was first observed and described in germanium and silicon crystals by Dresselhaus et al. in the early 1950s [1, 2]. Based on this first observation, a large number of experiments and techniques were performed and established, promoting this fundamental phenomenon as a standard experimental method widely used in solid state research [3]. To observe a distinct cyclotron resonance, it is desirable to satisfy the condition $\omega_c \tau_p \gg 1$, which necessitates the use of low temperatures and high radiation frequencies in the microwave or terahertz range. Common approaches are based on the study of radiation transmittance/reflectance, quenching of photoluminescence by cyclotron resonance absorption, and photoelectric methods (for a review see Ref. [4]). The latter, in particular, was described as early as 1958 by Zeiger et al. [5] and paved the way for the investigation of cyclotron resonance absorption via photoresistance and photovoltage. Since this method uses the sample itself as a detector, it allows the study of modern two-dimensional structures on the micrometer scale, where the exploration of cyclotron resonance by transmittance and reflectance measurements is almost infeasible.

Moreover, such studies facilitate the discovery and investigation of phenomena related to cyclotron resonance, or more precisely to its harmonics. A prominent example is microwave-induced resistance oscillations [6–12], reviewed in [13], and their terahertz analog [14–18], which reflect the commensurability between the incident radiation frequency and the quasiclassical cyclotron frequency. Most of the experiments exploring various phenomena made accessible by the photoelectric approach have been performed in gallium arsenide based heterostructures. In recent years, however, another two-dimensional material has attracted much attention: graphene – a single-layer crystal of hexagonally arranged carbon atoms. Due to its linear energy spectrum, the charge carriers behave like massless relativistic particles, leading to unique properties, see Refs. [19–26]. Since its discovery in 2004 [27], graphene has provided access to a multitude of fascinating phenomena in a variety of experiments and studies, particularly in the fields of optoelectronics [28–32] and plasmonics [33–38]. In fact, the interaction of electromagnetic radiation with graphene is one of the most promising and fastest growing fields, taking advantage of graphene's exceptional properties, such as fast and sensitive detection of light in a huge range of frequencies up to the terahertz domain [39–44]. Together with the fact that it is possible to fabricate graphene structures with a extremely high mobility, it is a very promising system to investigate and extend the field of magneto-optical phenomena.

The present work is devoted to the exploration of terahertz-induced photoelectric phenomena coupled to the cyclotron resonance and its harmonics. In particular, monolayer graphene structures of excellent quality revealed terahertz-driven nonlocal Bernstein modes [45], and terahertz-induced magnetooscillations [46]. Both have been observed for the first time in graphene. Furthermore, an anomalous helicity insensitivity of the cyclotron resonance absorption has been discovered during the study of conventional gallium arsenide and mercury telluride quantum wells [47, 48].

Terahertz-induced magnetoplasmonic excitations, the so-called Bernstein modes, are observed as huge photoresponse peaks near the cyclotron resonance overtones [45]. A comprehensive study shows that these features are induced by near-field effects in the vicinity of metallic contacts, which partially protrude into the Hall bar channel. The resulting magnetoplasmons exhibit a flat dispersion near the cyclotron resonance harmonics, leading to a strong heating of the electron gas, which is detected in the photoresponse. The influence of magnetoplasmons has also been recently observed in bilayer graphene structures [49] via the ratchet effect [50, 51]. Here, the near-field coupling has been provided by a large metallic interdigitated dual-grating gate structure leading to the coexistence of cyclotron and magnetoplasmon resonances.

Furthermore, the investigation of high-quality graphene structures leads to the discovery of terahertz-induced magnetooscillations [46]. Analysis of their variation with carrier density and radiation frequency reveals a common origin with microwave-induced resistance oscillations observed in gallium arsenide heterostructures [47, 48]. It is shown that their graphene analog is also governed by the ratio of the incident radiation frequency to the quasiclassical cyclotron frequency [46]. However, the magnetooscillations in graphene reveals significant differences, in particular that they persist up to $T = 90$ K and occur at much higher radiation frequencies.

Anomalous helicity insensitivity of cyclotron resonance absorption is observed in gallium arsenide and mercury telluride quantum wells. More specifically, the examination of cyclotron resonance and microwave-induced resistance oscillations demonstrates that the cyclotron resonance absorption occurs independently of the direction of the circularly polarized radiation [47, 48]. In contrast, the simultaneously measured radiation transmittance follows an ordinary helicity dependence. Moreover, it is shown that the amplitude ratio of the active and inactive sides of the cyclotron resonance strongly depends on the sample temperature T and the radiation power P. Under the condition of the lowest temperature T and the highest radiation power P, the signal responses at both polarities of the magnetic field reveal almost similar magnitudes.

The thesis is conceived as follows. In Chap. 2, the theoretical foundations are described, including the materials studied and the relevant physical concepts. First, the formation of a two-dimensional electron gas in a gallium arsenide based heterojunction is considered [Sec. 2.1.1], followed by a brief introduction to the peculiar properties of mercury telluride based quantum wells [Sec. 2.1.2]. Thereafter, Sec. 2.1.3 outlines the properties of graphene, focusing on its crystalline and electronic structure. Section 2.2 delineates the cyclotron resonance in both semiclassical and quantum mechanical frameworks, which is complemented by the modeling of the cyclotron resonance transmittance and absorptance in Sec. 2.2.1. Furthermore, the radiation-induced μ-photoconductivity is considered in Sec. 2.3. Finally, the chapter concludes with a description of the basic properties of plasmons with and without the application of a magnetic field in Sec. 2.4. Chapter 3 includes the description of the generation of continuous wave terahertz radiation via the optically pumped molecular gas laser [Sec. 3.1], the impact ionization avalanche transit time diode [Sec. 3.2], and the backward wave oscillator [Sec. 3.3]. This is followed by an illustration of the measurement techniques in Sec. 3, namely photoresistance/photovoltage and radiation transmittance. Before discussing the experimental results, the samples investigated are outlined in Sec. 4.

The experimental findings are presented in Chaps. 5 to 8. It starts with the investigation of the cyclotron resonance in two-dimensional electron systems with parabolic and linear dispersions [Chap. 5]. The chapter contains a general description of the observations based on the classical Drude theory. The experimental results and the associated discussion are presented in Secs. 5.1 and 5.2, respectively. Next, the terahertz-driven Bernstein modes observed in graphene are described in Sec. 6. The results are presented in Sec. 6.1 and discussed in Sec. 6.2. Chapter 7 presents the terahertz-induced magnetooscillations found in graphene. The experimental data are shown in Sec. 7.1 and the corresponding discussion is given in Sec. 7.2. Finally, the study of the anomalous helicity insensitivity is outlined in Sec. 8. The experimental results are presented in Sec. 8.1 and the corresponding analysis of the observed data in Sec. 8.2. Chapter 9 summarizes the work and provides a brief outlook on future studies in the field of magneto-optoelectronic phenomena. Supplemental experimental data supporting the discussed observations are given in Apps. A to E.

2 Theoretical Background

This chapter is devoted to theoretical concepts that are important for understanding the physical phenomena in the context of this work. It begins with an outline of the properties of two-dimensional electron systems (2DES), including gallium arsenide (GaAs), mercury telluride (HgTe), and monolayer graphene (MLG). Thereafter, the interaction of the electromagnetic (EM) wave with the 2DES exposed to a magnetic field is considered via the cyclotron resonance. The semiclassical as well as the quantum mechanical approach will serve to explain this fundamental phenomenon. After the foundations have been laid, the cyclotron resonance transmittance and absorptance are derived. Next, another radiation-induced optoelectronic phenomenon is introduced: μ-photoconductivity. Finally, a brief introduction to plasmonics in two dimensions is given. The effect of the magnetic field on their dispersion relation is emphasized.

2.1 Two-dimensional Electron Systems

In this section, a variety of 2DES are outlined. First, the properties of heterostructures based on GaAs and aluminum gallium arsenide (AlGaAs) are considered via an AlGaAs/GaAs heterojunction approximated by the triangular potential well model. Then, a second type of quantum wells (QWs) based on HgTe is briefly described, focusing on its particular band structure. Finally, the fundamental properties of graphene – a monolayer of graphite – are presented.

2.1.1 Gallium Arsenide-based Quantum Wells

The conduction electrons in a semiconductor can usually move freely in three dimensions. However, their motion in one dimension can be confined to discrete energy levels by placing them in a narrow potential well whose thickness has to be smaller than the Fermi or de Broglie wavelength. If this confinement is strong enough, it results in quantized energy levels and no free motion is possible in this direction. The result is a two-dimensional electron gas (2DEG).

One of the best-studied heterojunctions is the GaAs-based heterostructure consisting of multiple layers of GaAs and $\mathrm{Al}_x\mathrm{Ga}_{1-x}\mathrm{As}$ (x describes the composition of the compounds). An important advantage of these alloys is that the lattice constant changes less than 0.15 % with x. This allows high quality structures to be grown without significant lattice stress [52]. To introduce carriers into the junction, the corresponding regions of the heterostructure are usually doped. However, when the electrons or holes are released from the donor or acceptor atoms, the donors begin to act as charged scattering centers and interfere with the carrier propagation within the structure. To overcome this problem, doping is applied to one region to release the carriers, which then move to another region. This process is called remote or modulation doping and facilitates the fabrication of structures with high mobilities. Figure 2.1 shows the formation of a heterojunction between p-doped GaAs and n-doped AlGaAs alloys. At the beginning [Fig. 2.1(a)] the bands are flat and the electrons are bound to their donors. Released electrons move around with probability to reach the undoped GaAs layer. Since $\varepsilon_{\mathrm{C}}(n\text{-AlGaAs}) > \varepsilon_{\mathrm{C}}(p\text{-GaAs})$, the electrons lose their potential energy and are trapped in the GaAs region. This causes the formation of an electrostatic potential between the trapped electrons and the positively charged donors, resulting in band bending near the junction as shown in Fig. 2.1(b). Due to the discontinuity introduced in the conduction (CB) and valence (VB) bands, the electrons are pushed against the junction interface. If the equilibrated Fermi energy ε_{F} is substantially high, the electrons are trapped in a potential well that can be approximated by a triangular shape.

This confinement leads to a discrete energy spectrum and can be quantitatively described by the time-independent Schrödinger equation in three dimensions [52, 53]

$$\left[-\frac{\hbar^2}{2m^*}\nabla_{\boldsymbol{r}}^2 + V(\boldsymbol{r})\right]\Psi(\boldsymbol{r}) = \varepsilon\Psi(\boldsymbol{r}) \tag{2.1}$$

with m^* and ε denoting the in general anisotropic effective mass and the eigenenergies, respectively. Here, the three-dimensional vector is denoted as $\boldsymbol{r} = (x, y, z)$ and $\nabla_{\boldsymbol{r}}^2 = \partial^2/\partial x^2 + \partial^2/\partial y^2 + \partial^2/\partial z^2$ defines the Laplace operator in three dimensions. The expression for the potential energy $V(\boldsymbol{r})$ is in general non-trivial and requires proper knowledge of the system under study. In fact, for the layered heterostructures considered in this work, the potential energy is simplified to: $V(\boldsymbol{r}) = V(z)$, depending only on the coordinate z, which is perpendicular to the growth direction.

Using the plane-wave ansatz in the non-confined directions x and y, the wave function can be written in the form

$$\Psi(\boldsymbol{r}) = C\exp(\mathrm{i}k_x x)\exp(\mathrm{i}k_y y)\psi(z)\,, \tag{2.2}$$

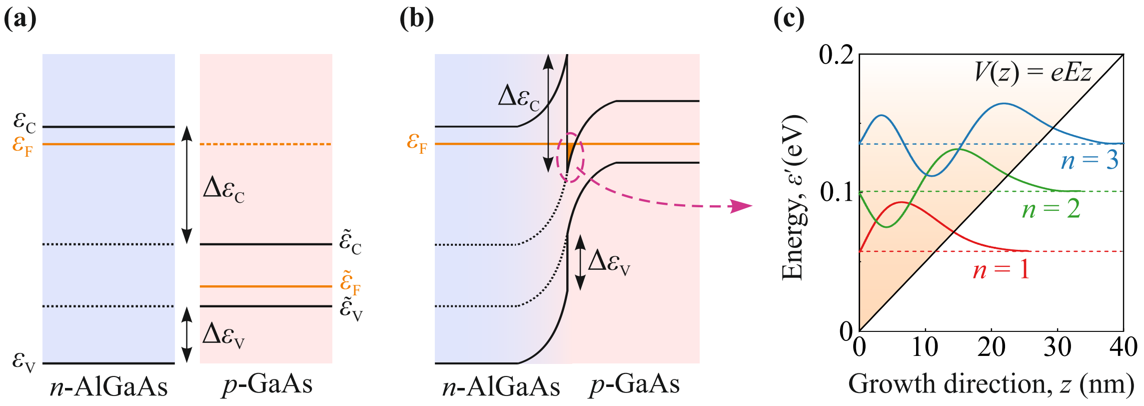

Figure 2.1: (a) Schematic illustration of the conduction and valence bands of n-AlGaAs and p-GaAs aligned to the vacuum level, whose Fermi energies are defined as ε_F and $\tilde{\varepsilon}_F$, respectively. The differences $\Delta\varepsilon_C$ and $\Delta\varepsilon_V$ are given by the differences between the respective conduction band minima (ε_C and $\tilde{\varepsilon}_C$) and valence band maxima (ε_C and $\tilde{\varepsilon}_V$), respectively. **(b)** Visualization of the band bending when the heterojunction is in equilibrium with aligned Fermi energy levels. The resulting two-dimensional electron gas, governed by a triangular potential well, is shaded in orange. **(c)** First three energy levels (dashed lines) and corresponding wave functions (solid colored lines) of a two-dimensional electron gas confined in a triangular potential well with potential energy $V(z) = eEz$. The axis values are given for an electric field of $E = 5\ \mathrm{MV\,m^{-1}}$ in GaAs. Figure adapted from Ref. [52].

where C is a normalization constant. Inserting this into Eq. (2.1) yields

$$\left[\frac{\hbar^2 k_x^2}{2m_x^*} + \frac{\hbar^2 k_y^2}{2m_y^*} - \frac{\hbar^2}{2m_z^*}\frac{\mathrm{d}^2}{\mathrm{d}z^2} + V(z)\right]\psi(z) = \varepsilon\psi(z) \tag{2.3}$$

with the effective masses m_x^*, m_y^* and m_z^*. Defining the expression for the energy as

$$\varepsilon' = \varepsilon - \frac{\hbar^2 k_x^2}{2m_x^*} - \frac{\hbar^2 k_y^2}{2m_y^*} \tag{2.4}$$

and substituting it into Eq. (2.3) results in

$$\left[-\frac{\hbar^2}{2m_z^*}\frac{\mathrm{d}^2}{\mathrm{d}z^2} + V(z)\right]\psi(z) = \varepsilon'\psi(z) \tag{2.5}$$

and, therefore, eliminates the dependencies on x and y revealing a purely one-dimensional Schrödinger equation as a function of z. A GaAs-based heterojunction consisting of GaAs and AlGaAs layers can be simplified as a triangular well, as illustrated in Figs. 2.1(b, c). It is assumed that the potential well is infinitely high for negative z and scales linearly for positive z values, consequently, it is defined according to

$$V(z) = \begin{cases} \infty\,, & \text{for} \quad z < 0\,; \\ eEz\,, & \text{for} \quad z > 0 \end{cases} \tag{2.6}$$

with $e > 0$. The one-dimensional Schrödinger equation [Eq. (2.3)] can be simplified to

$$\frac{\mathrm{d}^2\psi(u)}{\mathrm{d}u^2} = u\psi(u) \tag{2.7}$$

by introducing a dimensionless variable

$$u = \sqrt[3]{\frac{2m_z^* eE}{\hbar^2}} \left(z - \frac{\varepsilon'}{eE} \right) . \tag{2.8}$$

It is apparent that this equation reduces to the so-called Airy equation [54]. The solutions of Eq. (2.7) are given by the Airy functions $\mathrm{Ai}(u)$ and $\mathrm{Bi}(u)$. Since the wave function $\psi(u)$ should be finite at $z \to \infty$, i.e., $u \to \infty$, $\mathrm{Bi}(u)$ can be disregarded as a possible solution. Due to the infinitely high barrier for $z < 0$, the wave function has to satisfy the boundary condition $\psi(z = 0) = \psi\left(u = -\sqrt[3]{2m_z^* eE/(\hbar eE)^2}\varepsilon'\right) = 0$. To ensure that this condition is fulfilled, it is necessary to set $-\sqrt[3]{2m_z^* eE/(\hbar eE)^2}\varepsilon' = a_n$, which represents zero values of the Airy function, i.e., $\mathrm{Ai}(a_n) = 0$ with $n \in \mathbb{N}$. Therefore, the discrete energy spectrum in z direction is given by

$$\varepsilon_n' = a_n \left[\frac{(eE\hbar)^2}{2eEm_z^*} \right]^{1/3} , \quad n = 1, 2, 3, \ldots . \tag{2.9}$$

Since the potential well becomes wider at higher energies, the corresponding energy levels become closer as n grows. Note that this is in contrast to the energy spectrum of an infinitely deep square well, where the distance between the levels grows with increasing n. Thus, the corresponding unnormalized wave functions read

$$\psi_n(z) = \mathrm{Ai}(u), \tag{2.10}$$

where u is defined by Eq. (2.8).

The next section briefly discusses the peculiar behavior of HgTe QWs, whose energy dispersion can be modified by varying the QW confinement. This serves as a bridge before discussing the properties of massless Dirac fermions in graphene.

2.1.2 Mercury Telluride-based Quantum Wells

Mercury telluride is a direct II-VI semiconductor and crystallizes like GaAs in a zinc blende structure. For both materials, the important bands near the Fermi level are located close to the Γ point in the Brillouin zone (BZ). However, in contrast to GaAs, the energy dispersion of HgTe shows very unique properties owing to its large spin-orbit coupling. Here, the states of the conduction band are formed by $5p$ (Γ_8) electrons located at the telluride atoms, while the valence band consists of $6s$ (Γ_6) states from the mercury [56]. Subsequently, the band ordering of bulk HgTe is reversed [57–59] so that the light and heavy hole bands (LH and HH bands, respectively) of the Γ_8 states become the conduction and valence bands, respectively, as demonstrated in Fig. 2.2(a). Due to the LH and the HH bands degeneracy, bulk HgTe is considered a zero gap semiconductor [57].

Remarkably, this intriguing electronic structure of HgTe can be tuned over a wide range of energy dispersions. A common technique is to sandwich a thin layer of HgTe between cadmium telluride (CdTe) barriers. The latter is a conventional semiconductor with a trivial band structure, see Fig. 2.2(b). When the QW thickness d_{QW} of the CdTe/HgTe/CdTe structure is below a critical thickness d_{crit}, the energy levels within the HgTe are shifted, resulting in a regular energy band order. In fact, below the critical thickness, the heterostructure behaves like CdTe with normal band ordering. Here the Γ_6 states form the conduction subbands, whereas the Γ_8 bands yield the corresponding valence subbands. As d_{QW} exceeds the critical value, the structure resembles the inverted band ordering of HgTe. This behavior is illustrated in Fig. 2.2, showing an inverted band order at $d_{\mathrm{QW}} > d_{\mathrm{crit}}$ [panel (c)], where HH1 is energetically above the E1 state belonging to the electron band, and a normal one at $d_{\mathrm{QW}} < d_{\mathrm{crit}}$ [panel (d)], where E1 lies above the HH1 level. Note that for $d_{\mathrm{QW}} > d_{\mathrm{crit}}$, the HgTe QW structure forms a two-dimensional topological insulator with protected edge states. These occur at the interface of the HgTe QW with inverted band order and a topologically trivial material, e.g., ambient air, and are therefore energetically located in the band gap. For a detailed description, see Refs. [58, 60, 61]. The tunable behavior implies that at $d_{\mathrm{QW}} = d_{\mathrm{crit}}$ there is an inversion of the subbands. More precisely, at $d_{\mathrm{QW}} = 6.3$ nm the system exhibits a graphene-like linear energy dispersion and is described by the Dirac equation for massless particles [58].

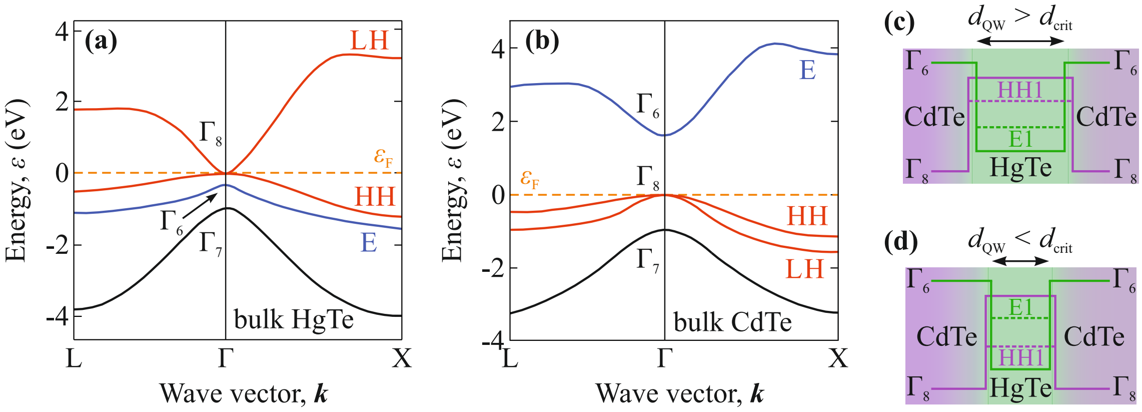

Figure 2.2: **(a, b)** Schematic representation of the band structure of bulk HgTe [panel (a)] and bulk CdTe [panel (b)] around the Γ point. The dashed orange lines mark the position of the Fermi energy ε_F in the corresponding material. While bulk CdTe has an energy gap between the HH and the E bands at the Γ point and behaves like a trivial semiconductor, bulk HgTe has no energy gap and an inverted band ordering. Here, the CB is represented by the LH band and the VB by the HH band. **(c, d)** CdTe/HgTe/CdTe QW structures with different HgTe layer thicknesses d_{QW}. Above the critical thickness ($d_{QW} > d_{crit}$) the band order of HgTe is inverted, while for $d_{QW} < d_{crit}$ the HH1 state moves over the E1 state and the band ordering becomes trivial. At $d_{QW} = d_{crit} = 6.3$ nm the QW structure exhibits a linear energy dispersion. Figure adapted from Ref. [55].

2.1.3 Graphene

Monolayer graphene is a special modification of carbon and is the first experimentally proven strictly two-dimensional structure [27, 62]. It forms a regular hexagonal lattice, similar to the honeycomb structure (point group of D_{6h}), with two equivalent sublattices A and B, see Fig. 2.3(a). These are shifted by a constant vector and can be described by the primitive unit vectors [24]

$$\boldsymbol{a}_1 = \frac{a_0}{2}(3, \sqrt{3}) \quad \text{and} \quad \boldsymbol{a}_2 = \frac{a_0}{2}(3, -\sqrt{3})\,, \tag{2.11}$$

where $a_0 \approx 1.42$ Å is the distance between neighboring carbon atoms. Accordingly, the corresponding reciprocal lattice vectors are

$$\boldsymbol{b}_1 = \frac{2\pi}{3a_0}(1, \sqrt{3}) \quad \text{and} \quad \boldsymbol{b}_2 = \frac{2\pi}{3a_0}(1, -\sqrt{3})\,. \tag{2.12}$$

It follows that the first BZ of a uniform hexagonal lattice also forms a hexagonal lattice, as illustrated in Fig. 2.3(b). In particular, the six corners of the BZ are of particular importance, playing a role similar to the Γ point in GaAs and HgTe heterostructures. At these so-called Dirac points, which are located at the K and K′ points in the BZ, given by $\boldsymbol{K} = (2\pi/3a_0, 2\pi/3\sqrt{3}a_0)$ and $\boldsymbol{K}' = (2\pi/3a_0, -2\pi/3\sqrt{3}a_0)$, respectively, the CB and VB touch each other, see inset in Fig. 2.3(c). Due to this fact, graphene has no band gap and thus exhibits the behavior of an electrical conductor. This peculiarity was already recognized by P. R. Wallace in 1947, who calculated the dispersion relation for graphene using the tight-binding approach [63]. Limiting the tight-binding approximation by the second-nearest neighbor hopping term, the corresponding Hamiltonian for electrons in graphene is given by [24]

$$\begin{aligned}\mathcal{H} = &- t \sum_{\langle i,j\rangle,\sigma} (a^\dagger_{\sigma,i} b_{\sigma,j} + \text{h.c.}) \\ &- t' \sum_{\langle\langle i,j\rangle\rangle,\sigma} (a^\dagger_{\sigma,i} a_{\sigma,j} + b^\dagger_{\sigma,i} b_{\sigma,j} + \text{h.c.}) \,. \end{aligned} \tag{2.13}$$

Here $a^\dagger_{\sigma,i}$ ($a_{\sigma,i}$) represents the creation (annihilation) of an electron with spin $\sigma \in \uparrow, \downarrow$ within the sublattice A. Correspondingly, $b^\dagger_{\sigma,i}$ and $b_{\sigma,i}$ provide the operators for the sublattice B. The hopping energies $t \approx 2.8$ eV (the value of t varies in the literature from 2.7 eV to 3.1 eV) and $t' \approx 0.1$ eV cover the intersublattice (A – B) and the intrasublattice (A – A or B – B) hopping, respectively [24, 25, 65–67]. Their corresponding manifolds are denoted by $\langle i, j\rangle$ and $\langle\langle i, j\rangle\rangle$. The calculation of the energy spectrum for the CB (+) and VB (−) results in [63]

$$\begin{aligned}\varepsilon_\pm(\boldsymbol{k}) =& \pm t\sqrt{3 + f(\boldsymbol{k})} - t' f(\boldsymbol{k}) \quad \text{with} \\ f(\boldsymbol{k}) =& 2\cos\left(\sqrt{3}k_y a_0\right) + 4\cos\left(\sqrt{3}k_y a_0/2\right)\cos\left(\sqrt{3}k_x a_0/2\right) \,. \end{aligned} \tag{2.14}$$

Apparently, the bands are symmetrically arranged around zero energy when only intersublattice hopping is considered ($t' = 0$). The dispersion according to Eq. (2.14) is presented in Fig. 2.3(c) for finite values of t and t'. Around the Dirac points, the energy dispersion in Eq. (2.14) can be expanded in terms of small momenta $|\boldsymbol{k}| \ll |\boldsymbol{k}|, |\boldsymbol{k}'|$ [24, 63], yielding

$$\varepsilon_\pm(\boldsymbol{k}) = \pm\hbar v_\mathrm{F}|\boldsymbol{k}| + \mathcal{O}\{(k/K)^2\} \tag{2.15}$$

with the Fermi velocity $v_\mathrm{F} = 3ta_0/(2\hbar) \approx 1 \times 10^6$ m/s. Note that the presence of carriers may lead to a many-body renormalization of this velocity, which is small for graphene. The first order contribution in Eq. (2.15) is fully sufficient to describe the properties of graphene that are important in the context of this work. In fact, the deviation of the energy spectrum from a pure Dirac-like dispersion occurs at $\varepsilon(\boldsymbol{k}) \approx 1.12$ eV, which is about five times larger than the energy scales used in the experiments. Hence, the higher order terms are neglected in the following.

The reason for such a high electron velocity in graphene is the vanishing effective

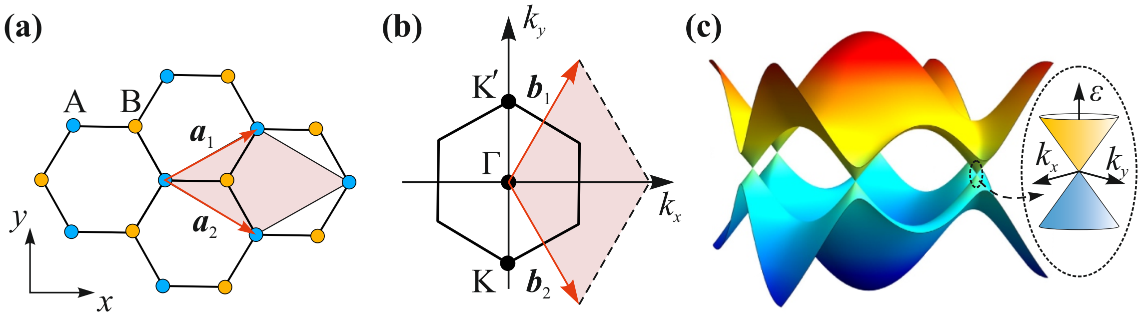

Figure 2.3: **(a)** Schematic representation of the honeycomb lattice of graphene consisting of two equivalent sublattices denoted by A and B. The respective lattice vectors are represented by $\boldsymbol{a}_1$ and $\boldsymbol{a}_2$ [see Eq. (2.11)] and shown as an example for sublattice A. **(b)** Corresponding hexagonal reciprocal lattice with the vectors $\boldsymbol{b}_1$ and $\boldsymbol{b}_2$ given by Eq. (2.12). The CB and VB touch at K and K′, forming a linear energy dispersion. **(c)** Three-dimensional visualization of the energy dispersion relation according to Eq. (2.14) for $t' = 0$. The inset shows an enlarged view of the Dirac cone where the electron and hole bands touch. Figures adapted from Refs. [24] and [64].

mass as a consequence of the linear dispersion. Thus, the charge carriers in graphene are described by the Dirac equation and thus resemble ultra-relativistic particles with spin 1/2, also referred to as massless Dirac fermions [25, 68]. A profound consequence of the two equivalent but independent sublattices A and B is that graphene exhibits a chiral pseudospin in addition to the conventional carrier spin. Due to a relatively weak intervalley coupling between $\boldsymbol{K}$ and $\boldsymbol{K}'$, graphene exhibits two equivalent valleys. This valley degeneracy, which should be considered together with the spin degeneracy, can be incorporated via the degeneracy factor $g_v = 2$.

Putting it all together, the resulting spinor-like two-component electron wave function $\boldsymbol{\Psi}(\boldsymbol{r})$ (due to the two atoms per unit cell) near the Dirac point obeys the two-dimensional Dirac equation [25, 68]

$$-\mathrm{i}\hbar v_{\mathrm{F}} \boldsymbol{\sigma} \cdot \nabla_r \boldsymbol{\Psi}(\boldsymbol{r}) = \varepsilon \boldsymbol{\Psi}(\boldsymbol{r})\,. \tag{2.16}$$

Hence, the effective low energy Hamiltonian reads

$$\mathcal{H} = \hbar v_{\mathrm{F}} \boldsymbol{\sigma} \cdot \boldsymbol{k} = \hbar v_{\mathrm{F}} \begin{pmatrix} 0 & k_x - ik_y \\ k_x + ik_y & 0 \end{pmatrix}\,, \tag{2.17}$$

containing the usual two-dimensional Pauli-matrices vector $\boldsymbol{\sigma} = (\sigma_x, \sigma_y)$ taking into account the pseudospin. In analogy to Eq. (2.17) the Hamiltonian for K′ is obtained by the transformation $\mathcal{H}_{\boldsymbol{K}'} = -\mathcal{H}_{\boldsymbol{K}}$. The product $\boldsymbol{\sigma} \cdot \boldsymbol{k}$ is also known as the helicity operator and proves the chiral nature of the graphene energy spectrum. In particular, electrons have positive (negative) chirality and holes negative (positive) chirality in the $\boldsymbol{K}$ ($\boldsymbol{K}'$) valley. The corresponding electron wave functions in momentum space are

$$\boldsymbol{\Psi}_{\pm}^{\boldsymbol{K}}(\boldsymbol{k}) = \frac{1}{\sqrt{2}}\begin{pmatrix} \mathrm{e}^{-\mathrm{i}\theta_k/2} \\ \pm\mathrm{e}^{\mathrm{i}\theta_k/2} \end{pmatrix} \quad \text{and} \quad \boldsymbol{\Psi}_{\pm}^{\boldsymbol{K}'}(\boldsymbol{k}) = \frac{1}{\sqrt{2}}\begin{pmatrix} \mathrm{e}^{\mathrm{i}\theta_k/2} \\ \pm\mathrm{e}^{-\mathrm{i}\theta_k/2} \end{pmatrix} . \tag{2.18}$$

Here $\theta_k = \arctan(k_x/k_y)$ is the angle in momentum space and the $\pm$ signs indicate the corresponding eigenergies $\varepsilon_{\pm}(k) = \pm\hbar v_{\mathrm{F}} k$ of CB (+) and VB (−). Note that the wave functions change their sign, which implies an additional phase of π when the angle θ_k is rotated by 2π. This additional phase is called Berry phase and is a characteristic of two-component spinors [24]. Furthermore, a non-zero Berry phase yields a half-integer shifted quantum Hall effect and a phase shift of the Shubnikov–de Haas quantum oscillations (SdHO) [21, 22, 25].

Now that the basics of the materials used in this work have been outlined, the next chapter will discuss fundamental phenomena, the understanding of which is of utmost importance for the discussion of the experimental results.

2.2 Cyclotron Resonance

In general, cyclotron resonance (CR) refers to the resonant absorption of EM waves by charged particles, such as free electrons or conduction electrons in a solid, when exposed to a constant magnetic field. This section provides a more quantitative description of this fundamental physical phenomenon based on the semiclassical and quantum mechanical approaches. While the semiclassical model originates from the Drude model [69, 70], the quantum mechanical approach treats CR via optical transitions between adjacent Landau levels. Landau quantization becomes important in the regimes of SdHO and quantum Hall effect. The description of both approaches follows the considerations covered in Refs. [3, 4, 71].

Consider a free carrier of charge q moving with velocity $\boldsymbol{v}$ in a uniform magnetic field $\boldsymbol{B}$ parallel to the z direction $\hat{e}_z$, the trajectory influenced by the Lorentz force $\boldsymbol{F} = q(\boldsymbol{v} \times \boldsymbol{B})$ constrains the carrier motion to spiral cyclotron orbits[1]. Note that the charge q is negative for electrons ($q = -e < 0$) and positive for holes ($q = e > 0$). The angular frequency of this trajectory around the direction of the applied magnetic

---

[1] The described trajectory applies to the consideration of motion in real space. Translating this behavior into $\boldsymbol{k}$-space yields the motion perpendicular to the magnetic field on planes of constant energy [72].

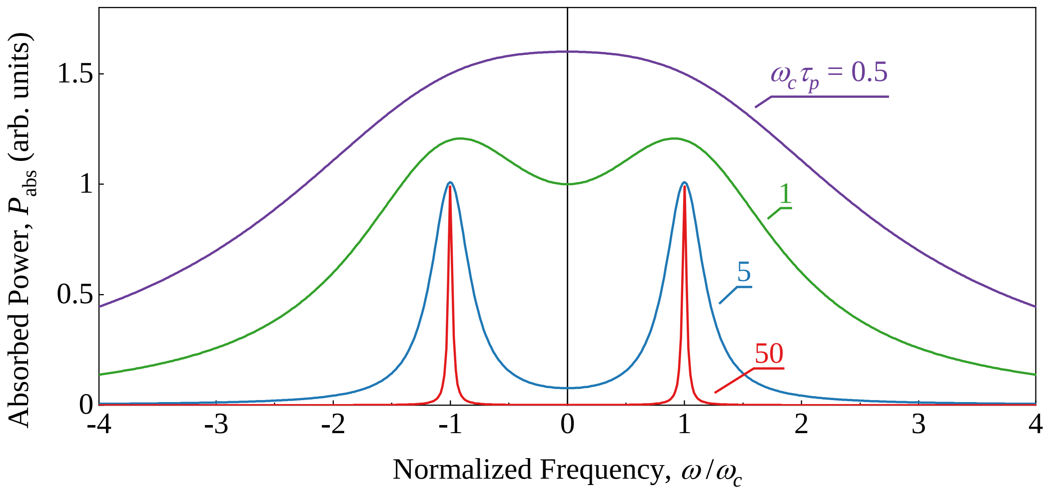

Figure 2.4: The absorbed power P_{abs}, Eq. (2.23), expressed in units of $E_0^2\sigma_0$ as a function of the ratio ω/ω_c for several representative values of $\omega_c\tau_p$. A distinct CR appears for $\omega = \omega_c$ for the condition $\omega_c\tau_p \gg 1$ (blue and red traces), while it is substantially suppressed for $\omega_c\tau_p \lesssim 1$ (green and purple traces). Figure adapted from Ref. [4].

field is given by (the absolute value of) the cyclotron frequency

$$\omega_c = \frac{qB_z}{m}\,, \tag{2.19}$$

where $\boldsymbol{B} = B_z\hat{e}_z$ and m is the free carrier mass. Projecting this helical motion onto the $x-y$ plane, perpendicular to the magnetic field, yields a circle with the cyclotron radius $R_c = v/\omega_c$ [3]. Considering a solid state system, the relation in Eq. (2.19) is modified by simply replacing the free carrier mass m by components of the effective mass tensor $\overset{\leftrightarrow}{m}^*$, taking into account the carrier dynamics influenced by the surrounding lattice potential [73]. If an incident EM wave with an electric field $\boldsymbol{E}$ interacts with charge carriers in a material, the corresponding equation of motion becomes

$$m^*\frac{\mathrm{d}\boldsymbol{v}}{\mathrm{d}t} = q(\boldsymbol{E} + \boldsymbol{v}\times\boldsymbol{B}) - \frac{m^*\boldsymbol{v}}{\tau_p} \tag{2.20}$$

under the assumption of an isotropic effective mass m^*. Here τ_p is the momentum relaxation time, which describes the time scale on which the electron randomizes its direction of motion due to scattering events. If the frequency of the EM wave matches the cyclotron frequency ω_c of the system, the carriers will effectively absorb the incoming radiation. This fundamental phenomenon is called cyclotron resonance [3]. Knowing the radiation frequency ω, which determines the magnetic field position of the CR B_{CR}, one can access the effective mass m^* via Eq. (2.19).

The equation of motion [Eq. (2.20)] can be solved by using $\boldsymbol{j} = qn_e\boldsymbol{v}$ and considering that the electric field $\boldsymbol{E}$ and the velocity $\boldsymbol{v}$ have a harmonic form proportional to $\exp(-\mathrm{i}\omega t)$ [4]. In the following considerations, the electric field of the EM wave is perpendicular to the applied magnetic field – a configuration called Faraday geometry. Using the obtained conductivity tensor, the absorbed power P_abs is given by the Joule losses formula as

$$P_\mathrm{abs} = \overline{\boldsymbol{jE}}\,, \tag{2.21}$$

where the overline represents the average over time. Assuming that the EM wave is linearly polarized, the absorbed power is then explicitly given by [3, 4]

$$P_\mathrm{abs}(\omega) = \frac{1}{2}E_0^2\sigma_0\Re\left\{\frac{\mathrm{i}\omega\tau_p + 1}{(\mathrm{i}\omega\tau_p + 1)^2 + \omega_c^2\tau_p^2}\right\}\,, \tag{2.22}$$

where E_0 is the amplitude of the electric field and $\sigma_0 = qn_e\mu = q^2n_e\tau_p/m^*$ is the static direct current (dc) conductivity including the carrier density n_e and the carrier mobility μ. As the linear polarization is the sum of the left-handed (P_+) and right-handed (P_-) circular polarization states, Eq. (2.22) can be further rearranged into

$$P_\mathrm{abs}(\omega) = \frac{1}{4}\Bigg[\underbrace{\frac{E_0^2\sigma_0}{1 + (\omega - \omega_c)^2\tau_p^2}}_{= P_+} + \underbrace{\frac{E_0^2\sigma_0}{1 + (\omega + \omega_c)^2\tau_p^2}}_{= P_-}\Bigg]\,. \tag{2.23}$$

Note that an additional factor of 1/2 comes from the fact that the root mean square field of the linearly polarized EM wave is smaller by a factor of $\sqrt{2}$ than that of the circularly polarized wave. Therefore, the intensity (Poynting vector) of the linearly polarized EM wave is given by $I = E_0^2/(2Z_0)$ and for the circularly polarized wave $I = E_0^2/Z_0$ with the vacuum impedance $Z_0 = 1/\epsilon_0 c \approx 377\ \Omega$. In contrast to the absorbed power, the dimensionless absorptance $\mathcal{A} = P_\mathrm{abs}/I$ for the linearly polarized wave denotes simply $\mathcal{A}_\mathrm{lin} = (\mathcal{A}_+ + \mathcal{A}_-)/2$, see also Sec. 2.2.1.

For illustration, the absorbed power is visualized in Fig. 2.4 for different values of the product $\omega_c\tau_p$. It is clearly seen that distinct and sharp resonances are present at $\omega = \omega_c$ and $\omega = -\omega_c$ for $\omega_c\tau_p \gg 1$. In other words, the CR absorption is significantly suppressed if the carriers loose information about their initial momentum due to scattering by impurities or phonons before completing a closed cyclotron loop [3, 72].

From Eq. (2.23) it is clear that CR under circularly polarized radiation provides a method to determine the dominant carrier type in a semiconductor: The resonant absorption is only possible if the polarization state of the radiation contains a component that rotates synchronously and in the same direction as the electric current associated with the cyclotron motion of the carriers. As a result, only left-handed (right-handed) circularly polarized radiation directed along the applied magnetic field is absorbed when electrons (holes) prevail in the structure. For an antiparallel configuration of incoming radiation and magnetic field, the resonance condition is reversed [72]. Subsequently, it is natural to introduce the CR active magnetic field polarity, where resonant absorption is obtained, and the CR inactive polarity, which does not fulfill the CR condition.

As touched on above, the absorption shape facilitates access to the momentum relaxation time τ_p. However, the classical Drude approach underestimates the width of the CR, especially in high-mobility 2DES such as GaAs QWs. In particular, electrons exposed to the incident EM wave try to follow its rapidly oscillating electric field. As a result, accelerated charges produce secondary radiation leading to a strong reflection of the incident EM wave at the CR condition, similar to a metallic surface [74]. This in turn produces an additional contribution, called radiative/superradiant decay, which broadens the linewidth of the resonance [17, 74, 75]. Consequently, the shape of the CR is determined by both the momentum relaxation rate $\gamma = 1/\tau_p$ and the radiative decay rate [17]

$$\Gamma = \frac{e^2 n_e}{2\epsilon_0 c m^* \omega} \,. \tag{2.24}$$

The ratio of these two contributions yields

$$\frac{\Gamma}{\gamma} = \frac{\sigma_0}{2\epsilon_0 c\omega} \,. \tag{2.25}$$

Considering the product of μ and n_e in the numerator, it is evident that this ratio is much larger than unity for high-mobility 2DES, resulting in a huge influence of the radiative decay on the CR linewidth. Indeed, only a small part of the radiation is absorbed by the 2DES due to the strong reflection under the CR condition [17, 74].

The above consideration is only valid under classical conditions, which include moderate magnetic fields and temperatures. However, when a semiconductor is subjected to a strong magnetic field, its energy bands transform into discrete levels due to Landau quantization [76, 77]. The emergence of Landau levels leads to a variety of new phenomena. The most fundamental is the quantum Hall effect in 2DES, which describes the appearance of quantized plateaus in the Hall resistance [3, 78]. In this picture, CR is facilitated by resonant optical transitions between adjacent LLs. Assuming a semiconductor permeated by a uniform magnetic field in the z direction, the Schrödinger equation for electrons becomes [3]

$$\left[\frac{1}{2m^*}(\boldsymbol{p}+e\boldsymbol{A})^2+V(z)\right]\psi(\boldsymbol{r})=\varepsilon\psi(\boldsymbol{r})\,, \tag{2.26}$$

and can be rewritten as [71] [2]

$$\left[\frac{1}{2m^*}(p_y+eB_zx)^2+\frac{p_x^2}{2m^*}+\frac{p_z^2}{2m^*}\right]\psi(\boldsymbol{r})=\varepsilon\psi(\boldsymbol{r})\,, \tag{2.27}$$

by considering a parabolic energy dispersion with the eigenenergies $\varepsilon(\boldsymbol{k})=\hbar^2k^2/2m^*$. The wave function can be expressed as $\psi(\boldsymbol{r})=\exp(-\mathrm{i}k_yy)\exp(-\mathrm{i}k_zz)U(x)$ and thus, Eq. (2.27) turns into [71]

$$\left[\frac{p_\zeta^2}{2m^*}+\frac{e^2B_z^2}{2m^*}\zeta^2\right]U(\zeta)=\left(\varepsilon-\frac{\hbar^2k_z^2}{2m^*}\right)U(\zeta)\,. \tag{2.28}$$

Here, the relative coordinate $\zeta=x+\frac{\hbar k_y}{eB_z}$ was used for convenience. This equation is the same as that describing the one-dimensional harmonic oscillator. Consequently, the parabolic dispersion (P) eigenenergies yield a discrete spectrum given by [3, 71]

$$\varepsilon_l^{\mathrm{P}}=\left(l+\frac{1}{2}\right)\hbar\omega_c+\frac{\hbar^2k_z^2}{2m^*}\quad\text{with}\quad l=0,1,2,... \tag{2.29}$$

by utilizing the expression for ω_c according to Eq. (2.19) with $q\to e$ and $m\to m^*$. As a result, the motion perpendicular to the applied magnetic field is quantized, whereas the spectrum parallel to $B_z\hat{e}_z$ remains unchanged. However, in 2DES the contribution along the z direction in Eq. (2.29) is also governed by an energy quantization by assuming that the magnetic field points in the direction of confinement (parallel to the growth direction), see, e.g., Eq. (2.9) in Sec. 2.1.1. The discrete energy levels feature an equidistant energy spacing $\Delta_l^{\mathrm{P}}=\hbar\omega_c$ for a parabolic band and are called Landau levels (LLs). It is clear that Δ_l^{P} is independent of the Fermi level position and is therefore not affected by changes in the carrier density. The LL spectrum is presented in Fig. 2.5(a). According to the selection rules in the dipole approximation, transitions are only possible between adjacent LL $l\to l\pm 1$ [71]. Considering instead a two-dimensional structure with linear energy dispersion (e.g., graphene, see Sec. 2.1.3), it becomes clear that the above equations can not be ap-

---

[2] Here, the Landau gauge is used for the vector potential $\boldsymbol{A}=(0,B_zx,0)^{\mathrm{T}}$, whereas the scalar potential is set to zero, $\varphi=0$.

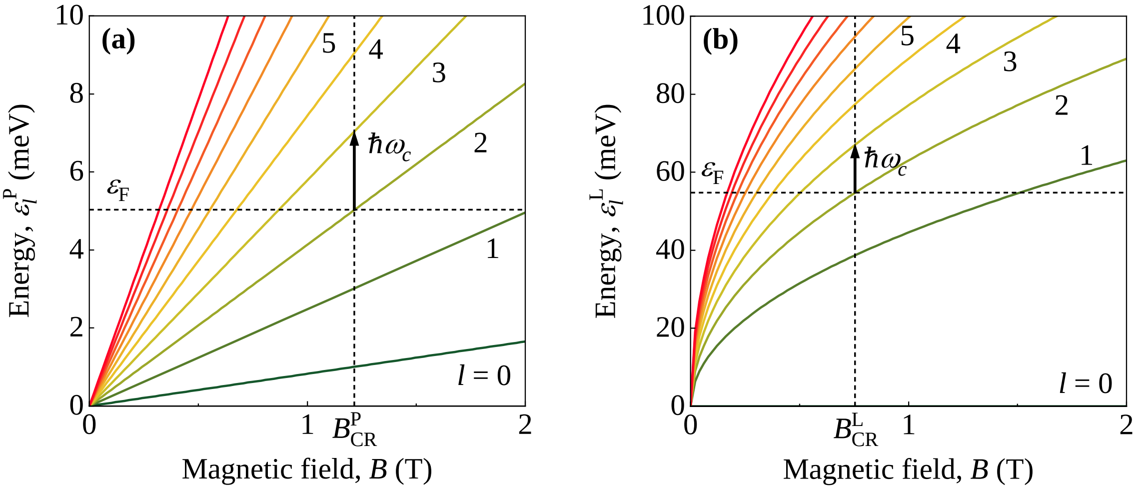

Figure 2.5: **(a)** Landau level spectrum for a system with parabolic energy dispersion, calculated according to Eq. (2.29) neglecting the contribution proportional to k_z. The first 10 LLs are plotted for $l = 0, 1, ..., 9$. **(b)** Calculated LL spectrum for massless Dirac fermions. The energies $\varepsilon_l^{\mathrm{L}}$ [see Eq. 2.30] are shown for the first 10 levels. At higher energies the distance between the levels can be well approximated by the semiclassical CR frequency. Cyclotron resonance transitions between the LLs are illustrated in both panels as examples for a given Fermi energy ε_{F}. The respective magnetic fields in which the CR occurs are denoted as $B_{\mathrm{CR}}^{\mathrm{P}}$ and $B_{\mathrm{CR}}^{\mathrm{L}}$. Figure adapted from Ref. [4].

plied, since the carriers are characterized as massless Dirac fermions[3]. The solution of the Dirac equation near the Dirac points in the presence of a uniform magnetic field yields linear dispersion (L) eigenergies [20, 24, 79–81]

$$\varepsilon_l^{\mathrm{L}} = \pm v_{\mathrm{F}} \sqrt{2e\hbar B|l|} \quad \text{with} \quad l = 0, \pm 1, \pm 2, ... \tag{2.30}$$

for the CB (+) and VB (−). The LL spectrum is plotted against the magnetic field in Fig. 2.5(b). It is noticeable that in contrast to Eq. (2.29), the Landau quantization of the linear dispersion has a zero-energy LL at $l = 0$, which is a direct consequence of the electron-hole symmetry. In systems such as graphene, the experimental observation of this zero-energy state attests to its Dirac-like nature [21, 82, 83]. Moreover, $\varepsilon_l^{\mathrm{L}}$ scales with the square root of the magnetic field and the LL number, which is a peculiar feature of linear dispersion. Indeed, the corresponding density of states (DOS) scales linearly as a function of energy in the absence of a magnetic field. As a result, when the magnetic field is turned on, the LLs require less spacing to achieve an equivalent number of states necessary to fully occupy each LL. This results in a nonequidistant LL spectrum [84].

Subsequently, the emergence of the CR, which is governed by the transition between

---

[3] For Dirac-like carriers the effective mass vanishes, which according to Eq. (2.19) yields $\omega_c \to \infty$.

adjacent LLs, involves the square root of l and B. Calculating the energy difference according to Eq. (2.30) for the transition $l \to l+1$ in the CB yields

$$\Delta_l^{\mathrm{L}} = \varepsilon_{l+1}^{\mathrm{L}} - \varepsilon_l^{\mathrm{L}} = \hbar\omega_c = v_{\mathrm{F}}\sqrt{2e\hbar B}\left(\sqrt{l+1} - \sqrt{l}\right) . \tag{2.31}$$

In the limit of small l ($l \sim 1$) of the involved LLs, or in other words for a large resonant photon energy with respect to the Fermi level of the system, the spacing between the LLs follows a strict square root behavior given by Eq. (2.31). However, for $l \gg 1$, under the condition that the Fermi energy $\varepsilon_{\mathrm{F}} \gg \max\{\hbar\omega, k_{\mathrm{B}}T\}$, the energy spacing can be approximated as [85]

$$\Delta_l^{\mathrm{L}} \approx \frac{v_{\mathrm{F}}}{2}\sqrt{\frac{2e\hbar B}{l}} \tag{2.32}$$

by using the series expansion $\sqrt{1+1/x} \approx 1 + 1/(2x)$ in the limit of $x \gg 1$. As the LL energy for high l is close to the Fermi energy, i.e., $\varepsilon_l^{\mathrm{L}} \approx \varepsilon_{\mathrm{F}}$, resulting in $\sqrt{l} \approx \varepsilon_{\mathrm{F}}/(v_{\mathrm{F}}\sqrt{2\hbar eB})$, the cyclotron frequency can be expressed as

$$\omega_c = \frac{\Delta_l^{\mathrm{L}}}{\hbar} \approx \frac{eB}{m_c} . \tag{2.33}$$

The corresponding density dependent cyclotron mass $m_c = \varepsilon_{\mathrm{F}}/v_{\mathrm{F}}^2 = \hbar\sqrt{\pi n_e}/v_{\mathrm{F}}$ [21, 86] is a peculiarity of the linear dispersion and the main difference to the parabolic one. According to Eq. (2.33), the obtained cyclotron frequency scales linearly with B, yielding an equidistant LL spectrum within the semiclassical approach, similar to the case of a parabolic dispersion. In fact, this is justified for the experimental conditions mostly used in this work for graphene. With $n_e = 1 \times 10^{12}$ cm^{-2} and $B = 1$ T, the Fermi energy is estimated as $\varepsilon_{\mathrm{F}} \approx 110$ meV, corresponding to the LL indices $l > 10$ relevant for optical transitions. A comparison of the semiclassical approach with the quantum mechanical limit for $l = 10$ reveals a deviation of less than 1%.

Finally, as the experiments are performed with a fixed radiation frequency, the corresponding cyclotron magnetic field positions for the parabolic and linear dispersions are given by

$$B_{\mathrm{CR}}^{\mathrm{P}} = \frac{m^*\omega}{e} \quad \text{and} \quad B_{\mathrm{CR}}^{\mathrm{L}} = \frac{\hbar\omega\sqrt{\pi n}}{ev_{\mathrm{F}}} . \tag{2.34}$$

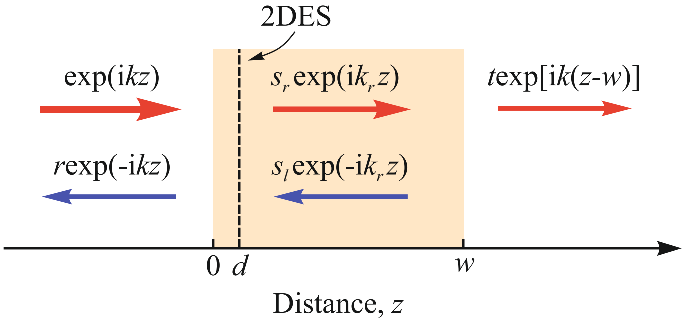

Figure 2.6: Schematic representation of the sample (orange shaded area) containing a 2DES (dashed line) for the theoretical derivation of transmittance, absorptance, and reflectance. Figure adapted from Ref. [17].

2.2.1 Cyclotron Resonance Transmittance and Absorptance

In the previous section we introduced the interaction of an EM wave with the conduction electrons via CR. This section extends this description by considering the relation between external incoming wave and internal EM wave acting on electrons. We will take into account multiple reflections within the dielectric substrate containing 2DES as well as resonant metallic reflection of the wave from 2DES itself. In this context, the modeling of radiation transmittance and absorptance becomes of major importance. In the following, the concept of transmission and absorption of a plane EM wave within the classical Drude approximation is addressed by considering a sample sheet containing a uniform isotropic 2DES [17, 87–89]. The sample consists of a dielectric substrate, characterized by thickness w and refractive index n_r, occupying $0 < z < w$, and a conducting 2DES located at $z = d$, see Fig. 2.6. Typical values for GaAs are $w = 500\ \mu\text{m}$ and $n_r = 3.6$. Since the 2DES sits very close at the front interface of the dielectric, so that $d \ll 1/k_r$ with the wave vector inside the substrate $k_r = \omega n_r/c$, it is sufficient to consider $d = 0$. However, due to a long optical path $\phi = k_r w \gg 1$ through the whole sample, it facilitates multiple reflections between the dielectric interfaces, resulting in a Fabry-Pérot interference.

Next, assume a well-defined circularly polarized wave propagating along the z direction, normally incident on the front interface of the sample where the 2DES is located. Its electric field is given by

$$\boldsymbol{E}_i = E_0 \Re \hat{e}_\eta \exp\left[-\mathrm{i}(\omega t - kz)\right], \tag{2.35}$$

where the polarization unit vector $\hat{e}_\eta = \hat{e}_x + \mathrm{i}\eta\hat{e}_y$ defines the circular polarization of the wave with the helicity $\eta = \pm 1$. Furthermore, considering that the transport in the 2DES, characterized by the local dynamic conductivity tensor $\overleftrightarrow{\sigma}(\omega)$, is isotropic, i.e., $\sigma_{xx} = \sigma_{yy}$ and $\sigma_{xy} = -\sigma_{yx}$, it can be shown that the conductivity tensor is diagonal in the helicity basis [17]

$$\overset{\leftrightarrow}{\sigma}(\omega)\hat{e}_\eta = \sigma_\eta \hat{e}_\eta, \quad \text{with} \quad \sigma_\eta = \sigma_{xx} + \mathrm{i}\eta\sigma_{xy}. \tag{2.36}$$

Note that the time-reversal symmetry is broken ($\sigma_{xy} \neq 0$) due to the magnetic field applied perpendicular to the sample surface. Thus, the polarization state of the incident wave is generally different from that of the transmitted and reflected waves. However, in the case of an isotropic 2DES and a normally incident circularly polarized wave, its axial symmetry is preserved, so the circular components do not couple and can be considered independently. The corresponding electric field of the wave propagating in the z direction can be written for the whole spatial range as [17]

$$\boldsymbol{E}(z,t) = E_i \Re \hat{e}_\eta a(z) \exp(-\mathrm{i}\omega t)\,, \tag{2.37}$$

introducing $a(z)$ according to

$$a(z) = \begin{cases} \exp(\mathrm{i}kz) + r\exp(-\mathrm{i}kz)\,, & \text{for} \quad z < 0\,; \\ s_r \exp(\mathrm{i}k_r z) + s_l \exp(-\mathrm{i}k_r z)\,, & \text{for} \quad w > z > 0\,; \\ t\exp[\mathrm{i}k(z-w)]\,, & \text{for} \quad z > w\,. \end{cases} \tag{2.38}$$

Here the transmission and reflection amplitudes are defined by t and r, respectively, while $s = s_r + s_l$ considers the amplitude E_η of the field screened by the electrons in the 2DES [i.e., $\Re \hat{e}_\eta E_\eta \exp(-\mathrm{i}\omega t) = E_i \Re \hat{e}_\eta s \exp(-\mathrm{i}\omega t)$] passing it from the right or left side. Note that in the equations above the index η of the amplitudes t, r and s has been omitted for better readability. The corresponding partial waves are presented in Fig. 2.6. As dictated by Maxwell equations, the tangential component of the electric field at the interfaces of the sample substrate is continuous. Furthermore, since the EM wave induces a current within the 2DES, the corresponding alternating magnetic field, which is related to the current density by Ampère's law, exhibits a jump at the position of the 2DES. Thus, defining the vector $\mathcal{V}(z) = [a(z), \partial_z a(z)]^T$ for convenience and using the above boundary conditions, we obtain [17]

$$\mathcal{V}(\delta) = \mathcal{M}_{\text{2DES}}\mathcal{V}(-\delta) \quad \text{and} \quad \mathcal{V}(w+\delta) = \mathcal{M}_{\text{diel}}\mathcal{V}(\delta)\,, \tag{2.39}$$

with δ being a positive infinitesimal and

$$\mathcal{V}(\delta) = \begin{pmatrix} s_r + s_l \\ \mathrm{i}k_r(s_r - s_l) \end{pmatrix}, \quad \mathcal{V}(-\delta) = \begin{pmatrix} 1 + r \\ \mathrm{i}k(1 - r) \end{pmatrix} \quad \text{and} \quad \mathcal{V}(w{+}\delta) = \begin{pmatrix} t \\ \mathrm{i}kt \end{pmatrix}. \tag{2.40}$$

The transfer matrices in Eq. (2.39) are given by [17]

$$\mathcal{M}_{\text{2DES}} = \begin{pmatrix} 1 & 0 \\ 2\mathrm{i}\omega\sigma_\eta Z_0/c & 1 \end{pmatrix} \quad \text{and} \quad \mathcal{M}_{\text{diel}} = \begin{pmatrix} \cos\phi & k_r^{-1}\sin\phi \\ -k_r\sin\phi & \cos\phi \end{pmatrix}, \tag{2.41}$$

with the interference phase $\phi = k_r w$ defined above. The former transfer matrix describes the discontinuity of $\mathcal{V}(z)$ due to the alternating current (ac) generated inside the 2DES, whereas the latter accounts for the propagation of the EM wave inside the dielectric substrate. Solving the equations in (2.39) gives the expression for the transmission amplitude [17, 89]

$$t = \frac{1}{(1 + \sigma_\eta Z_0/2)\cos\phi - \mathrm{i}\left(\dfrac{1 + n_r^2 + n_r\sigma_\eta Z_0/}{2n_r}\right)\sin\phi} = \frac{2}{\xi_1(1 + Z_0\sigma_\eta) + \xi_2}, \tag{2.42}$$

where the complex parameters $\xi_{1,2} = \cos\phi - \mathrm{i}n_r^{\mp 1}\sin\phi$ describe the Fabry-Pérot interference caused by multiple reflections in the dielectric substrate. The corresponding field screened by the 2DES plane reads

$$s = 1 + r = t(\cos\phi - \mathrm{i}n_r^{-1}\sin\phi) = t\xi_1\,. \tag{2.43}$$

It should be noted that the helicity dependence of the amplitudes t, r and s is governed only by σ_η [Eq. (2.36)], which enters Eq. (2.42). The related expressions for transmittance $\mathcal{T}(B)$ and absorptance $\mathcal{A}(B)$ are given by [17]

$$\mathcal{T}(B) = |t|^2 \quad \text{and} \quad \mathcal{A}(B) = 1 - |r|^2 - |t|^2 = Z_0|t\xi_1|^2\Re\sigma_\eta\,. \tag{2.44}$$

Taking the complex dynamic conductivity of the 2DES $\sigma_\eta = en_e/(\mu^{-1} - \mathrm{i}B_{\text{CR}} + \mathrm{i}\eta B)$ using the Drude approximation, the transmittance and absorptance get the form [17, 89]

$$\mathcal{T}(B) = |\alpha|^2\left|1 - \frac{\beta}{\mu^{-1} + \beta - \mathrm{i}B_{\text{CR}} + \mathrm{i}\eta B}\right|^2 \tag{2.45}$$

and

$$\mathcal{A}(B) = \frac{Z_0|\xi_1\alpha|^2 en_e/\mu}{|\mu^{-1} + \beta - \mathrm{i}B_{\mathrm{CR}} + \mathrm{i}\eta B|^2} \,. \tag{2.46}$$

For convenience, the parameters $\alpha = 2/(\xi_1 + \xi_2)$ and $\beta = en_eZ_0/(1 + \xi_2/\xi_1)$ are introduced. The latter is related to Γ [see Eq. (2.24)] as $\beta = \Gamma B_{\mathrm{CR}}$, assuming constructive interference, see Chap 5. It is important to note that Eqs. (2.45) and (2.46) are derived for the case where the sample is illuminated from the 2DES side. However, if the sample is illuminated from the substrate side, the relation for $\mathcal{T}(B)$ remains unchanged, but $\mathcal{A}(B)$ has to be divided by the constant factor $|\xi_1|^2$.

To connect this presentation to the power absorption P_{abs} considered in Sec. 2.2, we recall that $P_{\mathrm{abs}} = I\mathcal{A}(B)$ with the Poynting vector $I = E_0^2/Z_0$ of the incoming wave can be equivalently written as

$$P_{\mathrm{abs}} = IZ_0|t\xi_1|^2\Re\sigma_\eta = E_{\mathrm{2D}}^2\Re\sigma_\eta \,, \tag{2.47}$$

where we used Eq. (2.44) connecting the external field E_0 with the self-consistent screened electric field E_{2D} in the plane of the 2DES. Therefore, the absorbed power as a response to the left-handed and right-handed circularly polarized states yields

$$P_\eta = E_{\mathrm{2D}}^2\Re\left\{\frac{en_e}{\mu^{-1} - \mathrm{i}B_{\mathrm{CR}} + \mathrm{i}\eta B}\right\} = \frac{E_{\mathrm{2D}}^2 en_e\mu}{1 + (B_{\mathrm{CR}} - \eta B)^2} = \frac{E_{\mathrm{2D}}^2\sigma_0}{1 + (\omega - \eta\omega_c)^2\tau_p^2} \,, \tag{2.48}$$

utilizing $\sigma_0 = en_e\mu$, $\omega_c = eB/m^*$ and $\mu = e\tau_p/m^*$, in accord with Eq. (2.23).

As will be discussed in Chap. 5, the transmitted signal through a 2DES obtained experimentally can be straightforwardly matched by Eq. (2.45) using n_e and μ as fixed parameters determined via standard magnetotransport measurements. Its shape, especially in the vicinity of the CR, determines the complex interference parameters $\xi_{1,2}$, providing full knowledge to model the absorptance as a function of the magnetic field.

2.3 μ-Photoconductivity

Another fundamental optoelectronic phenomenon is photoconductivity, which manifests itself as a higher-order correction of the induced electric current. It characterizes the change in the conductivity of the material caused by the excitation of radiation and can be generally expressed as [90]

$$j_\alpha = \sum_{\beta\gamma\delta} \sigma^{(3'')}_{\alpha\beta\gamma\delta} E_\beta(\omega, \boldsymbol{q}) E^*_\gamma(\omega, \boldsymbol{q}) E_\delta(\omega = 0, \boldsymbol{q} = 0)\,, \tag{2.49}$$

where the dc current is proportional to the third-order electric field. The fourth-rank conductivity tensor $\sigma^{(3'')}_{\alpha\beta\gamma\delta}$ facilitates the interaction between the static electric field $E_\delta(\omega = 0, \boldsymbol{q} = 0)$, provided simply by applying a bias to the system, and a term proportional to the intensity of the incident radiation $I \propto E_\beta(\omega, \boldsymbol{q}) E^*_\gamma(\omega, \boldsymbol{q})$ with frequency ω and photon wave vector $\boldsymbol{q}$. The decomposition of this tensor into its symmetric and antisymmetric components allows to distinguish between the linear and the circular photoconductivity [40].

Within the Drude model, the static conductivity is given by $\sigma_0 = e n_e \mu$, which contains the density, n_e, and the mobility, μ, of the charge carriers [3]. It is evident that varying either n_e or μ will change the conductivity of the system. Considering only optical excitations, the former case is typically achieved by the generation of electron-hole pairs caused by transitions between the valence and conduction bands [3], or by the selective generation of a specific type of carriers due to photoionization of deep or shallow impurities within a semiconductor [91]. In contrast, the change in mobility is a result of intraband transitions caused by Drude absorption, a process that is particularly important when the energies of the exciting radiation are smaller than the band gap and Fermi energy in the material under study. Absorption leads to radiation-induced heating of the charge carriers, resulting in a change in their energy distribution and hence their mobility. The corresponding mechanism is called μ- or bolometric photoconductivity [91].

This work focuses on the examination of high-density 2DES with radiation energies of the order of a few millielectronvolts. Such experimental conditions facilitate the study of the bolometric photoconductivity, which will be outlined in the following. In general, radiation-induced heating can be described by the energy balance equation

$$\mathcal{A}(I) I = Q(I)\,, \tag{2.50}$$

accounting for the energy $\mathcal{A}(I)I$ absorbed by the carriers and the energy losses $Q(I)$ governed by the energy flow from hot electrons to the lattice [91, 92]. The latter is characterized by the energy relaxation time $\tau_{\mathrm{e-ph}}$, a measure of the equalization of electron T_e and lattice temperatures T by inelastic electron-phonon scattering. However, at low temperatures a high-density 2DES is characterized by a fast electron-

electron scattering time τ_{ee}, leading to a fast equilibration of the electron gas. Therefore, an average electron temperature T_e is established, which consequently gives a well-defined shape of the equilibrium Fermi-Dirac distribution governed by the elevated electron temperature $T_e > T$. This temperature fully characterizes radiation-induced heating effects and should be found self-consistently from Eq. (2.50). At the same time, variations of the chemical potential in a degenerate high-density 2DES induced by electron gas heating can be disregarded.

Assuming the limit $I \to 0$, which corresponds to linear heating, the absorptance $\mathcal{A}(I)$ in Eq. (2.50) yields the linear response $\mathcal{A}(I \to 0)$. Under the condition of CR, this linear-response absorptance of a 2DES can be replaced by Eq. (2.46). Furthermore, in the linear regime the energy losses can be expressed in terms of electron and lattice temperatures, i.e., $Q(I) \propto (T_e - T)\tau^{-1}_{\mathrm{e-ph}}(T)$, leading to $T_e - T \propto I\mathcal{A}\tau_{\mathrm{e-ph}}(T)$ [48]. It is worth noting that the I-independent inelastic scattering time $\tau_{\mathrm{e-ph}}$ is assumed to be a function of the lattice temperature T only, satisfying the condition $T_e - T \ll T$, which is generally not true for arbitrary radiation intensities, as will be reviewed in Chap. 8.

In the case of weak heating, the corresponding μ-photoconductivity and photoresistance, the latter being more convenient for further consideration, are obtained by [91]

$$\Delta\sigma = \frac{\partial\sigma}{\partial\mu}\frac{\partial\mu}{\partial T_e}(T_e - T)\,, \tag{2.51}$$

and [48, 93]

$$\Delta R = \frac{\partial R}{\partial\mu}\frac{\partial\mu}{\partial T_e}(T_e - T)\,, \tag{2.52}$$

respectively. For zero magnetic field, the resistance is related to the conductivity via $R \propto \sigma^{-1}$ and the signs of μ-photoconductivity $\Delta\sigma$ and photoresistance ΔR are opposite. However, in this work the focus lies on the investigation of 2DES that are exposed to a classically strong magnetic field (in the sense of $\omega_c\tau_p \gg 1$). Under this condition the μ-photoconductivity and photoresistance exhibit the same sign. An increase of the mobility with growing electron temperature, occurring for instance when scattering on charged impurities dominates the energy loss rate, results in a negative μ-photoconductivity. On the other hand, a decrease in mobility due to strong electron-phonon interaction leads to positive μ-photoconductivity [3, 94], a behavior that predominates in the samples studied in this work.

2.4 Plasmons and Magnetoabsorption

This chapter is dedicated to a brief overview of plasmons and their properties. In general, plasmons describe collective excitations in electronic systems caused by a relative displacement of electrons from their positively charged background. Qualitatively, their origin can be understood as follows: Electrons that experience a restoring force due to positive ions tend to overshoot slightly with respect to their intended position, which would screen the electric field of the ions. Their velocity is reduced and they are attracted towards the ion exceeding the equilibrium position again. The consequence of this oscillatory motion is the appearance of charge density oscillations [33, 95–97].

In 2DES, the plasmon dispersion can be characterized in terms of hydrodynamics, which is based on macroscopic considerations of electron dynamics. In this sense, to describe the charge density waves inside the 2DES, $\delta n_e(\boldsymbol{r}, t)$ is introduced as a small variation of the electron density from its mean value and $\delta \boldsymbol{j}(\boldsymbol{r}, t)$ is its corresponding induced current density. Note that both are collective quantities obeying macroscopic conservation laws. In the long-wavelength limit, $q \ll k_{\mathrm{F}}$, and additionally assuming that $|\delta n_e / n_e| \ll 1$ (n_e yields the average carrier density of the 2DES, which is independent of spatial coordinates and time), the periodic density fluctuations follow the linearized Euler equation of motion given by [33, 95]

$$\frac{\partial \boldsymbol{j}(\boldsymbol{r}, t)}{\partial t} = -\frac{\mathcal{D}}{\pi e^2} \nabla_r \int \mathrm{d}^2 \boldsymbol{r}' \frac{e^2}{\epsilon |\boldsymbol{r} - \boldsymbol{r}'|} \, \delta n_e(\boldsymbol{r}', t) \,. \tag{2.53}$$

Here ϵ is the dielectric constant of the surrounding medium and $\mathcal{D}$ is the Drude weight. The integral describes the electrostatic potential and is evaluated at $\boldsymbol{r}$ considering the charges at $\boldsymbol{r}'$ with the respective density $\delta n_e(\boldsymbol{r}', t)$. Taking the divergence of both sides of Eq. (2.53) and using the relation $\partial n_e(\boldsymbol{r}, t)/\partial t = -\nabla \boldsymbol{j}(\boldsymbol{r}, t)$, which is the continuity equation for conserved quantities, the Euler equation takes the form [33, 95]

$$\frac{\partial^2 \, \delta n_e(\boldsymbol{r}, t)}{\partial^2 t} + \frac{\mathcal{D}}{\pi e^2} \nabla_r^2 \int \mathrm{d}^2 \boldsymbol{r}' \frac{e^2}{\epsilon |\boldsymbol{r} - \boldsymbol{r}'|} \, \delta n_e(\boldsymbol{r}', t) = 0 \,. \tag{2.54}$$

Utilizing the Fourier transform with regard to $\boldsymbol{r}$ and t yields the following equation for the Fourier component of $\delta n_e(\boldsymbol{r}, t)$

$$\left[\omega^2 - \frac{\mathcal{D}}{\pi e^2} q^2 u_q \right] \delta n_e(\boldsymbol{q}, \omega) = 0 \,, \tag{2.55}$$

where $u_q = 2\pi e^2/\epsilon q$ is the Fourier transform of $u_r(|\boldsymbol{r} - \boldsymbol{r}'|) = e^2/\epsilon |\boldsymbol{r} - \boldsymbol{r}'|$. As a result, Eq. (2.55) predicts the emergence of a density wave, i.e., plasmons with the plasma frequency $\omega_{\mathrm{pl}}(q) = \sqrt{\mathcal{D}\pi e^2 q^2 u_q} = \sqrt{2\mathcal{D}q/\epsilon}$. It is important to note that the square root behavior on the wave vector is a special feature of plasmons in two dimensions [98]. Consulting the expression for the Drude weight $\mathcal{D}$, the plasma frequency can be rewritten as [99–102]

$$\omega_{\mathrm{pl}}(q) = \begin{cases} \sqrt{\dfrac{2\pi e^2 n_e q}{\epsilon m^*}}\,, & \text{for parabolic dispersion}\,; \\ \\ \sqrt{\dfrac{2e^2 v_{\mathrm{F}}\sqrt{\pi n_e} q}{\epsilon\hbar}}\,, & \text{for linear dispersion}\,. \end{cases} \tag{2.56}$$

It follows that for massless Dirac fermions the plasma frequency scales proportional to $n_e^{1/4}$.

Applying a classically strong magnetic field B ($\omega_c\tau_p \gg 1$) perpendicular to the 2DES plane alters the plasmonic dispersion relations outlined above. In particular, due to the interaction of the electron plasma with the magnetic field, the carriers undergo a cyclotron motion. As a result, $\omega_{\mathrm{pl}}(q)$ reaches a gap at zero wave vector q determined by the electron's cyclotron frequency ω_c [103]. Consequently, magnetoplasmons obey the dispersion relation

$$\omega_{\mathrm{mp}} = \sqrt{\omega_{\mathrm{pl}}^2(q) + \omega_c^2(B)}\,, \tag{2.57}$$

where $\omega_{\mathrm{pl}}(q)$ is given by Eq. (2.56) and $\omega_c(B)$ by the corresponding expressions in Sec. 2.2. A detailed derivation of the plasmon dispersion in a strong magnetic field can be found in Ref. [103]. For illustration, both the plasmon and magnetoplasmon dispersions are sketched in Fig. 2.7(a) and (b), respectively.

Moreover, these plasma oscillations [Eq. (2.57)] are governed by an interaction with harmonics of the CR at large q[4]. This interplay manifests so-called Bernstein modes – a series of magnetoplasmon branches separated by gaps located near the harmonics of the CR, i.e., $\omega = n\omega_c$ with $n = 2, 3, \ldots$. – illustrated in Fig. 2.7(c). These gaps are usually smeared out by fast electron-impurity collisions, resulting in the conventional magnetoplasmon dispersion [104]. However, if the splitting remains, the absorption of an incoming EM wave is strongly enhanced near $\omega = n\omega_c$.

In the following, the magnetoabsorption of an inhomogeneous electric field by a 2DES is briefly outlined. Detailed calculations can be found in Refs. [45, 105]. For simplicity, the lateral dimensions of the absorbing ungated 2DES are assumed to be

---

[4] Here, the condition $qR_c \gtrsim 1$ has to apply, where $R_c = v_{\mathrm{F}}/\omega_c$ denotes the cyclotron radius.

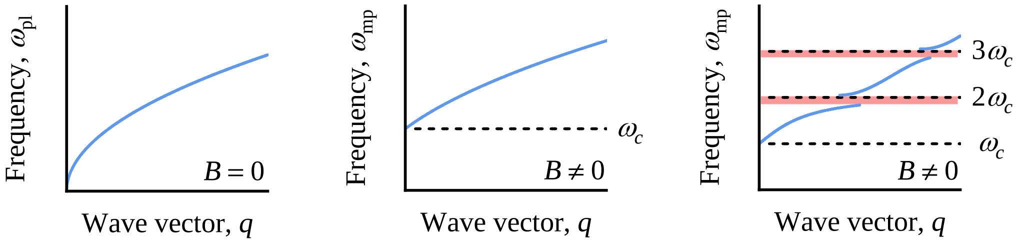

Figure 2.7: **(a)** Plot of the plasmon frequency ω_{pl} as a function of the wave vector q showing the plasmon dispersion at zero magnetic field B [see Eq. (2.56)]. **(b)** The corresponding magnetoplasmon dispersion of a 2DES exposed to a finite magnetic field demonstrating a gap at $q = 0$. The dispersion is calculated according to Eq. (2.57). **(c)** The interaction of the magnetoplasma dispersion with the harmonics of the CR is presented for the second and third harmonics. This behavior leads to a splitting of the magnetoplasmon dispersion into separate branches called Bernstein modes. These splittings are highlighted by the red shaded areas. In all panels, the sample containing the 2DES is assumed to be ungated. Figure adapted from Ref. [45].

infinite. The absorbed power is given by the Joule losses formula [45, 105]

$$P_{\mathrm{abs}} = 2 \int \Re\left\{\boldsymbol{E}(\boldsymbol{q},\omega)\boldsymbol{j}^*\right\} \mathrm{d}\boldsymbol{q}\,, \tag{2.58}$$

where $\boldsymbol{E}(\boldsymbol{q},\omega) = F_{\boldsymbol{q}\omega}\boldsymbol{E}_0$ represents the inhomogeneous electric field with its associated Fourier components $F_{\boldsymbol{q}\omega}$. Considering in addition Ohm's law $\boldsymbol{j} = \overleftrightarrow{\sigma}\boldsymbol{E}$ with the conductivity tensor defined as

$$\overleftrightarrow{\sigma} = \begin{pmatrix} \sigma_{xx} & -\sigma_{xy} \\ \sigma_{yx} & \sigma_{yy} \end{pmatrix}, \tag{2.59}$$

the absorbed power can be rewritten as [45, 105]

$$P_{\mathrm{abs}} = 2 \int \frac{\mathrm{d}\boldsymbol{q}}{(2\pi)^2} \Big(\Re\{\sigma_{xx}\}|\boldsymbol{E}(\boldsymbol{q},\omega)|^2 + \Im\{\sigma_{xy}\}\Im\{E_x^*(\boldsymbol{q},\omega)E_y(\boldsymbol{q},\omega)\}\Big)\,. \tag{2.60}$$

The incoming EM wave is screened by electrons in the 2DES. Assuming a sharp increase in the electron screening in the 2DES, the total potential in the electrostatic approximation created by the charge density $\rho(\boldsymbol{r}) \propto \mathrm{e}^{-\mathrm{i}\omega t}$ and governed by a short distance L from the 2DES plane reads

$$\varphi|_{z=0} = \frac{2\pi\rho(\boldsymbol{q})\mathrm{e}^{-qL}}{q\epsilon_0\epsilon(\boldsymbol{q},\omega)}\,. \tag{2.61}$$

Here ϵ_0 is the dielectric constant of the substrate and $\epsilon(\boldsymbol{q},\omega)$ represents the dielectric function. The latter can be obtained by solving the field equation of a symmetric and ungated 2DES with known conductivity $\overleftrightarrow{\sigma}$ under the condition $qL \ll 1$:

$$\left(\frac{\partial^2}{\partial z^2} - q^2\right)\varphi(\boldsymbol{q}, z) = \frac{4\pi}{\epsilon_0}\left[\rho_{\text{ind}}(\boldsymbol{q}) + \rho(\boldsymbol{q})\right]\delta(z)\,. \tag{2.62}$$

The induced charge density is defined as $\rho_{\text{ind}}(\boldsymbol{q}) = \boldsymbol{q}\boldsymbol{j}/\omega$. Thus, the dielectric function can be expressed as [45, 105]

$$\epsilon(q,\omega) = 1 + \mathrm{i}\frac{2\pi q}{\epsilon_0\omega}\sigma_{xx}(q,\omega)\,. \tag{2.63}$$

Considering the special case of absorption when an incident plane wave is diffracted by a thin contact resulting in an inhomogeneous charge field inside the 2DES [45], the respective absorbed power in Eq. (2.60) then takes the form [45]

$$P_{\text{abs}} = 2\int \frac{\mathrm{d}\boldsymbol{q}}{(2\pi)^2}\frac{\omega}{2\pi q}|\boldsymbol{E}(\boldsymbol{q},\omega)|^2\,\Im\left\{\epsilon(\boldsymbol{q},\omega)^{-1}\right\}\,. \tag{2.64}$$

Note that the second contribution proportional to $\Im\{\sigma_{xy}\}$ in Eq. (2.60) accounts for the polarization sensitivity of the regular CR at $\omega = \omega_c$. For the absorbed power near the CR harmonics, this term can be safely neglected because they are not affected by the polarization of the incoming EM wave diffracted by a thin contact. In fact, the electric field component perpendicular to the contact surface is enhanced whereas its tangential component is screened. Therefore, the resulting polarization of the diffracted wave is very close to a linear one.

3 Radiation Sources and Experimental Methods

First, the basic principles of the utilized THz sources are outlined, namely the optically pumped molecular gas laser, the impact ionization avalanche transit time diode, and the backward wave oscillator. Subsequently, the experimental techniques are described. These include the measurement of photoresistance, photovoltage, and transmittance, which are used to explore the CR-coupled effects. Finally, the investigated samples, namely GaAs and HgTe QWs as well as graphene, are discussed by examining their transport properties.

3.1 Optically Pumped Molecular Gas Laser

Stimulated far-infrared (FIR) radiation was first observed by Chang and Bridges in 1970 [106]. They obtained FIR continuous wave (cw) emission in methyl fluoride gas optically pumped by a carbon dioxide (CO_2) laser. Since then, a large number of emission lines have been found and characterized, ranging from tens of gigahertz to a few terahertz, with corresponding powers ranging from nanowatts to a few hundred milliwatts (for review, see, e.g., Refs. [107, 108]).

The physical concept of such lasers relies on transitions between rotational states in the vibrational spectrum of a molecule with a permanent dipole moment [91, 109]. The molecules are pumped by the cw CO_2 laser, which emits radiation in the mid-infrared (MIR) range with wavelengths from 9.2 to 11.2 μm within the P and R branches of the CO_2 molecule [110–112]. CO_2 is a linear molecule and has three vibrational modes, namely the symmetric stretching mode, the bending mode, and the antisymmetric stretching mode, which are assigned to four quantum numbers (ν_1, ν_2^l, ν_3). Here, l represents the angular momentum, quantized with $l = 0, \pm 1, \pm 2, \dots$. The gas mixture of the CO_2 pump laser usually comprises three molecules, namely CO_2, helium (He), and nitrogen (N_2). Figure 3.1(a) shows the energy scheme of the CO_2 laser. The N_2 molecules are excited to the first excited vibrational state ($\nu = 0 \to \nu = 1$), due to the longitudinal excitation of the gas admixture by electrical discharge [5]. Since N_2 has no permanent electric dipole moment, the transition is infrared inactive (IRI) and the state is metastable. This provides an effective way to transfer energy via collisions to the CO_2 molecules, whose first excited state of the antisymmetric stretching mode, (00^01), has nearly the same energy. Since (00^01) is infrared active (IRA), the creation of the population inversion in CO_2 yields transitions to (10^00) and (02^00) states, which generate the laser

---

[5] Excitation of the N_2 molecules by electron collisions is a more efficient process than the excitation of the much heavier CO_2 molecules.

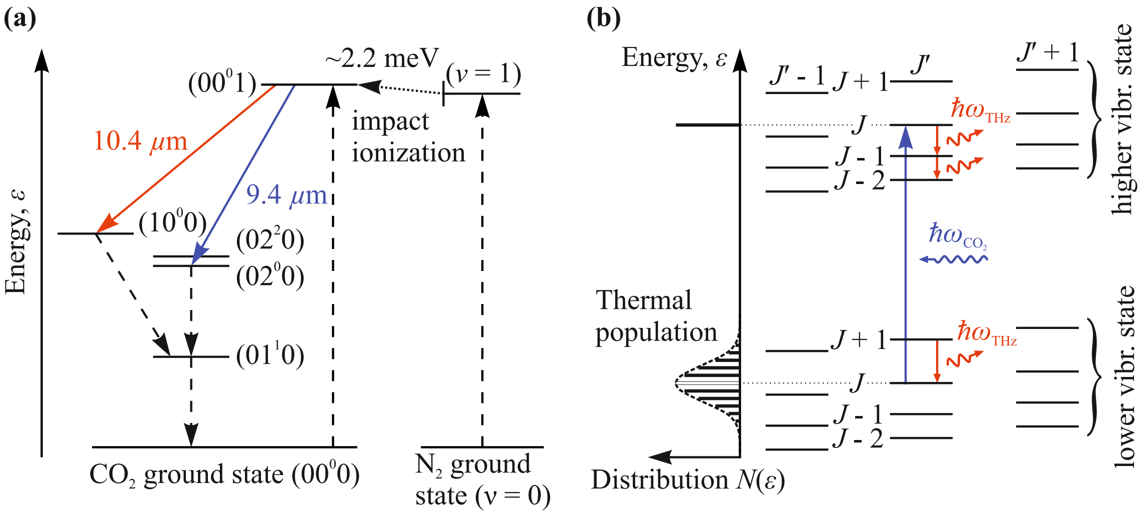

Figure 3.1: **(a)** Energy scheme of the lasing process of the CO_2 laser. N_2 is excited by an electrical discharge ($\nu = 0 \rightarrow \nu = 1$), which subsequently populates the antisymmetric stretching mode (00^01). The generated population inversion relaxes via radiative transitions, producing laser radiation (blue and red arrows). Dotted arrows indicate the excitation and relaxation processes. **(b)** Illustration of THz generation in a symmetric top molecule optically pumped by the CO_2 laser. J is the angular momentum quantum number and J' its projection on the symmetry axis of the molecule. The pump beam (blue arrow) excites a higher vibrational state causing a population inversion and a subsequent THz emission transition between the rotational states (red arrows). The scale on the left schematically shows the energy-state distribution $N(\varepsilon)$. The higher vibrational state is resonantly pumped, while the lower one is governed by the thermal distribution. Figure adapted from Ref. [91].

emission in the P and R branches of the CO_2 molecule. A Fermi resonance [113, 114] between the (10^00) and (02^00) states causes a splitting of the (02^00) and (02^20) states, which allows a radiative depopulation of (10^00) into (01^10). The latter also allows radiative transitions, since the bending mode causes a nonvanishing dipole moment and is therefore IRA. An effective non-radiative depletion of the energy states is additionally provided by the inelastic scattering of the CO_2 molecules with He atoms.

Wavelength selection is accomplished by a blaze grating, also known as an echelette. It is usually attached to the end of the laser near the rear resonator mirror and produces maximum reflection at a certain diffraction order, while the other orders are governed by high losses. By changing the angle between the optical axis and the mounted echelette grating, the desired laser line can be selected by effectively suppressing the other lines.

The CO_2 laser beam is then guided by mirrors into the FIR resonator, which is filled with a gaseous medium. The lasing process is shown in Fig. 3.1(b) as an example for a prolate top molecule[6] [115]. Here J' is the projection of the molecule's angular momentum onto its symmetry axis. Resonant pumping of the CO_2 laser excites the rotational states within the higher vibrational state, causing population inversion in both the excited and ground states. If the lifetime of the vibrational states is sufficiently long, the generation of THz radiation is achieved by relaxation of the rotational states. Importantly, radiative transitions between the excited states can only occur if the associated molecule has a permanent electric dipole moment. The generated FIR radiation is usually linearly polarized when excited by a linearly polarized pump beam. Indeed, under the condition that the angular momentum J is much larger than its projection J', the degree of linearly polarized radiation at the FIR output is high. This is facilitated by a low collisional reorientation time for $J' \ll J$ compared to transitions with $J' \approx J$. Furthermore, the polarization planes of the pump and FIR beams have the same orientation when the pump and laser transitions are governed by the same angular momentum change $|\Delta J|$. In other cases, the polarization planes are orthogonal [116].

Figure 3.4 shows the setup of the optically pumped molecular gas laser. The FIR is composed of a resonator cavity sealed with silver-coated quartz mirrors containing the gaseous molecular laser medium. Formic acid (HCOOH), difluoromethane (CH_2F_2), and methanol (CH_3OH) are used as active media, providing frequencies of $f = 0.69$, 1.63, and 2.54 THz with corresponding photon energies of 2.9, 6.7, and 10.5 meV, respectively. The FIR laser delivers maximum radiation powers in the range of 20 to 50 mW, see Tab. 1 for the main parameters. The laser output of the CO_2 can be brought into resonance with the desired laser line of the molecule by selecting the longitudinal laser mode by adjusting the echelette grating. A Brewster window at the MIR input ensures that the CO_2 radiation is vertically polarized. The longitudinal modes supported by the CO_2 can be selected by changing the length of the FIR resonator. Its length is mechanically varied by the mode controller. It should be noted that the different longitudinal modes strongly change the output power and intensity profile of the FIR beam and therefore have to be adjusted with care. In the case of the CO_2 resonator, a piezo element mounted on the decoupling mirror is used whose geometric parameters are varied by applying a bias voltage.

The next section covers the generation of THz radiation frequencies via the process of avalanche breakdown in semiconductor junctions.

---

[6] Prolate top molecules are characterized by two degenerate axes and one unique axis, where the inertia of the latter is less than the inertia of the degenerate axes. Examples of prolate molecules are fluoromethane (CH_3F) and ammonia (NH_3).

3.2 Impact Ionization Avalanche Transit Time Diode

The measurements were also performed for lower frequencies of fractions of terahertz, which could not be achieved with the laser. For this purpose, a continuously tunable cw source was used to provide frequencies in the range $f = 0.280$ to 0.312 THz (corresponding photon energies 1.1 to 1.3 meV) with a maximum output power of about 30 mW, which varies with the operating radiation frequency [see Tab. 1]. The source consists of two components connected by a coaxial connector of the type SMA (subminiature version A), see Fig. 3.4. The high-frequency radiation is generated by a local oscillator based on an impact ionization avalanche transit time (IMPATT) diode, providing frequencies in the range $f = 7.3$ to 14.6 GHz. Its output is fed into an amplifier multiplier chain that supports input frequencies from $f = 11.7$ to 13 GHz. The latter comprises a chain of Schottky diodes that generate the 24th harmonic of the input frequency to achieve the desired THz frequency range. A horn antenna is used to couple the radiation into the quasi-optical setup.

The operating principle of the IMPATT diode exploits the characteristics of a negative differential resistance caused by the combination of impact-ionization and transit-time effects in semiconductor devices [117–119]. William Shockley was the first to investigate the concept of negative differential resistance using the effect of the carrier transit time delay in 1954 [120]. Only after more than 10 years, Johnston et al. at Bell Telephone Laboratories succeeded in observing the first high-frequency oscillations using a silicon-based read-type diode [121, 122].

The fundamental phenomenon of high-frequency generation in an IMPATT diode is based on impact ionization. Consider a free-moving electron accelerated by an electric field in a material. If the kinetic energy of the accelerated electron is sufficiently high and an electron-atom collision occurs, the impact can ionize a secondary electron. As a result, it gains energy from the applied electric field and can release another electron. Repeating this process multiple times leads to an exponentially increasing number of ionized electrons and thus to an exponentially increasing current flow. This effect is called avalanche breakdown and results in a region of high resistance called the drift zone [3]. When a $p - n$ junction is reversely biased into avalanche breakdown, it can operate in the IMPATT regime. Figure 3.2(a) shows the cross-section of a high-low structure typically used to realize an IMPATT diode proposed by Read [121]. The $p^+ - n^+$ junction additionally comprises a n_A region of high doping and a n_B region of lower doping with a total length of W. This type is called a single-drift structure because only one type of charge carriers (electrons) travels through the drift region. The corresponding doping levels for each region are

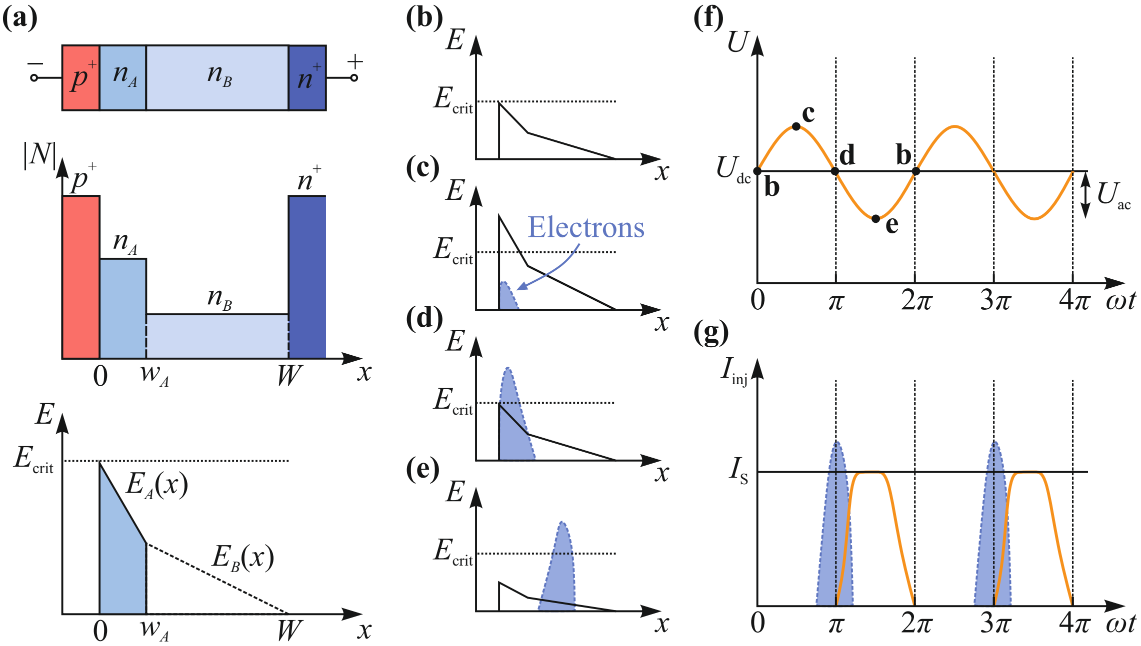

Figure 3.2: **(a)** Schematic illustration of a high-low IMPATT diode structure and its corresponding doping profile, as well as the electric field distribution just below the onset of the avalanche breakdown process at E_{crit}. The electric fields in the n_A and n_B regions are represented by $E_A(x)$ and $E_B(x)$, respectively. **(b – e)** Electric field distributions for different times shown in panel (f) of an ac voltage cycle applied to the high-low structure. The blue shaded areas indicate the corresponding generated electron densities. **(f)** Time evolution of the ac voltage with amplitude U_{ac} on top of the dc voltage U_{dc} applied to the structure. The bold letters b to e mark the time stamps for the corresponding panels. **(g)** Maximum carrier density (shaded blue) and the respective current flow (solid orange) generated in the structure by drifting carriers. The phase shift of π between U_{ac} and I_{inj} results in a negative differential resistance. Figure adapted from Ref. [117].

shown in the middle panel of Fig. 3.2(a). The ionization rate is strongly affected by the electric field. Therefore, the doping level of n_A and the thickness W of the drift region have to be chosen such that the majority of the avalanche processes (typically about 95 %) are located near the transition interface between the p^+- and n_A-doped regions. Here the electric field strength is highest. This region is indicated by the blue shaded area in the bottom panel of Fig. 3.2(a) displaying the respective electric field distribution [117, 121].

As a starting point, the diode is biased with a reverse dc voltage U_{dc}, chosen so that the threshold value for the avalanche electric field, denoted E_{crit}, is just not reached, see Fig. 3.2(b). In addition to U_{dc}, a small sinusoidal ac bias U_{ac} is applied. Initially ($t = 0$) U_{ac} is zero, see Fig. 3.2(f), which illustrates the time evolution of the ac voltage. For $t > 0$, the ac bias exceeds the avalanche threshold, causing the generation of electron-hole pairs due to impact ionization, see Fig. 3.2(c). As long as the applied bias is sufficiently high, resulting in an electric field above E_{crit}, the generation of electron-hole pairs grows exponentially with t. The ionized electrons are accelerated along the diode and drift towards the n^+ region, while the generated holes are collected at the p^+ contact. Even when the ac voltage begins to decrease again, the process of impact ionization remains intact, leading to a further increase in the electron-hole pair concentration. Since the density of generated electron-hole pairs also depends on the number of carriers already generated, there is a delay with respect to the applied electric field. Apparently, the concentration of the carrier peaks when the ac bias reaches the average voltage value U_{dc}, i.e., the ac component is zero, see Fig. 3.2(d). This delay results in a phase shift of $\pi/2$ due to the nature of the avalanche effect.

Subsequently, the ac contribution reaches the regimes where it falls below the avalanche threshold, see Fig. 3.2(e). The avalanche processes decrease exponentially and the electrons are injected into the n_B region drifting towards the n^+ contact. This results in the generation of a current in the external circuit, see Fig. 3.2(g). As the phase of this resulting current is opposite to that of the applied ac bias, the drifting electrons are slowed down by the ac field. This deceleration of the charges leads to a release of energy and can be used to form spontaneous oscillations in an appropriate circuit [117, 118, 121]. The transit time of the carriers gives a second shift that can be manipulated by adjusting the parameters of the diode. The ideal transit-time delay is achieved when the carriers traversing the drift region thickness W reaches the n^+ contact at the same time as the ac bias completes its negative half-cycle. Consequently, comparing the ac bias contribution and the external current shows that the transit-time delay exhibits a negative differential resistance characteristic [117, 121]. In this ideal case, the relation between the drift region thickness and the operating frequency reads [117, 121]

$$\frac{W - w_{\text{A}}}{v_{\text{sat}}} = \frac{1}{2f} \tag{3.1}$$

with the saturation velocity v_{sat}[7]. Adapting Eq. (3.1) yields the frequency of the system

$$f = \frac{v_{\text{sat}}}{W - w_{\text{A}}} \,. \tag{3.2}$$

Typical values used for a commercially available IMPATT diode with an operating

---

[7] The saturation velocity refers to the maximum velocity of charge carriers exposed to a high electric field in a semiconductor. Typical values for silicon and GaAs are of the order of 1×10^7 cm/s at $T = 300$ K, where the electric field strength can be several tens of kV/cm [123].

frequency of a few tens of gigahertz are in the range of a few micrometers. By changing the current in the diode or tuning the parameters of the connected circuits, the operating frequency of the diode can be varied. Indeed, by using specially designed cavities and circuits, these devices can be efficiently tuned over a wider range of frequencies [121, 124, 125]. It should be noted that the radiation generated by the IMPATT diode exhibits a high degree of phase noise. This is a consequence of the statistical nature of avalanche breakdown, which is due to random fluctuations in the impact ionization processes [117].

As mentioned above, the radiation produced by the IMPATT diode is fed into an amplifier multiplier chain that generates higher frequency harmonics. The chain is based on Schottky diodes, which have nonlinear current-voltage characteristics. Consider a sinusoidal signal $x(t) = x_0 \sin(2\pi f t)$ applied to a linear and a nonlinear circuit. The former reproduces the waveform, whereas the circuit with the nonlinear $I - V$ behavior distorts the sinusoidal signal, producing higher harmonics. This can be expressed by the Fourier series [121]

$$x(t) = \sum_{n=-\infty}^{\infty} c_n \exp(\mathrm{i}2\pi n f t) \quad \text{with} \quad c_n = \frac{1}{2\pi} \int_0^{t'} x(t) \exp(-\mathrm{i}2\pi n f t/t') \mathrm{d}t\,. \tag{3.3}$$

The latter describes the generated harmonics c_n, which are given by evaluating the integral within the interval determined by the fundamental period t'. The desired harmonic is then extracted by a bandpass filter and fed again into a nonlinear circuit in which the same process takes place. However, due to the relatively low efficiency of high harmonic generation, each conversion of the initially lower frequency to a higher one is associated with significant losses in output power. Consequently, such devices require very high input power in the range of a few watts [109, 121, 126].

The next section introduces another THz source belonging to the traveling-wave tube family. It is characterized by a wide continuous frequency tunability and covers a wide range of operating frequencies up to 1 THz.

3.3 Backward Wave Oscillator

The backward wave oscillator (BWO) is a special type of traveling-wave tube [127] in which an EM wave interacts with accelerated electrons to produce high-frequency radiation [109, 128–130]. The transfer of energy between a freely propagating EM wave and an electron beam is not possible, as the conservation laws for energy and momentum are not fulfilled for this process. However, this problem can be solved

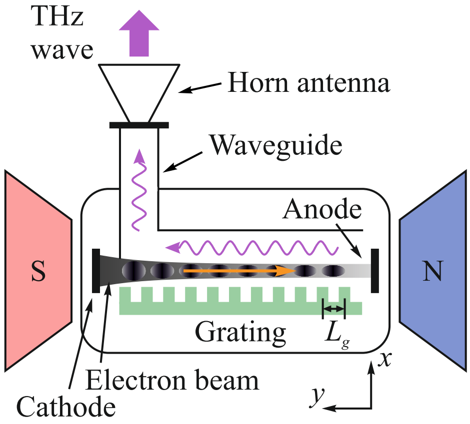

Figure 3.3: Structural design of the BWO. The electrons emitted by the cathode and focused by the magnetic field of a permanent magnet are generating a THz wave in the vicinity of a periodic grating with period L_g. The emerging THz radiation travels in the opposite direction of the electron beam and is guided through a waveguide. Figure adapted from Ref. [109].

by using a metallic periodic structure in the direction of the electron beam. The first BWOs were demonstrated as early as 1951, generating cw radiation in the frequency range from 1 to 40 GHz with corresponding powers of several hundred milliwatts [128, 131].

Usually the BWO is mounted in a quasi-optical setup where the THz radiation is coupled out of the waveguide by utilizing a horn antenna similar to the IMPATT diode system described in the previous section, see Fig. 3.4. The system used in this work was established at the technical university of Vienna and consists of several BWOs covering a frequency range between 50 and 500 GHz (corresponding photon energies 0.2 to 2.1 meV) with a maximum output power of a few milliwatts [see Tab. 1]. The corresponding experimental measurements were performed by Maxim Savchenko and Alexey Shuvaev in the group of Andrei Pimenov.

The BWO comprises a periodic metal structure, a strong permanent magnet and an electron gun, see Fig. 3.3. The heated cathode emits electrons, which gain energy from the applied dc electric field and are accelerated to the anode. The permanent magnets are mounted to collimate the electron beam. As the electrons move very close to the metallic periodic structure, they introduce surface charge waves via the Smith-Purcell effect [132]. This, in turn, produces an EM wave generated by Coulomb scattering at the boundaries of the structure, whose frequency is determined by the its period L_g. Since this EM wave also moves very close to the metallic structure, its phase velocity v_{ph} is reduced in the z direction. The harmonics m of the electric field of the EM wave depend on L_g and can be expressed in a Fourier series, which results in the corresponding phase velocity [109, 130]

$$v_{\mathrm{ph}} = \frac{\omega}{k_m} = \frac{\omega}{k_0 + 2\pi m/L_g}. \tag{3.4}$$

Apparently, harmonics with $m > 1$ experience a reduced phase velocity, which facilitates the interaction of the electron beam with the EM wave. Due to its electric-field components that are parallel to the path of the electrons, regions are formed in which the electrons are accelerated or decelerated. This causes a modulation in the density of the electron beam, known as bunching. The distance between the electron bunches is equal to the wavelength of the traveling EM wave. If the velocity of the electrons v_e is equal to the phase velocity of the EM wave, a synchronized state occurs and no energy transfer takes place between the electron beam and the EM wave. However, if the speed of the electrons is kept slightly higher than v_{ph} of the wave, the electrons will always be slightly decelerated by the components of the EM electric field that are parallel to their path, thus exchanging energy. This leads to an amplification of the propagating EM wave, which is decoupled by a waveguide. The resulting wave possesses a group velocity that is opposed to the direction of its phase velocity and is therefore called a backward wave [109, 128, 130, 133].

Now that the radiation sources have been outlined, the next section will examine the details of the measurement methods.

3.4 Measurement Techniques

This section outlines the experimental methods used to access the optoelectronic phenomena discussed in this thesis. First, the general setup for the different sources is presented, followed by specific descriptions of the measurement techniques, including photoresistance, photovoltage, and transmittance.

3.4.1 Experimental Setup

During the experiments, the sample was placed in a variable temperature insert (VTI) inside an Oxford Spectromag optical cryostat, accessible through optical windows made of z-cut quartz. The latter were covered with a polyethylene foil to avoid room light excitation, but at the same time allowing the to irradiate the sample with polarized THz radiation. A homogeneous magnetic field up to ±7 T was applied to the sample by a pair of superconducting solenoids. The achievable temperature range in the VTI lies between 1.8 and 300 K. For all measurements the THz beam was oriented perpendicular to the sample surface and parallel to the magnetic field

Source	f (THz)	λ (μm)	$\hbar\omega$ (meV)	d_{FWHM} (mm)	I (W/cm^2)
IMPATT	0.290	1034	1.20	5.9	0.03
IMPATT	0.297	1010	1.23	5.8	0.04
BWO	0.324	926	1.33	4.6	0.003
BWO	0.350	857	1.45	4.5	0.003
FIR laser	0.69	432	2.85	3.0	0.29
FIR laser	1.63	184	6.73	1.8	1.96
FIR laser	2.54	118	10.5	1.5	2.26

Table 1: The main parameters of the THz sources, including frequency f, corresponding wavelength λ, energy $\hbar\omega$, beam diameter at FWHM d_{FWHM} measured in the focal plane, and radiation intensity I.

in the so-called Faraday geometry. Figure 3.4 shows a schematic view of the laser (marked by a red dashed frame) and the IMPATT diode setup (marked by a cyan dashed frame). The generated THz radiation exiting the FIR laser cavity is collimated by a polymethylpentene (TPX) lens. The radiation then passes through a tilted mylar foil, resulting in a reflected beam and a transmitted beam. The former is guided and closely focused by a gold-coated off-axis parabolic mirror onto a pyroelectric reference detector. This detector feeds the CO_2 stabilizer, which controls the piezo-adjustable mirror inside the CO_2 resonator, stabilizing the FIR laser output via an internal phase-lock loop. The part of the beam passing through the mylar foil is modulated by a reflective opto-mechanical chopper. A fraction of the beam is reflected and then focused by a TPX lens onto a pyroelectric reference detector, which is used to monitor the laser power during measurements. The beam transmitted by the chopper traverses a number of auxiliary optical elements that are installed in the optical path depending on the type of measurement. To vary the beam power, two wire grid polarizers are used in a cross-polarizer configuration. In this configuration, the first polarizer can rotate freely to change the polarization and power of the initial beam. The second polarizer, however, remains fixed; thus, the radiation power is controlled and an unchanged output polarization is ensured for the whole power range [134, 135]. The polarization state itself is manipulated by rotating $\lambda/2$ and $\lambda/4$ waveplates made of x-cut quartz. The former changes the plane of the linear polarization component, while the latter affects the circular polarization contribution. After passing through the optical elements, the radiation was guided by gold-coated flat mirrors and then focused onto the mounted sample by an off-axis parabolic mirror. In addition, radiation transmitted through the sample can exit the cryostat through the rear windows and reach another pyroelectric detector directed by off-axis parabolic mirrors.

The radiation generated by the IMPATT diode is coupled into a linear or circular waveguide polarizer[8], which changes the polarization state as desired. The beam is then decoupled by a rectangular or conical horn antenna, depending on the polarization state used. A polytetrafluoroethylene (PTFE) lens collimates the beam, which is then directed by mirrors to the sample and transmittance detector using the same optical path as the laser. Modulation is provided by an internal waveguide modulator whose modulation frequency can be set by the lock-in amplifier. The power level of the delivered radiation is varied by the internal power attenuator.

As mentioned above, the BWO system is installed at the technical university of Vienna, and details of the actual setup can be found in Ref. [89]. However, it follows the same pattern as the IMPATT diode. The main difference is the control of the polarization state. Here, a so-called polarization transformer is used, which consists of a fixed polarizer mounted in parallel in front of a plane mirror. The polarization state can be adjusted by changing the distance between the two [12, 89]. The power level of the sources was calibrated using a thermopile sensor (3A-P-THz manufactured by Ophir Spiricon), which is calibrated for a spectral range of 0.3 to 10 THz. To record the intensity profile of the beam, a pyroelectric camera (PY-III-HR manufactured by Ophir Spiricon) was mounted at the sample position outside the cryostat. The camera has a spectral range of 0.1 to 300 THz and a pixel array with a size of 12.8×12.8 mm^2 with a resolution of 160×160 pixels. The analysis of the profiles showed an almost Gaussian intensity distribution, see Fig. 3.5(a) as a representative example measured at $f = 0.69$ THz. The spot diameters were determined as the full width half maximum (FWHM) of the recorded intensity profiles and ranged from 1.5 to 5.8 mm depending on the radiation frequency. As a result, the radiation intensities lie in the range of 0.05 to 3 W/cm^2. Figure 3.5 shows examples of laser [$f = 0.69$ and 2.54 THz] and IMPATT diode [$f = 0.297$ THz] beam spots. Table 1 shows a summary of the specific frequencies used in this work and their corresponding parameters.

In order to resolve the radiation-induced response of the sample and possible changes in the transmitted radiation, the signals were passed through coaxial cables with standard BNC (Bayonet Neill Concelman) connectors and then filtered using standard lock-in amplifiers. Depending on the signal strength, an operational amplifier with a gain of 100 is used in the setup. The cw THz beam is modulated either by an opto-mechanical chopper (laser, BWO) or by an internal waveguide modulator (IM-

---

[8] In contrast to conventional waveplates used in optical setups, the polarization state here is achieved by a geometric structure specially designed for the particular frequency band required.

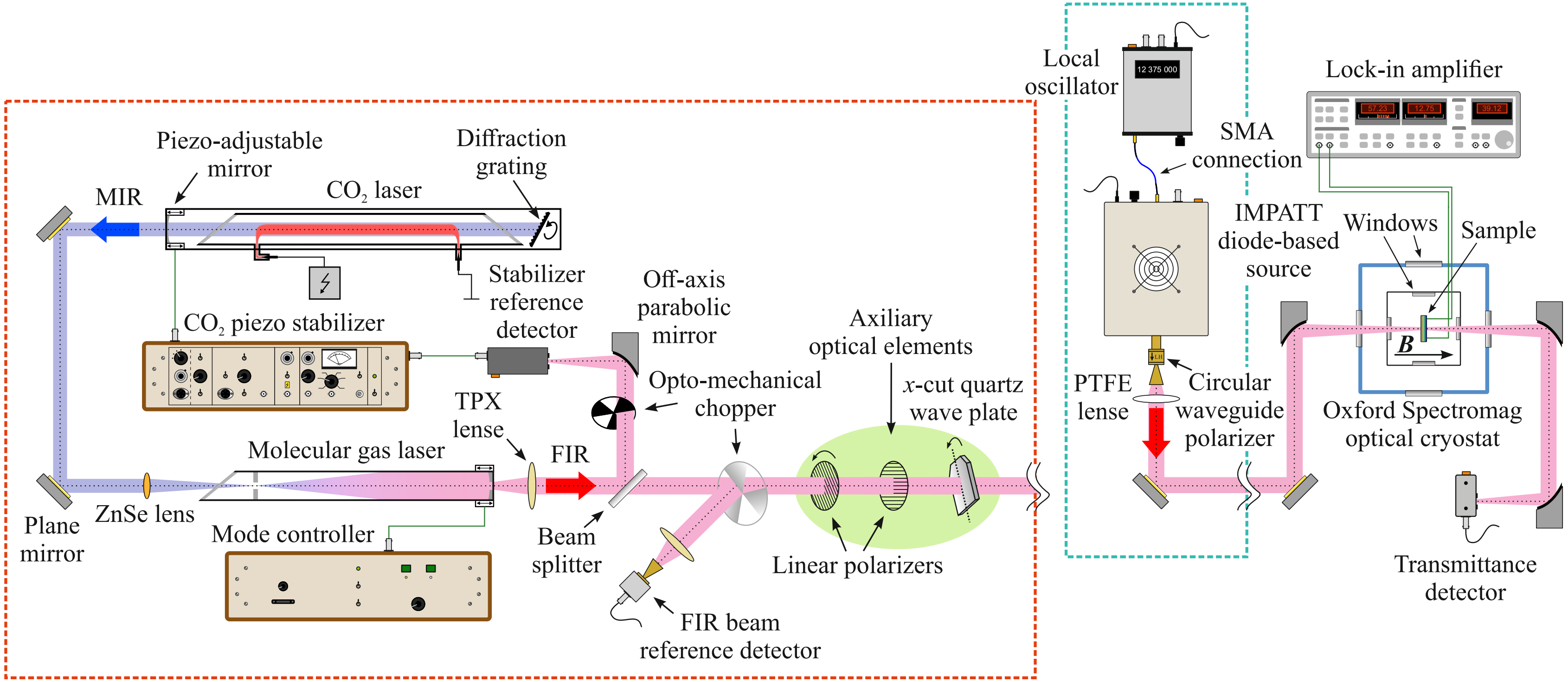

Figure 3.4: Setup sketch of the optically pumped molecular gas laser (framed by the red dashed rectangle) and the IMPATT diode (framed by the cyan dashed rectangle). Both setups use the same optical path to the sample, indicated by the s-shaped separator. The radiation passes through several optical elements before it is focused on the sample. For details, see the description in the main text. Figure adapted and modified from Ref. [91]

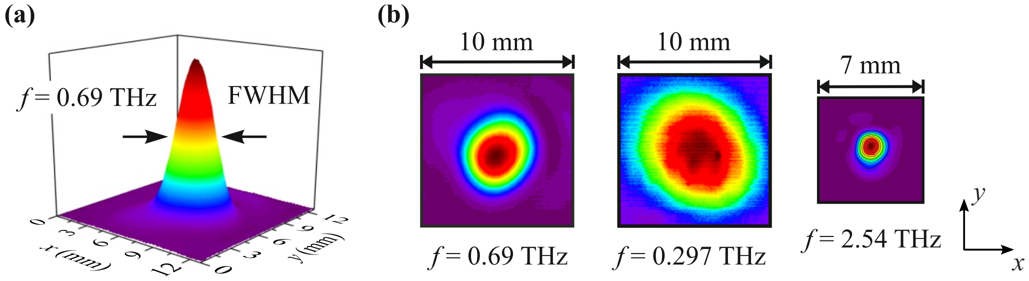

Figure 3.5: **(a)** Three-dimensional view of the intensity profile of the laser beam ($f = 0.69$ THz) recorded by a pyroelectric camera in the focal plane. The arrows represent the beam diameter at FWHM. **(b)** Two-dimensional intensity distribution of the beam spots at $f = 0.69$ and 2.54 THz (FIR laser) and $f = 0.297$ THz (IMPATT diode). Figure adapted from Refs. [47, 48].

PATT) with a frequency between 20 and 150 Hz. The data were recorded and stored by a LabVIEW instrument control script using the General Purpose Interface Bus (GPIB) protocol for communication with external measurement equipment. Details of the measurement techniques are described in the next section.

3.4.2 Photoresistance, Photovoltage, and Transmittance

The THz-induced changes in the samples were recorded via either the photoresistance or photovoltage method. The latter was performed by directly probing the desired contacts to obtain their potential difference generated in response to the chopper-modulated radiation, which was read out by standard lock-in technique. Importantly, this method does not require the application of any external bias to the sample. In contrast, the photoresistance is obtained by using both the modulated radiation and an additional ac bias U_{ac} applied via a load resistor R_{L} across the sample in either a four- or two-terminal contact configuration. This is called the double modulation technique [136–138]. Since the obtained photoresponse has to be demodulated twice, two lock-in amplifiers are connected in series. This provides a higher signal-to-noise ratio as compared to the photovoltage method.

Figure 3.6 shows the general measurement setup for photoresistance and transmittance [panel (a)] using a van der Pauw (vdP) configuration as an example, accompanied by a schematic illustration of the double-modulation technique [panel (b)]. Typically, the modulation frequency of the ac bias ($f_{\mathrm{ac}} = 5$ to 12 Hz) lies well below the modulation frequency of the radiation ($f_{\mathrm{chop}} = 130$ to 500 Hz). The optical response delivered by the sample is fed into the first lock-in amplifier phase-locked to f_{chop}, whose time constant is set to 10 ms (cutoff frequency at ≈ 16 Hz). As a result, the filtered total photosignal comprises a component proportional to the photovolt-

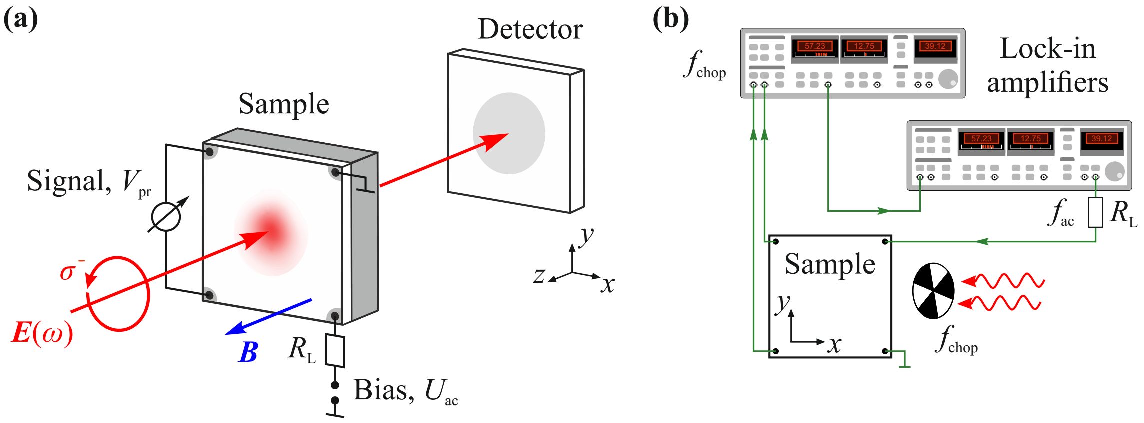

Figure 3.6: **(a)** Typical measurement configuration demonstrated for a sample in van der Pauw geometry. The sample is exposed to a magnetic field and illuminated by left-handed (σ^-) circularly polarized THz radiation. The transmitted radiation is recorded by the pyroelectric detector placed behind the sample. **(b)** Sketch of the double modulation technique with two lock-in amplifiers connected in series. The first receives the signal from the sample phase-locked to f_{chop} (modulation of the radiation, e.g., by an opto-mechanical chopper) and feeds the second, which modulates the current flowing through the sample with f_{ac}. Panel (a) is adapted from Refs. [47, 48].

age generated in the sample and a contribution alternating with f_{ac} proportional to the intended photoresistance. This total photosignal then enters the second amplifier (usually set to a time constant of 300 ms), which demodulates at f_{ac} and thus yields the desired photoresistance signal V_{pr}. Since the x channel is used to provide the signal filtered by the first lock-in amplifier, its sensitivity settings have to be taken into account. Finally, the measured signal is related to the photoresistance as

$$\Delta R = \frac{1}{10} \frac{S_1 V_{\text{pr}} R_{\text{L}}}{|U_{\text{ac}}|} \,, \tag{3.5}$$

where S_1 is the applied sensitivity setting of the first lock-in amplifier. Equation (3.5) assumes that the x channel of the first lock-in amplifier provides the majority of the induced photosignal. In this case, the photoresistance is the difference between the resistance of the sample measured with and without THz illumination. Note that it is also possible to invert this technique by first feeding the lock-in amplifier that provides the ac current and then connecting the second lock-in that is phase-locked to the radiation modulation, see, e.g., Ref. [89]. The modulation frequencies have to be adjusted accordingly.

Furthermore, the setup is prepared to measure the radiation transmitted by the sample simultaneously with the photovoltage or photoresistance. As mentioned in

Sec. 3.4.1, this is achieved by directing the radiation onto a low-noise pyroelectric detector using a lock-in amplifier phase locked to f_{chop}.

In the following, the fabrication processes of the investigated samples and their transport characteristics are outlined.

4 Samples

This chapter is dedicated to the description of the investigated samples. In the first part, GaAs and HgTe-based QWs are discussed, focusing on their fabrication process and transport characteristics. In this context, differences in the technological design of the samples, namely GaAs #A, #B, and #C, are highlighted. The graphene samples studied are then reviewed in a similar manner.

4.1 Gallium Arsenide and Mercury Telluride Quantum Wells

In this thesis, several 2DES are studied, among them AlGaAs/GaAs, including GaAs #A and #B with a QW thickness d_{QW} of 10 nm, and GaAs #C with $d_{\mathrm{QW}} = 16$ nm. In addition, HgCdTe/HgTe QWs are investigated, namely HgTe #A and #B with QW thicknesses of 8.1 (inverted band order) and 5.7 nm (regular band order). Both types of heterostructures were fabricated in vdP geometry.

Figure 4.1 shows the cross section of GaAs #A and #B [panels (a, b)] as well as GaAs #C [panel (c)]. All three AlGaAs/GaAs QWs heterostructures were grown on (001)-oriented GaAs substrates (thickness of 350 μm) by molecular beam epitaxy (MBE). For GaAs #A and #B, a 100 nm thick buffer layer was first deposited on the substrate, followed by an AlGaAs/GaAs superlattice containing 100 alternating periods of 7 nm AlGaAs and 3 nm GaAs to reduce the influence of impurities on the active layer. GaAs QWs with thicknesses of 10 nm were then grown on the prepared wafers, sandwiched between 85 nm (100 nm) AlGaAs layers on the bottom side and 30 nm (45 nm) AlGaAs on the top side for GaAs #A (GaAs #B). The aluminum content in the AlGaAs layers was 32 %. Finally, a GaAs coating was deposited on the heterostructures to avoid oxidation processes. In addition, silicon (Si)-delta dopants were introduced on both sides at 10 nm (GaAs #A) and 25 nm (GaAs #B) symmetrically around the QWs. The dopant concentration was also chosen to be symmetrical [139]. The overall growth temperature was 570 °C. However, to avoid segregation of the Si-delta dopants, the temperature was lowered to 500 °C, while the buffer layer was deposited at 620 °C.

The GaAs #C was grown on a 1 μm thick buffer layer deposited on the 350 μm thick GaAs substrate followed by 30 nm of AlGaAs. In contrast to GaAs #A and #B, the 16 nm thick QW in GaAs #C was covered from both sides by AlAs/GaAs superlattice barriers selectively doped with Si-delta dopants. The detailed layer thicknesses and locations of the Si-delta dopants are shown in Fig. 4.1(b).

The HgCdTe/HgTe heterostructures were also grown by MBE on GaAs substrates.

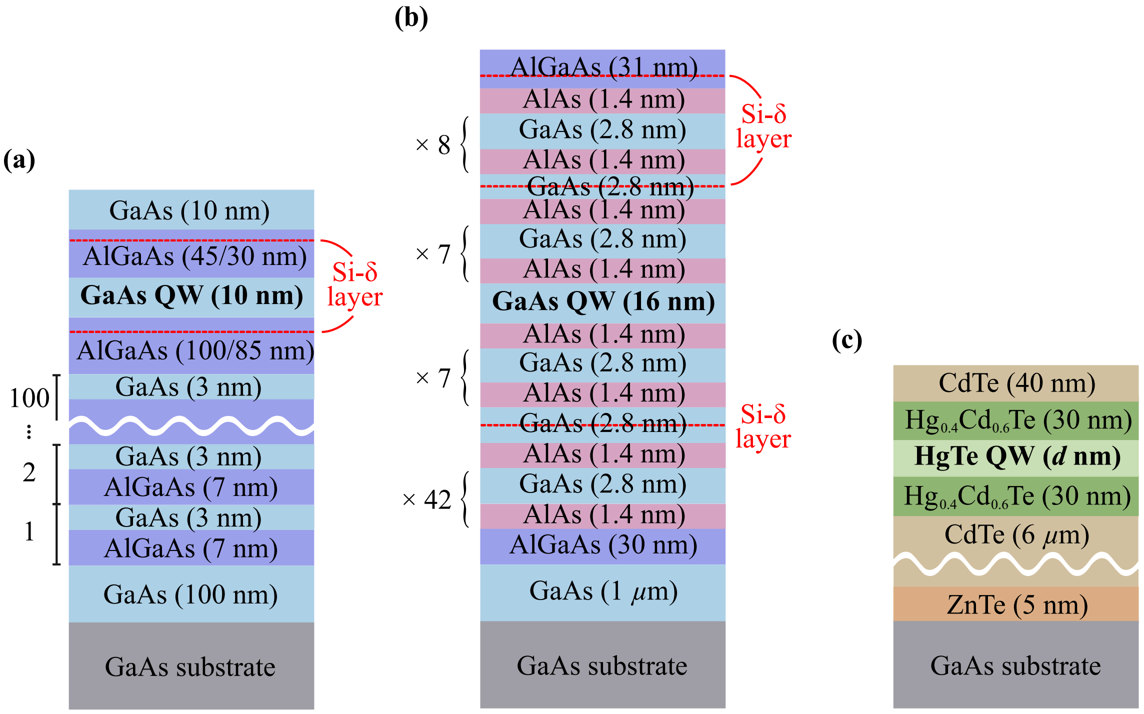

Figure 4.1: Cross sections of the investigated QW samples. **(a)** Composition of AlGaAs/GaAs QWs (GaAs #A and #B). The numbers in parentheses indicate the corresponding layer thicknesses. The samples differ in the thicknesses of the AlGaAs layers surrounding the QW denoted by $(d_{\#\mathrm{A}}/d_{\#\mathrm{B}})$. The red dashed lines represent the Si-delta doped layers. **(b)** Structure of the AlAs/GaAs QW (GaAs #C) fabricated with AlAs/GaAs superlattice barriers. **(c)** Cross section of the HgCdTe/HgTe QW with different QW thicknesses $d_{\mathrm{QW}} = 8.1$ nm (HgTe #A) and $d_{\mathrm{QW}} = 5.7$ nm (HgTe #B). Figures adapted from Refs. [47, 89] and supplemental material therein.

The latter was (013)-oriented and prepared by chemical etching and thermal annealing in arsenide flux. First, a 5 nm zinc telluride layer was deposited on the substrate, followed by a 6 μm CdTe layer to avoid strain-related effects due to lattice mismatch. Subsequently, 5.7 nm (HgTe #A) and 8.1 nm (HgTe #B) HgTe QWs were grown encapsulated by $\mathrm{Hg_{0.4}Cd_{0.6}Te}$ of 30 nm thickness from each side. These QWs possess normal (5.7 nm) and inverted (8.1 nm) band orders, see Sec. 2.1.2. A 40 nm thick layer of CdTe was deposited on top as a cap layer [140, 141]. During the growth procedure the temperature was kept between 180 and 190 °C. The cross section of the heterostructure with corresponding layer thicknesses is presented in Fig. 4.1.

The fabricated heterostructure wafers of GaAs and HgTe were cut into 10×10 mm^2 and 7×7 mm^2 square samples, respectively, and provided with ohmic contacts at the corners. These sizes exceed the FWHM diameters of the THz beam spots and thus exclude the contribution of edges and contacts to the photoresponse. Figure 3.5(b) shows the recorded intensity distribution of the beam spots for $f = 0.69$

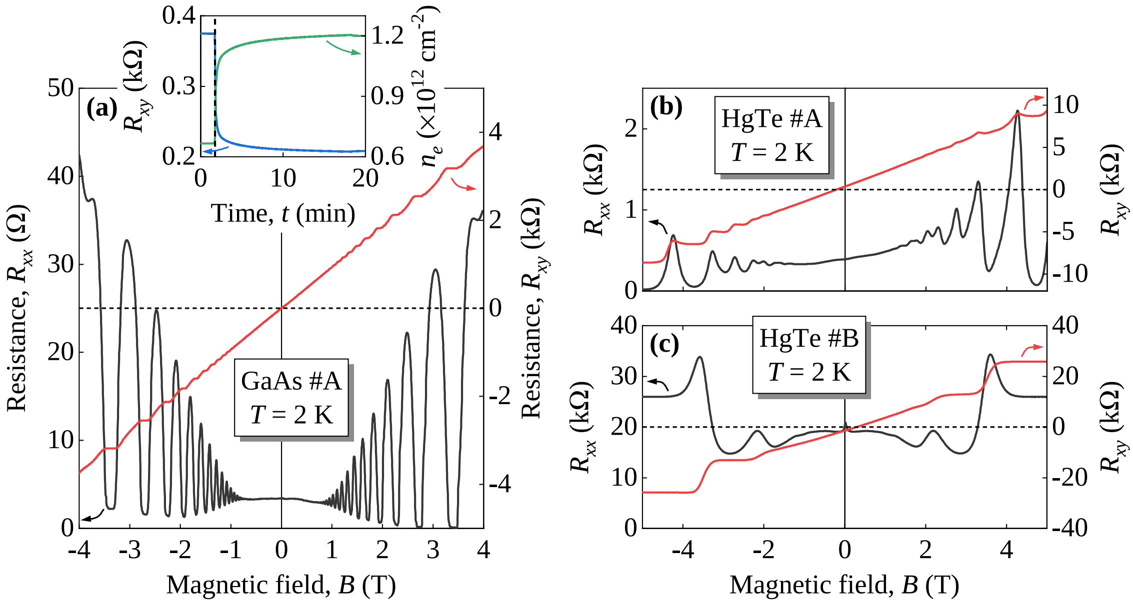

Figure 4.2: Representative traces for the longitudinal R_{xx} (black) and Hall R_{xy} resistances (red) of the QW samples measured at $T = 2$ K showing pronounced SdHO and Hall plateaus. **(a)** Magnetoresistance curves for GaAs #A. The inset shows the change in Hall resistance and carrier density as a function of time t during room light illumination. The black dashed line in the inset indicates the point in time at which the sample was started to be exposed to ambient light. **(b, c)** Traces for HgTe #A [panel (b)] and #B [panel (c)]. The latter was illuminated prior to the measurements. Figure adapted from Ref. [47] and supplemental material therein.

and 0.297 THz within a 10×10 mm^2 area representing the GaAs samples and the spot for $f = 2.54$ THz place in a 7×7 mm^2 area (HgTe samples). Thereafter, the samples were glued to carriers and attached to the sample probe. These carriers allowed to record the transmitted radiation by implementing apertures larger than the beam diameters. Soldered gold wires served as connections between the sample contacts and the socket pins of the carrier.

Figures 4.2(a) to (c) show typical magnetotransport traces of the GaAs- and HgTe-based QWs obtained at $T = 2$ K. The longitudinal resistance R_{xx} is dominated by pronounced SdHO starting at fields below 2 T, while the corresponding R_{xy} component exhibits well-defined plateaus. In addition, the QW structures were in some cases illuminated by ambient light prior to the measurements, leading to a substantial increase in carrier density. The inset in Fig. 4.2(a) shows the temporal evolution of the Hall resistance and the corresponding carrier density for GaAs #A during the exposure to ambient light. After the polyethylene cover was removed from the cryostat windows, the Hall resistance decreased significantly due to the persistent photoconductivity effect [3, 52, 142–146]. When the sample is exposed to ambient light, electrons from so-called DX centers – deep donor impurities with comparably

Sample	QW thickness (nm)	Lateral size (mm^2)	n_e 10^{11} (cm^{-2})	μ 10^4 (cm^2/Vs)	τ_p (ps)
GaAs #A	10	10 × 10	6.8 [12]	37 [66]	13 [24]
GaAs #B	10	10 × 10	6.7 [12]	20 [43]	7 [15]
GaAs #C	16	10 × 10	6.9	100	36
HgTe #A	8.1	7 × 7	3.6	1.8	0.3
HgTe #B	5.7	7 × 7	1.3	0.9	0.13

Table 2: Summary of the main parameters for the GaAs- and HgTe-based QW samples, namely GaAs #A to #C as well as HgTe #A and #B. The first two columns show the QW thicknesses and the corresponding lateral dimensions (length × width) of the square vdP samples. The data for carrier density n_e, mobility μ and momentum relaxation time τ_p were extracted from magnetotransport data obtained at $T = 1.8$ K. The parameters for GaAs QWs in square brackets were obtained after brief exposure to ambient light.

high energy barriers – are ionized, resulting in an increase of the density of mobile conduction carriers [52, 146]. These contribute to the conductivity of the QW, resulting in lower resistance. If the sample is kept in the dark, this state relaxes very slowly (the electrons are slowly trapped again) and lasts for a few hours below $T = 150$ K. Above this temperature, the DX centers are thermally ionized and a subsequent cooldown returns the sample to its previous state before illumination. It is worth noting that GaAs #C showed no significant changes in transport properties such as resistance, carrier density, and mobility, which are attributed to its different fabrication process. The main parameters for all samples obtained from magnetotransport measurements are presented in Tab. 2.

4.2 Encapsulated Monolayer Graphene

Besides the GaAs- and HgTe-based QWs presented in the last section, several monolayer graphene samples with different fabrication techniques are investigated. Details on the specific fabrication techniques for MLG #A, #B, and #C can be found in Refs. [47], [45], and [46], respectively, as well as in the corresponding supplemental material.

The encapsulated monolayer graphene samples used in this work were prepared by a hot-release method described in Ref. [147]. First, the graphene flakes were mechanically exfoliated from a high-purity pyrolytic graphite crystal using the scotch-tape technique [27]. Layers of hexagonal boron nitride (hBN) were used to encapsulate the graphene flake and protect it from adsorbates such as H_2O. The crystals were

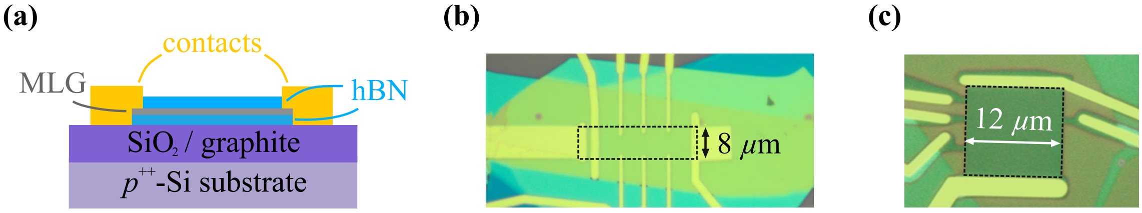

Figure 4.3: **(a)** Cross section of the graphene structures with a $\mathrm{SiO_2}$ (MLG #A and #B) or graphite (MLG #C) backgate. **(b)** Microphotograph of a MLG #B with special contacts protruding into the Hall channel. **(c)** Microphotograph of MLG #C equipped with conventional contacts. The graphene area is indicated by the dashed rectangle. Figures adapted from Refs. [45–47] and supplemental material therein.

stacked using a micromanipulator with a dome-shaped stamp from a polycarbonate film on polydimethylsiloxane. The resulting hBN/MLG/hBN van der Waals structure was picked up and stacked either on a prepared multilayer graphite backgate electrode (MLG #C) or on a conventional p^{++}-doped Si/$\mathrm{SiO_2}$ silicon wafer with 285 nm $\mathrm{SiO_2}$ thickness (MLG #A and #B). Electron beam lithography was then applied to the structure to form the contact regions in preparation for the Hall-bar configuration. The areas of the top hBN unprotected by the lithographic resist were removed by reactive ion etching with oxygen and sulfur hexafluoride gases. The resulting trenches were used to deposit gold and chromium electrical contacts with a typical total thickness of up to 100 nm by thermal evaporation in high vacuum. For MLG #B, an additional gold top gate etch mask was used to process the special contact geometry. Figure 4.3(a) shows a schematic cross section and Figs. 4.3(b) and (c) present microphotographs of MLG #B and #C, respectively. The dimensions of the structures are given in Tab. 3. The fabricated samples were mounted on a ceramic carrier using conductive silver paste to optionally attach the silicon backgate. The contact pads were connected with gold wires using a solderless bonding technique. Finally, the prepared samples were attached to a sample probe. Figure 4.4 presents transport and magnetotransport for MLG #B, representing a typical behavior of high-quality graphene samples. Clear resistance maxima are observed for all samples studied when the backgate voltage U_{BG} and thus the carrier density n_e were tuned. The dependence of the longitudinal resistance R_{xx} on n_e obtained at zero magnetic field is shown in Fig. 4.4(a). Due to the injection of carriers, an electric field is established between the Si wafer and the graphene flake, resulting in a carrier density n_e proportional to the effective gate voltage.

Since the tuning of the back gate voltage consequently controls the level of the Fermi energy via $\varepsilon_{\mathrm{F}} = \hbar v_{\mathrm{F}}\sqrt{\pi n_e}$, the resistance maxima are clearly attributed to the charge neutrality point (CNP), i.e., the Dirac point in the energy dispersion

Sample	Size length [width] (μm)	hBN top [bottom] (nm)	n_e 10^{11} (cm^{-2})	μ 10^4 (cm^2/Vs)	τ_p (ps)
MLG #A	24 [5]	32 [40]	21	24	4.5
MLG #B	32 [8]	48 [53]	39	30	8
MLG #C	11.5 [12]	18 [25]	27.5	30	5.8

Table 3: Summary of the main parameters for monolayer graphene sample MLG #A to #C. The dimensions of the graphene flakes and the thicknesses of the encapsulating hBN layers are given in the first two columns. Carrier density n_e, mobility μ, and momentum relaxation time τ_p were obtained from standard magnetotransport data at $T = 1.8$ K and the highest possible backgate voltage for each structure.

of graphene. This point represents the carrier type transition and the electron-like states are located to the right of the resistance maximum and the hole-like states to the left. Note that there may be a slight shift of the CNP and thus of the resistance maxima with respect to the applied gate voltage, revealing a low residual doping of the graphene structure. In addition, a minimal hysteresis was observed by comparing measurements with opposite gate sweep directions. To avoid any shifts, the experiments were always performed with the same sweep direction.

Exploiting the standard Drude model relation $R_{xx} = L/(en_e\mu W)$, where L and W represent the length and width of the measurement channel, yields the mobility μ, the momentum relaxation time τ_p as well as the mean free path l_{mfp} of the samples. The main parameters for MLG #A to #C are given in Tab. 3. As an example, Figs. 4.4(a, b) show the dependencies of μ, τ_p, and l_{mfp} on the carrier density for MLG #B. Note that the momentum relaxation time and the mean free path are almost independent of n_e. Furthermore, the mean free path $l_{\mathrm{mfp}} \approx 8$ μm resembles the width of the device, thus demonstrating ballistic electron transport at $B = 0$ mainly driven by scattering at the edges of the graphene channel. This behavior is further supported by the magnetoresistance $R_{xx}(B)$ shown in Fig. 4.4(c). Here, a strong decrease in resistance is observed as the magnetic field is increased, resulting in a negative differential magnetoresistance at $|B| < 1$ T. Such behavior can be understood in terms of skipping orbits formed by the magnetic field [148, 149]. The radius of these cyclotron orbits becomes smaller with increasing B, eventually reaching a diffusive transport regime characterized by cyclotron orbits smaller than the width of the device. In this regime, the transport properties are not affected by backscattering at the edges. The red trace in Fig. 4.4(c) shows the corresponding Hall resistance R_{xy}. A very similar transport and magnetotransport behavior was also observed in MLG #A and #C, see Refs. [46, 47] and supplemental material therein. However, in MLG #C the negative differential magnetoresistance was less pronounced because

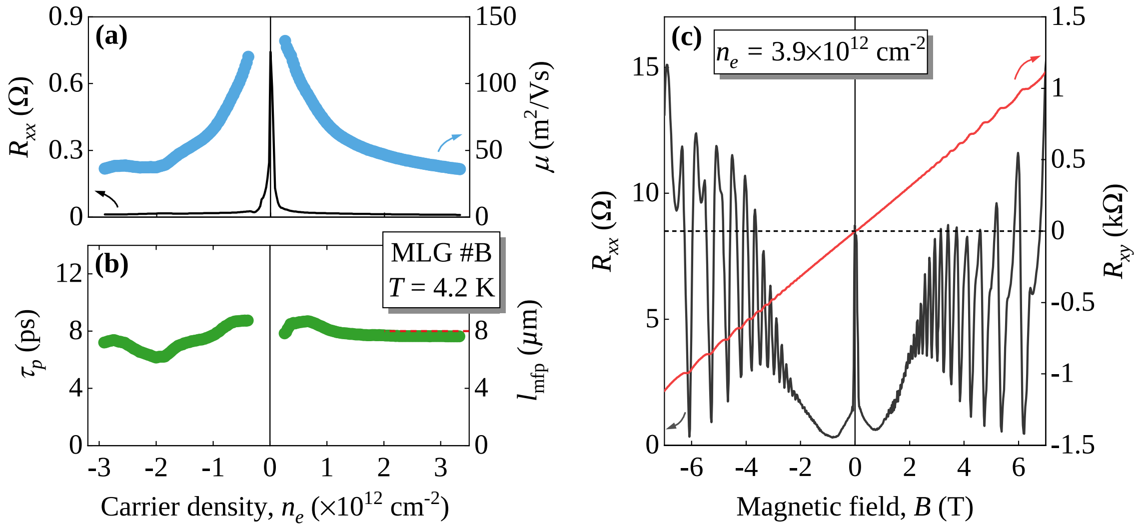

Figure 4.4: Transport and magnetotransport in MLG #B measured at $T = 4.2$ K. **(a)** Longitudinal resistance (black trace) and mobility (blue circles) as a function of the carrier density n_e. **(b)** Dependence of the momentum relaxation time τ_p and the corresponding mean free path l_{mfp} on n_e. The red dashed line indicates the width of the device channel, see Fig. 4.3(b). **(c)** Corresponding longitudinal R_{xx} and Hall resistance R_{xy}. Figure adapted from Ref. [45] and supplemental material therein.

the momentum relaxation time was shorter. These results clearly demonstrate the diffusive nature of the dc transport in the magnetic field range relevant for the studied effects and further confirm the excellent quality of the investigated structures.

A further evidence for the transition to the diffusive transport regime was observed by examining the transport properties of MLG #B, see Fig. 4.5(a). At $T > 15$ K, the SdHO are superimposed by less frequent phonon-induced resistance oscillations (PIRO), previously known from studies on GaAs-based QWs [13, 150, 151] and recently observed in high quality graphene samples [152]. This phenomenon is governed by the ratio of the acoustic phonon energy $\varepsilon_{\mathrm{phonon}} = 2\hbar k_{\mathrm{F}} v_{\mathrm{s}}$ (where v_{s} denotes the speed of sound) and the cyclotron energy $\hbar\omega_c$. The former is required to back-scatter an electron at the Fermi surface via inelastic scattering events by low-energy acoustic phonons. This process leads to resonant inter-LL transitions and the resistance is resonantly enhanced at

$$p = \frac{2\hbar k_{\mathrm{F}} v_{\mathrm{s}}}{\hbar\omega_c} = \frac{h v_{\mathrm{s}} n_e}{e B v_{\mathrm{F}}} \tag{4.1}$$

in graphene structures. The participating acoustic phonons require sufficiently high temperatures, in contrast to the SdHO, which are thermally suppressed at $T \approx 25$ K at relevant magnetic fields. This fact is reflected in a non-monotonic behavior of

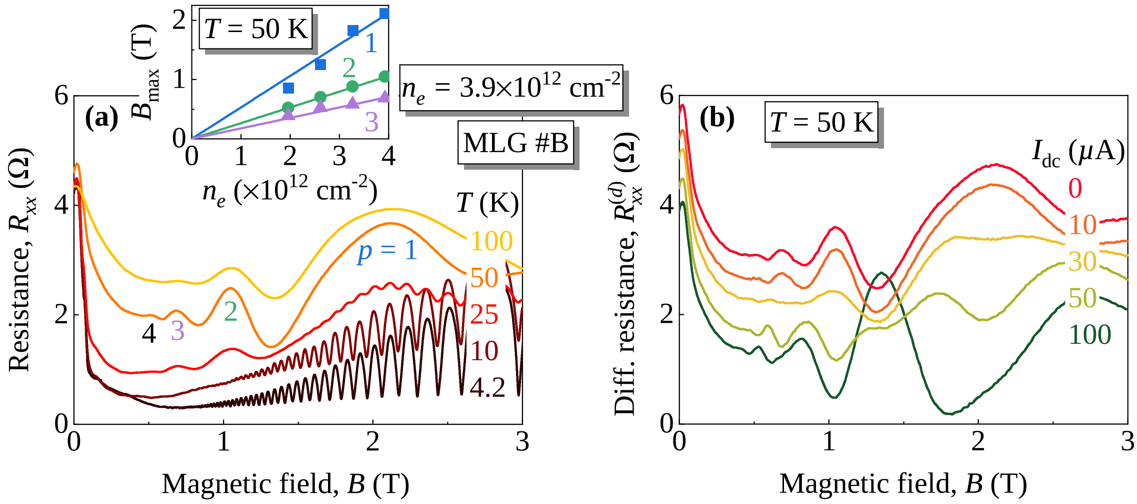

Figure 4.5: **(a)** Longitudinal resistance illustrating the evolution of PIRO and SdHO with temperature up to $T = 100$ K. While the SdHO are strongly suppressed, PIRO grow significantly with temperature. The maxima of the latter are marked with $p = 1, 2$ and 3. The inset shows the magnetic field values of the PIRO maxima B_{max} at $p = 1$ (blue squares), $p = 2$ (green circles), and $p = 3$ (purple triangles) plotted against n_e. The corresponding colored solid lines are fits according to Eq. (4.1) with $v_{\mathrm{F}} = 1.06 \times 10^6$ m/s and $v_{\mathrm{s}} = 1.36 \times 10^4$ m/s. **(b)** Longitudinal resistance $R_{xx}^{(d)} = (\mathrm{d}V_x/\mathrm{d}I_x)_{I_x=I_{\mathrm{dc}}}$ at $T = 50$ K under the influence of a strong dc bias. The traces are shown for different values of the injected current I_{dc} and are shifted vertically for clarity. The data in both panels were obtained for $n_e = 3.9\times10^{12}$ cm^{-2} in MLG #B. Figure adapted from Ref. [45] and supplemental material therein.

PIRO, see Fig. 4.5(a). They emerge at $T > 15$ K, become well pronounced at about 50 K, and then decrease due to strong LL smearing [152]. However, there first period appears well above 100 K. In addition, the inset in Fig. 4.5(a) displays the magnetic field values B_{max} of the first three PIRO maxima ($p = 1, 2$, and 3) as a function of the carrier density. The extracted points can be well fitted by Eq. (4.1) using the values $v_{\mathrm{F}} = 1.06 \times 10^6$ m/s and $v_{\mathrm{s}} = 1.36 \times 10^4$ m/s for Fermi and sound velocities, respectively, typical for high quality graphene structures [152].

In addition, Fig. 4.5(b) reveals a modification of PIRO at $T = 50$ K by applying a dc current I_{dc} up to 100 μA. By increasing I_{dc}, the maxima (minima) of PIRO are suppressed and eventually become minima (maxima). This behavior was previously observed in GaAs-based QWs [153] and is attributed to a LL tilt in the Hall field induced by the application of the dc current [154]. Pure PIRO without the use of a dc Hall field are governed by a well-defined spatial shift of the cyclotron orbit equal to $2R_c$ facilitated by backscattering on phonons. However, the introduction of the dc Hall field changes the electrostatic energy of the back-scattered electrons, leading to a modification of the resonance conditions of the inter-LL transitions, see Ref. [13] for further details.

5 Cyclotron Resonance in Two-Dimensional Electron Systems

Before presenting our main results, this chapter examines the conventional behavior of transmittance and photoresistance under the condition of CR in high-mobility 2DES at low T. Basic methods and mechanisms related to CR are outlined, thus serving as an introduction to the non-trivial CR-coupled phenomena discussed in subsequent chapters. It is shown that CR is indeed present in graphene and GaAs QWs. Furthermore, the differences between the parabolic and the linear energy dispersion relation are highlighted, where in the latter case the position of the CR depends on the effective carrier mass. The shapes of the transmittance and photoresistance are further analyzed. At high temperatures they follow the conventional Drude model within the picture of a uniform isotropic 2DES illuminated by a uniform circularly polarized wave. In addition, at low temperatures, where quantum corrections become important, the photoresistance is strongly affected by the emergence of SdHO-related oscillations. In this context, the importance of the electron gas heating induced by the THz radiation, which is the main origin of the observed signal in the photoresistance, is discussed.

5.1 Experimental Results

Starting with the conventional GaAs-based QW sample (GaAs #A), Fig. 5.1(a) shows a contour plot of the transmittance $\mathcal{T}(B)$ as a function of temperature in the range from $T = 1.8$ to 15.2 K. The traces were obtained as a response to left-handed (σ^-) circularly polarized radiation of frequency $f = 0.297$ THz using the highest possible power of the IMPATT-diode system. The QW was kept in the dark, i.e., no prior ambient light illumination was used for this series of measurements, see Sec. 4.1 for details. To allow a straightforward comparison of signal shape and amplitude, the transmittance curves were normalized to their zero magnetic field values $\mathcal{T}(B = 0)$. Note that the focus of this chapter lies on the CR condition only, and therefore the description and analysis of the data are limited to the positive magnetic field polarity. The contour plot reveals a clear feature in the transmittance at $B \approx 0.79$ T, see also the red trace in Fig. 5.1(c). This strong and wide dip reveals the emergence of the CR and is caused by resonant reflection and absorption of the incoming THz radiation. This behavior is well described by the conventional Drude model, as will be discussed below. Apart from the changes of the transmittance shape in the vicinity of the CR with temperature [see Fig. B.1 in App. B], which will

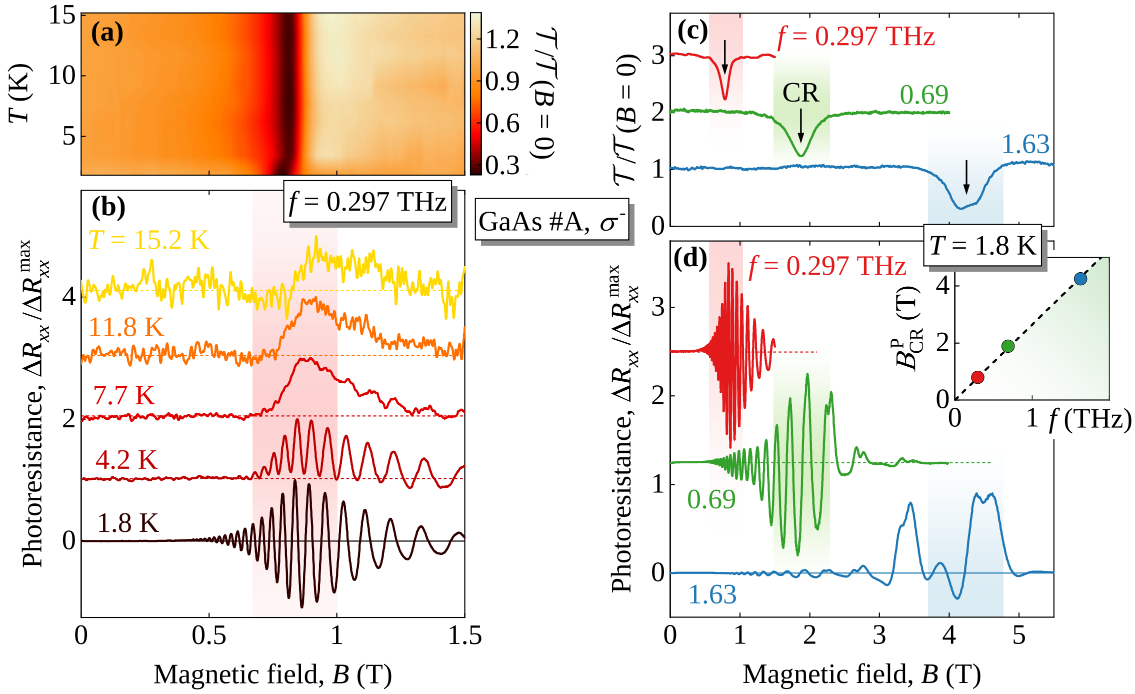

Figure 5.1: **(a)** Transmittance $\mathcal{T}(B)$ normalized to its value at zero field $\mathcal{T}(B = 0)$ measured as a response to a frequency of $f = 0.297$ THz. The data are displayed as a color map for a temperature range from $T = 1.8$ to 15.2 K. **(b)** Photoresistance traces ΔR_{xx} normalized to its maximum value $\Delta R_{xx}^{\max}$ plotted for several temperatures measured simultaneously with the transmittance. **(c, d)** Normalized transmittance $\mathcal{T}(B)/\mathcal{T}(B = 0)$ and corresponding photoresistance curves $\Delta R_{xx}/\Delta R_{xx}^{\max}$ for different THz frequencies, $f = 0.297, 0.69$ and 1.63 THz, labeled in the corresponding color. The vertical arrows mark the positions of the CR, termed $B_{\mathrm{CR}}^{\mathrm{P}}$, which are shown in the inset as a function of radiation frequency. The dashed line represents a fit according to $B_{\mathrm{CR}}^{\mathrm{P}} = 2\pi f m^*/e$ with $m^* = 0.074\, m_0$. All measurements were performed in GaAs #A with left-handed (σ^-) circularly polarized radiation. The dashed horizontal lines in panels (b, d) indicate the individual zero value for each curve, while the shaded areas in panels (b – d) highlight the vicinity of CR. The traces are shifted by a constant value for clarity. Figure adapted and modified from Refs. [47, 48] and supplemental material therein.

also be discussed in Sec. 5.2, the magnetic field position of the dip remained almost unchanged over the whole temperature range studied.

The simultaneously recorded temperature dependence of the corresponding photoresistance ΔR_{xx} is presented in Fig. 5.1(b). For illustration purposes, the photoresistance traces are normalized to their maximum value, denoted as $\Delta R_{xx}^{\max}$. At the highest temperature ($T = 15.2$ K) the photoresistance shows a clear enhancement near the position of the CR dip detected in the transmittance. As discussed below in Sec. 5.2, this behavior is attributed to resonant electron gas heating under CR-enhanced absorption, leading to a heating-induced reduction in electron mobility and hence to a positive photoresistance ΔR_{xx}. The slight shift between the

CR dip minimum and the photoresistance maximum is produced by variations of the Fabry-Pérot interference pattern in the substrate, see Sec. 5.2. Decreasing the sample temperature yields a gradually increasing oscillatory behavior, resulting in a strong modification of the photoresistance. At $T = 1.8$ K, the oscillations induce a B-dependent sign change, leading to an alternating photoresistance around $\Delta R_{xx} = 0$, where its envelope follows the CR-enhanced response. The photoresistance oscillations are confirmed to be $1/B$-periodic [see Fig. A.1 in App. A, where both helicities are shown for $f = 0.297$ THz] possessing the periodicity of SdHO.

This is due to the fact that the periodicity is determined by the carrier density, which is found to be fully consistent with the characterization by conventional magnetotransport measurements. Indeed, Fig. A.2 in App. A presents the dependence of the filling factor as a function of the inverse magnetic field position, demonstrating that the observed photoresistance oscillations are related to the SdHO visible in the dark magnetoresistance. Note that as illustrated in Fig. A.1, the period remains unchanged over the entire temperature range studied. This conventional behavior of the CR in transmittance and photoresistance was also observed in the GaAs #B sample with similar transport parameters and additionally in a HgTe-based QW. Both are discussed in more detail in Chap. 8.

As discussed in Sec. 2.2, a fundamental property of the CR is that its magnetic field position should scale linearly with the applied radiation frequency. To demonstrate this, the transmittance and the corresponding photoresistance were measured for different frequencies from different sources, see Figs. 5.1(c, d). Indeed, both the transmittance and the associated CR-enhanced photoresistance clearly show a shift of the CR towards higher magnetic fields as the applied radiation frequency is increased. The position of the CR is highlighted by shaded areas with the same color as the corresponding traces. Extracting the positions of the CR, $B_{\mathrm{CR}}^{\mathrm{P}}$, and plotting them as a function of the radiation frequency, see inset in Fig. 5.1(d), proves a clear linear-in-f behavior following accurately $B_{\mathrm{CR}}^{\mathrm{P}} = 2\pi f m^*/e$ [Eq. (2.34)] with $m^* = 0.074\, m_0$ (dashed line). Since for higher frequencies CR appears at higher magnetic fields, the period of the enhanced SdHO-periodic oscillations becomes longer and the shape of the envelope gets more distorted, see in particular the blue photoresistance trace recorded at $f = 1.63$ THz.

The data presented so far have been obtained in a GaAs QW, a conventional 2DES with a parabolic energy dispersion relation. Another 2DES under study is graphene, which in contrast exhibits a linear energy dispersion resulting in a different LL spectrum. Since the graphene devices used in this work are about four orders of magnitude smaller than the beam spot of the THz radiation, conventional transmittance

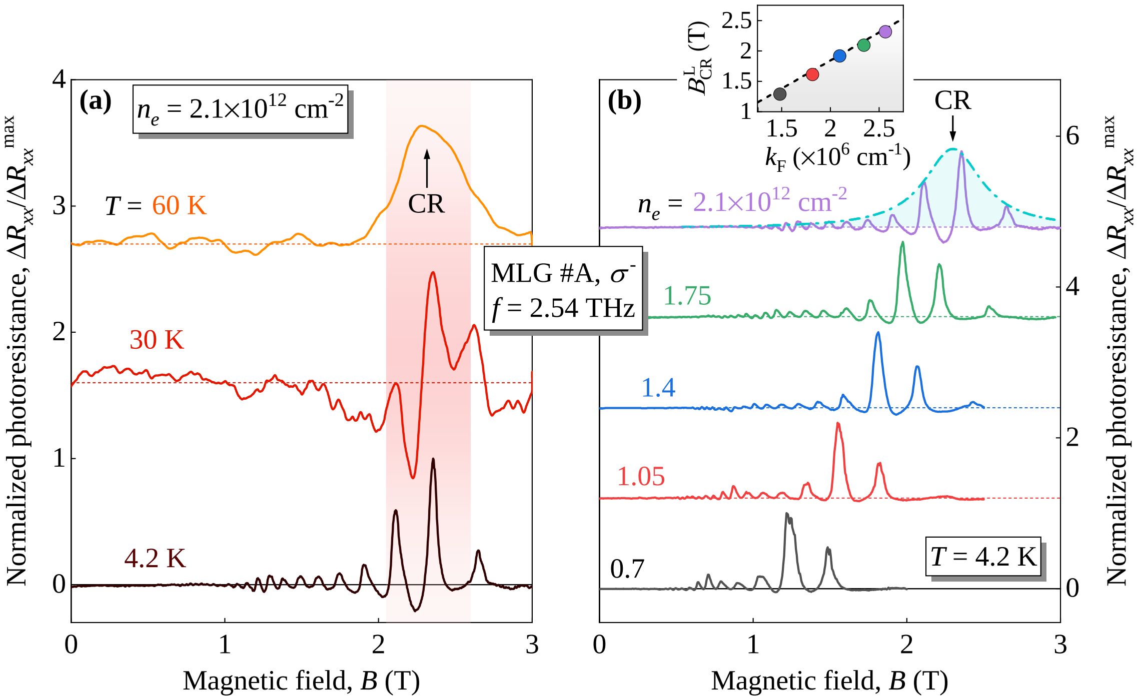

Figure 5.2: **(a)** Photoresistance ΔR_{xx} of MLG #A normalized to its maximum value $\Delta R_{xx}^{\text{max}}$ as a function of the magnetic field. The traces were obtained for different temperatures, $T = 4.2$, 30 and 60 K and a fixed carrier density $n_e = 2.1 \times 10^{12}$ cm^{-2}. The CR position is labeled as an example for the high-temperature trace. **(b)** Normalized photoresistance traces measured for a fixed temperature ($T = 4.2$ K) but continuously increasing carrier densities in the range $n_e = (0.7 - 2.1) \times 10^{12}$ cm^{-2}. The inset shows the magnetic field position B_{CR}^{L} of the CR as a function of the Fermi wave number $k_{\text{F}} = \sqrt{\pi n_e}$. The solid lines represent a fit according to $B_{\text{CR}}^{\text{L}} = 2\pi f \hbar k_{\text{F}} / e v_{\text{F}}$ with $v_{\text{F}} = 1.08 \times 10^6$ m/s. All measurements were taken at a frequency of $f = 2.54$ THz as a response to left-handed (σ^-) circularly polarized light and are shifted for clarity. The dashed horizontal lines indicate the individual zero value for each curve. Figure adapted and modified from Ref. [47] and supplemental material therein.

measurements in such structures are not feasible. Therefore, only photoresistance data are presented below.

Figure 5.2(a) shows the photoresistance ΔR_{xx} recorded in sample MLG #A for left-handed (σ^-) circularly polarized radiation at a frequency of $f = 2.54$ THz. As an example, traces are shown where the graphene sheet was kept at a carrier density of $n_e = 2.1 \times 10^{12}$ cm^{-2} by applying bias to the silicon back gate, for details on samples see Sec. 4.2. As before, the photoresistance is normalized to its maximum value $\Delta R_{xx}^{\text{max}}$ for better comparison. The traces reveal a typical picture of resonantly enhanced photoresistance, demonstrating that electron gas heating is maximized at the position of the CR. At $T = 60$ K, see top trace in Fig. 5.2(a), ΔR_{xx} exhibits a smooth and clear Lorentzian shape. When the sample is cooled to liquid helium temperature, the CR-enhanced photoresistance is modulated by the emerging SdHO-periodic oscillations, see traces for $T = 30$ and 4.2 K, similar to the observed photoresistance in the GaAs QW. This characteristic temperature dependence is observed for the whole range of carrier densities, $n_e = (0.7 - 2.1) \times 10^{12}$ cm^{-2}. To further support the statement that the increase in the photoresistance is indeed due to the CR, the carrier density and hence the Fermi wave number were varied. The dependence is shown in Fig. 5.2(b) using carrier densities in the aforementioned range and a fixed temperature of $T = 4.2$ K, chosen to maximize the magnitude of the photoresistance. Importantly, the data show a progressive shift of the CR position towards higher magnetic fields with an increasing carrier density. To determine the magnetic field positions of the CR $B_{\mathrm{CR}}^{\mathrm{L}}$ plotted in the inset of Fig. 5.2(b) as a function of the Fermi wave number $k_{\mathrm{F}} = \sqrt{\pi n_e}$, the photoresistance were mapped by a fit. The cyan dashed curve is an example of such a fit following the Lorentzian shape calculated according to classical Drude theory, see Sec. 2.2, which reproduces the envelope of the photoresistance. As expected, the CR position is governed by a linear dependence on k_{F}, as shown by the dashed line, which accurately follows $B_{\mathrm{CR}}^{\mathrm{L}} = 2\pi f \hbar k_{\mathrm{F}}/e v_{\mathrm{F}}$ [Eq. (2.34)] using $v_{\mathrm{F}} = 1.08 \times 10^6$ m/s. In addition, it should be noted that the amplitude of the CR-enhanced photoresistance decreases significantly with increasing k_{F}, which is not explicitly shown in Fig. 5.2. This behavior is due to increased radiation screening at high carrier densities, see discussion below.

To briefly summarize, clear CR has been observed in GaAs QWs and in monolayer graphene. Both has shown an increased photoresistance in the vicinity of the CR, which in GaAs was complemented by a CR dip in the simultaneously measured transmittance. While a single smooth peak was observed in the photoresistance of both structures at the highest temperature, lowering the temperature gradually revealed the emergence of strong SdHO-periodic oscillations superimposed on the CR-enhancement. The observed CR exhibits a linear in f dependence and shows a linear dependence on the Fermi wave number in graphene, reflecting the peculiar non-parabolicity of the Dirac fermions.

5.2 Discussion

As mentioned in the last section, the results presented above can be well understood in terms of the classical Drude model. In the following, the transmittance and absorptance properties are discussed in terms of the local dynamic and static Drude conductivity of an isotropic 2DES irradiated by a uniform circularly polarized wave.

In Sec. 2.2.1 the transmittance $\mathcal{T}(B)$ and the absorptance $\mathcal{A}(B)$ were derived in the

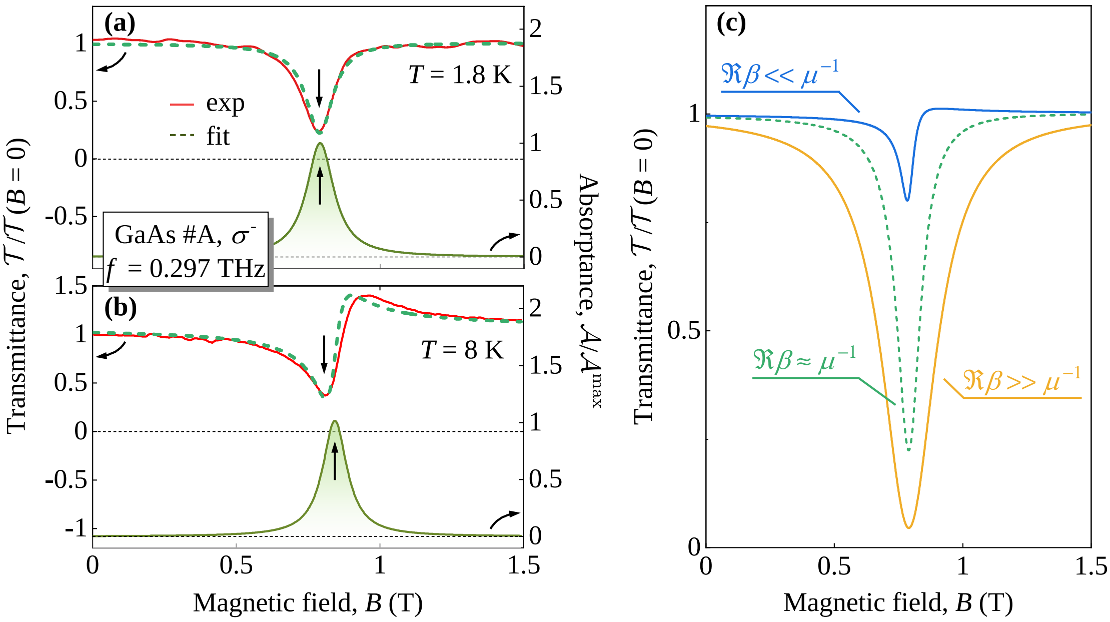

Figure 5.3: **(a)** Normalized transmittance $\mathcal{T}(B)/\mathcal{T}(B=0)$ (red solid trace) obtained in GaAs #A at $T = 1.8$ K for $f = 0.297$ THz and σ^- helicity. The green dashed curve shows the best fit according to Eq. (5.1) with $\eta = +1$, $B_{\mathrm{CR}}^{\mathrm{P}} = 0.79$ T and $\mu^{-1} = 0.027$ T using $\beta = (0.031 - \mathrm{i}0.0015)$ T as the fitting parameter. The green solid curve represents the calculated normalized absorptance according to Eq. (5.2) with the determined values. The vertical arrows mark the position of the CR in the transmittance and absorptance. Corresponding axes are indicated by the curved arrows on the sides. **(b)** Normalized experimental (red solid) and theoretical (green dashed) transmittance obtained in GaAs #A for $f = 0.297$ THz at $T = 8$ K and the corresponding calculated absorptance (green solid). **(c)** Modeled transmittance curves under strong reflection ($\Re\beta \gg \mu^{-1}$) or impurity scattering ($\Re\beta \ll \mu^{-1}$) dominating in 2DES, as well as when both effects are comparable ($\Re\beta \approx \mu^{-1}$). Figure adapted and modified from Ref. [48].

Drude approximation for a sample subjected to a perpendicular magnetic field and exposed to an EM wave with well-defined circular polarization directed normally to the sample surface. According to these relations, they are given by [48, 89]

$$\mathcal{T}(B) = |\alpha|^2 \left| 1 - \frac{\beta}{\mu^{-1} + \beta - \mathrm{i}B_{\mathrm{CR}} + \mathrm{i}\eta B} \right|^2 \tag{5.1}$$

and

$$\mathcal{A}(B) = \frac{Z_0 |\alpha \xi_1|^2 e n_e / \mu}{|\mu^{-1} + \beta - \mathrm{i}B_{\mathrm{CR}} + \mathrm{i}\eta B|^2} \,. \tag{5.2}$$

To briefly recapitulate, $\alpha = 2/(\xi_1 + \xi_2)$ and $\beta = e n_e Z_0 / (1 + \xi_2/\xi_1)$ are introduced, which are functions of the complex interference parameters describing the Fabry-Pérot interference pattern attributed to multiple reflections in the substrate with refractive index n_r (about 3.6 in GaAs). Specifically, they are denoted as $\xi_{1,2} = \cos\phi - \mathrm{i}n_r^{\mp 1}\sin\phi$ with $\phi = n_r k w = 2\pi w f n_r/c$, where w is the sample thickness. Furthermore, $\eta = \pm 1$ describes the helicity of the incident wave, and $Z_0 = 1/\epsilon_0 c \approx 377\ \Omega$ is the vacuum impedance.

Figure 5.3(a) presents the normalized transmittance $\mathcal{T}(B)/\mathcal{T}(B=0)$ (shown in red) taken from Fig. 5.1(c), obtained in GaAs #A at temperature $T = 1.8$ K and frequency $f = 0.297$ THz. The shape of the transmitted signal is accurately reproduced according to Eq. (5.1), which is shown by the green dashed line. Here a fixed radiation helicity ($\eta = +1$ for σ^- configuration) was used, $B_{\mathrm{CR}}^{\mathrm{P}} = 0.79$ T as the position of the CR and the reciprocal mobility $\mu^{-1} = 0.027$ T. The latter was obtained from dark magnetotransport measurements in GaAs #A, see Sec. 4.1. The effective mass was determined using the frequency dependence of $B_{\mathrm{CR}}^{\mathrm{P}}$, which was accurately fitted by $B_{\mathrm{CR}}^{\mathrm{P}} = 2\pi f m^*/e$, yielding a value $m^* = 0.074\, m_0$, see inset in Fig. 5.1(d). The complex parameter $\beta = (0.031 - \mathrm{i}0.0015)$ T was used as the fitting parameter and is remarkably close to the calculated value, $\beta = (0.030 - \mathrm{i}0.0030)$ T, assuming a total sample thickness of $w = 351.2\ \mu$m. Knowing all the parameters for the transmittance, one has full access to the shape of the absorptance via Eq. (5.2), shown as a green solid line in Fig. 5.3(a). It can be seen that the magnetic field position of the absorptance maximum corresponds to the CR minimum in the transmittance, highlighted by the vertical arrows. The considered condition yields $\Re\beta \gg \Im\beta$, therefore, let us first address $\Re\beta$. The real part describes the strong metallic reflection of the radiation from the 2DES (dynamic screening) in the vicinity of the CR and contributes to the linewidth of the CR in addition to μ^{-1}. For the trace obtained in GaAs #A, see Fig. 5.3(a), the broadening due to impurity scattering is comparable to that of the dynamic screening, i.e., $\Re\beta \approx \mu^{-1}$. In Fig. 5.3(c) the transmittance is plotted for three different regimes of $\Re\beta$ with μ^{-1} remaining fixed. For reference, the green dashed line corresponds to the transmittance in Fig. 5.3(a). It is evident that increasing $\Re\beta$ produces a wider CR, while decreasing its value yields a narrower shape. Note that $\Re\beta$ also contributes to the numerator in Eq. (5.1), so manipulating $\Re\beta$ also changes the depth of the CR, as seen in Fig. 5.3(c). Since, apart from the electron density, β is strongly sensitive to the interference phase ϕ, the most convenient way to change its value in the experiment is to vary the radiation frequency. Figure 5.4(a) shows an example of such a variation of the interference pattern, where the transmitted radiation of GaAs #A was measured by continuously varying the frequency in the range from $f = 0.220$ to 0.375 THz. The data were kindly provided

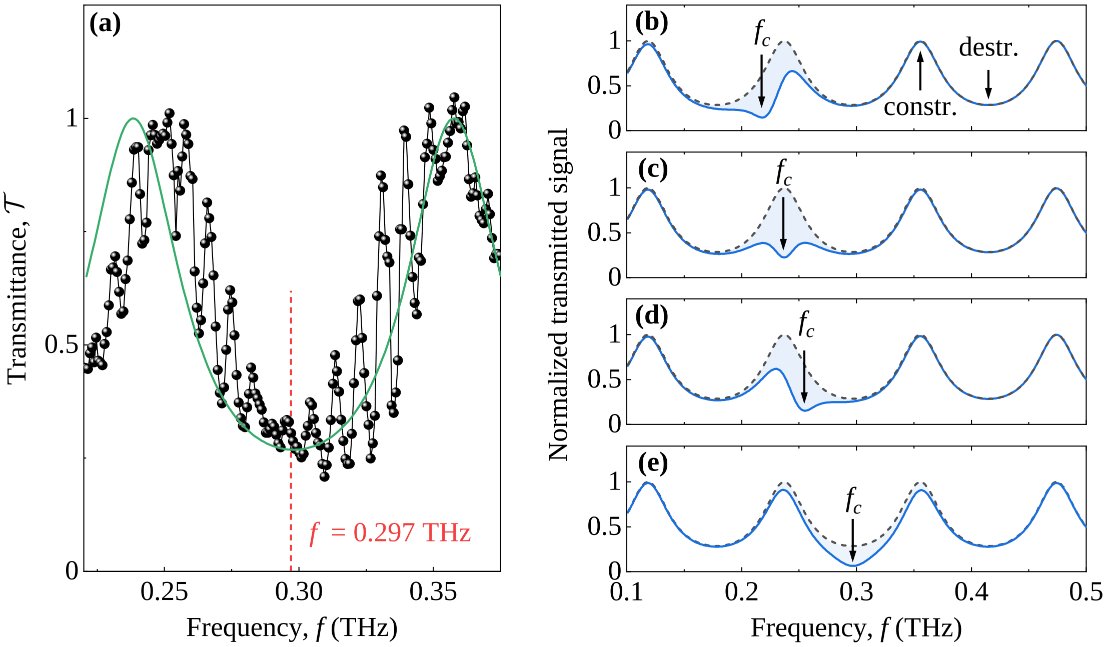

Figure 5.4: **(a)** Transmittance as a function of radiation frequency in the range $f = 0.220$ to 0.375 THz measured in GaAs #A with a BWO quasi-optical setup. The green solid line represents a fit following Eqs. (2.42) and (2.44) in Sec. 2.2.1 using the expression $\sigma_\eta = e^2 n_e/[m^*(\tau^{-1} - \mathrm{i}2\pi f + \mathrm{i}2\pi\eta f_c)]$ for the dynamic conductivity at zero B-field [$f_c = eB/(2\pi m^*) = 0$] and the parameters $\mu = 37$ m^2/Vs, $n_e = 6.65 \times 10^{11}$ cm^{-2}, $n_r = 3.58$, and $w = 351.2$ μm. The red dashed line indicates the position of the frequency used in Figs. 5.3(a, b). **(b − e)** Illustration of the influence of a Fabry-Pérot pattern inside the sample substrate on the shape of the CR in the transmittance visualized for different frequency positions of CR, f_c. The parameters $w = 351.2$ μm and $n_r = 3.58$ were used for its modeling. The frequency positions of CR are indicated by arrows in each panel. The constructive and destructive interference conditions are denoted with arrows in panel (b) as representative examples.

by our collaborators at the technical university of Vienna[9].

The pattern consists of pronounced long-ranged maxima and minima superimposed by rapid oscillations. The latter are attributed to standing waves due to multiple reflections from optical components – such as windows, polarizers, but also the detector surface – and are modified by changes in the optical setup. The long-ranged pattern, on the other hand, arises naturally from the multiple reflections from the back and front interfaces of the substrate, resulting in a Fabry-Pérot interference inside the sample [12, 87, 88, 155]. This pattern can be accurately reproduced by using the expression for the transmission amplitude [Eq. (2.42) in Sec. 2.2.1] and calculating the transmittance $\mathcal{T} = |t|^2$ with the relation for the dynamic conductivity given

---

[9] Measurements were performed by Maxim Savchenko and Alexey Shuvaev in the group of Andrei Pimenov, https://www.ifp.tuwien.ac.at/spectroscopy (accessed January 1st, 2024).

in terms of the radiation frequency f and cyclotron frequency $f_c = eB/(2\pi m^*)$ as $\sigma_\eta = e^2 n_e/[m^*(\tau^{-1} - \mathrm{i}2\pi f + \mathrm{i}2\pi\eta f_c)]$. In this case the magnetic field is zero yielding $f_c = 0$. The result is displayed in Fig. 5.4(a) as the green solid trace. The remaining parameters are given in the caption. To understand how this long-ranged pattern affects the shape of the CR, the transmitted signal was modeled as a function of radiation frequency and superimposed on the CR transmittance. Figures 5.4(b – e) show the results for several frequency positions of CR, f_c, i.e., different B-field values, namely constructive (c) and destructive (e) interference, as well as positions in between (b, d). In the regime of constructive ($\sin\phi = 0$, $\cos\phi = 1$) and destructive ($\sin\phi = 1$, $\cos\phi = 0$) interference, β becomes real, i.e., $\Im\beta = 0$, and the transmittance takes a symmetric form according to Eq. (5.1). This is clearly seen from the transmittance traces in Fig. 5.1(b) measured at different frequencies on GaAs #A. At $f = 0.297$ THz, the partial waves destructively overlap inside the substrate, resulting in a narrow shape of the CR. In contrast, at $f = 0.69$ THz, the interference is constructive, producing a wide CR shape. This difference in CR shapes is due to the fact that $\beta_{\text{constr.}} \gg \beta_{\text{destr.}}$. Under the condition of constructive interference, corresponding to Fig. 5.4(c), only a small fraction of the incident radiation is absorbed by the 2DES in the vicinity of the CR due to $\beta_{\text{constr.}} \gg \mu^{-1}$, while width of the dip in transmittance is mostly caused by strong resonant reflection [17, 74, 75, 89, 156, 157]. Note that as addressed in Sec. 2.2.1, β is related to Γ [17, 74, 75] as $\Gamma = \beta/B_{\text{CR}}^{\text{P}}$, considering constructive interference.

For an arbitrary interference phase ϕ, β remains a complex parameter and the shape becomes asymmetric. As an example, this condition is shown in Fig. 5.3(b) for GaAs #A, $f = 0.297$ THz and $T = 8$ K. Here the transmittance (red solid) possesses a strongly asymmetric shape with a higher shoulder at $B > B_{\text{CR}}^{\text{P}}$. Looking at the corresponding absorptance (green solid), calculated from the parameters provided by the fit of the transmittance (green dashed), it can be seen that its maximum is significantly shifted from the CR position determined by the transmittance dip. This is a consequence of the non-vanishing imaginary part of β ($\Im\beta = -0.02$ T), which leads to $B_{\text{CR}}^{\text{P}} \to B_{\text{CR}}^{\text{P}} + \Im\beta$ in the absorptance. Unlike $\mathcal{T}(B)$, the shape of the absorptance remains a symmetrical Lorentzian for all values of β.

Interestingly, although Figs. 5.3(a) and 5.3(b) show transmittance curves obtained for the same frequency and sample by varying only its temperature (from $T = 1.8$ to 8 K), the transmittance shape has changed considerably. Since a very small change of $\Im\beta$ influences the transmittance shape, even small variations of the standing wave pattern can significantly affect the transmittance. For example, the jump in the permittivity of the helium surrounding the sample caused by the transition between liquid and gaseous phases [158, 159] may significantly alter the transmittance.

Absorption of the THz radiation leads to heating of the electron gas, which changes the transport properties and results in a non-zero photoresistance, see Sec. 2.3. For sufficiently small radiation intensities, such a bolometric photoresistance is given by

$$\Delta R = \frac{\partial R}{\partial \mu}\frac{\partial \mu}{\partial T_e}(T_e - T) \tag{5.3}$$

with the electron T_e and lattice T temperatures. At sufficiently high temperatures, where quantum corrections are negligible, the longitudinal resistance does not depend on the magnetic field and simply follows the classical Drude expression, $R_0 = g/(en_e\mu)$, with a geometrical factor, g, to account for the type of measurements. Evaluating Eq. (5.3) under this condition, the B-dependence of the linear photoresistance is described by the μ-photoconductivity according to Eq. (5.2), i.e., $\Delta R \propto -I(\partial\mu/\partial T_e)\mathcal{A}(B)$; thus reproducing its Lorentzian shape, see the modeled orange trace in Fig. 5.5(c) and the green curve in Figs. 5.3(a, b). In Eq. (5.2), the energy losses given in the energy balance equation, see Eq. (2.50) in Sec. 2.3, are assumed to scale linearly with the temperature difference, resulting in $T_e - T \propto I\mathcal{A}(B)$. Such a bolometric photoresistance is consistent with our observations, see Figs 5.1(b) and 5.2(a), which clearly demonstrate a Lorentzian shape in the photoresistance data at high temperatures for GaAs and graphene, respectively. Moreover, the observed positive sign of the photoresistance is in agreement with the decrease in mobility due to acoustic phonon scattering [48, 91]. Importantly, at low temperatures, where quantum corrections have to be taken into account, the picture becomes more complex: the data exhibit a combined effect of CR heating on SdHO and mobility.

The dark magnetoresistance, measured in the absence of radiation, can be modeled by the conventional Lifshitz-Kosevich formula [13, 160–162]

$$R_{xx}(B) = R_0 + 4R_0\delta_{\text{inh}}\delta\frac{X(T_e)}{\sinh X(T_e)}\cos\left(\frac{2\pi\nu}{g_s g_v} - \pi + \phi_0\right), \tag{5.4}$$

describing an oscillatory correction to the classical Drude expression R_0 introduced above. The SdHO arise from the modulation of the DOS mapping the discrete LL spectrum of the 2DES. Their period is determined by the filling factor, $\nu = 2\pi\hbar n_e/e|B|$, and g_s and g_v account for spin and valley degeneracy. In GaAs there is no valley degeneracy, thus $g_s = 2$ and $g_v = 1$, while graphene has two inequivalent valleys, therefore, $g_s = g_v = 2$. The sign of the oscillatory contribution is determined by the Berry phase of the 2DES with $\phi_0 = 0$ for conventional QWs and

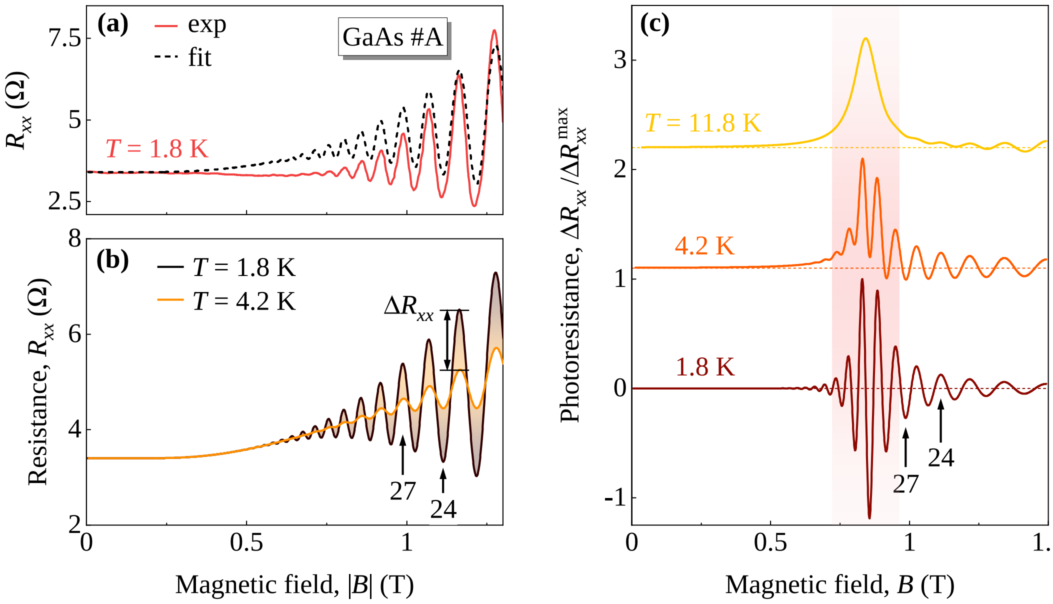

Figure 5.5: **(a)** Measured (red solid) and calculated (black dashed) dark longitudinal magnetoresistance at $T = 1.8$ K for GaAs #A. The corresponding parameters are $R_0 = 3.4\ \Omega$, $\tau_q = 1.3$ ps, $n_e = 6.63 \times 10^{11}$ cm^{-2}, $T = T_e = 1.8$ K, $m^* = 0.074\,m_0$, and $B_{\text{inh}} = 1.1$ T. **(b)** Dark magnetoresistance calculated for two temperatures, $T = 1.8$ and 4.2 K. The double arrow represents the difference in resistance ΔR_{xx}. **(c)** Modeled normalized photoresistance $\Delta R_{xx}/\Delta R_{xx}^{\max}$ at different temperatures, $T = 1.8$, 4.2 and 11.8 K. The curves are calculated using Eqs. (5.3) and (5.4) with the parameters obtained from the dark magnetoresistance fit [panel (a)]. The traces are up shifted for clarity. The vertical arrows in panels (b) and (c) label the odd ($\nu = 27$) and even ($\nu = 24$) filling factors, respectively, highlighting the relative phase of SdHO in photoresistance and dark magnetoresistance. Figure adapted from Ref. [48].

$\phi_0 = \pi$ for monolayer graphene [162, 163]. At very small temperatures ($T \to 0$) the decay of SdHO towards low B follows the so-called Dingle factor $\delta = \exp(-\pi/\omega_c\tau_q)$ containing the quantum relaxation time τ_q which accounts for the disorder broadening of the LLs separated by $\hbar\omega_c$, see Sec. 2.2. An increase in temperature leads to an additional thermal smearing of the LLs, which is accounted for by the factor $X(T_e) = 2\pi^2 k_{\text{B}} T_e/\hbar\omega_c$. A further damping parameter $\delta_{\text{inh}} = \exp(-B_{\text{inh}}^2/B^2)$ reflects possible smooth fluctuations and inhomogeneities of the filling factor across the sample [48].

Equation (5.4) closely reproduces the measured dark magnetoresistance at $T = 1.8$ K in GaAs #A, see Fig. 5.5(a) with the corresponding parameters given in the figure caption. Figure 5.5(b) shows the representative magnetoresistance for two different temperatures $T = 1.8$ and 4.2 K, calculated using the determined values. As expected, the SdHO are thermally suppressed, reflecting their strong sensitivity to the electronic temperature, as seen in Eq. (5.4). This picture remains in close analogy to the emergence of the photoresistance: The incoming THz radiation is absorbed by the CR and heats the electron gas. This in turn leads to an increase of the electron temperature, which results in a suppression of the SdHO amplitude and thus to ΔR_{xx}. The latter can be understood as the difference of the sample resistance at two temperatures, as indicated by ΔR_{xx} in Fig. 5.5(b). This radiation-induced reduction of the oscillation amplitude naturally leads to the same periodicity of the photoresistance oscillations as that of SdHO in conventional magnetotransport.

Figure 5.5(c) shows the result of the modeled photoresistance for different measurement temperatures as used in the experiment. The overall behavior of the photoresistance under CR conditions in GaAs #A [Fig. 5.1(b)] and MLG #A [Fig. 5.2(a)] is well reproduced, showing a strong enhancement of the SdHO-periodic oscillations at lower temperatures. These are superimposed on the envelope, which represents the shape of the magnetoabsorptance as it appears at higher temperatures. At low T this smooth Lorentzian-shaped contribution is distorted by the exponential decay of the SdHO towards low B, which are symmetric with respect to the abscissa for low radiation frequencies $f = 0.297$ and 0.69 THz. However, this is not the case for higher excitation frequencies such as $f = 1.63$ and 2.54 THz as shown in Figs. 5.1(d) and 5.2(a), respectively, where CR shifts into the region of well separated LLs. Here the carriers are fully localized and the SdHO exhibit plateaus of almost zero resistance, resulting in an asymmetric photoresistance shape. In contrast to the SdHO in the magnetoresistance, which feature maxima (minima) at odd (even) LL filling factors, the SdHO-periodic oscillations in the photoresistance exhibit maxima (minima) at even (odd) ν, see Figs. 5.5(b) and (c), respectively, where vertical arrows indicate representative values. This sign change is a direct consequence of the SdHO suppression and is in agreement with the data.

So far, the observations in both systems show a very similar qualitative behavior. Before concluding this chapter, the difference found in graphene is briefly discussed. Since graphene has a linear dispersion relation, its LL spectrum yields a square root behavior, a peculiarity that leads to the ability to manipulate the effective mass by the carrier density. Consequently, using the semiclassical approach and assuming CR transitions between high LLs ($l \gg 1$), i.e., far away from the CNP, the effective mass and thus the magnetic field position of the CR scales proportional to $k_{\mathrm{F}} = \sqrt{\pi n_e}$ [21], see detailed description in Sec. 2.2. This is clearly observed in Fig. 5.2(b), where the relation $B_{\mathrm{CR}}^{\mathrm{L}} = 2\pi f \hbar k_{\mathrm{F}} / e v_{\mathrm{F}}$ was evaluated to accurately fit the linear behavior of the Fermi wave number with $v_{\mathrm{F}} = 1.08 \times 10^6$ m/s – a value typical for graphene devices of similar quality [21, 22, 46, 152]. This is in strong contrast to GaAs, for which $B_{\mathrm{CR}}^{\mathrm{L}}$ is insensitive to carrier density variations ascribed to the equidistant LL spectrum, if one neglects small corrections due to density-dependent renormalization caused by electron-electron interactions [164, 165]. Note that with increasing n_e, the graphene sheet screens the incident THz field as a result of a larger radiative decay, thus lowering the absorption coefficient in the vicinity of the CR, which eventually leads to a degradation of the CR magnitude [17, 75, 88, 166]. For detailed calculations see Ref. [45] and supplemental material therein.

In conclusion, the observed THz-induced enhanced photoresistance in GaAs and graphene is indeed associated with CR. Its positions scales linearly with the radiation frequency. Furthermore, the magnetic field position of the CR in graphene is tunable by the carrier density, reflecting its linear energy dispersion. The CR-enhanced photoresistance is governed by the shape of the magnetoabsorptance at high temperatures, while at low T it shows a combined effect of the CR-induced heating on electron mobility and SdHO. In GaAs, this picture is supported by the CR dip in the simultaneously measured transmittance, whose shape is related to the CR absorptance at low and high T, taking into account SdHO. The following chapter demonstrates that this conventional CR behavior in a 2DES can be strongly influenced by magnetoplasmonic excitations caused by near-field effects, which are intentionally enhanced by a special contact geometry.

6 Terahertz-driven non-local Bernstein Modes in Graphene

Taking advantage of a special contact geometry and the exceptional quality of graphene devices, a qualitative deviation from the usually expected CR behavior is observed. The emergence of peculiar resonant peaks detected in the THz photoresponse at CR harmonics is presented and discussed. An extensive experimental analysis using various parameters, namely carrier density, radiation frequency, temperature, and radiation intensity, will reveal that this intriguing phenomenon originates from enhanced magnetoabsorption, which in turn is facilitated by branches of the THz-induced magnetoplasmonic excitations, called Bernstein modes. The enhanced absorption is caused by near fields arising in the vicinity of metallic contacts with sharp edges, resembling structures usually implemented for plasmonic experiments. A theoretical model will demonstrate that the resulting Bernstein modes exhibit a flat dispersion leading to a divergent plasmonic DOS, which significantly enhances the absorption of radiation and consequently leads to a strongly increased photoresponse.

6.1 Experimental Results

Figure 6.1(a) shows the magnetic field dependence of the low temperature longitudinal resistance R_{xx} in sample MLG #B at a carrier density of $n_e = 3.9 \times 10^{12}$ cm^{-2}. Here, the black trace represents the dark resistance, while the effect of THz irradiation on the magnetoresistance is demonstrated by the red trace. The dark resistance exhibits a negative differential magnetoresistance (see Sec. 4.2) for small magnetic fields ($|B| < 0.5$ T) followed by SdHO at $|B| > 0.5$ T. This is a standard behavior typical for high-quality graphene devices. When the sample is exposed to THz radiation at frequency $f = 0.69$ THz, the behavior changes significantly: while the resistance remains unchanged at low fields, the amplitude of the SdHO appearing at higher fields is suppressed due to the radiation-induced increase in electron temperature. Moreover, in the presence of THz illumination, a strong resistance peak is observed at $B \approx 0.5$ T. Strikingly, this pronounced peak occurs close to the position of the second CR harmonic, $B \approx B_{\mathrm{CR}}^{\mathrm{L}}/2$ (purple line), corresponding to the condition $\omega = 2\omega_c$, determined via Eq. (2.34). Although the regular CR, marked by a black dashed line, is a distinct effect as described in Chap. 5, it is hardly visible in the data and appears only at lower carrier densities or higher THz frequencies. Figure 6.1(b) shows the photoresistance ΔR_{xx}, obtained as the difference between

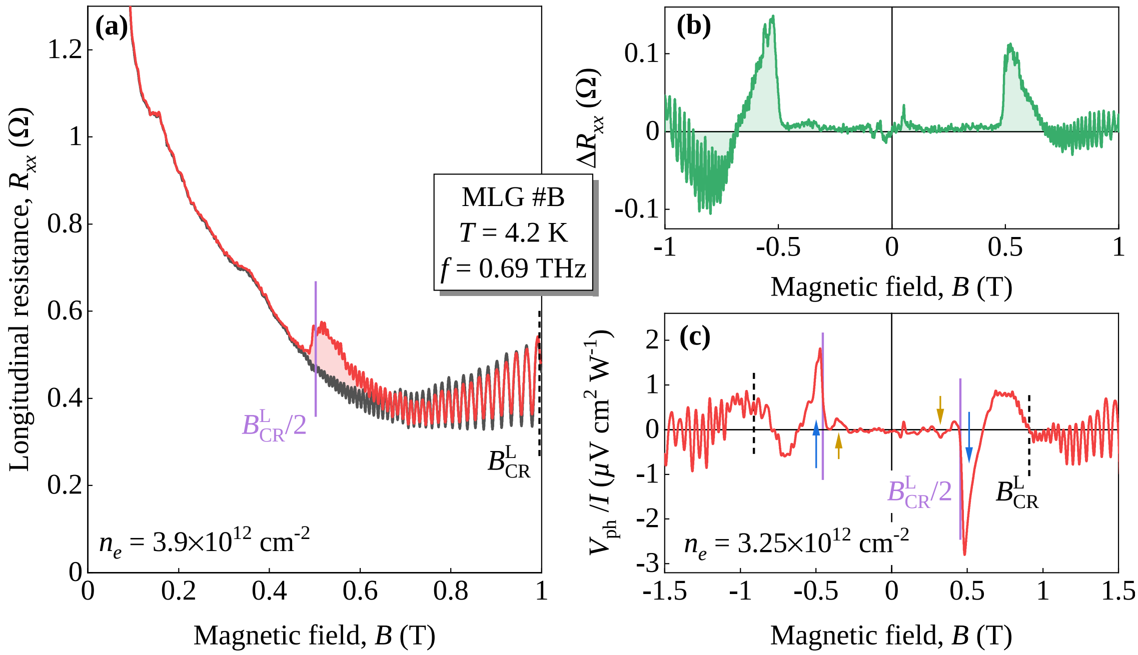

Figure 6.1: **(a)** Longitudinal magnetoresistance R_{xx} obtained in MLG #B at frequency $f = 0.69$ THz and carrier density $n_e = 3.9 \times 10^{12}$ cm^{-2}. The dark resistance is indicated by the black trace, while the red trace shows the change in magnetoresistance of the sample caused by THz radiation. **(b)** Photoresistance ΔR_{xx} obtained as the difference between the red and black traces in panel (a), isolating the distinct feature from the smooth magnetoresistance background. **(c)** Photovoltage trace obtained in MLG #B for $n_e = 3.25 \times 10^{12}$ cm^{-2}. The blue and yellow arrows denote the features near the second and third CR harmonics. The black dashed and purple solid lines in panel (a) and (c) mark the position of the main CR, B^{L}_{CR}, and its second harmonic, $B^{L}_{CR}/2$, determined according to Eq. (2.34). All curves were obtained at a temperature of $T = 4.2$ K. Figure adapted from Ref. [45].

the dark and illuminated traces, isolating the pronounced peak from the magnetoresistance background. This presentation of the data clearly reveals large asymmetric peaks for both magnetic field polarities, representing a steep rise followed by a slower decay at higher B fields.

This unusual and pronounced signature is also observed in the photovoltage, i.e., without any bias applied to the sample shown in Fig. 6.1(c). Similar to the photoresistance data, the signal at the position of the main CR is small, while highly asymmetric peaks appear in the vicinity of the main CR harmonics for both magnetic field polarities. In addition, at $B \approx 0.3$ T, the trace exhibits signatures of asymmetric but weaker peaks (indicated by yellow arrows), which are also attributed to the resonant features, but associated with higher order CR harmonics, as will be discussed below. Unlike in photoresistance, where these prominent features appear as peaks, in photovoltage their sign is an odd function of the magnetic field, as indicated by the blue arrows. Indeed, the parity of the signal strongly depends on the direction of the generated photovoltage. In order to keep the complexity within reasonable limits, the following considerations will focus on the photoresistance data.

Figure 6.2(a) presents a color map of the measured photoresistance, normalized to the radiation intensity, as a function of magnetic field (horizontal axis) and carrier density (vertical axis). The latter was varied in the range $n_e = (0.65 - 3.9) \times 10^{12}$ cm^{-2}. The data were obtained at frequency $f = 0.69$ THz and temperature $T = 20$ K, chosen to avoid any influence of SdHO-periodic oscillations, resulting in a smooth and non-oscillating magnetoresistance background. Examples of sectional views are illustrated in Fig. 6.2(b) for several representative carrier densities, offset for clarity. The pronounced peak marked with red arrows in panels (a) and (b) is observed over the entire carrier density range. Although much weaker at higher n_e, the regular CR is also present (black arrows) and is strongly enhanced at doping levels closer to the CNP. This evolution is attributed to the radiative decay of the CR. Figure 6.2(c) shows the resonant magnetic field positions of the peak and CR plotted against the Fermi wave number k_F. It shows that B_peak scales accurately according to

$$B_\mathrm{peak} \approx B^\mathrm{L}_\mathrm{CR}/2 = \pi f \hbar k_\mathrm{F}/ev_\mathrm{F}\,, \tag{6.1}$$

while CR follows Eq. (2.34) as expected, with both relations utilizing $v_\mathrm{F} = 1.06 \times 10^6$ m/s for the Fermi velocity. The B-field position of the peak shows that the anomalous resonance occurs very close to the main CR overtone in the studied range of n_e.

In addition, a broader peak was observed emerging at slightly higher magnetic fields, partially superimposed on the regular CR, especially at lower n_e. These photoresistance maxima correspond to the minima of PIRO, which in this sample also appear in the conventional magnetoresistance, see Sec. 4.2. The inset of Fig. 6.2(c) shows the maxima in ΔR_{xx} plotted against the Fermi wave number following Eq. (4.1) (dashed green lines), with $p = 1.5$, $v_\mathrm{F} = 1.06 \times 10^6$ m/s, and a sound velocity of $v_\mathrm{s} = 1.36 \times 10^4$ m/s. The occurrence of PIRO in the photoresistance can be understood in terms of radiation-induced electron-phonon coupling, as will be addressed below.

The evolution of the photoresistance with temperature is shown in Fig. 6.3(a). The traces are obtained for a carrier density of $n_e = 3.9 \times 10^{12}$ cm^{-2} and a frequency of $f = 0.69$ THz. It is clearly seen that the sharp and highly asymmetric peaks in the vicinity of the main CR overtone are most pronounced at $T = 2$ K and

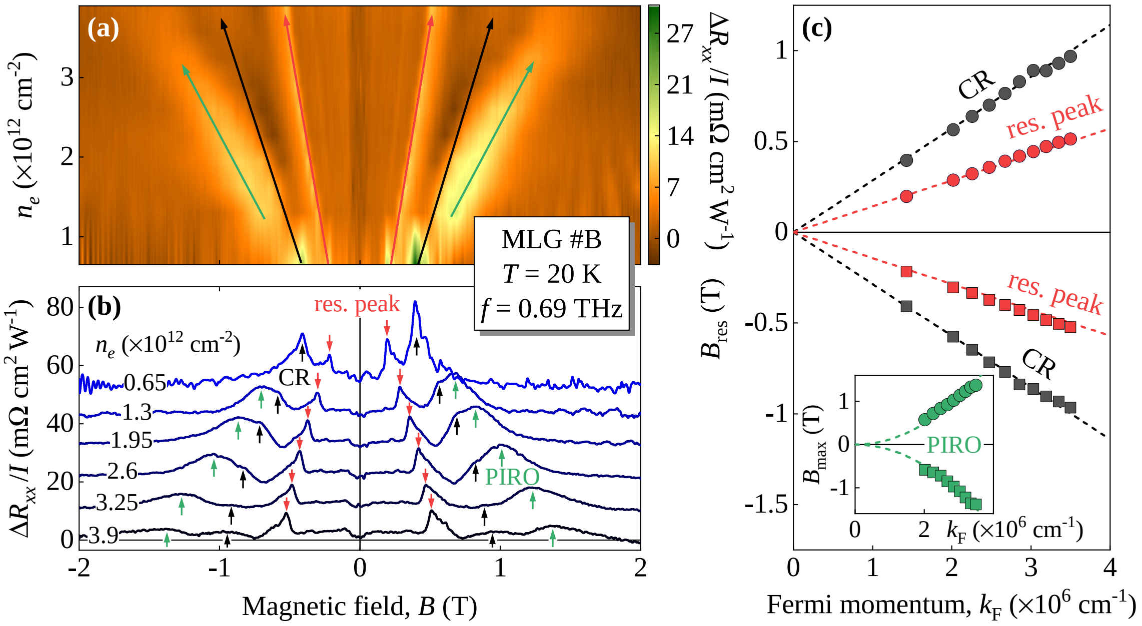

Figure 6.2: (a) Color map of THz-induced photoresistance as a function of magnetic field (horizontal axis) and carrier density (vertical axis). The red arrows indicate resonant peaks close to the main CR overtone, the black arrows mark the main CR, and the green ones denote PIRO. **(b)** Magnetic field dependencies of the photoresistance corresponding to the data in panel (a) shown for several carrier densities. The colored arrows mark the resonant peaks (red), CR (black), and PIRO (green) corresponding to the lines in panel (a). The traces are upshifted for clarity. **(c)** The resonant magnetic field position B_{res} of the peak feature (red) and the main CR (black) as a function of the Fermi wave number k_{F} for both magnetic field polarities. The black and red dashed lines follow Eq. (2.34) and Eq. (6.1), respectively, using $v_{\mathrm{F}} = 1.06 \times 10^6$ m/s. The inset shows the peak position of PIRO as a function of k_{F}. The dashed lines are calculated according to Eq. (4.1) with $p = 1.5$. All results were obtained at $f = 0.69$ THz and $T = 20$ K. Figure adapted from Ref. [45] and supplemental material therein.

are suppressed with increasing T. At $T \approx 50$ K the resonant peak almost disappears. While a small feature is present at the position of the regular CR, similar to Fig. 6.1(c), additional signatures were observed at higher harmonics of the CR, $B_{\mathrm{CR}}/3$ and $B_{\mathrm{CR}}/4$, see Fig. 6.3(b) that shows an enlarged window of the temperature dependence. However, these features are less pronounced at lower B-fields, experiencing a faster decrease with rising temperature. To visualize the thermal damping of the photoresistance peak, its magnitude was plotted as a function of T on a log-linear scale, see Fig. 6.3(c). Here, the blue and green circles indicate the peak height for the positive and negative magnetic field polarities of the data set shown in panels (a) and (b), while the red squares indicate the peak magnitude obtained at $f = 2.54$ THz. The dependencies are normalized to the amplitude values of ΔR_{xx} at $T = 2$ K for the corresponding radiation frequency. The amplitudes

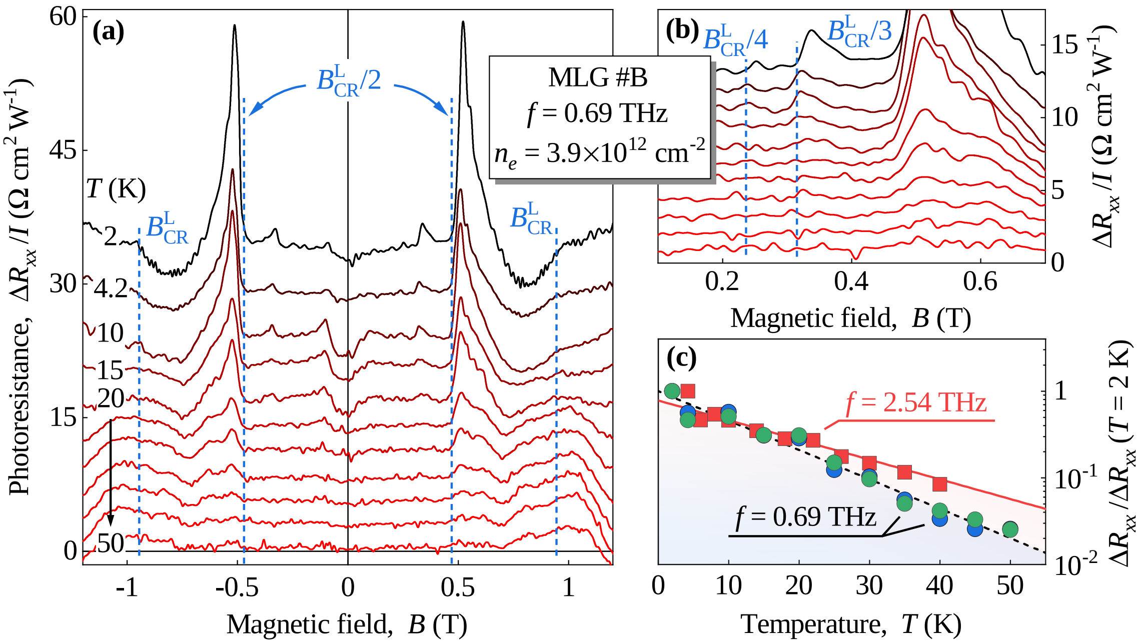

Figure 6.3: **(a)** Photoresistance curves recorded at $f = 0.69$ THz for different temperatures up to $T = 50$ K. The blue dashed lines indicate the positions of the main CR and its second harmonic. The traces are offset for clarity. **(b)** Enlarged data window showing the thermal damping of the features close to the higher CR harmonics, $B_{\mathrm{CR}}/3$ and $B_{\mathrm{CR}}/4$. **(c)** Amplitude of the photoresistance peak, normalized to the amplitude values of ΔR_{xx} at $T = 2$ K for the corresponding radiation frequency, plotted on a log-linear scale. The blue and green circles correspond to the amplitude values determined at positive and negative magnetic field polarities shown in panels (a) and (b). The red squares represent the temperature dependence obtained at $f = 2.54$ THz. The black dashed and red solid lines denote fits according to $\Delta R \propto \exp(-T/T_0)$, yielding $T_0(f = 0.69\ \mathrm{THz}) \approx 12.8$ K and $T_0(f = 2.54\ \mathrm{THz}) \approx 20.1$ K. All traces were recorded at $n_e = 3.9 \times 10^{12}$ cm^{-2}. Figure adapted from Ref. [45] and supplemental material therein.

approximately follow an exponential decay given by $\exp(-T/T_0)$ (black dashed and red solid lines), yielding characteristic temperatures $T_0(f = 0.69\ \mathrm{THz}) \approx 12.8$ K and $T_0(f = 2.54\ \mathrm{THz}) \approx 20.1$ K.

The pronounced peaks were also detected when THz radiation at higher frequencies was applied to the sample. Figures 6.4(a, b) display examples of photoresistance traces for several carrier densities obtained at $T = 40$ K for frequencies $f = 1.63$ and 2.54 THz. Although their amplitudes slightly vary, the peaks are clearly visible for both frequencies over the range of investigated densities. However, the overall behavior of the photoresistance is rather complex. In fact, besides a prominent CR at lower n_e, especially at $f = 2.54$ THz a strong admixture of two oscillatory phenomena was observed, namely the THz-induced magnetooscillations (TIMO) and PIRO. While the extrema of PIRO exhibit a quadratic-in-k_{F} dependence, see inset in

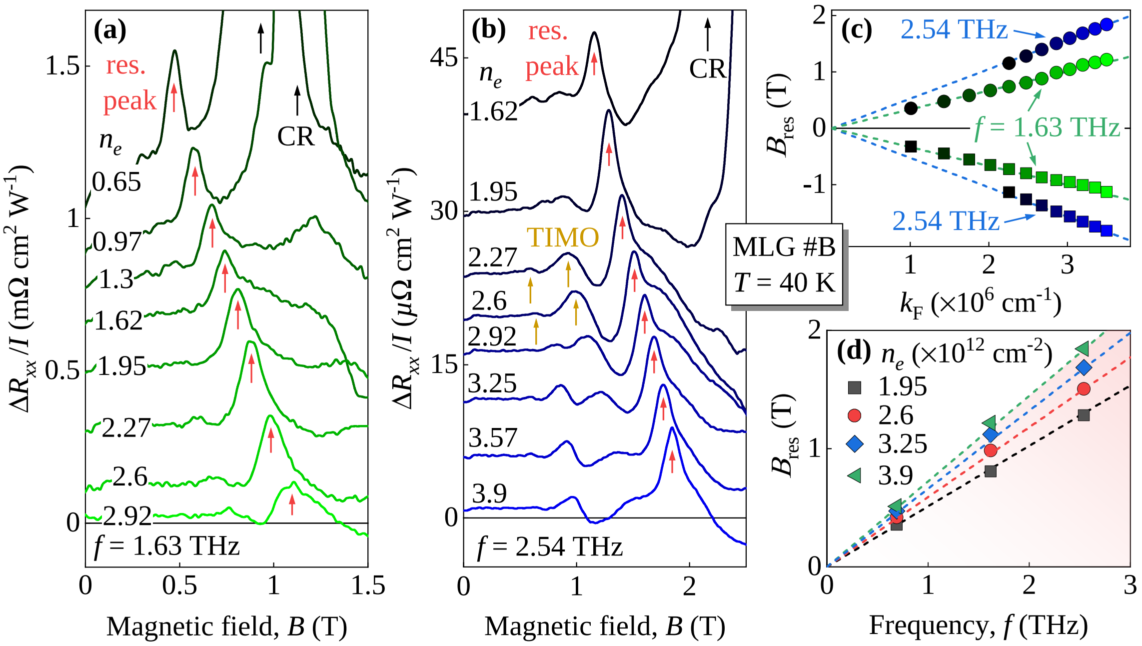

Figure 6.4: **(a, b)** Magnetic field dependencies of the photoresistance at $f = 1.63$ and 2.54 THz recorded for a wide range of carrier densities given in units of 10^{12} cm^{-2}. The resonant peaks near the main CR overtone are marked with red arrows. At lowest carrier densities, the main CR becomes apparent, indicated by black arrows. In addition, the traces for $f = 2.54$ THz show the appearance of TIMO (marked by yellow arrows) at moderate electron densities, which are superimposed by PIRO at the highest densities. The traces are shifted for clarity. **(c)** Magnetic field positions B_{res} of the photoresistance peaks determined for both magnetic field polarities plotted against the Fermi wave number k_{F} for the data measured at $f = 1.63$ and 2.54 THz, represented by green and blue circles/squares, respectively. The blue and green dashed lines follow Eq. (6.1) using $v_{\mathrm{F}} = 1.06 \times 10^6$ m/s. **(d)** Frequency dependence of B_{res} shown for several carrier densities. The corresponding colored dashed lines are calculated via Eq. (6.1). Figure adapted from Ref. [45] and supplemental material therein.

Fig. 6.2(c), the period of TIMO scales linearly with k_{F} similar to the photoresistance peak, but has a damped sinusoidal shape. In Chap. 7 TIMO are analyzed and discussed in detail. Figure 6.4(c) shows the resonant magnetic field positions of the peak near the main CR overtone as a function of k_{F} for both frequencies. The dependencies accurately exhibit a linear behavior according to Eq. (6.1) (blue and green dashed lines). To further confirm the validity of this equation, B_{res} was plotted as a function of f at several fixed carrier densities, see Fig. 6.4(d). It reveals that the resonant peak follows the dashed lines in corresponding colors calculated via Eq. (6.1), demonstrating a linear scaling with the radiation frequency.

The dependence of the anomalous photoresistance peak was also investigated with respect to the intensity I of the incident radiation. Figure 6.5(a) presents photore-

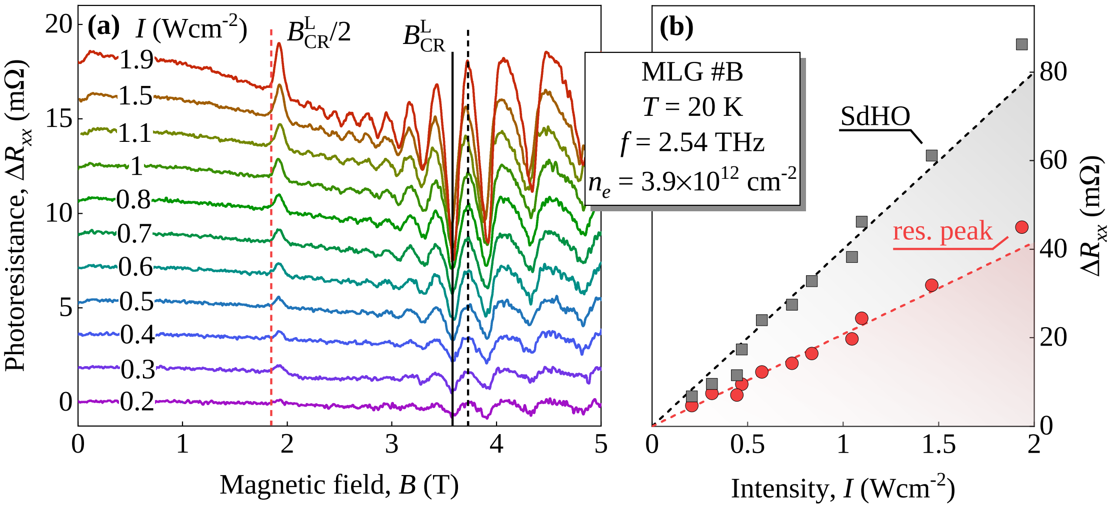

Figure 6.5: **(a)** Photoresistance traces recorded for different radiation intensities I for a given f and n_e. The red dashed line marks the position of the main CR overtone, while the two black dashed and solid lines indicate the extrema of the SdHO-periodic oscillations used to determine the amplitude value for the intensity dependence in panel (b). The solid line also represents the position of the regular CR. **(b)** Photoresistance peak height (red circles) and the amplitude of the SdHO-periodic oscillations (dark gray squares) as a function of radiation intensity. The dashed red and black lines denote linear fits to $\Delta R_{xx} \propto I$. The traces were obtained at $f = 2.54$ THz, $T = 20$ K, and $n_e = 3.9\times10^{12}$ cm^{-2}. Figure adapted from Ref. [45] and supplemental material therein.

sistance traces ΔR_{xx} measured for different intensity levels in the range $I = 0.2$ to 1.9 W cm^{-2}, recorded at $f = 2.54$ THz. At this frequency, the radiation has a small spot diameter and a high laser output power at the same time, thus providing the highest possible intensity, see Sec. 3. The analysis shows that the strength of the photoresistance peak near the main CR overtone scales linearly with the applied radiation intensity, see red circles in Fig. 6.5(b). This direct proportionality is illustrated by the red dashed line following $\Delta R_{xx} \propto I$. For comparison, the intensity dependence of the amplitude of SdHO-periodic oscillations in the vicinity of the regular CR was also analyzed. To determine their amplitude, half of the difference of the maximum and minimum values was extracted, which is indicated by black dashed and solid lines in Fig. 6.5(a). As for the photoresistance peak, the SdHO-periodic oscillations show a linear-in-I dependence, following the black dashed line.

Summarizing, giant photoresistance peaks induced by THz radiation have been observed in a high-quality graphene. These resonant peaks have been studied over a wide range of Fermi wave number, temperature, radiation frequency, and intensity. Data analysis have provided strong evidence that the asymmetric peaks couple to harmonics of the CR. Their theoretical description is the subject of the next chapter.

6.2 Discussion

The results presented above can be ascribed to signatures of near-field magnetoabsorption facilitated by metallic contacts, resulting in the excitation of so-called Bernstein modes (BM). According to the model, which describes the absorption of an inhomogeneously diffracted incoming EM wave enhanced by electron plasma oscillations, see Sec. 2.4, the total absorbed power is obtained as an integral over the wave vectors $\boldsymbol{q}$:

$$P_{\text{abs}} = 2\int \frac{\mathrm{d}\boldsymbol{q}}{(2\pi)^2}\frac{\omega}{2\pi q}|\boldsymbol{E}(\boldsymbol{q},\omega)|^2\,\Im\left\{\epsilon(\boldsymbol{q},\omega)^{-1}\right\}\,. \tag{6.2}$$

Here $\boldsymbol{E}(\boldsymbol{q},\omega) = F_{\boldsymbol{q}\omega}\boldsymbol{E}_0$ represents the amplitude of the $\boldsymbol{q}$-th spatial harmonic of the near field, defined by the product of the incident electric field $\boldsymbol{E}_0$ and the corresponding diffraction amplitude $F_{\boldsymbol{q}\omega}$. The latter is very small at $q \to 0$ due to the influence of the sample substrate, which acts as a gate leading to a large screening [45]. As q increases, the diffraction amplitude reaches a maximum and then decays due to the finite length and width of the sample contacts. This rapid decay for large q is shown in Fig. 6.6(a), where the diffraction amplitude $\langle|F_{\boldsymbol{q}\omega}|^2\rangle_\varphi$ averaged in the sample plane over the angle φ is plotted as a function of q. The imaginary part of the inversed dielectric function $\Im\{\epsilon(\boldsymbol{q},\omega)^{-1}\}$, also called the loss function, which depends on the wave vector and the frequency, is associated with the magnetoplasmon-assisted absorption. It is determined by the nonlocal conductivity $\sigma(\omega,\omega_c,\boldsymbol{q})$ of the 2DES following from the classical kinetic equation for the electrons' distribution function, for details see Ref. [45] and supplemental material therein. For the sake of simplicity, the following discussion is limited to the ungated case, where the loss function can be approximated by

$$\Im\left\{\epsilon(\boldsymbol{q},\omega)^{-1}\right\} = \sum_i \frac{\delta(q-q_{\text{mp}}^{(i)})}{|\partial\epsilon'/\partial\omega|v_{\text{g}}^{(i)}}\,. \tag{6.3}$$

This relation holds in the vicinity of the magnetoplasmon dispersion, where $q_{\text{mp}}^{(i)}$ is the real wave vector of the magnetoplasmon such that $\epsilon(q_{\text{mp}},\omega,\omega_c) = 0$ and $v_{\text{g}}^{(i)} = (\partial\omega/\partial q)|_{q=q_{\text{mp}}^{(i)}}$ is the magnetoplasmon group velocity. Note that the summation is applied to all branches of the plasmon dispersion at given ω and ω_c, resulting in the appearance of anti-crossings at $\omega = n\omega_c$. These are characterized by two branches just below each CR harmonic and a single branch just above. An illustration of Eq. (6.3) in Figs. 6.7(a, b) shows well-defined BMs.

The collective mode contribution [Eq. (6.3)] reveals that the total absorbed power

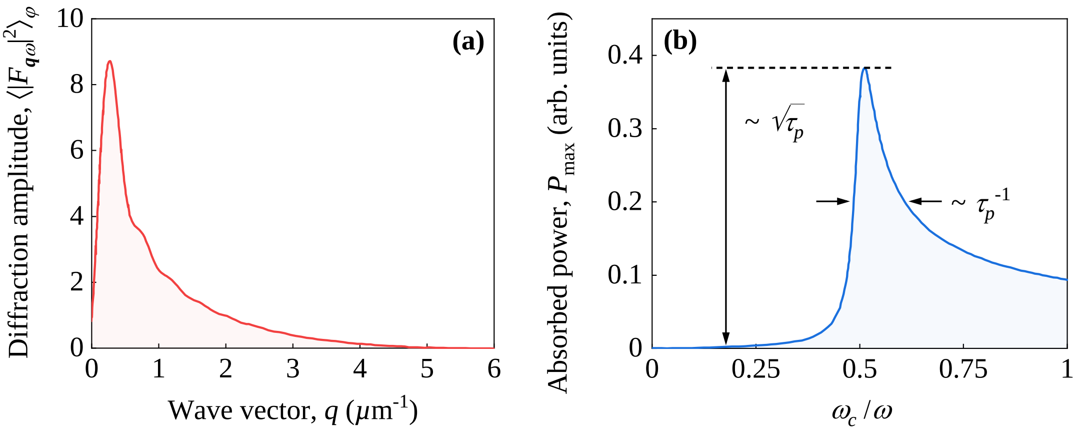

Figure 6.6: **(a)** Diffraction amplitude $\langle |F_{\boldsymbol{q}\omega}|^2 \rangle_\varphi$ averaged in the sample plane over the angle φ as a function of q. The calculations were performed for a contact length and width of 15 μm and 1 μm, respectively. **(b)** Absorbed power plotted against the frequency ratio ω_c/ω. The magnetoabsorption is significantly enhanced at the second harmonic of the CR ($\omega_c/\omega = 0.5$). The height and width of the absorption peak depend on the momentum relaxation time τ_p. Figure adapted from Ref. [45] and supplemental material therein.

P_{abs} in Eq. (6.2) is proportional to the reciprocal magnetoplasmon group velocity $v_{\text{g}}(\omega)^{-1}$. A vanishing group velocity in the immediate vicinity of the anti-crossings of the magnetoplasmon dispersion leads to a divergence of the loss function. Under this condition, the absorbed power is limited by the plasmon losses related to the electron momentum relaxation time τ_p as $P_{\text{abs}} \propto \sqrt{\tau_p}$, which directly affects the magnitude of the resonant peaks in the photoresponse. The resulting shape of the absorption at the second harmonic of the CR is shown in Fig. 6.6(b). Its width is proportional to $1/\tau_p$.

The above expressions can be understood qualitatively as follows: the sample is excited by the incident THz radiation, which is scattered by sharp metallic contacts located inside the Hall-bar region of the graphene structure (see microphotograph of MLG #B in Sec. 4.2 for comparison). This particular contact configuration leads to highly non-uniform near-fields with electric near field components $\boldsymbol{E}(\boldsymbol{q}, \omega)$, which are screened by the bare magnetoplasmon mode $\omega_{\text{mp}}(\boldsymbol{q})$ [Eq. (2.57)]. Strikingly, in regions where the magnetoplasmon mode crosses CR harmonics ($q \sim 1/R_c$), screening turns into anti-screening, resulting in a resonant field enhancement. Indeed, $\omega_{\text{mp}}(\boldsymbol{q})$ exhibits gaps at $\omega/\omega_c = 2, 3, ...$ and splits into branches. The emerging anti-crossings near these gaps produce plateaus in the magnetoplasmon dispersion, see Figs. 6.7(a, b). Here, the plasmonic group velocity vanishes and thus their DOS becomes exceptionally high. This in turn leads to a large loss function, see Eq. (6.3), which causes a strong enhancement of the near fields. Since the absorbed power is

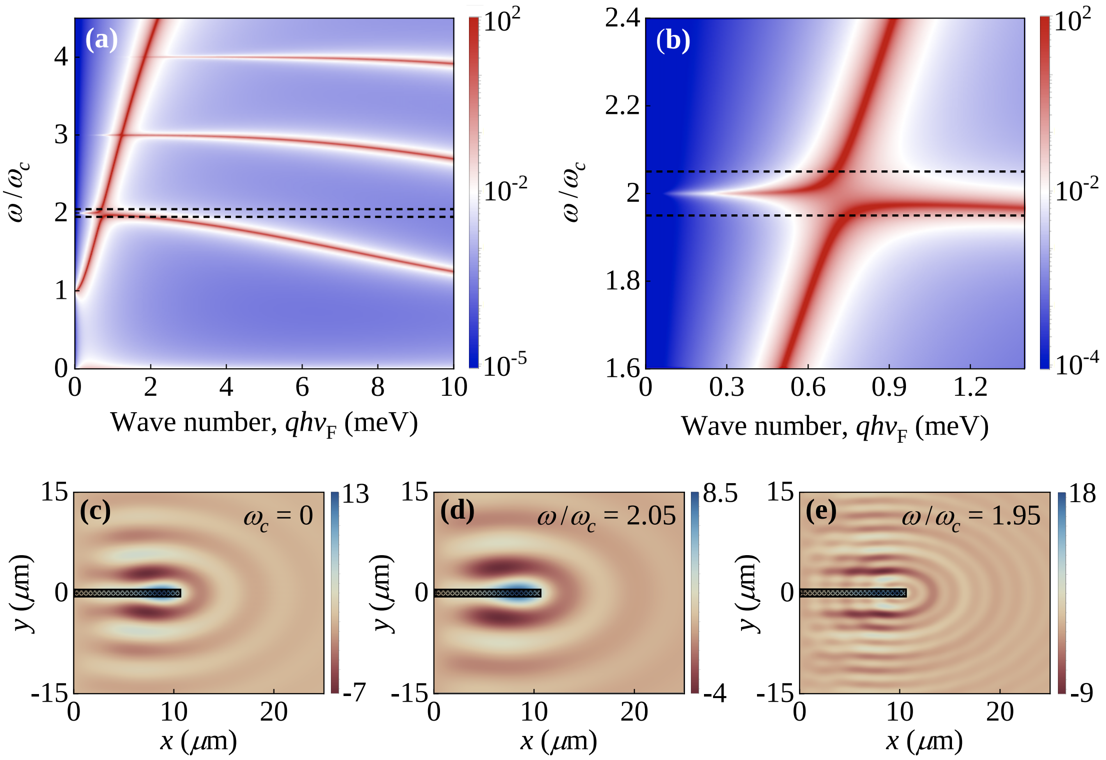

Figure 6.7: **(a)** Color map of the loss function $\Im\{\epsilon(\boldsymbol{q},\omega)^{-1}\}$ calculated in the presence of a magnetic field, assuming that the silicon substrate acts as a perfectly conducting metal gate. The dashed horizontal lines indicate the frequency ratios $\omega/\omega_c = 2.05$ and 1.95 used in the simulations [(d) and (e)]. **(b)** Enlarged region from (a) close to the main CR overtone. **(c − e)** Simulated plasmonic near-field distribution, i.e., the real part of the vertical field component $\Re\{E_z(x,y)\}$, facilitated by a metal lead (shaded rectangles) that is excited by THz radiation. This metal lead is located above the silicon gate and placed in contact with the graphene sheet. The panels show the distribution for graphene plasmons at zero B-field (c) and above (d) as well as below (e) the anti-crossing at $\omega/\omega_c = 2$, using $\omega/2\pi = 1$ THz and $n_e = 0.65 \times 10^{12}$ cm^{-2} as parameters for numerical calculations. Figure adapted from Ref. [45].

strongly enhanced in these regions of high plasmonic density, the sample exhibits resonant electron gas heating, revealing a large photoresistance at the harmonics of the CR.

Figures 6.7(c – e) illustrate the calculated distribution of the scattered THz electric field around a metal lead in real space [45]. For vanishingly small magnetic fields ($\omega_c = 0$) as well as for frequencies above the BM plateau ($\omega \gtrsim 2\omega_c$), the irradiated contacts excite plasmons or magnetoplasmons, respectively, with a well-defined period of the electric field in real space referring to the wave vector $q_{\mathrm{mp}}(\omega)$ [167], see Figs. 6.7 (c, d). However, due to the fact that the BM branch exhibits a maximum just below the gap at $\omega = 2\omega_c$ followed by a downward bend, there are two mag-

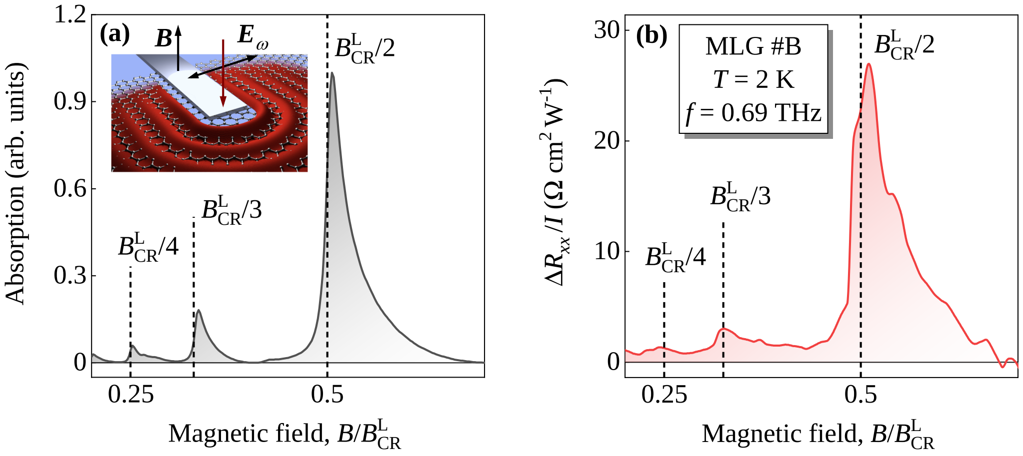

Figure 6.8: **(a)** BM-assisted absorption of THz radiation calculated according to Eq. (6.2) and plotted against the magnetic field normalized to $B^{\rm L}_{\rm CR}$. The inset shows a graphical representation of the magnetoplasmons launched at the graphene-metal interface by the incident radiation. **(b)** Experimentally measured photoresistance obtained in sample MLG #B at $T = 2$ K and $f = 0.69$ THz. The dashed vertical lines in both panels indicate the harmonics of the CR. Figure adapted from Ref. [45].

netoplasmon modes with different q values initiated by a given radiation frequency, see the bottom dashed vertical line in Figs. 6.7(a, b). This results in a double-mode beating, where a short-period fringing of the electric field is superimposed by a low-frequency pattern. These two periods merge at the plateau, causing a resonant enhancement of the radiation absorption.

Exploiting the absorbed power expression [Eq. (6.2)], the corresponding magnetoabsorption was calculated and compared with the experimentally observed photoresistance. Both are shown in Figs. 6.8(a, b), plotted as a function of the magnetic field normalized to $B^{\rm L}_{\rm CR}$. They reveal an excellent qualitative agreement. In particular, the resonant peaks appear close to the CR harmonics (see dashed vertical lines) and exhibit a strong asymmetry. Indeed, going to higher B-fields, the latter is characterized by a steep increase before approaching the maximum, followed by a gradual decrease. This asymmetry can be understood by looking at the BM dispersion near the gap: as the ratio ω/ω_c converges from the gap side to the plateau of the lower BM branch, the absorption and thus the photoresistance increase sharply. After approaching its maximum value, a slowly increasing group velocity leads to a smooth decay, mapping the regime of conventional magnetoplasmon excitation, where non-locality no longer plays an essential role. This asymmetric shape is also preserved for the higher harmonics of the CR, specifically the third and fourth, as can be seen in Figs. 6.8(a, b). This strongly supports the explanation of the sharp photoresistance peaks in terms of the BM-assisted resonances. Similar to the regular

CR analyzed in Chap. 5, the positive photoresistance [see Figs. 6.1(a, b)] is due to an enhanced absorption, which enables a strong THz-induced electron gas heating and consequently an enhanced electron-phonon scattering (see also Sec. 2.3).

Another strong confirmation that the peaks are related to anti-crossings of the BM dispersion appearing at CR overtones is the fact that their magnetic field positions are precisely determined by integer fractions of $B_{\mathrm{CR}}^{\mathrm{L}}$ given by Eq. (2.34). As expected, the dominant photoresistance peak scales linearly with the Fermi wave number and the applied radiation frequency, see Figs. 6.2(c) and 6.4(c, d). Note that when comparing the photoresistance values at different THz frequencies, the magnitudes of the resonant peaks show a clear decrease towards higher radiation frequencies. A possible explanation is that the increase in frequency shifts the BM dispersion to larger q values, where the diffraction amplitude $F_{\boldsymbol{q}\omega}$, which determines the scattered near field amplitude, decreases significantly, see Fig. 6.6(a). As a consequence, the electron gas heating is suppressed, resulting in a less pronounced photoresistance peak.

It is worth noting that the BMs fully evolve in sufficiently clean systems, which provide a ballistic regime, i.e., $\omega\tau_{ee} \gg 1$ [105]. In Fig. 6.9 the magnetoplasmon dispersion around the second harmonic of the CR is visualized using three regimes of electron transport determined by the electron-electron (e-e) scattering time, τ_{ee}. Panel (a) shows the ballistic regime ($\tau_{ee} = 10$ ps) where the anti-crossing is clearly visible. Apparently, moving to shorter τ_{ee} [panel (b) with $\tau_{ee} = 1$ ps] reveals a smearing of the BM anti-crossing, which finally disappears completely at $\tau_{ee} = 0.1$ ps, see panel (c). The latter condition corresponding to the hydrodynamic regime [105]. Consequently, the BM-assisted photoresistance not only confirms that the ballistic regime is fully applicable, but also directly attests a superior quality of MLG #B, as supported by the corresponding transport characterization, see Sec. 4.2.

Under certain conditions, the main CR overtone in the photoresponse significantly exceeds the signal of the regular CR. In particular, the latter is strongly pronounced at sufficiently low carrier densities and high radiation frequencies. However, this peculiar behavior is attributed to the radiative decay, which is a consequence of the screening of the radiation by electrons in graphene [45]. In contrast to regular CR, the strength of the photoresponse peaks should not be affected by radiation screening, since magnetoabsorption at the CR overtones is facilitated by BM-assisted near-field excitations. In fact, the results show a relatively weak decay of the peak strength at higher carrier densities, which is due to a small decrease of the diffraction amplitude $F_{\boldsymbol{q}\omega}$.

Let us now say a few words about PIRO in the photoresistance. The appearance

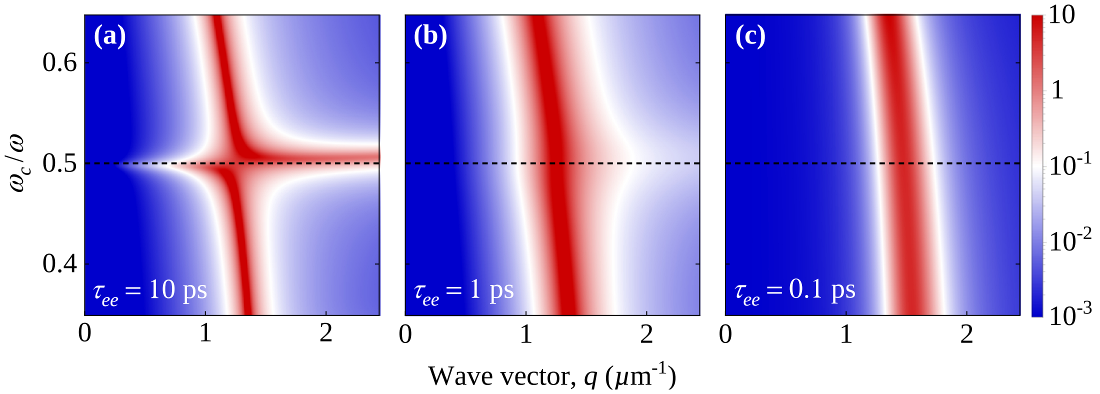

Figure 6.9: Magnetoplasmon dispersion visualized by the loss function against the wave vector. **(a)** Ballistic regime with $\tau_{ee} = 10$ ps, **(b)** intermediate regime with $\tau_{ee} = 1$ ps, and **(c)** hydrodynamic regime with $\tau_{ee} = 0.1$ ps. The contour plots were obtained using $n_e = 0.65 \times 10^{12}$ cm^{-2} and $f = 2$ THz. Figure adapted from Ref. [45] and supplemental material therein.

of PIRO is somewhat unexpected and may be understood as follows: in the non-resonant case, the incoming THz radiation is mostly absorbed by the electron gas. Since the energies required to reach optical phonons are too large, the absorbed energy is transferred to acoustic phonon branches via electron-phonon coupling. Subsequently, this increase in the acoustic phonon population leads to the formation of PIRO in the THz photoresistances due to resonant absorption of phonons by carriers [168]. The maxima of PIRO observed in the photoresistance seem to correspond to the first minima of the conventional dark magnetoresistance at conditions where PIRO appear. They follow accurately Eq. (4.1) with $p = 1.5$. The value for the sound velocity given by $v_s = 1.36 \times 10^4$ m/s according to the fit in the inset of Fig. 6.2(c) agrees well with the analysis of PIRO in dark magnetoresistance, see Sec. 4.2, and with previous studies in similar high quality graphene structures [152]. This, and the fact that PIRO emerge at elevated T in the dark magnetoresistance, provide compelling arguments that the photoresistance does indeed exhibit PIRO-related oscillations. However, a detailed analysis of PIRO in photoresistance requires further intensive studies beyond the scope of this work.

Finally, the discussion is supplemented by another possible description of the resonant photoresponse close to the CR harmonics. In particular, it has recently been proposed that a high-frequency flow of a two-dimensional electron fluid exposed to a magnetic field may lead to viscoelastic resonances related to the generation of the transverse magnetosound [169]. Moreover, these resonances associated with the viscous electron transport regime have been discussed in relation to the resonant photoresistivity observed in GaAs-based heterostructures near the main CR overtone [170]. However, in the proposed scenario, it is not feasible to explain our experimental findings.

First, the asymmetry of the resonant peaks in our experiments is different from that proposed in Refs. [105, 169]. Indeed, a smooth tail at low B-fields and a steep decrease of the photoresponse at higher fields is predicted, which is in strong contrast to our observations, see Figs. 6.1(a – c). Furthermore, these works confirm that there is only a single peak appearing around the second CR harmonic. However, the results here also show resonances at double and even triple the cyclotron frequency, see, e.g., Fig. 6.3(b), which are not predicted by the hydrodynamic model, but are in accordance with BM theory. Next, the regime of hydrodynamics in high-quality graphene is achieved at rather large temperatures, exceeding $T \gtrsim 100$ K [171]. This is in sharp contrast to the observed resonant photoresistance, which vanishes already at about $T \approx 50$ K, considering the most dominant peak at the main CR overtone, see Fig. 6.3(a). This behavior is in line with the theory of BM-assisted magnetoabsorption [105]. Considering that the e-e collision rate becomes more dominant with increasing T, this significantly reduces the magnitude of the photoresistance around the harmonics of the CR and smears the anti-crossing in the BM dispersion, as demonstrated in Fig. 6.9. Moreover, the photoresistance peak observed here scales linearly with radiation intensity, which is consistent with the overall linear-in-P scaling of the photoresistance, as confirmed by the comparison between the peak and the SdHO-periodic signal in Fig. 6.5(b). The absence of a saturation or threshold behavior apparently precludes the scenario discussed in terms of possible instabilities of the electron plasma [172] that accounts for the observations of photoresistance peaks in GaAs-based heterostructures. Furthermore, the linear scaling with radiation intensity also excludes possible multiphoton effects [13].

Before concluding this chapter, we will briefly refer to our related study without a detailed discussion. Very recently, a strong near-field coupling in bilayer graphene structures, facilitated by metallic interdigitated dual-grating gate fingers located at the top of the devices, has been exploited to induce plasmonic splitting of the CR [49]. In contrast to MLG #B, the periodic metallic structure in this work covers a substantial part of the sample, see the microphotograph in Fig. 6.10(b), and thus enhances the near-field diffraction used to force an even stronger interaction of the magnetoplasma with the THz radiation. Figure 6.10(a) shows our central result, the photovoltage response as a function of the applied magnetic field, using a similar experimental setup. Figures 6.10(b, c) present the modeled ratchet response at both limits of the developed theory, in the regimes of $\tau_{ee} \ll \tau_p$ [panel (b)] and $\tau_{ee} \gg \tau_p$ [panel (c)]. While the measured response at the second CR overtone

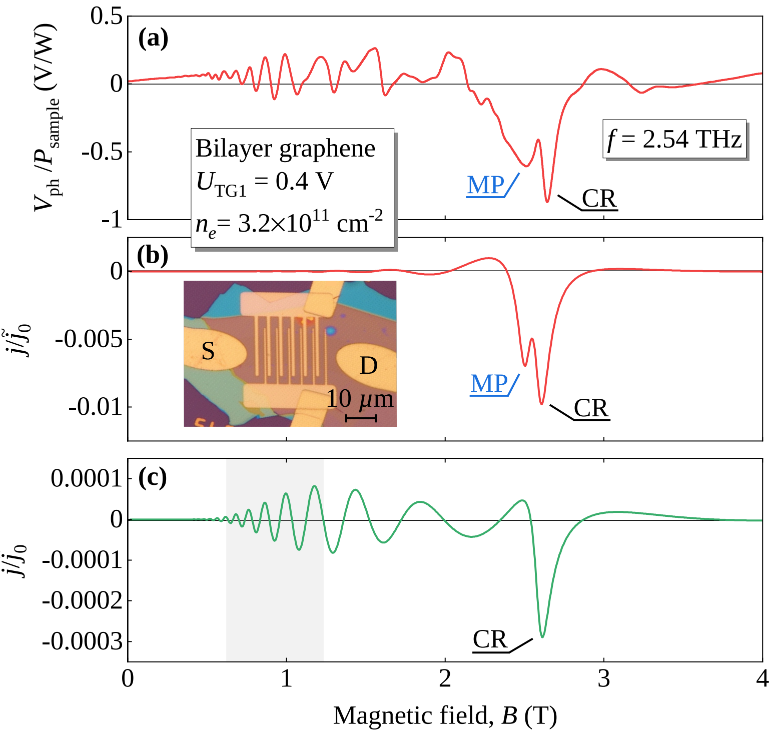

Figure 6.10: **(a)** Magnetic field dependence of the induced photovoltage, normalized to the effective power P_{sample} incident on the sample surface. The trace was obtained in a bilayer graphene device under THz radiation with frequency $f = 2.54$ THz and biased top gate voltage ($U_{\text{TG1}} = 0.4$ V). **(b, c)** Calculated normalized ratchet current in the regime of sufficiently fast e-e collisions (b) and dominant impurity scattering (c). The inset shows a microphotograph of the investigated structure. The source and drain contacts are marked with S and D. The gray shaded area highlights the enhanced region near the CR overtone. The cyclotron and magnetoplasmon resonances are denoted by CR and MP, respectively. The data were obtained at $T = 4.2$ K and a carrier density of $n_e = 3.2 \times 10^{11}$ cm^{-2}. Figure adapted from Ref. [49].

is substantially suppressed ($B \approx 1$ T), two distinct dips are observed near the regular CR ($B \approx 2.5$ T): the CR itself and a magnetoplasmon resonance. The coexistence of both resonances is attributed to a combination of the dominant e-e collisions in the structured bilayer graphene, resulting in an almost hydrodynamic system, and the nonlinear nature of the observed ratchet effect. The latter describes the conversion of the ac THz electric field into a dc electric current and has been extensively studied in monolayer [173, 174] and bilayer graphene [49–51]. Due to the metallic structure on top of the graphene sandwich, the radiation field has a homogeneous and an inhomogeneous component modulated by a finite wave vector $q = 2\pi/L$, where L is the superlattice period. The former gives rise to the regular CR, while the latter yields the magnetoplasmon resonance, which reflects the nonlinear conversion of an ac drive into a dc current. Thus, structured graphene-based devices provide a fruitful platform and promising tool for studying the properties of the two-dimensional electron plasma via optical excitation.

Summarizing, it has been demonstrated that the experimental results are accurately described by the developed theory. In particular, the resonant peaks coupled to the CR harmonics observed in the photoresponse unambiguously stem from BM-assisted magnetoabsorption facilitated by THz-induced near fields. Based on the calculations of the loss function, it has been shown that under the condition of strong photoresponse, the BM dispersion exhibits plateaus. This in turn leads to a divergent plasmonic DOS and a resonantly enhanced radiation absorption, manifested in strong electron gas heating and resonant photoresistance peaks. The above observations have already shown signatures of TIMO at higher radiation frequencies. The next chapter is devoted to a detailed study of these oscillations in graphene using a Hall bar geometry with conventional contacts.

7 Magnetooscillations in Graphene induced by Terahertz Radiation

After studying graphene with a special contact geometry, this chapter focuses on a standard Hall bar with conventional contacts, using metal leads outside the main graphene channel. Pronounced TIMO are observed at low magnetic fields. The analysis of their variation with radiation frequency and carrier density reveals a common origin with the well-known microwave-induced resistance oscillations (MIRO) detected in GaAs QWs. Similar to the latter, their graphene analog is also governed by the ratio of the incident radiation frequency to the quasiclassical cyclotron frequency. To this end, theoretical descriptions based on the shift of the cyclotron resonance orbit center, known as the displacement mechanism, and the inelastic mechanism, considering a radiation-induced variation of the distribution function, are reviewed.

7.1 Experimental Results

Figure 7.1 shows the magnetic field dependencies of the photosignals obtained in MLG #C as a response to linearly polarized radiation with frequency $f = 0.69$ THz. The different traces of the photoconductive signal, $\Delta\sigma$, [panel (a)] and the photovoltage, V_{ph}, [panel (b)] are presented for several representative values of the carrier density in the range of $n_e = (0.14 - 2.75) \times 10^{12}$ cm^{-2}, labeled next to the curves. The signals are normalized to the radiation intensity, which is estimated as $I \approx 0.24$ W cm^{-2}. For low carrier densities, the traces exhibit the conventional behavior: the photoresponse undergoes a clear enhancement that shifts to higher magnetic fields with increasing n_e, which is additionally superimposed by fast $1/B$-periodic oscillations. These are clearly attributed to an admixture of CR-enhanced μ-photoconductivity and CR heating-induced suppression of SdHO. Both result from the THz-induced electron gas heating, as addressed in Chap. 5. Strikingly, at higher carrier densities ($n_e > 1\times10^{12}$ cm^{-2}), see Fig. 7.1(b), the picture changes qualitatively: at lower fields, in the region where SdHO-periodic oscillations are exponentially suppressed, the photoresponse exhibits a second type of magnetooscillations, termed as TIMO (THz-induced magnetooscillations). As will be discussed below, these low-B oscillations share a common origin with MIRO, first observed in GaAs-based heterostructures [6], but remarkably reveal some peculiarities specific to graphene.

To follow up on this, Figs. 7.2(a, b) show the transmittance and corresponding nor-

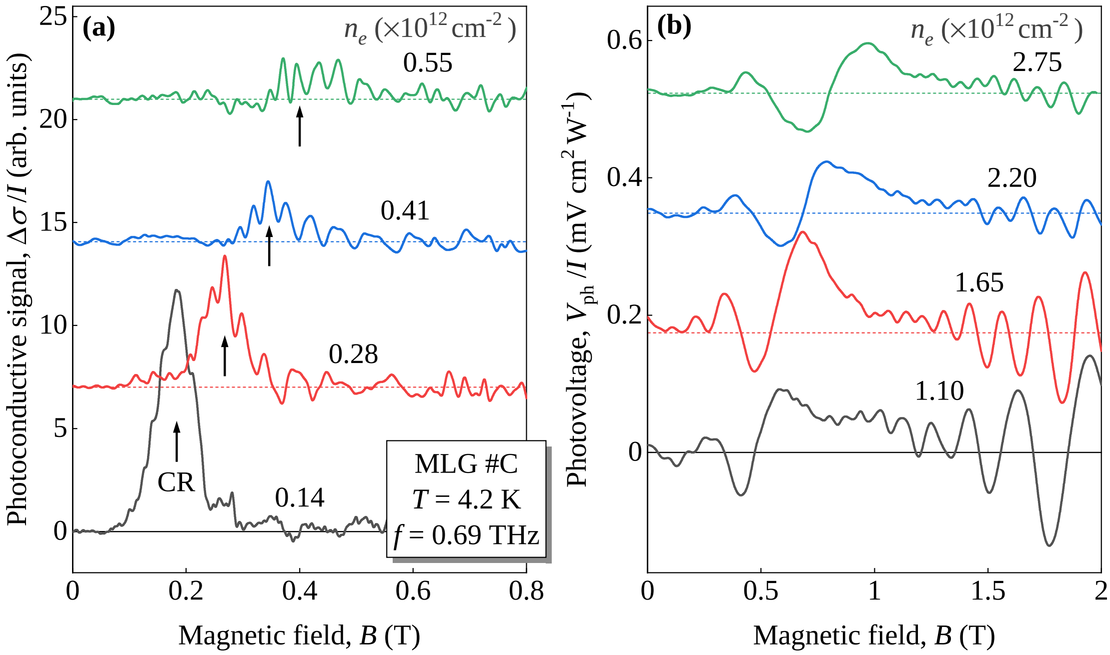

Figure 7.1: Photosignal traces for low **(a)** and high **(b)** carrier densities n_e versus the magnetic field obtained at $T = 4.2$ K in response to radiation with $f = 0.69$ THz. The traces are up-shifted for clarity and correspond to the different carrier densities in units of 10^{12} cm^{-2}, which are labeled near the curves. The black arrows in panel (a) mark the position of the CR. The dashed horizontal lines indicate the zero line for each photoresponse curve. Figure adapted from Ref. [46].

malized photoresistance traces obtained in GaAs #A at $T = 1.8$ K for $f = 0.297$ (red) and 0.69 THz (black). In contrast to the results shown in Fig. 5.1, here GaAs #A was illuminated with ambient light prior to the measurements, resulting in higher electron density and mobility due to the persistent photoconductivity effect, see Sec. 4.1 for details. This property allows to resolve clear MIRO. Note that due to the change in electron mobility, the width of the CR dip in the transmittance becomes considerably wider, while the shape gets slightly asymmetric [see the trace for $f = 0.297$ and 0.69 THz in Fig. 5.1(c) for comparison]. Figures 7.2(c, d) present the photoresistance as a function of the inverse magnetic field, which is additionally normalized to the magnetic field position of the CR determined by the transmittance. The data clearly show a damped sinusoidal behavior with exponential growth towards the CR ($B_{\mathrm{CR}}^{\mathrm{P}}/B = 1$). In addition, the $1/B$-periodicity of MIRO is revealed, with nodes at the CR harmonics, i.e., $B_{\mathrm{CR}}^{\mathrm{P}}/2$, $B_{\mathrm{CR}}^{\mathrm{P}}/3$, ..., indicated by the gray guidelines.

A very similar picture is observed for TIMO. Figure 7.3(a) shows the corresponding traces from Fig. 7.1(b) replotted as a function of the inverse magnetic field. Since TIMO appear below the onset of the SdHO-periodic oscillations, only the low

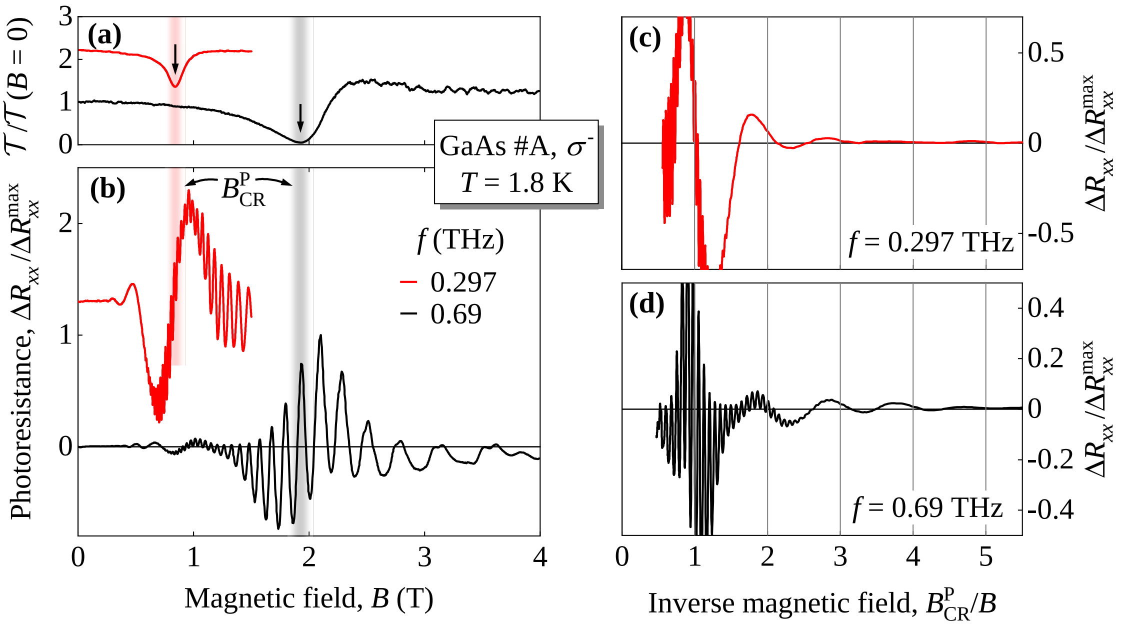

Figure 7.2: **(a)** Normalized radiation transmittance obtained in GaAs #A after brief illumination with room light prior to measurements for two radiation frequencies, $f = 0.297$ and 0.69 THz, represented by the red and black traces, respectively. The arrows mark the CR dips. **(b)** Simultaneously measured normalized photoresistance $\Delta R_{xx}/\Delta R_{xx}^{\rm max}$. The shaded areas labeled $B_{\rm CR}^{\rm P}$ indicate the CR position. **(c, d)** Photoresistance for both frequencies plotted as a function of the inverse magnetic field normalized to $B_{\rm CR}$ determined from the corresponding transmittance dip. The gray lines point to the nodes of MIRO. All measurements were performed at $T = 1.8$ K. Figure adapted from Refs. [47, 48].

magnetic field region is shown here, excluding higher fields. To rigorously prove the $1/B$-periodicity, each successive peak and dip of TIMO was assigned an integer number. This procedure is exemplified for the red curve, where the extrema were consecutively labeled with index numbers $N = 1, 2, ..., 5$ corresponding to the inverse magnetic field values $1/B_N$ at which the extrema appear. This functional relationship is illustrated in Fig. 7.3(b) for various carrier densities following the color code in panel (a), clearly demonstrating that the positions of all the extrema for each carrier density accurately follow straight lines. This analysis confirms that TIMO are $1/B$-periodic, while the slopes of these lines simultaneously reveal their fundamental frequency $B_{\rm F}$. Although the slope becomes steeper as the carrier density increases, the intercept of the lines with the vertical axis remains almost unchanged, yielding a value of -0.25 ± 0.1. This result can then be transformed into a functional behavior for the extrema given by $N/2 = B_{\rm F}/B_N - 0.25$, where the offset represents the phase shift of the extrema with respect to the nodes. Consequently, the oscillatory

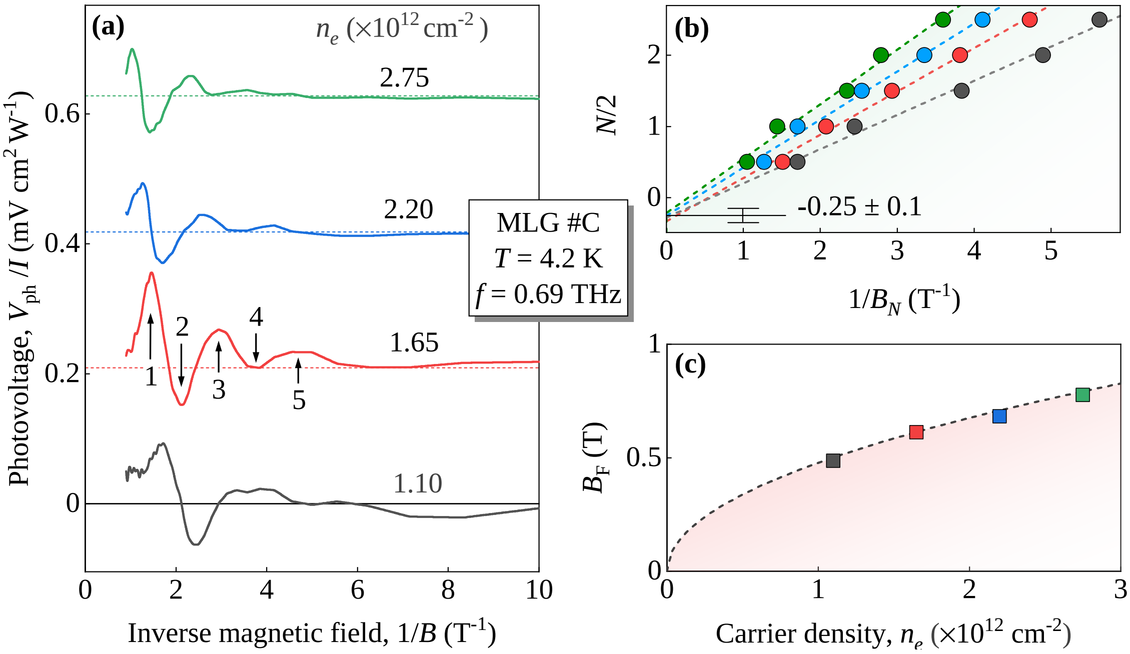

Figure 7.3: **(a)** TIMO data from Fig. 7.1(b) as a function of the inverse magnetic field. Only the low magnetic field region is shown here, omitting the SdHO-periodic oscillations at higher fields for convenience. The curves are up-shifted for clarity. **(b)** TIMO extrema assigned with index numbers $N = 1, 2, ...5$ plotted against the inverse magnetic field values $1/B_N$ at which the peaks and dips occur. The assignment is illustrated in panel (a) with vertical arrows for the red trace. The dashed colored lines correspond to linear fits of the data points providing the fundamental frequency B_F and the phase of TIMO. **(c)** Dependence of B_F on the carrier density n_e. The dashed line follows B_CR^L, see Eq. (2.34) in Sec. 2.2 with $v_\mathrm{F} = 1.06 \times 10^6$ m/s as the Fermi velocity. Figure adapted from Ref. [46].

behavior of TIMO is described by a sinusoidal expression according to the relation

$$V_\mathrm{ph}^\mathrm{TIMO} \propto -\sin\left(\frac{2\pi B_\mathrm{F}}{B}\right) , \tag{7.1}$$

therefore, determining their phase. From Eq. (7.1) it becomes clear that the value of B_F coincides with the last node of TIMO, while all other nodes correspond to higher harmonics of the fundamental frequency. Figure 7.3(c) shows B_F, determined by the slopes in Fig. 7.3(b), as a function of n_e. It demonstrates that the fundamental frequency of TIMO closely follows the magnetic field position of the CR in graphene $B_\mathrm{F} = B_\mathrm{CR}^\mathrm{L} = hf\sqrt{\pi n}/ev_\mathrm{F}$ with $v_\mathrm{F} = 1.06 \times 10^6$ m/s for the Fermi velocity. This already gives a strong evidence that similar to MIRO in GaAs QW, TIMO in graphene are coupled to the harmonics of the CR.

The periodicity of MIRO has a linear frequency dependence, as can be seen from the traces in Fig. 7.2(b). Indeed, extracting B_CR^P from MIRO recorded at $f = 0.297$

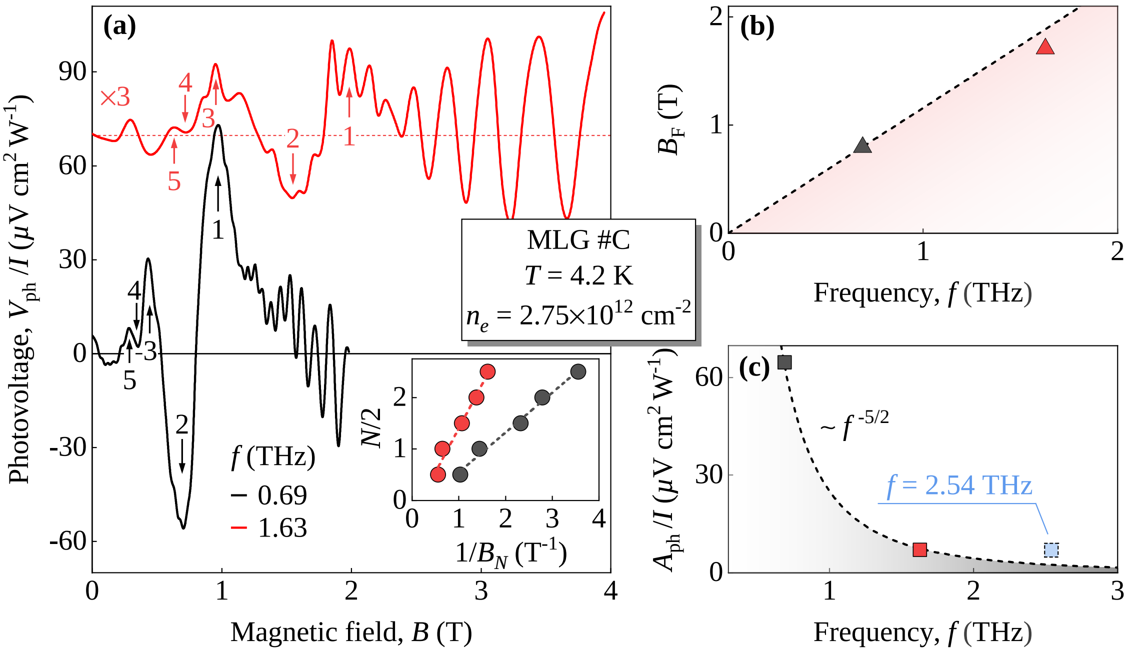

Figure 7.4: **(a)** Normalized photoresponses for two different excitation frequencies $f = 0.69$ (black trace) and 1.63 THz (red trace) offset for clarity. The vertical arrows indicate the extrema of TIMO and assign integer numbers to the peaks and dips. These numbers are plotted in the inset against the inverse magnetic field values $1/B_N$ of the corresponding extrema. The dashed lines are fits to the data points, yielding values for B_F. **(b)** Fundamental frequency as a function of f. Here the dashed line was calculated according to the semiclassical expression for B^L_CR, see Eq. (2.34) in Sec. 2.2. **(c)** The amplitude A_ph of TIMO determined from half the difference of the two extrema of the first oscillation period. Additionally, the value for the frequency $f = 2.54$ THz was included as a data point (sheer and blue square). The dashed line is a fit according to $\propto f^{-5/2}$. All panels use the same color code for the corresponding frequency. All results were obtained at $n_e = 2.75 \times 10^{12}$ cm^{-2} and $T = 4.2$ K. Figure adapted from Ref. [46] and supplemental material therein.

and 0.69 THz gives $B^\mathrm{P}_\mathrm{CR}(0.297\ \mathrm{THz}) = 0.84$ T and $B^\mathrm{P}_\mathrm{CR}(0.69\ \mathrm{THz}) = 1.90$ T; thus, the ratio is about 2.2, which, assuming a linear dependence, corresponds to the frequency scaling factor ($0.69/0.297 \approx 2.3$). Returning to TIMO, Fig. 7.4(a) shows photovoltage traces recorded as a response to $f = 0.69$ (black trace) and 1.63 THz (red trace) for $n_e = 2.75 \times 10^{12}$ cm^{-2} and $T = 4.2$ K. Note that the trace obtained at $f = 1.63$ THz has been multiplied by a factor of three for clarity. Surprisingly, at such a high frequency, i.e., well above 1 THz, the first period of TIMO is still clearly distinguishable from the smooth background and the fast SdHO-periodic oscillations. The influence of the latter is considerable, since TIMO are shifted into the region where they are already strongly developed. Since MIRO were completely suppressed in GaAs #A at these frequencies, this observation is particularly remarkable. The inset shows the analysis of the periodicity of TIMO by plotting the index numbers of peaks and dips against the corresponding inverse magnetic field using the same procedure as introduced in Fig. 7.3. The linear behavior for both traces proves a $1/B$-periodicity, while the slope determines the B_{F}. The latter scales linearly with the excitation frequency as shown in Fig. 7.4(b) and is well fitted by the semiclassical expression for $B_{\mathrm{CR}}^{\mathrm{L}}$, see Eq. (2.34) in Sec. 2.2. This is an additional feature in common with the MIRO effect, confirming that TIMO are indeed a MIRO analog.

Figure 7.4(c) presents the TIMO amplitude as a function of the excitation frequency. The amplitudes were determined by taking half the difference between the peak and dip values (indicated by 1 and 2, respectively) of the first oscillation period for both frequencies. The black and red squares represent the values for $f = 0.69$ and 1.63 THz, which follow the black dashed curve in good agreement, yielding $A_{\mathrm{ph}} \propto f^{-5/2}$. Despite this intriguing behavior in graphene, excitation frequencies above 2 THz prove that the detection of TIMO is already challenging. This is not least due to the strong superposition of SdHO-periodic oscillations, making TIMO almost indistinguishable at high frequencies. However, a roughly estimated value for the trace at $f = 2.54$ THz (not explicitly shown) is indicated as a blue and sheer square in Fig. 7.4(c). This observation is further supported by the appearance of TIMO in MLG #B at $f = 2.54$ THz and similar carrier densities, see Fig. 6.4(b) in Chap. 6. Here the SdHO-periodic oscillations are thermally suppressed revealing clear TIMO denoted by yellow arrows. This behavior underlines an exceptional stability of TIMO towards higher frequencies.

So far, the temperature dependence of TIMO has been disregarded, as all previous data have been obtained at liquid helium temperature. However, this degree of freedom plays a crucial role in understanding the microscopic mechanism associated with TIMO observed in graphene. Figure 7.5(a) shows normalized photovoltage traces recorded at temperatures ranging from $T = 4.2$ to 90 K for $f = 0.69$ THz. Remarkably, in sharp contrast to the SdHO-periodic response, TIMO and especially its first period are well resolved even above liquid nitrogen temperatures $T > 77$ K. Indeed, as illustrated in the inset of Fig. 7.5(a), the traces for $T = 80$ and 90 K exhibit an oscillatory signature where the first period of TIMO is expected (indicated by the black vertical arrows), while the SdHO-periodic oscillations are already clearly suppressed. To explore this behavior, the amplitudes of TIMO, $A(T)_{\mathrm{ph}}^{\mathrm{TIMO}}$, and SdHO-periodic oscillations, $A(T)_{\mathrm{ph}}^{\mathrm{SdHO}}$, normalized to the amplitude value at $T = 4.2$ K, were plotted as a function of temperature in Fig. 7.5(b). The amplitudes of TIMO were obtained as the half difference between the respective maxima and minima of the first oscillation period. The values for the SdHO periodic response were estimated by the same procedure, except that a magnetic field was chosen where the oscillations are well

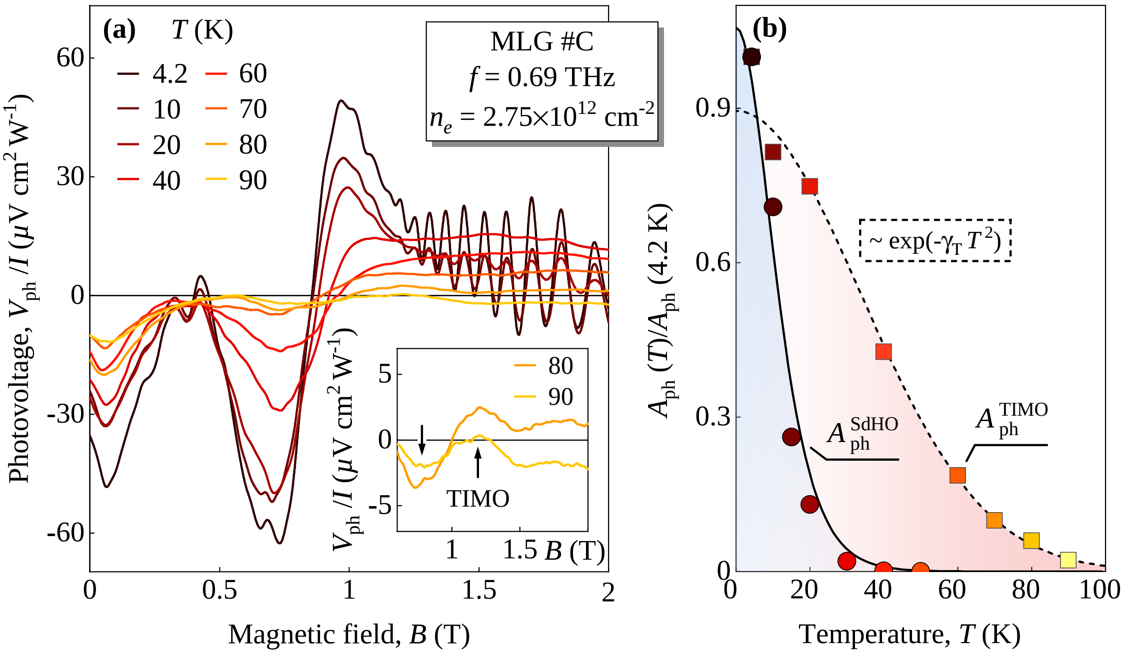

Figure 7.5: **(a)** Photovoltage traces for different temperatures recorded in response to $f = 0.69$ THz at a fixed carrier density $n_e = 2.75 \times 10^{12}$ cm^{-2}. The inset shows a close-up of the curves for $T = 80$ and 90 K with the TIMO signatures indicated by vertical arrows. **(b)** The corresponding temperature dependencies of the first period of TIMO ($A_{\rm ph}^{\rm TIMO}$) and of the SdHO-periodic photovoltage ($A_{\rm ph}^{\rm SdHO}$). The values were determined by calculating half the difference between the peak and the dip of one oscillation period (for TIMO the first one and for SdHO the one near $B \approx 1.8$ T). The former is fitted for $T \geq 10$ K by the function $\propto \exp(-\gamma_{\rm T} T^2)$ which gives the damping parameter $\gamma_{\rm T} = 4.4 \times 10^{-4}$ K^{-2}. The dashed line is calculated by the conventional Lifshitz-Kosevich formula following the data points of $A_{\rm ph}^{\rm SdHO}$ and providing an estimate for the effective mass $m^* = 0.03\, m_e$ with m_e as the free electron mass. Figure adapted from Ref. [46] and supplemental material therein.

established and less disturbed by the background. As can be seen, both follow a very different temperature dependence: while TIMO remains visible up to 90 K, the SdHO-periodic signal disappears completely at $T \approx 40$ K over the whole B-range under study. The former follows closely $V_{\rm ph} \propto \exp(-\gamma_{\rm T} T^2)$ (shown by the dashed line) for temperatures above 10 K with $\gamma_{\rm T} = 4.4 \times 10^{-4}$ K^{-2}, a dependence characteristic for the displacement mechanism of MIRO [175, 176]. The SdHO-periodic signal is well fitted by the conventional Lifshitz-Kosevich formula [160, 161] as indicated by the solid line, see Eq. 5.4.

Of no less importance is the study of the photovoltage signal in relation to the excitation power. The previously presented data were measured at the highest possible radiation intensity of about $I \approx 0.24$ W cm^{-2}. Figure 7.6(a) shows the photovoltage obtained for a frequency of $f = 0.69$ THz, $T = 4.2$ K, and $n_e = 1.65 \times 10^{12}$ cm^{-2}. Despite the fact that TIMO and the SdHO-periodic oscillations remained visible by

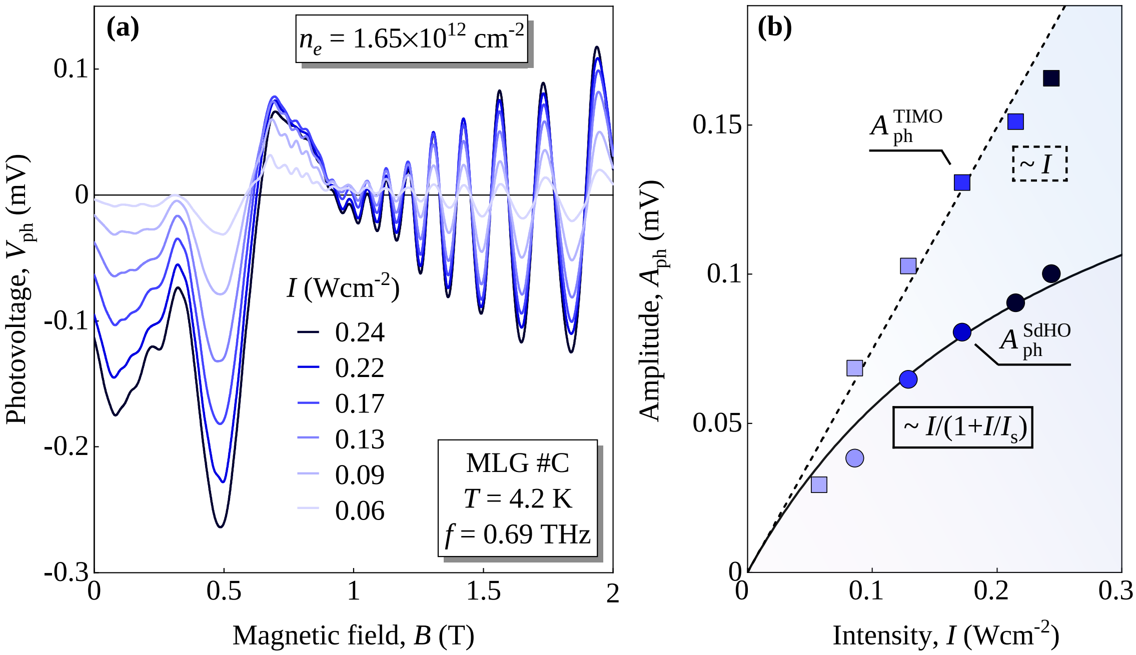

Figure 7.6: **(a)** Photovoltage recorded at different radiation intensities, obtained for $f = 0.69$ THz at $n_e = 1.65 \times 10^{12}$ cm^{-2} and $T = 4.2$ K. **(b)** The corresponding amplitudes of TIMO $A_{\mathrm{ph}}^{\mathrm{TIMO}}$ and SdHO-periodic oscillations $A_{\mathrm{ph}}^{\mathrm{SdHO}}$ plotted against the corresponding radiation intensity. The values were determined by calculating half the difference between the peak and the dip of an oscillation period (for TIMO the first one and for SdHO the one near $B \approx 1.8$ T). The dashed line follows a linear dependence on I, which represents the TIMO amplitude, while the solid line is calculated according to the expression $A_{\mathrm{ph}}^{\mathrm{SdHO}} \propto I/(1 + I/I_{\mathrm{s}})$ with a saturation intensity of $I_{\mathrm{s}} = 0.26$ W cm^{-2}. Figure adapted from Ref. [46] and supplemental material therein.

reducing the radiation intensity down to $I = 0.06$ W cm^{-2}, the evolution of both is found to be different as demonstrated in Fig. 7.6(b) for $A(I)_{\mathrm{ph}}^{\mathrm{TIMO}}$ and $A(I)_{\mathrm{ph}}^{\mathrm{SdHO}}$. The dependence of the TIMO amplitude is rather linear corresponding to the fit $A_{\mathrm{ph}} \propto I$ (dashed line) with a weak tendency to saturate above 0.22 W cm^{-2}. In contrast, the SdHO-periodic response clearly shows a sublinear power dependence. To emphasize this behavior, the data points were fitted by the saturation dependence according to the empirical expression $A_{\mathrm{ph}}^{\mathrm{SdHO}} \propto I/(1 + I/I_{\mathrm{s}})$ (solid line) with a saturation power $I_{\mathrm{s}} = 0.26$ W cm^{-2}.

In conclusion, the emergence of a new type of strong low-field magnetooscillations induced by THz radiation in the photovoltage response has been demonstrated. These oscillations have been studied in terms of several parameters, such as carrier density, excitation frequency, temperature and radiation intensity, which have proved that TIMO in graphene share a common origin with the MIRO phenomenon in GaAs. However, the presented analysis has also revealed strong qualitative differences, namely that TIMO appear at much higher frequencies, well above 1 THz, and persist up to $T = 90$ K, which is beyond the boiling point of liquid nitrogen. These found similarities and differences are the focus of the following discussion.

7.2 Discussion

The experimental results and highlighted features of TIMO presented above are discussed in terms of a theoretical model developed for linear energy dispersion. Furthermore, the following discussion will substantiate that TIMO are indeed a MIRO analog in monolayer graphene structures.

The central feature of MIRO is that the effect develops nodes at the positions of the CR harmonics, related to its nature as a result of resonant photon-assisted transitions between distant LLs [13]. As only transitions between adjacent LLs are dipole-allowed, these processes require simultaneous impurity scattering, which leads to a disorder broadened LL spectrum and thus to the lifting of the selection rules [86, 177, 178]. To describe the origin of MIRO, there are two closely related mechanisms: the displacement [179–183] and the inelastic mechanisms [178, 184]. Both provide similar contributions to the photovoltage [185] and photoresistance [186] responses. The former mechanism is easier to understand on a qualitative level, thus in the following we will first focus on the displacement mechanism to describe the main features of TIMO.

Figure 7.7(a) provides a schematic illustration of the displacement mechanism. The Landau quantization caused by the perpendicularly applied magnetic field leads to a modulation of the DOS. The purple solid stripes indicate the corresponding resulting LL spectrum, representing the maxima of the local DOS of the l-th disorder-broadened and strongly overlapping LLs shown in shaded purple. The LLs are nonequidistant according to $\varepsilon_l \propto \sqrt{l}$, $l = 0, 1, 2, ...$, reflecting the linear dispersion relation of graphene as shown in Sec. 2.2, and are further tilted by the presence of a static electric field $\boldsymbol{E}$ – here, for example, pointing to the right. Note that the latter can be interpreted as a local gradient of the electrostatic potential introduced either by the application of an external dc potential or by the formation of built-in electric fields within the sample. In fact, a nonzero difference between the work functions of the contact probes, e.g., caused by an asymmetric contact configuration or the presence of intrinsic inhomogeneities, produces a band mismatch that should be compensated. This compensation leads to the formation of built-in electric fields, which take over the role of an applied electric field in photovoltage measurements [185, 187–190]. The origin of the oscillatory current is attributed to the interplay between

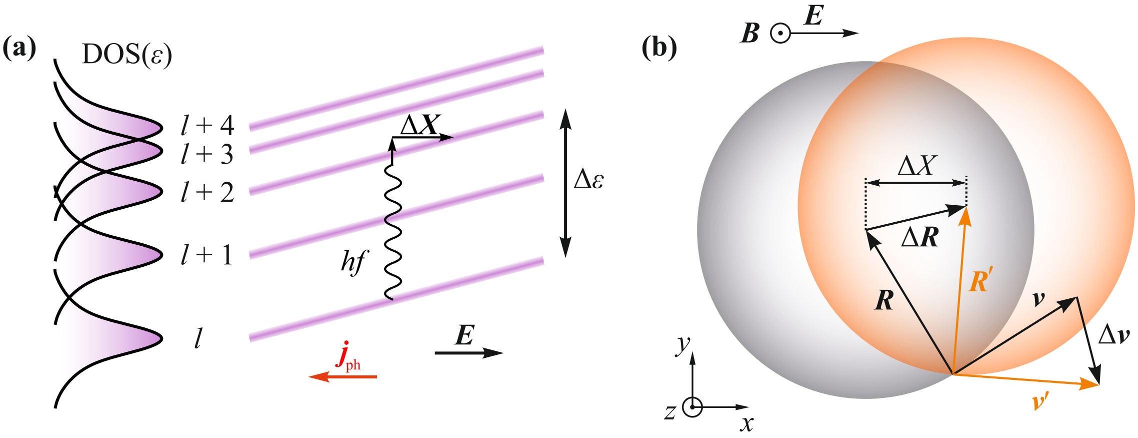

Figure 7.7: **(a)** Sketch of the displacement mechanism for TIMO. The purple stripes represent the local maxima of the DOS of the nonequidistant LL spectrum in real space (shown on the right) tilted by a static electric field $\boldsymbol{E}$. The $l + i$ LLs with $i = 0, 1, 2, ...$ overlap strongly due to impurity induced disorder broadening. The energy separation $\Delta\varepsilon$ between the involved LLs is slightly exceeded by the incident photon energy hf.This results in a spatial shift of the cyclotron orbit center of the electron $\Delta\boldsymbol{X}$ towards $\boldsymbol{E}$ due to an impurity assisted scattering event, pointing to a larger final DOS. This generates a photocurrent $\boldsymbol{j}_{\text{ph}}$ pointing in the opposite direction of $\boldsymbol{E}$. **(b)** Cyclotron orbits before (gray shaded circle) and after (orange shaded circle) the shift ΔR induced by elastic scattering off disorder. $\boldsymbol{R}$ and $\boldsymbol{R}'$ represent the vectors pointing to the guiding centers of the cyclotron orbits, while $\boldsymbol{v}$ and $\boldsymbol{v}'$ define the corresponding cyclotron velocities. Figure adapted from Refs. [13, 46].

the photon energy and the energy difference of the involved LLs. Let us assume that the applied magnetic field induces a quantized LL spectrum such that the incoming radiation with photon energy hf slightly exceeds the energy separation $\Delta\varepsilon$ between the involved LLs. Due to the fact that any impurity-scattering process leads to a displacement $\Delta\boldsymbol{X}$ of the electron cyclotron orbit center in real space, see Fig. 7.7(b), this facilitates the carriers to move between the LLs by absorbing incoming photons. The preferred direction of the scattering event is in accordance with Fermi's golden rule [13, 179]; hence, in the statistical mean, the displacement vector in Fig. 7.7(a) points towards the local DOS maximum of the (l-th + 2) LL and thus along the static electric field vector $\boldsymbol{E}$. This results in a spatial separation of the carriers, which enables the generation of a nonzero photocurrent $\boldsymbol{j}_{\text{ph}}$, pointing in the opposite direction to the spatial displacement of the electron. Now, considering that a sweeping magnetic field changes the energy separation $\Delta\varepsilon$, it ultimately controls the direction of the displacement, and thus the orientation of the generated photocurrent. In general, if $hf - \Delta\varepsilon > 0$ ($hf - \Delta\varepsilon < 0$), the photocurrent points against (along) the static electric field, producing the oscillatory behavior. Note that in our work this generated photocurrent is then recorded via the photovoltage technique using an open circuit, see Sec. 3.4.2. In this picture it is immediately clear that for a direct transition between the maxima of the local DOS of the involved LLs, i.e., $hf - \Delta\varepsilon = 0$, there is no preferred scattering direction: the average displacement is negligibly small due to a symmetric decrease of the local DOS. Therefore, the photocurrent vanishes when the photon energy matches direct transitions corresponding to the CR harmonics.

According to this theoretical model, the oscillations are controlled by the ratio $\omega/\omega_c = B_{\mathrm{CR}}/B$ [6, 8, 13, 17], where B_{CR} defines the magnetic field of the CR via Eq. (2.34) in Sec. 2.2 for the parabolic, $B^{\mathrm{P}}_{\mathrm{CR}}$, or linear energy dispersions, $B^{\mathrm{L}}_{\mathrm{CR}}$. Since the corresponding LL spectrum in GaAs is equidistant, the CR position is insensitive to changes in the carrier density, as discussed in Chap. 5, and thus to the periodicity of MIRO. This consideration is not valid for graphene due to its nonequidistant LL spectrum. Within the semiclassical approach, see Sec. 2.2, the density-dependent magnetic field of the CR, and therefore the fundamental frequency of TIMO, is given by $B_{\mathrm{F}} \equiv B^{\mathrm{L}}_{\mathrm{CR}} = 2\pi f\sqrt{\pi n_e}/ev_{\mathrm{F}}$. This suggests that the period of TIMO scales as the square root of n_e and is proportional to the radiation frequency. The experimental results in Figs. 7.3(c) and 7.4(b) for MLG #C show excellent agreement with this behavior. They are accurately reproduced by the corresponding fits using $B^{\mathrm{L}}_{\mathrm{CR}}$ with a Fermi velocity of $v_{\mathrm{F}} = 1.06 \times 10^6$ m/s, which is a typical value for the relevant regions in graphene [21, 22, 152] and, moreover, agrees well with the values obtained in MLG #A and #B, see Chaps. 5 and 6, respectively. Furthermore, TIMO exhibit a vanishing photoresponse at integer B_{F}/B and an exponential damping at low magnetic fields – features common to MIRO [13, 191]. In the regime of strongly overlapping LL and sufficiently small radiation intensities, the waveform of conventional MIRO in systems with parabolic energy dispersion is given by [13, 191]

$$V_{\mathrm{ph}} = -A \exp\left(-\frac{\kappa B^{\mathrm{P}}_{\mathrm{CR}}}{B}\right) \sin\left(\frac{2\pi B^{\mathrm{P}}_{\mathrm{CR}}}{B}\right) , \tag{7.2}$$

with amplitude A and damping amplitude κ. Figure 7.8(a) presents TIMO for various carrier densities as a function of the inverse magnetic field, similar to Fig. 7.3 but normalized to B_{F}. The photovoltage was additionally smoothed by a moving average procedure with a window size larger than the period of TIMO to subtract the nonoscillating background. The traces are approximated by Eq. (7.2) illustrated as solid lines in the corresponding color. To fit the waveform we used A, B_{F} and κ as fitting parameters. The notable disagreement for the maximum of the first period is in line with previous studies on MIRO and can be attributed to the regime of already

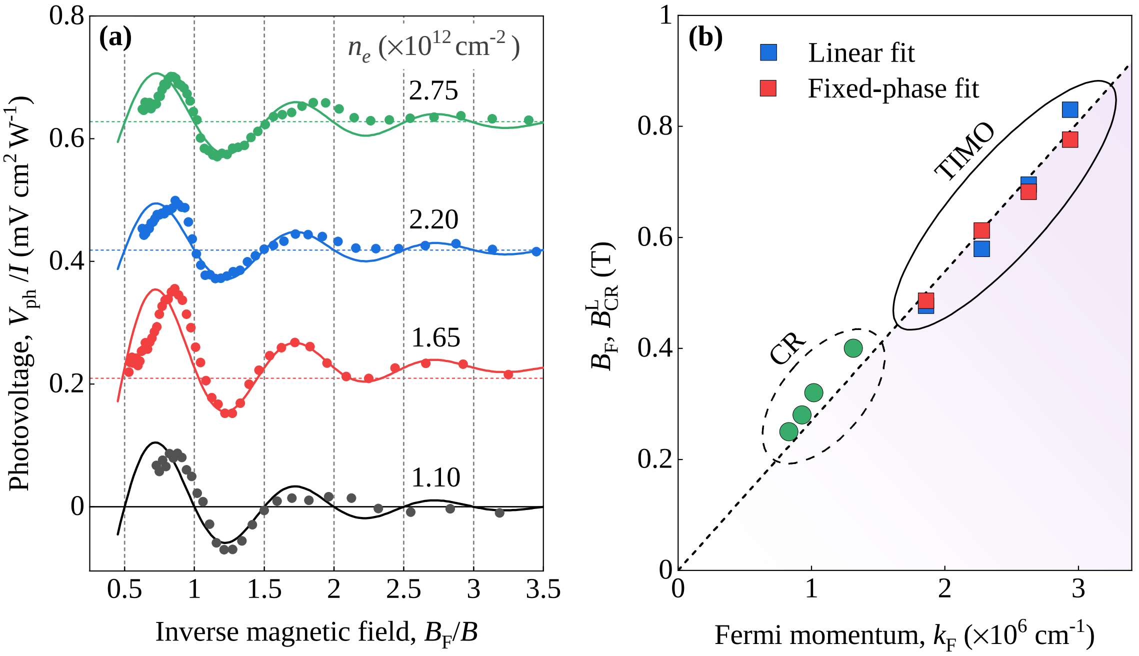

Figure 7.8: **(a)** The colored circles show the replotted data of Fig. 7.3(a) normalized to the fundamental frequency B_{F}, which was chosen to give the best fit to the period of TIMO with a phase fixed by Eq. (7.2) for each carrier density. The photovoltage was smoothed by a moving average procedure with a window size larger than the period of TIMO to subtract the nonoscillating background. **(b)** B_{F} values of TIMO (indicated by a solid ellipse) determined by linear fits (red squares) from Fig. 7.3(b) and fixed-phase fits (blue squares) by Eq. (7.2) [panel (a)] as a function of the Fermi wave number k_{F}. The dashed line illustrates the fit of the fundamental frequency of TIMO according to $B^{\mathrm{L}}_{\mathrm{CR}}$, see Eq. (2.34) in Sec. 2.2, with a Fermi velocity of $v_{\mathrm{F}} = 1.06 \times 10^6$ m/s. The green circles (indicated by a dashed ellipse) represent the magnetic field positions of the CR peaks $B^{\mathrm{L}}_{\mathrm{CR}}$ recorded for small carrier densities, see Fig. 7.1(a). Figure adapted from Ref. [46].

separated LLs and thus a strong modulation of the DOS [182, 184, 192, 193]. The values for B_{F} obtained from Eq. (7.2) (red squares) are plotted against the Fermi wave number $k_{\mathrm{F}} = \sqrt{\pi n_e}$ in Fig. 7.8(b). Together with the values estimated from the linear fits (blue squares), see Fig. 7.3(b), the data follow $B^{\mathrm{L}}_{\mathrm{CR}}$ (dashed line) with $v_{\mathrm{F}} = (1.06 \pm 0.06) \times 10^6$ m/s, see Eq. (2.34) in Sec. 2.2. To further support this analysis of TIMO, the magnetic field positions of the CR peaks $B^{\mathrm{L}}_{\mathrm{CR}}$ (green circles) have been included. These were obtained for lower carrier densities [see Fig. 7.1(a)] and fit well to the dashed line.

As mentioned above, the exponential damping of TIMO at low B is also an important property shared with conventional MIRO. The damping is well reproduced by the exponential decay $\exp(-\kappa B_{\mathrm{F}}/B)$ with $\kappa \approx 1$, see Fig. 7.8(a), which characterizes the overlap of broadened LLs and can be rewritten in terms of the conventional Dingle factor squared, $\exp(-\kappa B_{\mathrm{F}}/B) \equiv \exp(-2\pi/\omega_c\tau_q)$. The calculation of the corresponding quantum scattering time leads to $\tau_q = 1/\kappa f \approx 1.5$ ps, a value which is several times smaller than the estimation for the momentum relaxation time, $\tau_p \approx 5 - 10$ ps. However, τ_q significantly exceeds the values obtained from the exponential decay of SdHO towards lower B-fields in graphene devices of similar quality [194]. These scattering times, which are at least one order of magnitude shorter than typical values in GaAs QWs used to study conventional MIRO [13], indicate the importance of higher frequencies (in the THz range) to probe such phenomena in graphene. This is in accordance with the observation of TIMO at higher frequencies beyond 1 THz, see Fig. 7.4, where the photovoltage clearly exhibits signatures of the first period of TIMO at $f = 1.63$ THz. In addition, weak but clear traces of TIMO were detected even at $f = 2.54$ THz, resulting in an amplitude decay that scales with $f^{-5/2}$. This is a slightly faster decay as compared to the Drude absorption ($\propto f^{-2}$). However, the fact that TIMO are still visible at such frequencies implies a remarkable stability against electron gas heating compared to MIRO in conventional GaAs heterostructures [10, 13, 14, 195, 196] and extends the field of MIRO-like phenomena well into the THz domain.

Also remarkable is the surprisingly slow decay of the TIMO amplitude with temperature compared to GaAs heterostructures [13]. Figure 7.9(a) presents the data from Fig. 7.5 of the normalized photovoltage amplitude around $B = B_\mathrm{F}$ replotted on a log-linear scale. It is clearly seen that the behavior accurately follows the exponentially damped dependence proportional to $\exp(-\gamma_\mathrm{T} T^2)$ for temperatures above $T > 10$ K. At these temperatures, an additional contribution to the damping amplitude κ of TIMO in Eq. (7.2) becomes essential, which is determined by the e-e scattering time τ_{ee}, yielding $\kappa = 1/f(\tau_q + \tau_{ee})$ [175, 176, 186, 198]. The e-e collisions result in an effective broadening of the LLs with increasing temperature, which is given by $\tau_{ee} = 1/f\gamma_\mathrm{T} T^2$ [175, 176, 186, 198]; thus, providing a value of $\tau_{ee} \approx (57 \text{ K}/T)^2$ ps for the e-e scattering time by using the estimated damping amplitude $\gamma_\mathrm{T} = 4.4 \times 10^{-4}$ K^{-2}. This extracted value is confirmed by experimental values reported for graphene [197]. Figure 7.9(b) compares the temperature dependencies of τ_{ee} determined from the TIMO amplitude (colored squares) with the data from Ref. [197] (black solid line), which supports our analysis. Furthermore, the e-e lifetime is determined by the e-e scattering rate $\tau_{ee}^{-1} = cT^2/\varepsilon_\mathrm{F}\hbar$ of a Fermi liquid [199, 200] with a constant c including numerical factors [184, 186]. For a reasonable value ($c \approx 5.6$), the experimentally obtained τ_{ee} is in agreement with the theoretical prediction for graphene [201, 202], which further substantiates the experimental findings. It should be noted that the relevant Fermi energies of graphene lie in the range of $\varepsilon_\mathrm{F} \approx 200$ meV, which is at least one order of magnitude larger

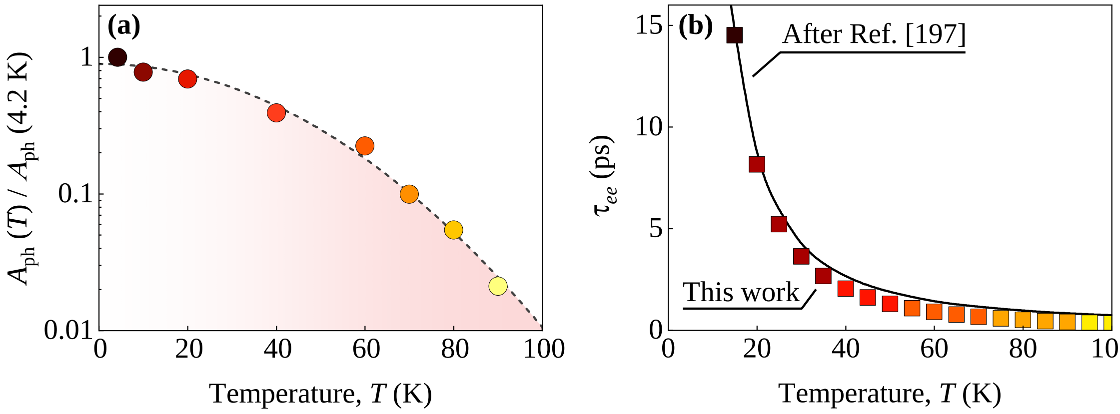

Figure 7.9: **(a)** The normalized photovoltage amplitude of TIMO $\Delta A_{\mathrm{ph}}(T)/\Delta A_{\mathrm{ph}}(T = 4.2\text{ K})$ [see Fig. 7.5(b)] plotted on a log-linear scale as a function of temperature. The dashed curve follows $\propto \exp(-\gamma_{\mathrm{T}} T^2)$ with a damping amplitude of $\gamma_{\mathrm{T}} = 4.4 \times 10^{-4}\text{ K}^{-2}$. **(b)** Temperature dependence of the e-e scattering time, shown as colored squares, calculated from $\tau_{ee} = 1/\gamma_{\mathrm{T}} f T^2$ with the value of γ_{T} determined from the experimental data given in panel (a). The solid curve represents the results of τ_{ee} taken from Ref. [197]. Figure adapted from Ref. [46] and supplemental material therein.

than the values of GaAs QWs used for conventional MIRO measurements well below 1 THz. Considering the frequencies used to excite TIMO, the temperature damping amplitude $\gamma_{\mathrm{T}} \propto 1/f\varepsilon_{\mathrm{F}}$ is more than 100 times smaller, proving that graphene is well suited for MIRO-related studies over an exceptionally wide temperature range.

The features of TIMO observed and discussed above are also compatible with the inelastic mechanism [178, 203]. Although the displacement and inelastic mechanisms yield a similar phase and periodicity of MIRO and are proportional to the sinusoidal behavior $-\sin(2\pi B_{\mathrm{F}}/B)$, their origins are rather different. While the displacement mechanism assumes an equilibrium energy distribution of the electrons, the inelastic model considers a radiation-induced variation of the distribution function. Indeed, resonant transitions between the involved LLs of the oscillating DOS cause a modification of the Fermi energy distribution, leading to a change in the occupation of the electronic states. This correction of the Fermi energy distribution oscillates periodically, governed by the period $\omega/\omega_c \equiv B_{\mathrm{CR}}/B$, enabling a net current flow. Since the direction of the current depends on the phase difference between the oscillations of the DOS and the nonequilibrium correction, it exhibits an oscillatory behavior determined also by the ratio ω/ω_c with a flowing direction coinciding with that of the displacement mechanism. The change of the electronic state occupancy is controlled by inelastic scattering processes [178, 204], thus the mechanism is usually referred to as inelastic.

The analysis of the temperature dependence of TIMO clearly shows that the dominant source of damping is the e-e scattering induced broadening of LLs. Considering that the data additionally indicate that the amplitude A in Eq. (7.2) is independent of temperature for $T > 10$ K, the discussed exponential damping $\exp(-\gamma_{\mathrm{T}}T^2)$ is in agreement with the theory for the displacement mechanism [175, 176] and is assumed to prevail in the considered temperature range, where $\tau_p \gg \tau_{ee}$ [186]. However, at lower T, i.e., in the limit of $\tau_p \ll \tau_{ee}$, the inelastic mechanism is expected to dominate the photoresponse [184], resulting in a temperature-dependent amplitude $A(T) \propto \tau_{ee} \propto T^{-2}$ and consequently a much steeper temperature decay $\propto T^{-2}\exp(-\gamma_{\mathrm{T}}T^2)$ [186, 193, 196, 205]. Recall the evaluated values for $\tau_p \approx 5-10$ ps and $\tau_{ee} \approx (57\ \mathrm{K}/T)^2$ ps, the crossover of both regimes is estimated to occur at $T \approx 20$ K, while the actual data reveal only a weak deviation from the exponential decay at the lowest T. This may reflect the special thermalization processes of graphene and requires further extensive investigation at low temperatures.

Before concluding this chapter, let us briefly discuss the intensity dependence of TIMO. At sufficiently low intensities, the amplitude of MIRO is expected to scale linearly with I [13, 206]. This is consistent with the recorded intensity dependence of TIMO shown in Fig. 7.6, where only a slight saturation is visible at the highest intensities $I = 0.25\ \mathrm{W\,cm^{-2}}$. This may indicate the existence of two distinct regimes in the weak and strong intensity limits. In fact, this crossover is characterized by a linear dependence at low I and translates into a strongly sublinear response at high I. This behavior is in conformity with a number of experimental works studying MIRO [7, 187, 207–209]. Despite the fact that TIMO exhibit a slight tendency to saturate, this may pave the way to observe even stronger TIMO by extending the intensity range using more powerful sources of THz radiation. However, the SdHO-periodic response in the photovoltage shows a distinct behavior and a strong saturation in the considered intensity range. The origin of the saturation lies in the electron gas heating and is attributed to a strong temperature dependence of the energy losses. This behavior can be well described by the empirical expression $A_{\mathrm{ph}}^{\mathrm{SdHO}} \propto I/(1 + I/I_{\mathrm{s}})$, with the saturation intensity I_{s} depending on the reciprocal energy relaxation time and the cross section of the Drude absorption [135, 210]. A possible explanation for a nonlinear intensity dependence of the electron gas heating is discussed in the next chapter.

Overall, it has been demonstrated that TIMO observed in graphene are indeed a MIRO analog. The experimental investigation has revealed common features such as periodicity and phase that follow the theory of the MIRO effect, including the displacement and inelastic mechanisms adapted to the linear energy dispersion of graphene. However, in sharp contrast to MIRO in GaAs, TIMO in graphene have shown a remarkably slow decrease in amplitude with increasing temperature, due to a slower e-e scattering rate, and have appeared at much higher frequencies.

So far, a very general and common property of CR- and MIRO-induced photoresponses has been omitted in the above presentation, namely their expected strong dependence on the radiation helicity. Its study is the subject of the following chapter.

8 Anomalous Helicity Insensitivity of the Cyclotron Resonance

The experimental results in Chap. 5 have been obtained under a well-defined CR condition, demonstrating conventional CR absorption and reflection of the 2DES. The observations presented in this chapter, however, will reveal intriguing anomalies that contrasts with the regular CR. Specifically, it is shown that CR absorption within a 2DES can occur independently of the sense of circularly polarized THz radiation. Remarkably, a detailed study of the CR- and MIRO-induced photoresistance in GaAs and HgTe QWs reveals that at lowest temperatures and highest radiation powers, the amplitude of the photoresistance is observed to be almost the same for both CR active (CRA) and inactive (CRI) magnetic field polarities. This puzzling behavior is rather expected for linearly polarized radiation where both magnetic field polarities satisfy the CR condition.

Moreover, the anomalous ratio between the amplitudes of the CRA and CRI sides shows a strong dependence on the sample temperature T and the radiation power P, which contradicts the simultaneously measured radiation transmittance that exhibits an ordinary helicity dependence for all T and P. A closer inspection of the results reveals a distinct saturation behavior for the CRA and CRI polarities of the electron gas heating at low T and higher P, caused by a fast increase of the energy losses leading to a short electron-phonon relaxation time. To explain the anomalous CRI absorption, the emergence of scattered near-fields close to the 2DES is proposed, which distort the incoming THz wave with well-defined polarization and thus may provide CR absorption in the CRI regime.

8.1 Experimental Results

Before presenting the findings for GaAs and HgTe QWs, which reveal the helicity anomalies observed in the photoresistance, we briefly report the results for graphene. Figure 8.1 shows the normalized photoresistance $\Delta R_{xx}/\Delta R_{xx}^{\max}$ obtained in MLG #A, recorded for left- and right-handed circularly polarized radiation at a frequency of $f = 2.54$ THz. It reveals the typical picture expected for conventional CR absorption at the CRA side (see Sec. 2.2), which clearly exhibits a resonantly enhanced photoresponse only at $B < 0$ for σ^+ helicity (dashed traces) and at $B > 0$ for σ^- helicity (solid traces), where the electron gas heating is maximized. Indeed, on the CRI side, the response is significantly weaker, showing only very small signatures. In graphene, this behavior remains unchanged and has been observed for the whole

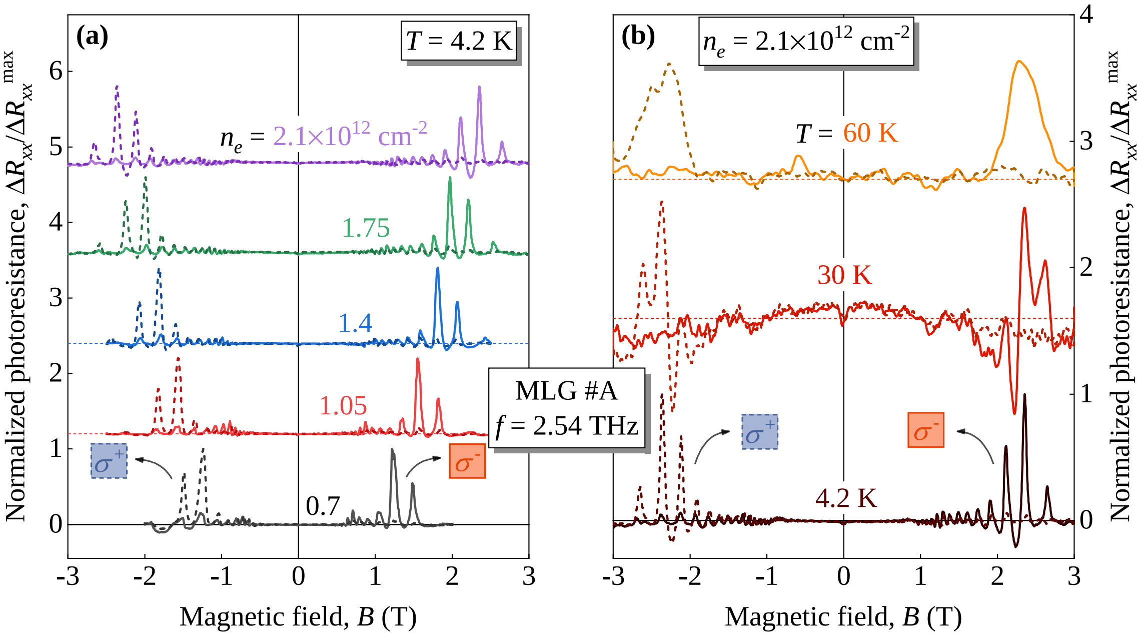

Figure 8.1: **(a)** Carrier density [$n_e = (0.7 - 2.1) \times 10^{12}$ cm^{-2}] and **(b)** temperature (T = 4.2 to 60 K) dependencies of the normalized photoresistance of MLG #A. The data were recorded as a function of left-handed (σ^-) and right-handed (σ^+) radiation helicity, corresponding to the solid and dashed traces, respectively. Each pair is offset for clarity. All results were performed at a frequency of f = 2.54 THz. Figure adapted from Ref. [47] and supplemental material therein.

range of carrier densities [$n_e = (0.7 - 2.1) \times 10^{12}$ cm^{-2}] and temperatures (up to T = 60 K) studied, see Figs. 8.1(a, b). Note that the data measured at σ^- for different carrier densities and temperatures have been already discussed in Chap. 5 in Fig. 5.2, but with the focus on the positive magnetic field polarity.

While the results in graphene are conventional and consistent with the classical Drude model of CR absorption, the behavior of the photoresistance obtained in GaAs and HgTe QWs is substantially different. Figures 8.2(b, d) present the temperature dependencies of the normalized photoresistance and Figs. 8.2(a, c) the simultaneously recorded normalized transmittance $\mathcal{T}/\mathcal{T}(B = 0)$ for GaAs #A obtained at a frequency of f = 0.297 THz. These data have already been presented in Fig. 5.1 in Chap. 5, considering only the range $B > 0$. The transmittance shows a clear CR at all investigated T, see the contour plots in Figs. 8.2(a, c) for σ^- and σ^+ helicities. The traces for the lowest temperature (T = 1.8 K) are plotted in Figs. 8.2(b, d) (black dashed traces) for the corresponding helicity, revealing a distinct CR dip that appears for only one magnetic field polarity ($B > 0$ for σ^- and $B < 0$ for σ^+ helicity). As discussed in Chap. 5, these strong dips are caused by resonant reflection and

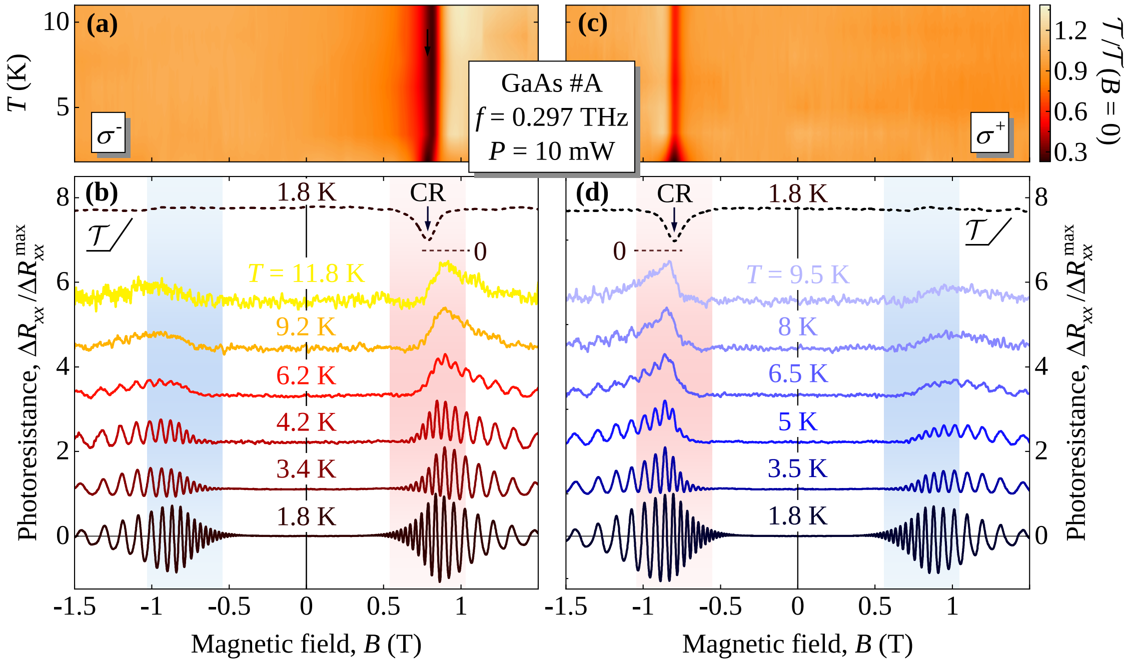

Figure 8.2: **(a, c)** Transmittance $\mathcal{T}(B)$ normalized to its value at zero field $\mathcal{T}(B = 0)$ measured as a response to left-handed (σ^-) and right-handed (σ^+) radiation helicity. The data are plotted as contour maps for a temperature range of $T = 1.8-11.8$ K. **(b, d)** Corresponding normalized photoresistance traces $\Delta R_{xx}/\Delta R_{xx}^{\max}$ obtained at σ^- [panel (b)] and σ^+ [panel (d)] helicity for several temperatures. The traces are offset for clarity. The dashed curve represents the transmittance at $T = 1.8$ K. Vertical arrows indicate the positions of the CR, and the red and blue shaded areas denote the vicinity of the CRA and CRI sides, respectively. Dashed horizontal lines near the CR dips mark the zero transmittance value. All results were performed in GaAs #A at a frequency of $f = 0.297$ THz. Figure adapted from Ref. [47] and supplemental material therein.

absorption of the incoming THz radiation whose shape is affected by the standing waves inside the substrate. The detected transmittance remained similar over the entire temperature range studied and, importantly, exhibits no significant features at the CRI polarity, confirming a high purity of the polarization state of the incident THz radiation. Figure E.1 in App. E supports this statement by demonstrating the deviations of the recorded polarization state from a perfect circle obtained at the sample position. This deviation was determined by measuring the signal transmitted through a linear polarizer while it was rotated by 360°. A perfectly circularly polarized beam has the same intensity level when passing through any angle of a linear polarizer, so performing a 360° scan yields a constant value. At worst, the deviation from a circle of the polarization state at $f = 0.297$ THz with σ^- helicity is less than 6 %, providing a minimum purity level of 94 %. In addition, due to the large lateral dimensions of the GaAs QWs compared to the THz beam spot, illumination of edges and contacts has been excluded, thus eliminating an additional potential source of polarization distortion.

Strikingly, the simultaneously measured photoresistance [Figs. 8.2(b, d)] contradicts the regular Drude-like behavior observed in the transmittance: At the highest temperature, the photoresistance shows the well-established behavior attributed to resonant electron gas heating under CR-enhanced absorption (dominated by μ-photoconductivity, see Chap. 5). Lowering the temperature leads to a superposition of the CR-enhanced photoresistance with SdHO-periodic oscillations. Most importantly, an anomalous enhancement of the photoresponse at the CRI polarity is observed, yielding almost similar magnitudes of the resonant signal for positive and negative B-fields, see the traces for $T = 1.8$ K in Figs. 8.2(b, d). Such results would be expected for a linearly polarized THz wave rather than a circular one, since the former can be decomposed into the sum of the two circular components and thus satisfies the CR condition for both magnetic field polarities, see Eq. 2.23 in Sec 2.2. Moreover, for the sequence of temperatures studied, the relative magnitude of the resonant photosignals at the CRI polarity shows a gradual decrease to higher T. This general behavior of the anomalous photoresistance is confirmed by additional measurements in GaAs #A shown in Figs. B.2 and B.3 as well as the corresponding analysis in Fig. B.6 in App. B obtained for $f = 0.69$ and 1.63 THz, respectively. This is further supported by similar findings for the same frequencies in GaAs #B, see Figs. B.4 and B.5 in App. B.

The anomalous helicity dependence is also observed in the photoresistance of HgTe QWs of different QW thicknesses. Figure 8.3 shows the temperature dependence of $\Delta R_{xx}/\Delta R_{xx}^{\max}$ for HgTe #A ($d_{\mathrm{QW}} = 8.1$ nm) and #B ($d_{\mathrm{QW}} = 5.7$ nm) obtained at σ^+ helicity and $f = 2.54$ THz, revealing a similar qualitative behavior. While at low T the magnitudes for both B polarities are almost equal, the CRI side decreases progressively with increasing temperature, until at the highest T the CRI response disappears, restoring the behavior expected for circularly polarized radiation. At the same time, the simultaneously measured transmittance is almost not affected by temperature and exhibits no resonant features on the CRI side for all considered T. Note that compared to GaAs, the transmittance dips in Fig. 8.3 are much less pronounced. For instance, in HgTe #A the transmittance drops by less than 35 % at the CR condition, a behavior that can be attributed to a much lower electron mobility in these structures, see Sec. 4.1.

The above qualitative picture is quantitatively elaborated in Fig. 8.4. To determine the relative magnitudes of the photoresistance, the amplitudes of the CRA and CRI signals, termed A^{CRA} and A^{CRI}, respectively, were extracted. At low temperatures,

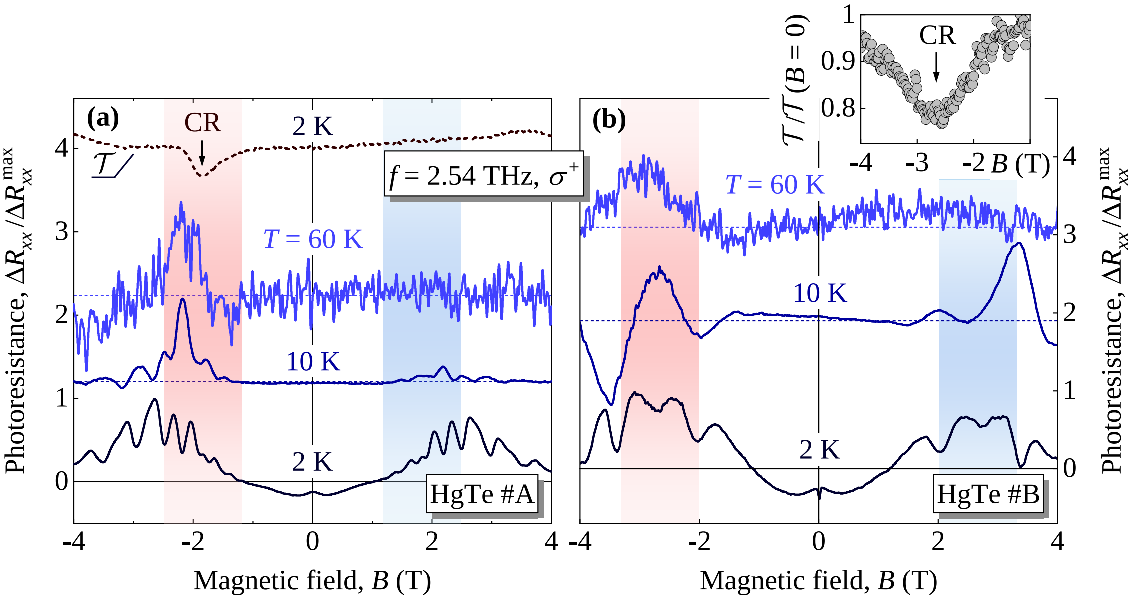

Figure 8.3: **(a)** Normalized transmittance (black dashed curve) at T = 2 K and normalized photoresistance at T = 2, 10, and 60 K (colored solid curves) obtained in HgTe #A (d_{QW} = 8.1 nm). **(b)** Normalized photoresistance measured in HgTe #B (d_{QW} = 5.7 nm) presented for the same temperatures T = 2, 10 and 60 K. The inset shows the CR in the corresponding transmittance data obtained at T = 90 K. The curves are offset for clarity. All results were obtained in response to right-handed (σ^+) circularly polarized radiation with a frequency of f = 2.54 THz. Vertical arrows indicate the positions of the CR, and the red and blue shaded areas denote the vicinity of the CRA and CRI sides, respectively, in both panels. Figure adapted from Ref. [47] and supplemental material therein.

the photoresistance is dominated by the SdHO-periodic oscillations, whose envelope corresponds to a Lorentzian function given by the CR absorptance, as discussed in Chap. 5. Therefore, to accurately determine the magnitude, a Lorentzian fit was used to reproduce ΔR_{xx}, which subsequently yielded a clean peak height of the signal, see Fig. 8.4(a). At intermediate T beyond the SdHO regime, where the photoresistance is completely dominated by the μ-photoconductivity, A^{CRA} and A^{CRI} were determined by the full photoresponse height, see Fig. 8.4(b). Here, the ΔR_{xx} value at zero field (indicated by the horizontal red dashed line) was used as a reference to determine the full height of the CR-enhanced response. Since at the highest temperatures, e.g., for $T \gtrsim 10$ K, the noise level becomes almost comparable to the THz-induced signal, the estimation of the amplitudes is a delicate task. To overcome this, the data were processed by a moving average procedure before amplitude analysis, see the blue trace in Fig. 8.4(b). An example of the amplitude analysis is given in Fig. 8.4(c) for GaAs #A, f = 0.297 THz and σ^- helicity. An equivalent analysis was also performed for higher radiation frequencies f = 0.69 and 1.63 THz, as presented in Fig. B.6 in App. B. Overall, the data show that the amplitude values for both

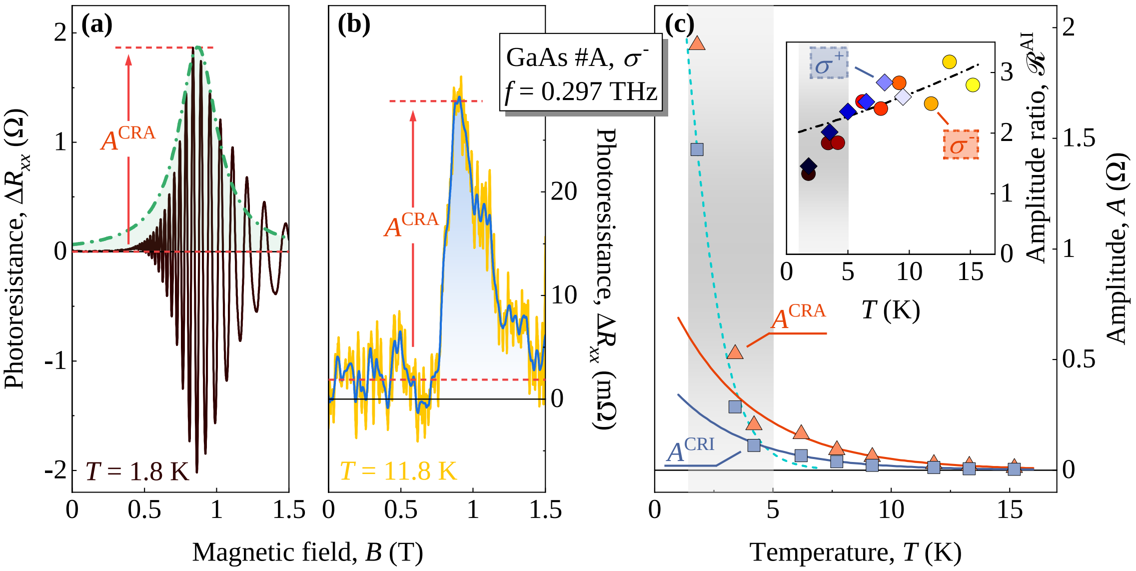

Figure 8.4: **(a, b)** Positive B-field polarity of the unnormalized photoresistance obtained at σ^--helicity, presented for $T = 1.8$ and 11.8 K as examples to demonstrate the amplitude estimation procedure. The green dashed curve in (a) shows a Lorentzian fit that yields the envelope of the fast oscillating signal. The peak of this fit curve is then used to estimate the amplitude A^{CRA}, denoted by the red arrow. The solid blue curve in (b) shows the moving average of the experimental data (indicated in orange) used to determine the photoresistance amplitude at higher temperatures beyond the SdHO regime. **(c)** Photoresistance amplitude values of the CRA side (A^{CRA}) and the CRI side (A^{CRI}) as a function of sample temperature for the data recorded at $f = 0.297$ THz and σ^- helicity. The cyan dashed curve represents a fit using the Lifshitz-Kosevich formula [160, 161] with an effective mass of $m^* = 0.066\, m_e$. The red and blue solid lines represent guides for the eye following an exponential decay. The inset shows the corresponding amplitude ratio $\mathscr{R}^{\mathrm{AI}}$ [Eq. 8.1] for both helicities. Here, the black dashed-dotted line is calculated by taking the ratio from the guiding curves in panel (c). The gray shaded areas in (c) and its inset denote the region where the SdHO-periodic oscillations dominate the photosignal. All results were obtained in GaAs #A. Figure adapted from Ref. [48] and supplemental material therein.

polarities decrease significantly with increasing temperature. To characterize this behavior, the amplitude ratio is introduced

$$\mathscr{R}^{\mathrm{AI}} = \frac{A^{\mathrm{CRA}}}{A^{\mathrm{CRI}}}\,. \tag{8.1}$$

The ratio is illustrated in the inset of Fig. 8.4(c) for both σ^- and σ^+ helicities. For both helicities it is clearly seen that the ratio increases about three times with temperature due to the faster decrease of the CRI amplitude. Furthermore, $\mathscr{R}^{\mathrm{AI}}$ depends only slightly on the radiation frequency, yielding similar values for $f = 0.69$ and $f = 1.63$ THz, see Fig. B.6 in App. B. Note that these values are still far from the conventional ratio that can be estimated using the Drude model, see Sec. 8.2. For comparison, the ratio extracted from the measurements in graphene at $T = 4.2$ K is about $\mathscr{R}^{\mathrm{AI}} \approx 20$. At higher temperatures, where the signal is dominated by the μ-photoconductivity, the amplitude dependencies in Fig. 8.4(c) are guided by solid, correspondingly colored curves showing an exponential decay. The ratio of these curves is also shown in the inset as a black dashed-dotted line, reproducing the increase at higher T. On the contrary, at low T (gray shaded area) the SdHO-periodic oscillations in the photoresistance dominate, leading to a strong deviation from the high-T behavior. Their temperature dependence can be well fitted by the conventional Lifshitz-Kosevich formula, see cyan dashed curve, using the effective mass $m^* = 0.066\, m_e$. In addition, the enhanced photoresistance is less sensitive to temperature at higher radiation frequencies. In particular, comparing the amplitudes for $f = 0.297$ [Fig. 8.2] and 1.63 THz [Fig. B.3 in App. B], the photosignal begins to disappear at $T \approx 15$ K in the former case, while it is still pronounced at $T = 40$ K in the latter.

The above results were obtained by varying the sample temperature while keeping the radiation power constant at the highest possible level to maximize the photoresponse. As discussed in Chap. 5, under this condition the main origin of the photoresistance is the radiation-induced electron gas heating. Based on the data presented, it is intuitive to explore the regime of electron gas heating by exploiting its dependence on the radiation power. Representative results of transmittance and photoresistance at different power levels are shown in Fig. 8.5 for GaAs #A, $f = 0.297$ THz, σ^- helicity, and $T = 1.8$ K. Equivalent results for the opposite helicity (σ^+) as well as a higher radiation frequency ($f = 0.69$ THz) are given in Figs. C.1 and C.2 in App. C. In addition, Figs. C.3 and C.4 in App. C support the presented results by illustrating the analysis of the photoresistance traces for $f = 0.69$ THz. The transmittance remains conventional over the whole power range, while the photoresistance shows an intriguing behavior. At the highest power, the CRA and CRI amplitudes are almost equal, which is consistent with Fig. 8.2(b). Strikingly, a reduction of P by about two orders of magnitude significantly lowers the response of the CRI polarity, see the yellow trace in Fig. 8.5(b). Furthermore, a closer look at the CR-enhanced signal reveals that the long tail towards higher magnetic fields becomes less pronounced at lower P, resulting in a more symmetric shape. To emphasize this, the data shown in Fig. 8.5(b) are replotted, dividing the photoresistance magnitude by its corresponding radiation power. The results in Figs. 8.5(d, e) reveal a remarkable deviation of the shape near the CR at the CRA polarity, while the shape of the CRI response remains almost the same. This

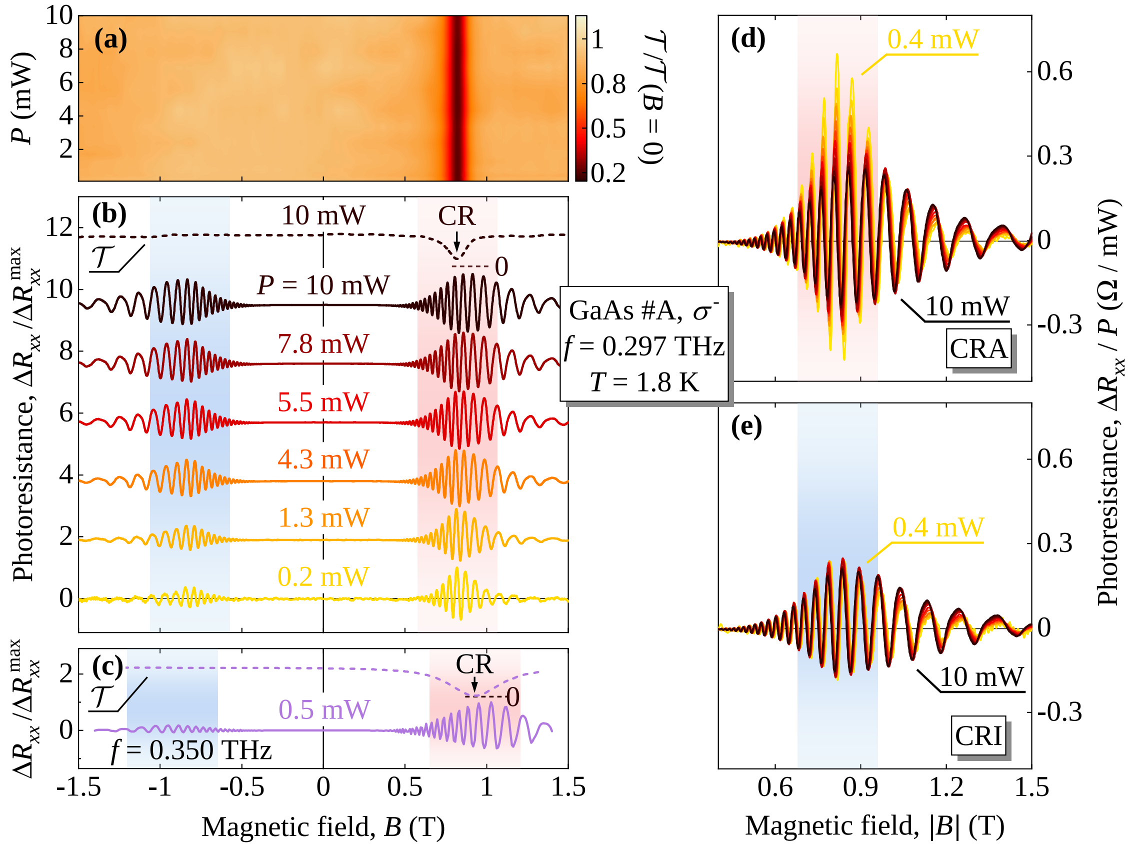

Figure 8.5: **(a)** Color-contour plot of the normalized radiation transmittance $\mathcal{T}(B)/\mathcal{T}(B = 0)$ as a function of power obtained at $f = 0.297$ THz with σ^- helicity. **(b)** Corresponding photoresistance curves $\Delta R_{xx}/\Delta R_{xx}^{\max}$ for various radiation powers down to fractions of milliwatt. The curves are up-shifted for clarity. The black dashed line represents the transmittance measured at the highest power, $P = 10$ mW. **(c)** Transmittance (dashed) and photoresistance (solid) for left-handed circularly polarized radiation, a radiation power of $P = 0.5$ mW, and a radiation frequency of $f = 0.350$ THz generated by the BWO quasi-optical setup. In panels (b, c), the CR dip is denoted by a vertical arrow and the zero transmittance is indicated by a dashed horizontal line near the dip. The shaded red and blue areas mark the CRA and CRI polarities. **(d, e)** Photoresistance ΔR_{xx} for the CRA and CRI polarity normalized to the corresponding radiation power in milliwatts. The data sets are plotted without offsets as functions of the absolute value of the magnetic field. All results were obtained at $T = 1.8$ K in GaAs #A. Figure adapted from Ref. [48].

already indicates a strong nonlinear behavior of the CRA photoresistance, which is most pronounced near the CR, where the absorption and thus the heating of the electron gas is maximized.

In addition, Fig. 8.5(c) shows the radiation transmittance and the corresponding photoresistance measured for the frequency $f = 0.350$ THz at the same radiation helicity and temperature[10]. The coherent radiation was generated by a BWO quasi-optical system providing a radiation power of $P \approx 0.5$ mW at the position of the sample, see Sec. 3.4.1. The observed ratio $\mathscr{R}^{\mathrm{AI}}$ is significantly larger compared to the low-power measurements at $f = 0.297$ THz. Under these conditions, it is evident that the CR dip is substantially broader than that at $f = 0.297$ THz, which is related to the shape of the photoresistance. These different shapes can be attributed to the difference in the interference pattern inside the sample substrate, which is strongly dependent on the radiation frequency [see Chap. 5] and can also significantly influence the amplitude ratio, as will be addressed below.

Let us now quantify this anomalous power dependence by estimating the amplitudes $A^{\mathrm{CRA}}(P)$, $A^{\mathrm{CRI}}(P)$, and the corresponding ratio $\mathscr{R}^{\mathrm{AI}}(P)$. Since the photoresistance is clearly dominated by SdHO-periodic oscillations over the whole power range, the amplitude values of the traces were determined in the same way as shown in Fig. 8.4(a). The results of the amplitude analysis for $f = 0.297$ THz are presented in Fig. 8.6(a) for $T = 1.8$ and 10 K, where the triangles represent the CRA and the squares the CRI polarities. We begin with the low-temperature data. For low P the amplitudes $A^{\mathrm{CRA}}(P)$ and $A^{\mathrm{CRI}}(P)$ exhibit an almost linear behavior with the radiation power and are therefore well fitted by dashed straight lines. However, at higher powers, the CRA signal reveals a clear deviation from this linear-in-P behavior, while the CRI response shows only a relatively weak saturation. At high powers, both data sets are well fitted by the empirical formula

$$A(P) = \frac{aP}{1 + P/P_{\mathrm{s}}}, \tag{8.2}$$

where a is a scaling parameter and P_{s} the saturation power, specifically yielding $P_{\mathrm{s}}^{\mathrm{CRA}} = 12$ mW and $P_{\mathrm{s}}^{\mathrm{CRI}} = 25$ mW. These values demonstrate that the saturation power for the CRA polarity is about twice that for the CRI polarity. Furthermore, the scaling parameters for these fits yield $a^{\mathrm{CRA}} = 0.46\ \Omega\,\mathrm{mW}^{-1}$ and $a^{\mathrm{CRI}} = 0.24\ \Omega\,\mathrm{mW}^{-1}$, so that their ratios satisfy the relation $P_{\mathrm{s}}^{\mathrm{CRA}}/P_{\mathrm{s}}^{\mathrm{CRI}} \approx a^{\mathrm{CRI}}/a^{\mathrm{CRA}}$. Taking the amplitude ratio $\mathscr{R}^{\mathrm{AI}}(P)$, illustrated as black circles in Fig. 8.6(b), it initially has a value close to unity at the highest power, but eventually increases significantly to a value of about 3.5 at lower powers. This behavior clearly reflects the strong amplitude dependencies and in particular the strong saturation of the CRA response. This behavior is supported by the results for $f = 0.69$ THz and $T = 1.8$ K in GaAs #A, see Fig. C.4 in App. C, which shows a similar illustration

---

[10] Measurements were performed at the technical university of Vienna by Maxim Savchenko and Alexey Shuvaev in the group of Andrei Pimenov, https://www.ifp.tuwien.ac.at/spectroscopy (accessed January 1, 2024).

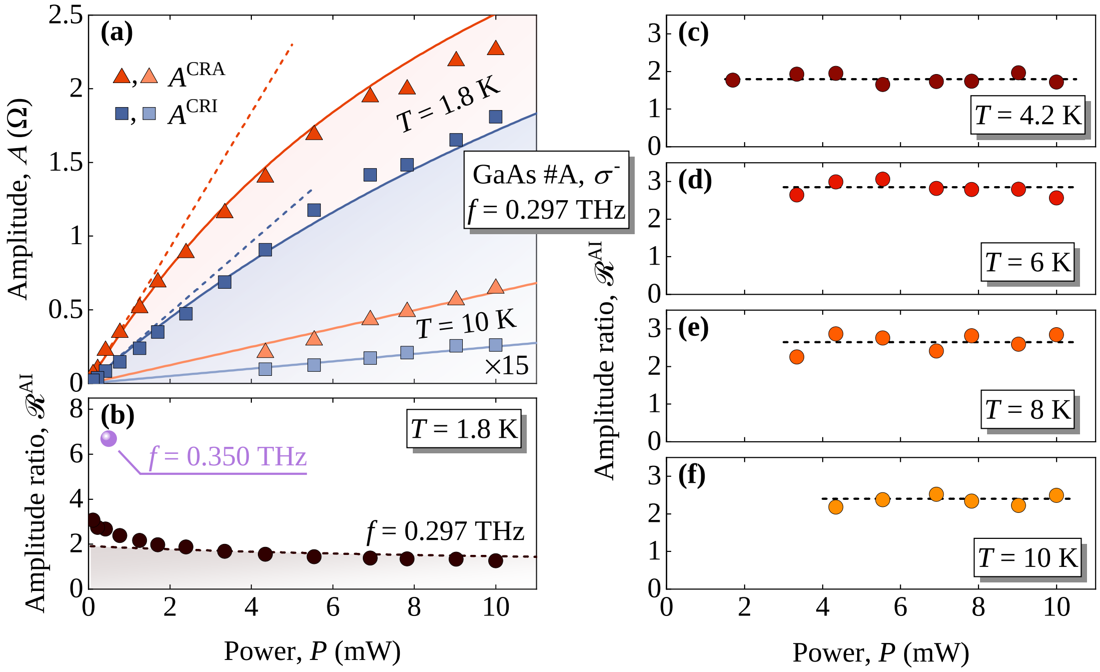

Figure 8.6: **(a)** Amplitudes A^{CRA} and A^{CRI} of the photoresistance traces as a function of radiation power evaluated at $f = 0.297$ THz for $T = 1.8$ K (dark red triangles and dark blue squares) and $T = 10$ K (brighter associates). The solid colored curves are fits according to Eq. (8.2) using $P_{\mathrm{s}}^{\mathrm{CRA}} = 12$ mW and $P_{\mathrm{s}}^{\mathrm{CRI}} = 25$ mW for the saturation powers as well as $a^{\mathrm{CRA}} = 0.46\ \Omega\,\mathrm{mW}^{-1}$ and $a^{\mathrm{CRI}} = 0.24\ \Omega\,\mathrm{mW}^{-1}$ as scaling parameters at $T = 1.8$ K. To emphasize the deviations from a linear behavior, the low-power amplitude ($P_{\mathrm{s}} \to \infty$) was also plotted. These are represented by dashed lines colored accordingly. The data for $T = 10$ K are magnified by a factor of 15 and fitted with a linear-in-P dependence. **(b – f)** Corresponding amplitude ratios $\mathscr{R}^{\mathrm{AI}}$ as a function of radiation power obtained at $f = 0.297$ THz and different temperatures. The corresponding data sets for panel (c – f) are shown in Figs. C.5 and C.6 in App. C. The dashed curves are results of the ratios of the amplitude fits. The purple circle in panel (b) represents the ratio of the photoresistance curve measured with the BWO quasi-optical setup at $f = 0.350$ THz shown in Fig. 8.5(c). All results were obtained in GaAs #A for σ^- helicity. Figure adapted from Ref. [48] and supplemental material therein.

of the power dependence of the CRA and CRI amplitudes and their ratio $\mathscr{R}^{\mathrm{AI}}(P)$. Although the sublinearity of $A^{\mathrm{CRI}}(P)$ for high powers is quite strong compared to the corresponding amplitude response for $f = 0.297$ THz, the overall behavior is the same and the ratio covers an equal range of values, approaching nearly unity at the highest powers and reaching a value of about 3.2 at the lowest power. The saturation powers used to fit the data are given by $P_{\mathrm{s}}^{\mathrm{CRA}} = 8.0$ mW and $P_{\mathrm{s}}^{\mathrm{CRI}} = 16$ mW and the corresponding scaling parameters yield $a^{\mathrm{CRA}} = 3.5\,\Omega\,\mathrm{mW}^{-1}$ and $a^{\mathrm{CRI}} = 1.7\,\Omega\,\mathrm{mW}^{-1}$, satisfying the condition $P_{\mathrm{s}}^{\mathrm{CRA}}/P_{\mathrm{s}}^{\mathrm{CRI}} \simeq a^{\mathrm{CRI}}/a^{\mathrm{CRA}}$. Note that at low powers the fits deviate from the data, revealing that Eq. (8.2) does not apply correctly at very low

P. While the fits exhibits a linear regime towards lower powers, the experimental results do not. This deviation is particularly evident in the amplitude ratio, where the data do not fully saturate at low P as predicted for the linear regime.

At higher temperatures, the change of the amplitude ratio with the radiation power disappears, as demonstrated in Figs. 8.6(c – f) (full photoresistance sets are shown in Figs. C.5 and C.6 in App. C). Interestingly, the ratio remains constant for $T \geq 4.2$ K. The reason is clear: due to the fact that both amplitude responses exhibit no saturation and follow a linear-in-P dependence [see, e.g., the data for $T = 10$ K in Fig. 8.6(a)], the ratio shows no dependence on P and consequently yields a constant value. Note that at the highest powers in Figs. 8.6(b – f), $\mathscr{R}^{\mathrm{AI}}$ shows an increase with temperature, consistent with the previous discussion of the inset in Fig. 8.4(c). For comparison, we have included the ratio of ΔR_{xx} shown in Fig. 8.5(c) as a purple circle. The ratio is about twice the value for the lowest power of the data at $f = 0.297$ THz.

Besides studying the general CR in photoresistance, we also studied MIRO and its dependence on temperature and radiation power in the GaAs samples. Some results of MIRO have already been shown in Chap. 7, where their general properties have been discussed in the context of TIMO in graphene structures. In GaAs #A and #B these quantum oscillations emerge due to the persistent photoconductivity effect induced by the illumination of ambient light, as described in Sec. 4.1 and Chap. 7. Figure 8.7 shows the temperature (a, b) and power (c, d) dependencies of the transmittance and the corresponding photoresistance curves for GaAs #A [$f = 0.297$ THz and σ^- helicity] obtained after brief illumination with room light. Similar measurements were carried out for $f = 0.69$ THz in GaAs #A and #B for both helicities, see Figs. D.3 and D.4 in App. D. The radiation transmittance is regular and follows the expected behavior over the entire temperature and power range considered. A closer comparison of the transmittance with Fig. 8.2 shows that the CR dip becomes deeper and wider after the sample is illuminated with room light. This change is expected and can be attributed to the change in electron density and mobility, which strongly influences the CR shape, as discussed in Chap. 7. In close analogy to the bolometric effect caused by electron gas heating [see Figs. 8.2(b, d) and 8.5(b)], the amplitudes of the CRA and CRI polarities of the MIRO-related response are almost identical at the lowest temperature and highest power. Here the photoresistance exhibits the strongest MIRO, which is superimposed by SdHO-periodic oscillations. With increasing T both types of quantum oscillations are thermally suppressed, until at $T \approx 15$ K only the first period of MIRO remains visible. At $T \approx 4.2$ K, a dominant bolometric photoresistance starts to evolve in

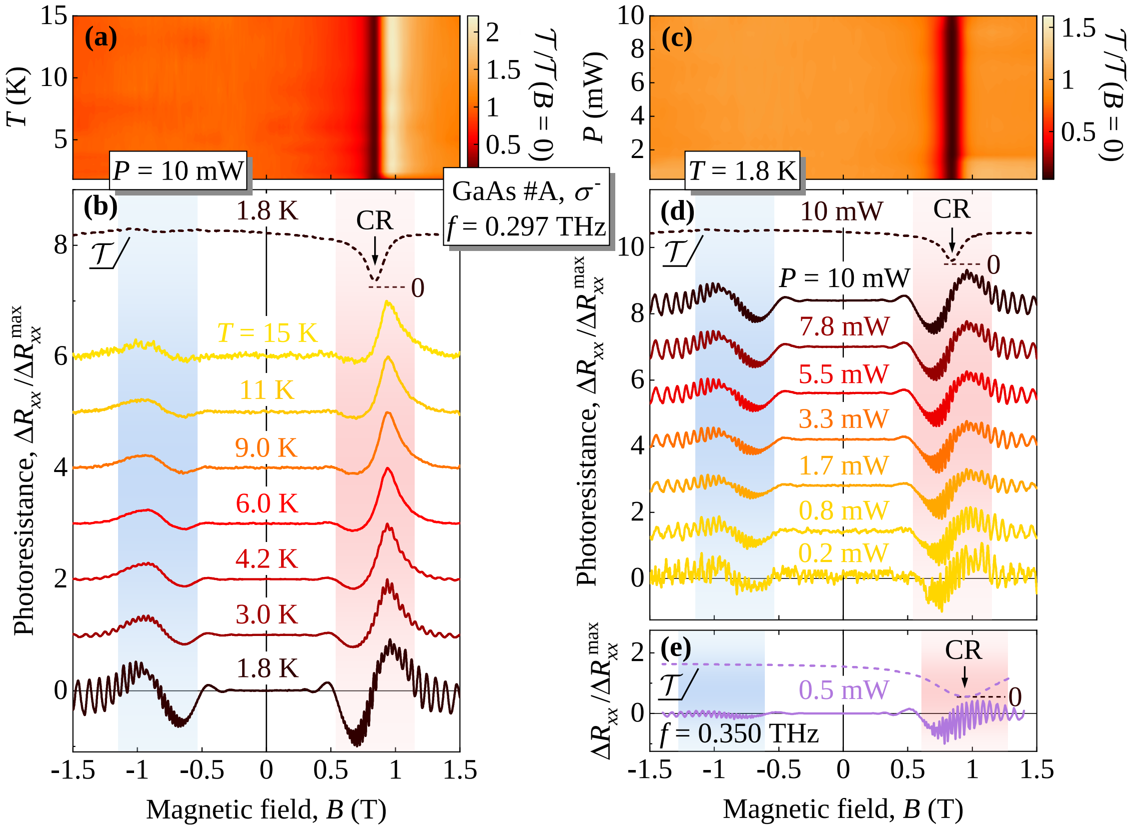

Figure 8.7: **(a, c)** Color-contour maps of normalized transmittance for a range of temperatures ($T = 1.8-15$ K) and radiation powers ($P = 0.2-10$ mW). The former [panel (a)] was measured at $P = 10$ mW and the latter [panel (c)] by keeping the sample at $T = 1.8$ K. **(b, d)** Corresponding traces of the normalized photoresistance $\Delta R_{xx}/\Delta R_{xx}^{\max}$ for different temperatures [panel (b)] and power levels [panel (d)]. The black dashed curves at the top of both panels represent the transmittance at the lowest temperature ($T = 1.8$ K) and the highest available power ($P = 10$ mW). The CR dips are denoted by vertical arrows, and zero transmittance is indicated by dashed horizontal lines near the dips. The shaded red and blue areas mark the CRA and CRI polarities. **(e)** Transmittance (dashed) and photoresistance (solid) traces recorded at a frequency of $f = 0.350$ THz generated by a BWO quasi-optical setup with a radiation power of $P \approx 0.5$ mW. All results were obtained by σ^- helicity configuration in GaAs #A after brief illumination with room light. The measurements in panel (a – d) were recorded at $f = 0.297$ THz. Figure adapted and modified from Ref. [48].

the vicinity of the CR. Its appearance leads to a significant distortion of the MIRO shape and also increases the amplitude ratio with rising temperature.

At lower power MIRO continue to dominate the signal and persist down to $P \approx 0.5$ mW. Here the noise becomes almost comparable to the photosignal. In contrast to the temperature dependence, the dependence on the radiation power shows only a weak influence on the amplitude ratio. In addition, the measurements performed at the technical university of Vienna[11] with a BWO-based quasi-optical setup at a frequency of $f = 0.350$ THz and an estimated power of $P \approx 0.5$ mW are included, shown in Fig. 8.7(e). The ratio is notably larger, similar to the result of the bolometric photoconductivity in GaAs #A, see Fig. 8.5.

We will now briefly discuss the results obtained in GaAs #C. While the fabrication scheme of GaAs #A and #B is very similar, GaAs #C features a selectively doped 16 nm GaAs QW with AlAs/GaAs superlattice barriers, see Sec. 4.1. Figure D.1 in App. D shows the temperature and power dependencies of the transmittance (a, c) and the corresponding photoresistance (b, d) at $f = 0.290$ THz generated by the IMPATT diode setup and σ^+ helicity configuration. Measurements were performed after room light illumination, similar to GaAs #A and #B. Note that in GaAs #C the latter procedure does not reveal any significant changes in carrier density and mobility, see Sec. 4.1 for details, but still facilitates the observation of strong MIRO in the photoresistance. The radiation transmittance shows a clear dip at the CRA polarity for the whole range of T and P. The broadened and highly asymmetric shape of the CR dip is attributed to interference effects, see Chap. 5. The fact that the value of the transmittance at the position of the CR is well below the value for GaAs #A and #B can be attributed to a higher mobility in GaAs #C, see Sec. 4.1 for transport properties. However, the dependence of the photoresistance on temperature and power shows a familiar picture similar to that observed for GaAs #A. At $T = 1.8$ K distinct MIRO are observed superimposed on high frequency SdHO-periodic oscillations. Both are gradually suppressed with temperature and eventually vanish at $T = 18$ K, where the photoresistance is dominated by the CR-induced μ-photoconductivity, which significantly enhances the ratio. Decreasing the radiation power at a fixed temperature ($T = 1.8$ K), both MIRO and SdHO-periodic oscillations are visible down to $P = 0.1$ mW. As for GaAs #A, the ratio shows only a slight tendency towards higher values with decreasing P.

Figure D.1(e) in App. D shows an additional measurement taken with the authors' permission from Ref. [89]. The traces were obtained with a BWO setup ($f = 0.324$ THz, $P \approx 0.5$ mW). The transmittance and especially the photoresistance show a very regular behavior. The latter reveals a strong sensitivity of MIRO to circularly polarized radiation, in agreement with the simultaneously measured transmittance. The analysis yields an amplitude ratio of approximately 30 between the CRA and CRI polarities for the first period of MIRO.

---

[11] Measurements were performed at the technical university of Vienna by Maxim Savchenko and Alexey Shuvaev in the group of Andrei Pimenov, https://www.ifp.tuwien.ac.at/spectroscopy (accessed January 1, 2024).

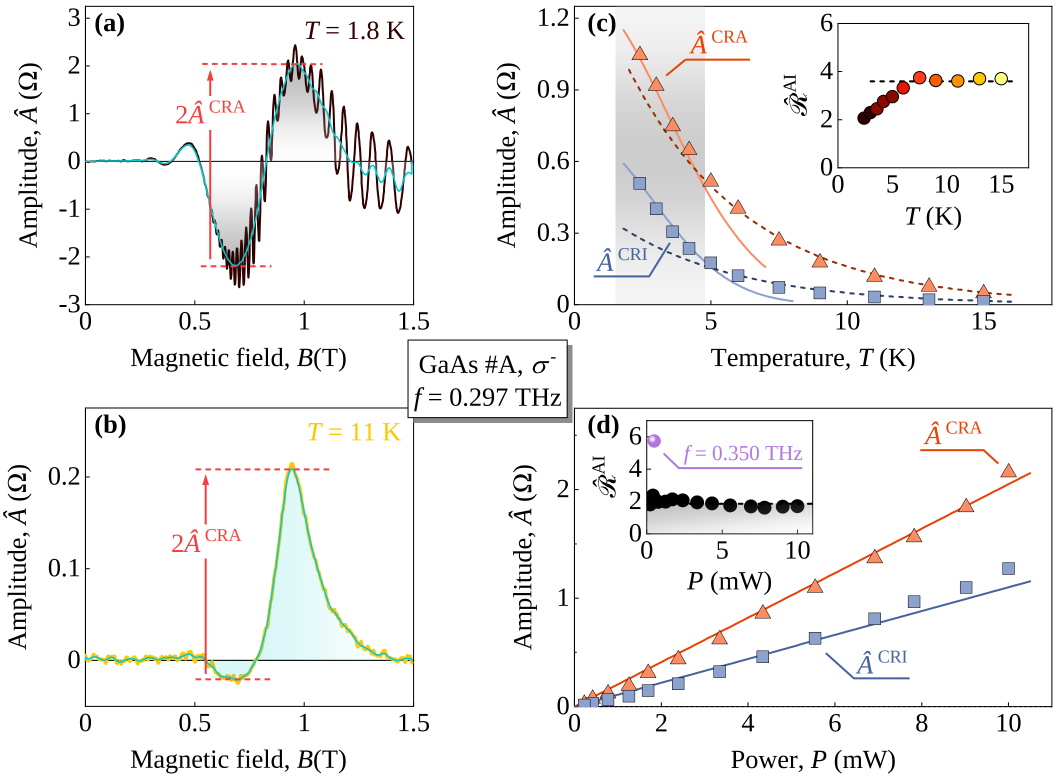

Figure 8.8: **(a, b)** Estimation of the MIRO amplitude shown exemplarily for the CRA polarity at two representative temperatures $T = 1.8$ K and $T = 11$ K of the data obtained at $f = 0.297$ THz. To overcome the amplitude distortion caused by SdHO-periodic oscillations, the data were smoothed with via a moving-average procedure before amplitude evaluation, see cyan traces. **(c)** Amplitude values of MIRO $\hat{A}^{\mathrm{CRA}}$ and $\hat{A}^{\mathrm{CRI}}$ as well as the corresponding ratio $\hat{\mathscr{R}}^{\mathrm{AI}}$ (shown in the inset) as a function of sample temperature. The colored curves are fits according to $\hat{A}^{\mathrm{CRA,CRI}}(T) \propto \exp(-T^2/T_1^2)$ with a corresponding characteristic temperature of $T_1 \approx 4.5$ K. The colored dashed curves are guides for the eye following an exponential decay. The gray shaded area denotes the region where MIRO dominate the photoresistance. The dashed line in the inset indicates the constant values at higher temperatures. **(d)** Power dependence of the amplitudes $\hat{A}^{\mathrm{CRA}}$ and $\hat{A}^{\mathrm{CRI}}$ obtained at $f = 0.297$ THz. The data are well fitted by linear-in-P dependencies, represented by the colored lines. The inset shows the ratio for the data in panel (d) (black circles) and for the photoresistance trace measured in Vienna at $f = 0.350$ THz, see Fig. 8.7(e), (purple circle). The data were recorded in GaAs #A in the σ^- configuration. Figure adapted from Ref. [48].

To determine the full amplitude of the MIRO-induced photoresistance, the traces were processed by a moving-average smoothing similar to the μ-photoconductivity traces at high T, see Fig. 8.4. This significantly reduces the influence of the SdHO-periodic oscillations at low temperatures as well as the increasing noise at higher T. Representative examples are shown in Figs. 8.8(a, b) for GaAs #A and $f =$ 0.297 THz, where the cyan curves illustrate the moving average of the experimental traces shown in black ($T = 1.8$ K) and orange ($T = 11$ K) color. The amplitudes for the CRA and CRI polarities are denoted by $\hat{A}^{\mathrm{CRA}}$ and $\hat{A}^{\mathrm{CRI}}$, respectively, and defined as half the difference of the maximum and minimum values around the CR position. It is worth noting that, as discussed above, the μ-photoconductivity response strongly increases with growing temperature, resulting in a superposition with MIRO. Similar to the analysis of the pure bolometric signal in Fig. 8.4, we introduce the ratio of the amplitudes according to

$$\hat{\mathscr{R}}^{\mathrm{AI}} = \frac{\hat{A}^{\mathrm{CRA}}}{\hat{A}^{\mathrm{CRI}}}\,, \tag{8.3}$$

which quantifies the anomalous behavior. Figure 8.8 shows the photoresistance amplitudes as a function of temperature [panel (c)] and power [panel (d)] for both polarities obtained from the photoresistance data presented in Figs. 8.7(b, d). The T-dependence exhibits a superimposed behavior. Below $T \approx 5$ K the photoresistance is dominated by MIRO, marked by the gray shaded area, and the amplitudes clearly follow $\hat{A}^{\mathrm{CRA,CRI}}(T) \propto \exp(-T^2/T_1^2)$. This temperature behavior is attributed to the displacement mechanism, see Chap. 7. In contrast, at higher temperatures ($T \gtrsim 5$ K), where the μ-photoconductivity begins to dominate the photoresponse, the amplitudes deviate from the low-T behavior and instead follow an exponential decay, represented by the dashed lines in the corresponding color. Looking at $\hat{\mathscr{R}}^{\mathrm{AI}}(T)$, illustrated in the inset, the ratio first increases (by a factor of two) in the region where MIRO dominate and eventually flattens out, revealing that the ratio remains almost independent of temperature at $T > 5$ K.

As per power dependence, see Fig. 8.8(d), the μ-photoconductivity does not appear here, instead showing only MIRO and SdHO-periodic oscillations in contrast to the temperature dependence. The MIRO amplitudes clearly exhibit a linear behavior with a slight tendency to a superlinear increase at the highest P. Thus, due to the almost linear scaling of the CRA and CRI amplitudes, the ratio [see inset of Fig. 8.8(d)] remains nearly constant and only grows slightly towards lower radiation powers. This is in strong contrast to the analysis of the pure bolometric photoresistance, see Fig. 8.6, where a clear saturation of A^{CRA} and A^{CRI} is visible. In addition, the ratio of the photoresistance trace performed in Vienna, shown in Fig. 8.7(c), is represented by the purple circle in the inset of Fig. 8.8(d). Qualitatively similar results for the temperature and power dependence have also been obtained for GaAs #C, see Fig. D.2 in App. D. Note that the photoresistance curve in Fig. D.1(e) obtained with the BWO setup at $T = 3.7$ K demonstrates a very high amplitude ratio of about 30, see Ref. [89] for detailed analysis.

In conclusion, photoresistance measurements in response to circularly polarized THz radiation have been performed in MLG, HgTe with different QW thicknesses as well as several GaAs QWs. While MLG exhibits conventional helicity sensitivity resulting in CR-enhanced photoresistance only at CRA polarity, the QWs have revealed anomalous resonant features for CRI magnetic field polarity. This puzzling behavior is in strong contrast to the simultaneously measured radiation transmittance, which demonstrates a regularly strong dependence on the radiation helicity for the whole range of T and P. At lowest temperatures and highest radiation powers, the amplitudes of the resonances at the CRA and CRI polarities have been observed to be almost the same. Furthermore, the ratio of these amplitudes has increased towards higher temperatures and lower radiation powers. However, even here the values of the photoresistance ratio are anomalously small, contradicting the expected helicity sensitivity of conventional radiation absorption based on classical Drude theory. In addition to the pure bolometric photoresistance at CR induced by electron gas heating, MIRO have also been observed and studied. While the ratio of MIRO amplitudes for both magnetic field polarities clearly increases with temperature, they are only slightly affected by the radiation power.

The observed saturation of the THz CR absorption is discussed in the next section on the basis of nonlinear electron gas heating. This mechanism explains the observed temperature and power dependence of the anomalous photoresistance. Furthermore, possible microscopic origins of the helicity anomalies are proposed to explain the puzzling CRI absorption.

8.2 Discussion

The results presented above reveal an anomalous response to the helicity of the incoming THz radiation in GaAs and HgTe QWs. While the measured transmittance shows a clear dependence on the helicity for all temperature and radiation powers, the generated bolometric and MIRO-induced photoresistance exhibits an almost symmetric resonant signal for both magnetic field directions at low T and high P. The observed temperature and power dependencies of the anomalous photoresistance are discussed in terms of nonlinear electron gas heating. Thereafter, a possible explanation for the anomalous CRI absorption is provided.

As detailed in Chap. 5 at the CRA polarity, the measured photoresistance and transmittance are well described in terms of classical Drude theory, including the influence of the Fabry-Pérot interference. Figure 8.9 presents the full transmittance trace (red solid) recorded in GaAs #A at $f = 0.297$ THz, $T = 1.8$ K, $P = 10$ mW, and σ^-

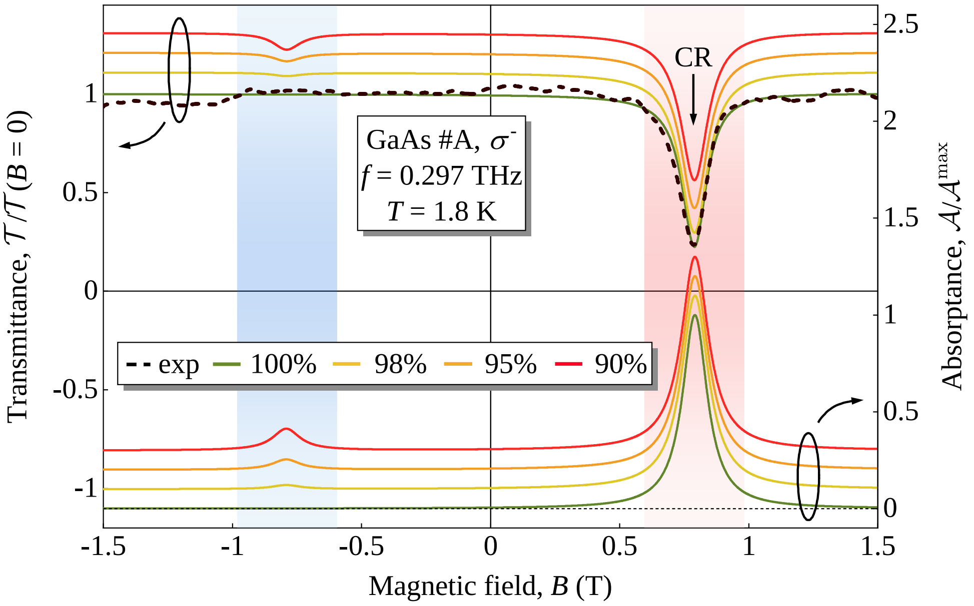

Figure 8.9: Normalized transmittance $\mathcal{T}(B)/\mathcal{T}(B = 0)$ (top colored traces) and corresponding absorptance $\mathcal{A}/\mathcal{A}^{\max}$ (bottom colored traces) modeled according to Eq. (2.45) in Sec. 2.2.1 with $\eta = +1$, $B_{\mathrm{CR}}^{\mathrm{P}} = 0.79$ T, $\mu^{-1} = 0.027$ T and $\beta = 0.031 - \mathrm{i}0.0015$ T using the experimental transmittance trace shown as a black dashed line. This was obtained in GaAs #A at $T = 1.8$ K for $f = 0.297$ THz, $P = 10$ mW and σ^- helicity. The theoretical curves are illustrated for different purities of circularly polarized radiation assigned to the trace color. The curves are up-shifted for clarity. Figure adapted from Ref. [48].

configuration. The shape is accurately reproduced by Eq. (2.45) [see Sec. 2.2.1], assuming that the incoming radiation is 100 % σ^- polarized. Spoiling the well-defined polarization state with small admixtures (2, 5, and 10 %) of the σ^+-polarization component leads to apparent changes in CRI polarity, see the colored transmittance and corresponding absorptance curves in Fig. 8.9. Here a purity of about 95 % is already visible as a clear feature. Thus, the almost flat CRI side of the measured transmittance attests a very high purity of the circular polarization in the transmitted and thus also in the incident wave. Furthermore, the THz beam spot focused on the sample is significantly smaller than the lateral dimensions of the GaAs and HgTe QWs, which excludes the influence of edges and contacts and thus a possible breakdown of the circular polarization in terms of antenna effects [89]. This proves that the anomalous CRI response detected in the photoresistance, see Fig. 8.2(b), cannot originate from an external admixture of the opposite helicity components. In fact, the calculated absorptance in Fig. 8.9 shows that a few percent admixture of the opposite helicity should reveal a similar CRI signal in the photoresistance, also not exceeding a few percent of the CRA signal. Note that the high purity of the circular polarization, confirmed by the transmittance obtained for the σ^- configuration, also holds for measurements with the opposite helicity (σ^+) and, furthermore, for the whole range of temperatures, powers, and frequencies used in this work.

The observed striking behavior in the photoresistance, which reveals almost equal signals for the CRA and CRI polarities, clearly contradicts the regular transmittance, see, e.g., Figs. 8.2 and 8.3 for GaAs and HgTe QWs, respectively. For quantitative comparison, we estimate the amplitude ratio $\mathscr{R}^{\mathrm{AI}}$ [Eq. (8.1)] at $B = B_{\mathrm{CR}}^{\mathrm{P}} - \Im\beta$ and its CRI counterpart using the Drude absorptance [Eq. (2.46) in Sec. 2.2.1] and assuming that the incoming radiation is 100 % σ^- polarized ($\eta = +1$). Taking $A^{\mathrm{CRA,CRI}} \propto \mathcal{A}^{\mathrm{CRA,CRI}}$ and $\mathcal{A}^{\mathrm{CRA}} \to \mathcal{A}(B), \mathcal{A}^{\mathrm{CRI}} \to \mathcal{A}(-B)$ the ratio is given by

$$\mathscr{R}^{\mathrm{AI}} = \frac{\mathcal{A}^{\mathrm{CRA}}}{\mathcal{A}^{\mathrm{CRI}}} = \frac{|\mu^{-1} + \beta - \mathrm{i}B_{\mathrm{CR}}^{\mathrm{P}} - \mathrm{i}\eta B|^2}{|\mu^{-1} + \beta - \mathrm{i}B_{\mathrm{CR}}^{\mathrm{P}} + \mathrm{i}\eta B|^2} = \frac{|\mu^{-1} + \beta - 2\mathrm{i}B_{\mathrm{CR}}^{\mathrm{P}} + \mathrm{i}\Im\beta|^2}{|\mu^{-1} + \beta - \mathrm{i}\Im\beta|^2} \,. \tag{8.4}$$

As discussed in Chap. 5, the CR width is maximal (minimal) for the constructive (destructive) interference condition, thus providing the minimal (maximal) limit of the CRA/CRI ratio. Under these conditions, $\beta \in \mathbb{R}$ and thus $\Im\beta = 0$, so Eq. (8.4) is simplified to

$$\mathscr{R}^{\mathrm{AI}} = \frac{(\mu^{-1} + \beta)^2 + 4(B_{\mathrm{CR}}^{\mathrm{P}})^2}{(\mu^{-1} + \beta)^2} \,. \tag{8.5}$$

Evaluating the relation for β, as introduced in Chap. 5, yields $\beta = 0.21$ T ($\beta = 0.03$ T) for constructive (destructive) interference. Using $\mu^{-1} = 0.027$ T and $B_{\mathrm{CR}} = B_{\mathrm{CR}}^{\mathrm{P}} = 0.79$ T, the ratio is

$$\mathscr{R}^{\mathrm{AI}}_{\mathrm{constr.}} \approx 45 \quad \text{and} \quad \mathscr{R}^{\mathrm{AI}}_{\mathrm{destr.}} \approx 769 \,. \tag{8.6}$$

These values are substantially larger than the observed behavior in the photoresistance, see inset in Figs. 8.4(c) and 8.6(b).

The observed power dependencies of the photoresistance amplitudes suggest that the CR-induced signal arises from nonlinear electron gas heating. This mechanism has already been discussed in Chap. 5 for the limit of small intensities $I \to 0$, i.e., in the linear regime, in terms of the energy balance equation [Eq. (2.50) in Sec. 2.3]. In general, two possible scenarios have to be considered, which may lead to a nonlinear dependence of the electron gas heating: the saturation of the radiation absorptance $\mathcal{A}(I)$ and/or the nonlinear dependence of the energy losses $Q(I)$. The former necessitates a very high radiation intensity of the order of $I \approx 100\ \mathrm{kW\,cm^{-2}}$ [135, 211–213], which is almost five orders of magnitude larger than the intensities used in this work and therefore does not play a significant role here. However, the nonlinear dependence of $Q(I)$ becomes important when the electron temperature T_e increases such that the heating $\Delta T = T_e - T$ starts to be comparable to the lattice temperature T. A prominent example resulting in a pronounced nonlinear behavior is the mechanism of low-angle electron-phonon scattering. It has been addressed theoretically [92] and observed experimentally in Si MOSFET structures where it leads to saturation of the THz induced photoconductivity [91, 214, 215]. Under the condition of low T, the energy losses depend strongly superlinearly on the electron temperature, yielding $Q(I) \propto (T_e - T)^5$ due to low-angle electron-phonon scattering. This leads to an extremely fast growth of $Q(I)$ with increasing radiation intensity and thus to a rapid rise of the inelastic scattering rate $\tau_{\mathrm{e-ph}}^{-1}$. As a consequence, the electrons lose their heat to the lattice more and more efficiently, leading to a saturation of the electron heating. Since the photoresistance is proportional to ΔT, see Eq. (2.52) in Sec. 2.3, it also exhibits a sublinear behavior. The stronger radiation absorption on the CRA side results in a higher electron temperature and thus a stronger saturation compared to the CRI polarity. This picture is consistent with our data, see Figs. 8.6(a) for $f = 0.297$ THz and Fig. C.4(a) in App. C for $f = 0.69$ THz. Although the frequencies differ by a factor of two, the saturation powers $P_{\mathrm{s}}^{\mathrm{CRA}}$ and $P_{\mathrm{s}}^{\mathrm{CRI}}$ are almost the same, while the corresponding saturation intensity is about four times higher for $f = 0.69$ THz. This behavior is in line with the Drude absorptance, which exhibits a f^{-2} scaling. For A^{CRI}, the saturation powers are twice as high as for the CRA amplitude, which agrees with the ratio of the linear coefficients $a^{\mathrm{CRA}}/a^{\mathrm{CRI}}$. Furthermore, this interpretation is supported by the broadening of the CR-enhanced signal shape. Figures 8.5(c, d) illustrate this behavior. The photoresistance traces, normalized to the applied radiation power, show similar shapes and magnitudes for the entire CRI side and at the wings of the CRA signal, clearly demonstrating a linear power dependence. In strong contrast, the photoresponse reveals a clear deviation at high P on the CRA side, where electron gas heating is the strongest. This behavior is governed by a transition from linear to nonlinear heating, which explains the growth of the CRA/CRI ratio [Eq. (8.1)] at lower powers. Remarkably, the measured $\mathscr{R}^{\mathrm{AI}}$ remains anomalously small even at the lowest available P.

This nonlinearity becomes weaker at higher T, which is well reproduced by the obtained photoresistance, see Fig. C.7 in App. C showing traces at $T = 6$ K. Here, the shapes and magnitudes of the traces for the entire power range are nearly equal at both polarities, yielding an almost constant ratio, see Fig. 8.6(d). This behavior is intuitively clear: since at higher T the relative radiation-induced change in T_e becomes smaller, higher intensities are required to facilitate its saturation. At even higher T, when a certain temperature limit is reached, the involved phonon modes are all equally occupied and large-angle scattering becomes possible, yielding a universal linear dependence of the energy losses on the electron temperature, $Q(I) \propto T_e - T$. Under this condition, the energy losses scale linearly with the applied radiation intensity, and the nonlinearity for the electron temperature is absent. It is noteworthy that the photoresistance may still exhibit a nonlinear behavior even in this high-T regime. In particular, at high intensities, Eq. (2.52) in Sec. 2.3, is not always valid and should be replaced by a more general form $\Delta R = R[T_e(I), T] - R[T_e(I \to 0), T]$. The increased photoresistance obtained at different radiation frequencies shows that the features near the CR at higher frequencies survive much higher temperatures. Indeed, a comparison of the amplitudes for $f = 0.297$ [Fig. 8.2], $f = 0.69$ THz [Fig. B.2 in App. B] and 1.63 THz [Fig. B.3 in App. B] demonstrates that the photosignal for the CRA polarity at the lowest frequency starts to disappear already at $T \approx 15$ K, while for the highest it is still pronounced at $T = 40$ K. This observation is consistent with the fact that for higher frequencies, the CR condition occurs at higher magnetic fields between less broadened LL, which are more resilient to temperature smearing. Consequently, higher T are required to quench the photosignal.

Summarizing the discussion above, the photoresponse at the CRA side is conventional and can be well described within the bolometric mechanism combined with the nonlinear electron gas heating. The anomalous photoresponse on the CRI side has very similar shape, while evolution of the CRA/CRI ratio with radiation intensity can be well understood as a result of nonlinear heating. At the same time, the microscopic origin of the anomalous CRI absorption remains unclear. In the following we present a possible explanation proposed in Refs. [47, 48] that may resolve this puzzling behavior assuming the emergence of near fields.

The electrons in an isotropic and uniform 2DES experience the electric field $\boldsymbol{E}$ of an incident circularly polarized plane wave as a driving force, resulting in a uniform circular electric current of the same helicity, which is defined by $\boldsymbol{j} = \overset{\leftrightarrow}{\sigma}\boldsymbol{E}$ with the local dynamic conductivity $\overset{\leftrightarrow}{\sigma}(\omega, \boldsymbol{q} \to 0)$. Depending on the helicity, this current is only resonantly enhanced near CR at $B > 0$ (σ^-) or $B < 0$ (σ^+) [3, 4, 13]. In order to obtain a resonant CRI response, the observations in the photoresistance inevitably require a mechanism that converts the uniform THz radiation into nonuniform evanescent near-fields, thus affecting the polarization state of the incoming wave within the 2DES. The emergence of evanescent near fields within the sample locally perturbs the incoming circularly polarized radiation, leading to a mixing of the otherwise independent helicity components. This results in a non vanishing absorption at the CRI polarity. Possible sources of such near fields may be rare and strong impurities or inhomogeneities [13, 216–223]. Indeed, in the vicinity of such impurities, the induced electron flow is substantially modified, leading to local anisotropy. Consequently, this scattering centers should facilitate the coupling of both helicity modes, thus allowing CR-enhanced absorption for both magnetic field polarities. Since most of the incoming radiation is reflected under CR condition [see Chap. 5], the uniform, high-density and high-mobility 2DES containing such strong impurities can be viewed as an old mirror with randomly distributed dark spots. The radiation is not effectively reflected near these dark or "dirty" spots, resulting in enhanced absorption. This means that the near-field absorption inducing resonant heating at both CRA and CRI polarities is enhanced near these scattering centers both due to stronger scattering and a larger $\boldsymbol{E}$-field acting on the carriers. At higher T the near fields become thermally suppressed due to more frequent phonon and electron-electron scattering, leading to a decrease in the passive helicity component and hence a smaller CRI signal. Moreover, the induced helicity coupling produced by THz near fields is only present in the immediate vicinity of the sample, leaving the transmittance shape unaffected as it is measured in the far field at a large distance from the sample, see Sec. 3.4.2. On the contrary, the radiation absorption in the 2DES and thus the obtained photoresistance are directly sensitive to both far-field and near-field components. Related considerations of strong impurities and their ability to alter the electron transport properties within a 2DES in both static and dynamic regimes can be found in Refs. [13, 216–223].

In view of the high quality of the investigated QWs, especially GaAs, the observed photoresistance with almost equal amplitudes for both polarities is still remarkable. In fact, such near-field coupling is usually mediated by macroscopic metallic objects [224–226] as presented in Chap. 6 in a graphene structure with long metallic contacts, where strong induced near-fields have been observed. In the graphene experiments, the focused THz beam was much larger than the structure. This is excluded here by the choice of larger lateral sample dimensions, which prevents the influence of contacts and edges and provides the illumination of a nominally uniform 2DES. However, it should be noted that the CRI polarity is dominated by much stronger near fields compared to the CRA side. In fact, at the CRA polarity, most of the incident radiation is reflected, suppressing the plane-wave component reaching the 2DES and thus the emergence of potential near-fields. At the CRI side, the radiation is almost completely transmitted, allowing the formation of stronger near fields, leading to an increased absorption. Once the absorbed energy per unit area of the 2DES reaches a certain value, the nonlinearity of the electron gas heating leads to a helicity immune photoresistance, regardless of the nature of the initial absorbing source.

Let us now comment briefly on the helicity anomaly observed in the MIRO regime. Since the samples were exposed to ambient light prior to the measurements, which changed their transport properties as discussed in Sec. 4.1, this also affected the transmittance curve. A comparison of Figs. 8.2(b) and 8.7(b) [or Figs. 8.5(b) and 8.7(d)] clearly shows that an increase in mobility leads to a narrower shape and a deeper minimum. Despite these changes, the overall behavior of the transmittance remains regular and exhibits no features on the CRI side. However, similar to the bolometric response, the MIRO-induced photoresistance shows almost the same magnitude for both magnetic field polarities under certain experimental conditions. The observation of the intriguing helicity immunity of MIRO was already investigated in previous works conducted in GaAs QW structures, which contradict the established theories [13]. These studies were performed with comparable powers in the milliwatt range [12, 17] and in the ultra-high power regime of the order of a few tens of watts [18] achieved by pulsed operation. Most importantly, the observation of the anomalous helicity dependence of the bolometric photoresistance demonstrates that the insensitivity of MIRO to circularly polarized radiation is not an intrinsic property of MIRO itself, but rather a direct consequence of the helicity-insensitive absorption. In this view, MIRO simply provides an alternative way to probe the helicity anomalies in the CR absorption.

As can be seen in Figs. 8.7(d) and 8.8(d), the MIRO CRA and CRI amplitudes show linear-in-P dependencies, indicating no sublinear behavior. Subsequently, the amplitude ratio $\hat{\mathscr{R}}^{\mathrm{AI}}$ shows almost no substantial changes over the entire range of available radiation powers, even at the lowest temperature $T = 1.8$ K. This behavior is different from that observed for the bolometric response discussed above, which exhibits a clear saturation and hence a substantial change in the ratio with P. However, the linear-in-P dependencies of MIRO amplitudes are consistent with the understanding that the appearance of MIRO is not related to the electron gas heating mechanism. At the same time, according to the displacement and inelastic mechanisms, see Chap. 7 for details, MIRO are proportional to the radiation absorption under the assumption of not too large radiation powers [13]. Thus, the enhanced CRI absorption due to scattered near-fields described above should influence the helicity dependence of MIRO in the same way as the bolometric photoresistance. Considering that the obtained CRA/CRI ratios for MIRO are in line with the range of values for the bolometric response, it substantiates that the helicity immunity of MIRO only reflects the anomalous resonant CRI absorption. However, the amplitude ratio of the photoresistance trace in Fig. D.1(e) in App. D obtained by the BWO setup in GaAs #C at $T = 3.7$ K and $f = 0.324$ THz reveals a surprisingly high value of

$\hat{\mathscr{R}}^{\mathrm{AI}} \approx 30$ [89]. This regular behavior reproduces the theoretically predicted ratio and accurately fits the observed transmittance. At the same time, it is still unclear why only GaAs #C under these experimental conditions shows the expected conventional behavior, while the other QWs, including GaAs and HgTe, exhibit anomalous photoresponses. This is indeed puzzling and requires a clarification.

The amplitudes of the MIRO of the CRA and CRI polarities, and thus the ratio $\hat{\mathscr{R}}^{\mathrm{AI}}$, are clearly affected by temperature, see Fig. 8.8(c) for GaAs #A and also Fig. D.2(a) in App. D for GaAs #C. While at low T MIRO clearly dominate the photoresistance with almost complete helicity immunity, at higher temperatures, where MIRO are strongly suppressed, the ratio increases significantly. Note that this rapid temperature decay of MIRO after $\hat{A}^{\mathrm{CRA,CRI}}(T) \propto \exp(-T^2/T_1^2)$ is predicted by the displacement mechanism, which is in agreement with previous works (for review, see Ref. [13]). At $T \gtrsim 9$ K, the μ-photoconductivity response dominates the photoresistance, resulting in a slower T-decay. Together with the linear power dependence, this behavior demonstrates that the large values of the amplitude ratio at higher T are not due to MIRO, but rather to the temperature dependence of the nonlinear electron gas heating causing the bolometric photoresistance.

Before concluding, the CR-enhanced photoresistance in MLG shown in Fig. 8.1 is briefly addressed. The obtained photoresponse exhibits a regular CR behavior with no resonant features on the CRI side and a remarkably high CRA/CRI ratio [$\mathscr{R}^{\mathrm{AI}}(T = 4.2\text{ K}) \approx 20$] over the whole range of carrier densities and temperatures. This is a surprising result since the sample is several orders of magnitude smaller than the focused THz beam and thus edges and contacts are inevitably illuminated. As described above, this should apparently lead to the emergence of evanescent near-fields and thus modify the radiation polarization leading to resonant CRI absorption. Furthermore, it is not fully understood whether rare and strong impurities, responsible for the enhanced CRI absorption mentioned above, are present in encapsulated monolayer graphene. In our samples, the electron mean free path, determined from magnetotransport measurements see Sec. 4.2, is constrained by the width of the Hall bar structure, thus proving that electron transport is mostly dominated by edge scattering. However, the influence of the latter on the polarization of the incident plane wave is still unclear and requires further investigation. Taken together, these results show that the helicity anomaly in CR absorption reflects peculiarities of the dynamic response in specific 2DES, and thus demonstrates that its occurrence is not universal.

To summarize, it has been demonstrated that the observed anomalous CR photoresistance in GaAs and HgTe QWs is strongly affected by the nonlinear electron gas heating. A sufficiently high radiation power leads to saturation of the electron temperature at low T, resulting in sublinear dependencies of the CRA and CRI amplitudes on the applied radiation power. Due to the different absorption strengths, the CRA and CRI amplitudes exhibit different saturation powers. Although the amplitude ratio increases significantly with increasing power, it remains anomalously small even at the lowest P. This puzzling behavior can originate from the resonant absorption in the CRI regime by scattered near-fields in the proximity of the 2DES. Their appearance should significantly affect the polarization characteristics of the incoming plane wave and thus provide a resonant CR photoresistance at both B-field polarities. The assumption that the 2DES also absorbs at the CRI side also explains the helicity insensitivity of the CR-coupled MIRO, which have shown a linear-in-P dependence and whose appearance is not related to electron gas heating. On the contrary, the small graphene structure, which has been exposed to a THz beam orders of magnitude larger than the entire structure, has shown a regular CR in the photoresistance, demonstrating non-universality of the helicity immunity.

9 Conclusion and Outlook

In this thesis, various terahertz-induced optoelectronic phenomena coupled to the cyclotron resonance and its harmonics have been observed and thoroughly investigated. Different classes of two-dimensional electron systems characterized by linear and parabolic energy dispersions, the latter with inverted and normal band orders, served as fruitful playgrounds for the observation of intriguing effects probed by magnetophotoresistance and photovoltage. The studies include encapsulated graphene-based structures and gallium arsenide and mercury telluride heterostructures. The observed phenomena have been explored in the semiclassical regime where the photon energy is significantly smaller than the Fermi energy. Graphene structures of excellent quality have revealed Bernstein modes facilitated by near-field enhanced magnetoabsorption [45] and terahertz-driven magnetooscillations [46]. While studying the latter in gallium arsenide quantum wells, an anomalous insensitivity of the cyclotron absorption to the helicity of the radiation has been found. This behavior is in contrast to the obtained radiation transmittance, which accurately follows the well-established Drude theory [47, 48].

Basic properties and approaches describing the cyclotron resonance in transmittance and corresponding absorptance have been outlined in Chap. 5. The main experimental results and discussions of the observed effects have been presented in Chaps. 6, 7 and 8.

Terahertz-induced Bernstein modes, manifested as sharp photoresponse peaks near the cyclotron resonance harmonics, have been observed. An extensive study, described in Chap. 6, has revealed that these originate from enhanced magnetoabsorption caused by near-field effects arising in the vicinity of metallic contacts that partially protrude into the Hall bar channel. It has been shown that the emerging Bernstein modes exhibit a flat dispersion leading to a divergent plasmonic density of states. This in turn resonantly enhances the radiation absorption, resulting in strong electron gas heating and consequently a resonantly enhanced photoresponse [45]. Extending these considerations, a strong near-field coupling mediated by metallic interdigitated dual-grating gate fingers has been exploited in bilayer graphene-based structures [49–51]. The structure yields enhanced near-field diffraction, which has been used to impose an even stronger coupling of terahertz radiation and magnetoplasma excitations. Exploiting the nonlinear nature of the ratchet effect – the generation of a dc electric current in response to an ac electric field – revealed the coexistence of cyclotron and magnetoplasmon resonances.

Furthermore, the emergence of terahertz-induced magnetooscillations coupled to the harmonics of the cyclotron resonance has been demonstrated in graphene with conventional contacts in Chap. 7. Analysis of their variation with carrier density and radiation frequency has revealed a common origin with the well-known microwave-induced resistance oscillations observed in gallium arsenide heterostructures [13]. It has been shown that, similar to the latter, their graphene analog is governed by the ratio of the incident radiation frequency to the quasiclassical cyclotron frequency [46]. In this context, the theory of microwave-induced resistance oscillations has been adapted to the linear energy dispersion of graphene. The displacement mechanism based on the shift of the cyclotron resonance orbit center and the inelastic mechanism describing a radiation-induced variation of the distribution function have been considered. Importantly, the presented analysis has also revealed strong qualitative differences, namely that terahertz-induced magnetooscillations appear at much higher frequencies, well above 1 THz, and persist up to $T = 90$ K, which is attributed to a slower electron-electron scattering rate [46]. However, the present study still lacks a clear assignment of the dominant mechanism in graphene and requires further investigation to identify its contributions. This necessitates more focused studies at low temperatures. The observation of the presented phenomena demonstrates that such high-quality graphene structures provide an excellent platform for the exploration of novel effects and, furthermore, offer a valuable opportunity to gain a more profound understanding of the rich spectrum of radiation-induced phenomena in two-dimensional electron systems.

Cyclotron resonance absorption in gallium arsenide and mercury telluride quantum wells has revealed an anomalous insensitivity to the helicity of the incident terahertz radiation, as demonstrated in Chap. 8. In contrast to the investigated graphene structures, it has been observed that the amplitude of the photoresistance is almost the same for both the cyclotron resonance active and inactive magnetic field polarities at lowest temperatures and highest radiation powers [47, 48]. The amplitude ratio of the active and inactive sides of the cyclotron resonance has been shown to be strongly dependent on sample temperature and radiation power. This is in strong contrast to the simultaneously measured radiation transmittance, which has demonstrated an ordinary helicity dependence for all T and P. It has been proposed that this dependence is caused by nonlinear heating of the electron gas. This heating leads to saturation of the photoresistance with different saturation behaviors for the cyclotron resonance active and inactive polarities. However, even at the lowest powers, the value of the amplitude ratio remains much lower than predicted by the conventional Drude theory. This puzzling behavior may be resolved by assuming resonant absorption of the incident radiation via the occurrence of near-field effects in the vicinity of the two-dimensional electron system in the cyclotron resonance inactive regime. Furthermore, this may also explain the helicity insensitivity demonstrated for the observed microwave-induced resistance oscillations. The presented anomalies are indeed remarkable and of great importance for polarization-sensitive photoelectric studies in two-dimensional electron systems. As a perspective, it is worth mentioning that a more comprehensive understanding of the regular helicity sensitivity of microwave-induced resistance oscillations under certain conditions may provide an access to the solution of the long-standing immunity puzzle. An explanation of this behavior may further classify the origin of near-field sources and, more importantly, shed light on the appearance of cyclotron resonance inactive absorption.

References

[1] G. Dresselhaus, A. F. Kip, and C. Kittel, *Observation of cyclotron resonance in germanium crystals*, Phys. Rev. **92**, 827–827 (1953).

[2] G. Dresselhaus, A. F. Kip, and C. Kittel, *Cyclotron resonance of electrons and holes in silicon and germanium crystals*, Phys. Rev. **98**, 368–384 (1955).

[3] K. Seeger, *Semiconductor physics: An introduction*, Advanced Texts in Physics (Springer, 2004).

[4] D. J. Hilton, T. Arikawa, and J. Kono, "Cyclotron resonance", in *Characterization of Materials* (John Wiley & Sons, Ltd, 2012).

[5] H. J. Zeiger, C. J. Rauch, and M. E. Behrndt, *Observation of microwave cyclotron resonance by cross modulation*, Phys. Rev. Lett. **1**, 59–60 (1958).

[6] M. A. Zudov, R. R. Du, J. A. Simmons, and J. L. Reno, *Shubnikov–de Haas-like oscillations in millimeterwave photoconductivity in a high-mobility two-dimensional electron gas*, Phys. Rev. B **64**, 201311(R) (2001).

[7] P. D. Ye, L. W. Engel, D. C. Tsui, J. A. Simmons, J. R. Wendt, G. A. Vawter, and J. L. Reno, *Giant microwave photoresistance of two-dimensional electron gas*, Appl. Phys. Lett. **79**, 2193–2195 (2001).

[8] R. G. Mani, J. H. Smet, K. von Klitzing, V. Narayanamurti, W. B. Johnson, and V. Umansky, *Zero-resistance states induced by electromagnetic-wave excitation in GaAs / AlGaAs heterostructures*, Nature **420**, 646–650 (2002).

[9] M. A. Zudov, R. R. Du, L. N. Pfeiffer, and K. W. West, *Evidence for a new dissipationless effect in 2D electronic transport*, Phys. Rev. Lett. **90**, 046807 (2003).

[10] C. L. Yang, M. A. Zudov, T. A. Knuuttila, R. R. Du, L. N. Pfeiffer, and K. W. West, *Observation of microwave-induced zero-conductance state in corbino rings of a two-dimensional electron system*, Phys. Rev. Lett. **91**, 096803 (2003).

[11] S. I. Dorozhkin, *Giant magnetoresistance oscillations caused by cyclotron resonance harmonics*, J. Exp. Theo. Phys. Lett. **77**, 577–581 (2003).

[12] J. H. Smet, B. Gorshunov, C. Jiang, L. Pfeiffer, K. West, V. Umansky, M. Dressel, R. Meisels, F. Kuchar, and K. von Klitzing, *Circular-polarization-dependent study of the microwave photoconductivity in a two-dimensional electron system*, Phys. Rev. Lett. **95**, 116804 (2005).

[13] I. A. Dmitriev, A. D. Mirlin, D. G. Polyakov, and M. A. Zudov, *Nonequilibrium phenomena in high Landau levels*, Rev. Modern Phys. **84**, 1709–1763 (2012).

[14] A. Wirthmann, B. D. McCombe, D. Heitmann, S. Holland, K.-J. Friedland, and C.-M. Hu, *Far-infrared-induced magnetoresistance oscillations in GaAs / $Al_xGa_{1-x}As$-based two-dimensional electron systems*, Phys. Rev. B **76**, 195315 (2007).

[15] L.-C. Tung, C. Yang, D. Smirnov, L. Pfeiffer, K. West, R. Du, and Y.-J. Wang, *Submillimeter wave induced resistance oscillations in ultra-high mobility two-dimensional electron systems*, Solid State Commun. **149**, 1531–1534 (2009).

[16] Z. D. Kvon, D. A. Kozlov, S. N. Danilov, C. Zoth, P. Vierling, S. Stachel, V. V. Bel'kov, A. K. Bakarov, D. V. Dmitriev, A. I. Toropov, and S. D. Ganichev, *Terahertz radiation-induced magnetoresistance oscillations of a high-density and high-mobility two-dimensional electron gas*, JETP Lett. **97**, 41–44 (2013).

[17] T. Herrmann, I. A. Dmitriev, D. A. Kozlov, M. Schneider, B. Jentzsch, Z. D. Kvon, P. Olbrich, V. V. Bel'kov, A. Bayer, D. Schuh, D. Bougeard, T. Kuczmik, M. Oltscher, D. Weiss, and S. D. Ganichev, *Analog of microwave-induced resistance oscillations induced in GaAs heterostructures by terahertz radiation*, Phys. Rev. B **94**, 081301(R) (2016).

[18] T. Herrmann, Z. D. Kvon, I. A. Dmitriev, D. A. Kozlov, B. Jentzsch, M. Schneider, L. Schell, V. V. Bel'kov, A. Bayer, D. Schuh, D. Bougeard, T. Kuczmik, M. Oltscher, D. Weiss, and S. D. Ganichev, *Magnetoresistance oscillations induced by high-intensity terahertz radiation*, Phys. Rev. B **96**, 115449 (2017).

[19] C. Berger, Z. Song, T. Li, X. Li, A. Y. Ogbazghi, R. Feng, Z. Dai, A. N. Marchenkov, E. H. Conrad, P. N. First, and W. A. de Heer, *Ultrathin epitaxial graphite: 2D electron gas properties and a route toward graphene-based nanoelectronics*, J. Phys. Chem. B **108**, 19912–19916 (2004).

[20] V. P. Gusynin and S. G. Sharapov, *Unconventional integer quantum Hall effect in graphene*, Phys. Rev. Lett. **95**, 146801 (2005).

[21] K. S. Novoselov, A. K. Geim, S. V. Morozov, D. Jiang, M. I. Katsnelson, I. V. Grigorieva, S. V. Dubonos, and A. A. Firsov, *Two-dimensional gas of massless Dirac fermions in graphene*, Nature **438**, 197–200 (2005).

[22] Y. Zhang, Y.-W. Tan, H. L. Stormer, and P. Kim, *Experimental observation of the quantum Hall effect and Berry's phase in graphene*, Nature **438**, 201–204 (2005).

[23] A. K. Geim and K. S. Novoselov, *The rise of graphene*, Nat. Mater. **6**, 183–191 (2007).

[24] A. H. Castro Neto, F. Guinea, N. M. R. Peres, K. S. Novoselov, and A. K. Geim, *The electronic properties of graphene*, Rev. Modern Phys. **81**, 109–162 (2009).

[25] S. Das Sarma, S. Adam, E. H. Hwang, and E. Rossi, *Electronic transport in two-dimensional graphene*, Rev. Modern Phys. **83**, 407–470 (2011).

[26] A. F. Young and P. Kim, *Electronic transport in graphene heterostructures*, Annu. Rev. Condens. Matter Phys. **2**, 101–120 (2011).

[27] K. S. Novoselov, A. K. Geim, S. V. Morozov, D. Jiang, Y. Zhang, S. V. Dubonos, I. V. Grigorieva, and A. A. Firsov, *Electric field effect in atomically thin carbon Films*, Science **306**, 666–669 (2004).

[28] F. Bonaccorso, Z. Sun, T. Hasan, and A. C. Ferrari, *Graphene photonics and optoelectronics*, Nat. Photonics **4**, 611–622 (2010).

[29] F. H. L. Koppens, D. E. Chang, and F. J. García de Abajo, *Graphene plasmonics: A platform for strong light–matter interactions*, Nano Lett. **11**, 3370–3377 (2011).

[30] R. bin Mohd Yusoffx, *Graphene optoelectronics: Synthesis, characterization, properties, and applications* (Wiley, 2014).

[31] J. Wang, X. Mu, M. Sun, and T. Mu, *Optoelectronic properties and applications of graphene-based hybrid nanomaterials and van der Waals heterostructures*, Appl. Mater. Today **16**, 1–20 (2019).

[32] K. Roy, *Optoelectronic properties of graphene-based van der Waals hybrids* (Springer International Publishing, 2020).

[33] A. N. Grigorenko, M. Polini, and K. S. Novoselov, *Graphene plasmonics*, Nat. Photonics **6**, 749–758 (2012).

[34] T. Low and P. Avouris, *Graphene plasmonics for terahertz to mid-infrared applications*, ACS Nano **8**, 1086–1101 (2014).

[35] F. J. García de Abajo, *Graphene plasmonics: Challenges and opportunities*, ACS Photonics **1**, 135–152 (2014).

[36] S. Huang, C. Song, G. Zhang, and H. Yan, *Graphene plasmonics: Physics and potential applications*, Nanophotonics **6**, 1191–1204 (2016).

[37] G. X. Ni, A. S. McLeod, Z. Sun, L. Wang, L. Xiong, K. W. Post, S. S. Sunku, B.-Y. Jiang, J. Hone, C. R. Dean, M. M. Fogler, and D. N. Basov, *Fundamental limits to graphene plasmonics*, Nature **557**, 530–533 (2018).

[38] L. Cui, J. Wang, and M. Sun, *Graphene plasmon for optoelectronics*, Rev. Phys. **6**, 100054 (2021).

[39] L. Vicarelli, M. S. Vitiello, D. Coquillat, A. Lombardo, A. C. Ferrari, W. Knap, M. Polini, V. Pellegrini, and A. Tredicucci, *Graphene field-effect transistors as room-temperature terahertz detectors*, Nat. Mater. **11**, 865–871 (2012).

[40] M. Glazov and S. Ganichev, *High frequency electric field induced nonlinear effects in graphene*, Phys. Rep. **535**, 101–138 (2014).

[41] F. H. L. Koppens, T. Mueller, P. Avouris, A. C. Ferrari, M. S. Vitiello, and M. Polini, *Photodetectors based on graphene, other two-dimensional materials and hybrid systems*, Nat. Nanotechnology **9**, 780–793 (2014).

[42] D. A. Bandurin, D. Svintsov, I. Gayduchenko, S. G. Xu, A. Principi, M. Moskotin, I. Tretyakov, D. Yagodkin, S. Zhukov, T. Taniguchi, K. Watanabe, I. V. Grigorieva, M. Polini, G. N. Goltsman, A. K. Geim, and G. Fedorov, *Resonant terahertz detection using graphene plasmons*, Nat. Commun. **9** (2018).

[43] J. A. Delgado-Notario, V. Clericò, E. Diez, J. E. Velázquez-Pérez, T. Taniguchi, K. Watanabe, T. Otsuji, and Y. M. Meziani, *Asymmetric dual-grating gates graphene FET for detection of terahertz radiations*, APL Photonics **5**, 066102 (2020).

[44] J. A. Delgado-Notario, W. Knap, V. Clericò, J. Salvador-Sánchez, J. Calvo-Gallego, T. Taniguchi, K. Watanabe, T. Otsuji, V. V. Popov, D. V. Fateev, E. Diez, J. E. Velázquez-Pérez, and Y. M. Meziani, *Enhanced terahertz detection of multigate graphene nanostructures*, Nanophotonics **11**, 519–529 (2022).

[45] D. A. Bandurin, E. Mönch, K. Kapralov, I. Y. Phinney, K. Lindner, S. Liu, J. H. Edgar, I. A. Dmitriev, P. Jarillo-Herrero, D. Svintsov, and S. D. Ganichev, *Cyclotron resonance overtones and near-field magnetoabsorption via terahertz Bernstein modes in graphene*, Nat. Phys. **18**, 462–467 (2022).

[46] E. Mönch, D. A. Bandurin, I. A. Dmitriev, I. Y. Phinney, I. Yahniuk, T. Taniguchi, K. Watanabe, P. Jarillo-Herrero, and S. D. Ganichev, *Observation of terahertz-induced magnetooscillations in graphene*, Nano Lett. **20**, 5943–5950 (2020).

[47] E. Mönch, P. Euringer, G.-M. Hüttner, I. A. Dmitriev, D. Schuh, M. Marocko, J. Eroms, D. Bougeard, D. Weiss, and S. D. Ganichev, *Circular polarization immunity of the cyclotron resonance photoconductivity in two-dimensional electron systems*, Phys. Rev. B **106**, L161409 (2022).

[48] E. Mönch, S. Schweiss, I. Yahniuk, M. L. Savchenko, I. A. Dmitriev, A. Shuvaev, A. Pimenov, D. Schuh, D. Bougeard, and S. D. Ganichev, *Nonlinear helicity anomalies in the cyclotron resonance photoresistance of two-dimensional electron systems*, arXiv:2311.05468 [cond-mat.mes-hall], accessed on Nov. 9, 2023 (2023).

[49] E. Mönch, S. O. Potashin, K. Lindner, I. Yahniuk, L. E. Golub, V. Y. Kachorovskii, V. V. Bel'kov, R. Huber, K. Watanabe, T. Taniguchi, J. Eroms, D. Weiss, and S. D. Ganichev, *Cyclotron and magnetoplasmon resonances in bilayer graphene ratchets*, Phys. Rev. B **107**, 115408 (2023).

[50] E. Mönch, S. O. Potashin, K. Lindner, I. Yahniuk, L. E. Golub, V. Y. Kachorovskii, V. V. Bel'kov, R. Huber, K. Watanabe, T. Taniguchi, J. Eroms, D. Weiss, and S. D. Ganichev, *Ratchet effect in spatially modulated bilayer graphene: Signature of hydrodynamic transport*, Phys. Rev. B **105**, 045404 (2022).

[51] E. Mönch, S. Hubmann, I. Yahniuk, S. Schweiss, V. V. Bel'kov, L. E. Golub, R. Huber, J. Eroms, K. Watanabe, T. Taniguchi, D. Weiss, and S. D. Ganichev, *Nonlinear intensity dependence of ratchet currents induced by terahertz laser radiation in bilayer graphene with asymmetric periodic grating gates*, J. Appl. Phys. **134**, 123102 (2023).

[52] J. H. Davies, *The physics of low-dimensional semiconductors: An introduction* (Cambridge University Press, 1997).

[53] E. Schrödinger, *Quantisierung als Eigenwertproblem*, Ann. Phys. **385**, 437–490 (1926).

[54] G. Airy, *On the intensity of light in the neighbourhood of a caustic* (Printed at the Pitt Press, by John William Parker, 1838).

[55] B. A. Bernevig, T. L. Hughes, and S.-C. Zhang, *Quantum spin Hall effect and topological phase transition in HgTe quantum wells*, Science **314**, 1757–1761 (2006).

[56] X.-L. Qi and S.-C. Zhang, *Topological insulators and superconductors*, Rev. Modern Phys. **83**, 1057–1110 (2011).

[57] N. N. Berchenko and M. V. Pashkovskiĭ, *Mercury telluride – a zero-gap semiconductor*, Soviet Physics Uspekhi **19**, 462–480 (1976).

[58] M. König, S. Wiedmann, C. Brüne, A. Roth, H. Buhmann, L. W. Molenkamp, X.-L. Qi, and S.-C. Zhang, *Quantum spin Hall insulator state in HgTe quantum wells*, Science **318**, 766–770 (2007).

[59] A. S. Junhao Chu, *Physics and properties of narrow gap semiconductors* (Springer New York, 2008).

[60] M. König, H. Buhmann, L. W. Molenkamp, T. Hughes, C.-X. Liu, X.-L. Qi, and S.-C. Zhang, *The quantum spin Hall effect: Theory and experiment*, J. Phys. Soc. Japan **77**, 031007 (2008).

[61] M. Z. Hasan and C. L. Kane, *Colloquium: Topological insulators*, Rev. Modern Phys. **82**, 3045–3067 (2010).

[62] A. K. Geim and A. H. MacDonald, *Graphene: Exploring carbon flatland*, Phys. Today **60**, 35–41 (2007).

[63] P. R. Wallace, *The band theory of graphite*, Phys. Rev. **71**, 622–634 (1947).

[64] G. Garcia, P. Porfírio, D. Moreira, and C. Furtado, *Graphene wormhole trapped by external magnetic field*, Nuclear Phys. B Proc. Suppl. **950**, 114853 (2020).

[65] S. Reich, J. Maultzsch, C. Thomsen, and P. Ordejón, *Tight-binding description of graphene*, Phys. Rev. B **66**, 035412 (2002).

[66] R. S. Deacon, K.-C. Chuang, R. J. Nicholas, K. S. Novoselov, and A. K. Geim, *Cyclotron resonance study of the electron and hole velocity in graphene monolayers*, Phys. Rev. B **76**, 081406 (2007).

[67] N. M. R. Peres, *Colloquium: The transport properties of graphene: An introduction*, Rev. Modern Phys. **82**, 2673–2700 (2010).

[68] G. W. Semenoff, *Condensed-matter simulation of a three-dimensional anomaly*, Phys. Rev. Lett. **53**, 2449–2452 (1984).

[69] P. Drude, *Zur Elektronentheorie der Metalle*, Ann. Phys. **306**, 566–613 (1900).

[70] N. Ashcroft and N. Mermin, *Solid State Physics*, HRW international editions (Holt, Rinehart and Winston, 1976).

[71] C. Hamaguchi, *Basic semiconductor physics* (Springer International Publishing, 2017).

[72] H. Ibach and H. Lüth, *Solid-state physics: An introduction to principles of materials science* (Springer Berlin Heidelberg, 2009).

[73] D. Neamen, *Semiconductor physics And devices*, McGraw-Hill Series in Electrical and Computer Engineering (McGraw-Hill Education, 2003).

[74] S. A. Mikhailov, *Microwave-induced magnetotransport phenomena in two-dimensional electron systems: Importance of electrodynamic effects*, Phys. Rev. B **70**, 165311 (2004).

[75] Q. Zhang, T. Arikawa, E. Kato, J. L. Reno, W. Pan, J. D. Watson, M. J. Manfra, M. A. Zudov, M. Tokman, M. Erukhimova, A. Belyanin, and J. Kono, *Superradiant decay of cyclotron resonance of two-dimensional electron gases*, Phys. Rev. Lett. **113**, 047601 (2014).

[76] L. Landau, *Diamagnetismus der Metalle*, Zeitschrift für Physik **64**, 629–637 (1930).

[77] L. Landau and E. Lifshitz, *Quantum mechanics: Non-relativistic theory*, Course of theoretical physics (Elsevier Science, 1991).

[78] K. von Klitzing, G. Dorda, and M. Pepper, *New method for high-accuracy determination of the fine-structure constant based on quantized Hall resistance*, Phys. Rev. Lett. **45**, 494–497 (1980).

[79] R. Jackiw, *Fractional charge and zero modes for planar systems in a magnetic field*, Phys. Rev. D **29**, 2375–2377 (1984).

[80] F. D. M. Haldane, *Model for a quantum Hall effect without Landau levels: Condensed-matter realization of the "parity anomaly"*, Phys. Rev. Lett. **61**, 2015–2018 (1988).

[81] N. M. R. Peres, F. Guinea, and A. H. Castro Neto, *Electronic properties of disordered two-dimensional carbon*, Phys. Rev. B **73**, 125411 (2006).

[82] Y. Zhang, Z. Jiang, J. P. Small, M. S. Purewal, Y.-W. Tan, M. Fazlollahi, J. D. Chudow, J. A. Jaszczak, H. L. Stormer, and P. Kim, *Landau-level splitting in graphene in high magnetic fields*, Phys. Rev. Lett. **96**, 136806 (2006).

[83] D. L. Miller, K. D. Kubista, G. M. Rutter, M. Ruan, W. A. de Heer, P. N. First, and J. A. Stroscio, *Observing the quantization of zero mass carriers in graphene*, Science **324**, 924–927 (2009).

[84] Y. Zhang and P. Kim, "Electronic transport in graphene", PhD thesis (Columbia University, 2006).

[85] A. M. Witowski, M. Orlita, R. Stępniewski, A. Wysmołek, J. M. Baranowski, W. Strupiński, C. Faugeras, G. Martinez, and M. Potemski, *Quasiclassical cyclotron resonance of Dirac fermions in highly doped graphene*, Phys. Rev. B **82**, 165305 (2010).

[86] U. Briskot, I. A. Dmitriev, and A. D. Mirlin, *Quantum magneto-oscillations in the ac conductivity of disordered graphene*, Phys. Rev. B **87**, 195432 (2013).

[87] K. Chiu, T. Lee, and J. Quinn, *Infrared magneto-transmittance of a two-dimensional electron gas*, Surf. Sci. **58**, 182–184 (1976).

[88] G. Abstreiter, J. P. Kotthaus, J. F. Koch, and G. Dorda, *Cyclotron resonance of electrons in surface space-charge layers on silicon*, Phys. Rev. B **14**, 2480–2493 (1976).

[89] M. L. Savchenko, A. Shuvaev, I. A. Dmitriev, S. D. Ganichev, Z. D. Kvon, and A. Pimenov, *Demonstration of high sensitivity of microwave-induced resistance oscillations to circular polarization*, Phys. Rev. B **106**, L161408 (2022).

[90] B. I. Sturman and V. M. Fridkin, *The photovoltaic and photorefractive effects in noncentrosymmetric materials* (Routledge, 2021).

[91] S. D. Ganichev and W. Prettl, *Intense terahertz excitation of semiconductors* (Oxford University Press, Oxford, 2005).

[92] V. F. Gantmakher and Y. B. Levinson, *Carrier scattering in metals and semiconductors*, North Holland (2012).

[93] S. Hubmann, G. Di Battista, I. A. Dmitriev, K. Watanabe, T. Taniguchi, D. K. Efetov, and S. D. Ganichev, *Infrared photoresistance as a sensitive probe of electronic transport in twisted bilayer graphene*, 2D Mater. **10**, 015005 (2022).

[94] P. Valov, B. Ryvkin, I. Yaroshetskii, and I. Yassievich, *Intraband photoconductivity in n-type Ge caused by optical heating of electrons*, Sov. Phys. Semicond. **5**, 797–801 (1971).

[95] G. Giuliani and G. Vignale, *Quantum theory of the electron liquid* (Cambridge University Press, 2005).

[96] S. A. Maier, *Plasmonics: Fundamentals and applications* (Springer US, 2007).

[97] N. B. Stefan Enoch, *Plasmonics: From basics to advanced topics* (Springer Berlin Heidelberg, 2012).

[98] S. Das Sarma and E. H. Hwang, *Collective modes of the massless Dirac plasma*, Phys. Rev. Lett. **102**, 206412 (2009).

[99] B. Wunsch, T. Stauber, F. Sols, and F. Guinea, *Dynamical polarization of graphene at finite doping*, New J. Phys. **8**, 318–318 (2006).

[100] E. H. Hwang and S. Das Sarma, *Dielectric function, screening, and plasmons in two-dimensional graphene*, Phys. Rev. B **75**, 205418 (2007).

[101] M. Polini, R. Asgari, G. Borghi, Y. Barlas, T. Pereg-Barnea, and A. H. MacDonald, *Plasmons and the spectral function of graphene*, Phys. Rev. B **77**, 081411(R) (2008).

[102] S. H. Abedinpour, G. Vignale, A. Principi, M. Polini, W.-K. Tse, and A. H. MacDonald, *Drude weight, plasmon dispersion, and ac conductivity in doped graphene sheets*, Phys. Rev. B **84**, 045429 (2011).

[103] K. W. Chiu and J. J. Quinn, *Plasma oscillations of a two-dimensional electron gas in a strong magnetic field*, Phys. Rev. B **9**, 4724–4732 (1974).

[104] A. V. Chaplik and D. Heitmann, *Geometric resonances of two-dimensional magnetoplasmons*, J. Phys. C: Solid State Phys. **18**, 3357–3363 (1985).

[105] K. Kapralov and D. Svintsov, *Ballistic-to-hydrodynamic transition and collective modes for two-dimensional electron systems in magnetic field*, Phys. Rev. B **106**, 115415 (2022).

[106] T. Chang and T. Bridges, *Laser action at 452, 496, and 541 μm in optically pumped CH_3F*, Opt. Commun. **1**, 423–426 (1970).

[107] S. Jacobsson, *Optically pumped far infrared lasers*, Infrared Phys. **29**, 853–874 (1989).

[108] I. Mukhopadhyay and S. Singh, *Optically pumped far infrared molecular lasers: molecular and application aspects*, Spectrochimica Acta Part A: Molecular and Biomolecular Spectroscopy **54**, 395–410 (1998).

[109] Y.-S. Lee, *Principles of terahertz science and technology* (Springer US, 2009).

[110] C. K. N. Patel, *Interpretation of CO_2 optical Maser experiments*, Phys. Rev. Lett. **12**, 588–590 (1964).

[111] F. K. Kneubühl and M. W. Sigrist, *Laser* (Springer-Verlag, 2008).

[112] O. Svelto, *Principles of Lasers* (Springer, Berlin Heidelberg, 2010).

[113] E. Fermi, *Über den Ramaneffekt des Kohlendioxyds*, Zeitschrift für Physik **71**, 250–259 (1931).

[114] G. Amat and M. Pimbert, *On Fermi resonance in carbon dioxide*, J. Mol. Spectrosc. **16**, 278–290 (1965).

[115] G. Herzberg and B. L. Crawford, *Infrared and raman spectra of polyatomic molecules.* J. Phys. Chem. **50**, 288–288 (1946).

[116] T. Y. Chang, "Optical pumping in gases", in *Nonlinear Infrared Generation* (Springer Berlin Heidelberg, 1977), 215.

[117] S. Sze and M. Lee, *Semiconductor devices: Physics and technology* (Wiley-Blackwell, 2012).

[118] M. Shur, *Physics of semiconductor devices*, Prentice-Hall electrical engineering series: Series in solid state physical electronics (Prentice-Hall, 1990).

[119] S. Sze and K. K. Ng, *Physics of semiconductor devices* (Wiley, 2006).

[120] W. Shockley, *Negative resistance arising from transit time in semiconductor diodes*, Bell Syst. Tech. J. **33**, 799–826 (1954).

[121] W. T. Read, *A proposed high-frequency, negative-resistance diode*, Bell Syst. Tech. J. **37**, 401–446 (1958).

[122] R. L. Johnston, B. C. De Loach, and B. G. Cohen, *A silicon diode microwave oscillator*, Bell Syst. Tech. J. **44**, 369–372 (1965).

[123] P. Y. Yu and M. Cardona, "Electronic band structures", in *Graduate Texts in Physics* (Springer Berlin Heidelberg, 2005).

[124] T. P. Lee and R. D. Standley, *Frequency modulation of a millimeter-wave IMPATT diode oscillator and related harmonic generation effects*, Bell Syst. Tech. J. **48**, 143–161 (1969).

[125] M. Tyagi, *Introduction to semiconductor materials and devices* (Wiley India Pvt. Limited, 2008).

[126] D. Pavlidis, *Fundamentals of terahertz devices and applications* (Wiley, 2021).

[127] A. Gilmour and A. Gilmour, *Klystrons, traveling wave tubes, magnetrons, crossed-field amplifiers, and gyrotrons*, Artech House microwave library (Artech House, 2011).

[128] K. J. Botton, *Infrared and millimeter waves* (Elsevier, 1979).

[129] B. Levush, T. Antonsen, A. Bromborsky, W. Lou, D. Abe, S. Miller, Y. Carmel, J. Rodgers, V. Granatstein, and W. Destler, "Relativistic backward wave oscillators: Theory and experiment", in International Electron Devices Meeting (1991).

[130] E. Bründermann, H. Hübers, and M. Kimmitt, *Terahertz techniques*, Springer Series in Optical Sciences (Springer Berlin Heidelberg, 2012).

[131] B. Epsztein, *Backward flow travelling wave devices*, FR patent 1035379 (1951).

[132] S. J. Smith and E. M. Purcell, *Visible light from localized surface charges moving across a grating*, Phys. Rev. **92**, 1069–1069 (1953).

[133] S. S. Mitra and S. Nudelman, *Far-infrared properties of solids: Proceedings of a NATO advanced study institute* (Springer US, 1970).

[134] S. Hubmann, S. Gebert, G. V. Budkin, V. V. Bel'kov, E. L. Ivchenko, A. P. Dmitriev, S. Baumann, M. Otteneder, J. Ziegler, D. Disterheft, D. A. Kozlov, N. N. Mikhailov, S. A. Dvoretsky, Z. D. Kvon, D. Weiss, and S. D. Ganichev, *High-frequency impact ionization and nonlinearity of photocurrent induced by intense terahertz radiation in HgTe-based quantum well structures*, Phys. Rev. B **99**, 085312 (2019).

[135] S. Candussio, L. E. Golub, S. Bernreuter, T. Jötten, T. Rockinger, K. Watanabe, T. Taniguchi, J. Eroms, D. Weiss, and S. D. Ganichev, *Nonlinear intensity dependence of edge photocurrents in graphene induced by terahertz radiation*, Phys. Rev. B **104**, 155404 (2021).

[136] R. Heron, R. Lewis, R. Clark, R. Starrett, B. Kane, G. Facer, N. Lumpkin, D. Rickel, L. Pfeiffer, and K. West, *Far-infrared studies of extremely high mobility gated GaAs / AlGaAs structures in magnetic fields*, Phys. B: Condens. Matter **256–258**, 481–485 (1998).

[137] D. A. Kozlov, Z. D. Kvon, N. N. Mikhailov, S. A. Dvoretskii, and J. C. Portal, *Cyclotron resonance in a two-dimensional semimetal based on a HgTe quantum well*, JETP Letters **93**, 170–173 (2011).

[138] M. Otteneder, I. A. Dmitriev, S. Candussio, M. L. Savchenko, D. A. Kozlov, V. V. Bel'kov, Z. D. Kvon, N. N. Mikhailov, S. A. Dvoretsky, and S. D. Ganichev, *Sign-alternating photoconductivity and magnetoresistance oscillations induced by terahertz radiation in HgTe quantum wells*, Phys. Rev. B **98**, 245304 (2018).

[139] V. Lechner, L. E. Golub, P. Olbrich, S. Stachel, D. Schuh, W. Wegscheider, V. V. Bel'kov, and S. D. Ganichev, *Tuning of structure inversion asymmetry by the δ-doping position in (001)-grown GaAs quantum wells*, Appl. Phys. Lett. **94** (2009).

[140] S. Dvoretsky, N. Mikhailov, Y. Sidorov, V. Shvets, S. N. Danilov, B. Wittman, and S. D. Ganichev, *Growth of HgTe quantum wells for IR to THz detectors*, J. Electron. Mater. **39**, 918–923 (2010).

[141] S. Dvoretsky, N. Mikhailov, V. Remesnik, Y. Sidorov, V. Shvets, D. Ikusov, V. Varavin, M. Yakushev, J. Gumenjuk-Sichevska, A. Golenkov, I. Lysiuk, Z. Tsybrii, A. Shevchik-Shekera, F. Sizov, A. Latyshev, and A. Aseev, *MBE-grown MCT hetero- and nanostructures for IR and THz detectors*, Opto-Electron. Rev. **27**, 282–290 (2019).

[142] R. J. Nelson, *Long-lifetime photoconductivity effect in n-type GaAlAs*, Appl. Phys. Lett. **31**, 351–353 (1977).

[143] D. V. Lang and R. A. Logan, *Large-lattice-relaxation model for persistent photoconductivity in compound semiconductors*, Phys. Rev. Lett. **39**, 635–639 (1977).

[144] H. J. Queisser and D. E. Theodorou, *Hall-effect analysis of persistent photocurrents in n-GaAs layers*, Phys. Rev. Lett. **43**, 401–404 (1979).

[145] M. I. Nathan, *Persistent photoconductivity in AlGaAs / GaAs modulation doped layers and field effect transistors: A review*, Solid-State Electron. **29**, 167–172 (1986).

[146] P. M. Mooney, *Deep donor levels (DX centers) in III-V semiconductors*, J. Appl. Phys. **67**, R1–R26 (1990).

[147] D. G. Purdie, N. M. Pugno, T. Taniguchi, K. Watanabe, A. C. Ferrari, and A. Lombardo, *Cleaning interfaces in layered materials heterostructures*, Nat. Commun. **9** (2018).

[148] H. Ehrenreich and D. Turnbull, *Advances in research and applications: Semiconductor heterostructures and nanostructures*, Solid State Physics (Elsevier Science, 1991).

[149] S. Masubuchi, K. Iguchi, T. Yamaguchi, M. Onuki, M. Arai, K. Watanabe, T. Taniguchi, and T. Machida, *Boundary scattering in ballistic graphene*, Phys. Rev. Lett. **109**, 036601 (2012).

[150] M. A. Zudov, I. V. Ponomarev, A. L. Efros, R. R. Du, J. A. Simmons, and J. L. Reno, *New class of magnetoresistance oscillations: Interaction of a two-dimensional electron gas with leaky interface phonons*, Phys. Rev. Lett. **86**, 3614–3617 (2001).

[151] O. E. Raichev, *Theory of acoustic-phonon assisted magnetotransport in two-dimensional electron systems at large filling factors*, Phys. Rev. B **80**, 075318 (2009).

[152] P. Kumaravadivel, M. T. Greenaway, D. Perello, A. Berdyugin, J. Birkbeck, J. Wengraf, S. Liu, J. H. Edgar, A. K. Geim, L. Eaves, and R. Krishna Kumar, *Strong magnetophonon oscillations in extra-large graphene*, Nat. Commun. **10** (2019).

[153] W. Zhang, M. A. Zudov, L. N. Pfeiffer, and K. W. West, *Resonant phonon scattering in quantum Hall systems driven by dc electric fields*, Phys. Rev. Lett. **100**, 036805 (2008).

[154] I. A. Dmitriev, R. Gellmann, and M. G. Vavilov, *Phonon-induced resistance oscillations of two-dimensional electron systems drifting with supersonic velocities*, Phys. Rev. B **82**, 201311(R) (2010).

[155] T. Kennedy, R. Wagner, B. McCombe, and J. Quinn, *Lineshape distortions in FIR cyclotron resonance of MOS structures*, Solid State Commun. **18**, 275–278 (1976).

[156] M. J. Chou, D. C. Tsui, and G. Weimann, *Cyclotron resonance of high-mobility two-dimensional electrons at extremely low densities*, Phys. Rev. B **37**, 848–854 (1988).

[157] M. L. Savchenko, A. Shuvaev, I. A. Dmitriev, A. A. Bykov, A. K. Bakarov, Z. D. Kvon, and A. Pimenov, *High harmonics of the cyclotron resonance in microwave transmission of a high-mobility two-dimensional electron system*, Phys. Rev. Research **3**, L012013 (2021).

[158] C. Chase, E. Maxwell, and W. Millett, *The dielectric constant of liquid helium*, Physica **27**, 1129–1145 (1961).

[159] J. E. Jensen, W. A. Tuttle, R. B. Stewart, H Brechna, and A. G. Prodell, *Brookhaven national laboratory selected cryogenic data notebook: Volume 1, Sections 1-9*, (1980).

[160] T. Ando, A. B. Fowler, and F. Stern, *Electronic properties of two-dimensional systems*, Rev. Modern Phys. **54**, 437–672 (1982).

[161] D. Shoenberg, *Magnetic oscillations in metals* (Cambridge University Press, 1984).

[162] Z. Tan, C. Tan, L. Ma, G. T. Liu, L. Lu, and C. L. Yang, *Shubnikov–de Haas oscillations of a single layer graphene under dc current bias*, Phys. Rev. B **84**, 115429 (2011).

[163] M. Koshino and T. Ando, *Quantum Hall effect in graphene*, Internat. J. Modern Phys. B **21**, 1140–1144 (2007).

[164] X. Fu, Q. A. Ebner, Q. Shi, M. A. Zudov, Q. Qian, J. D. Watson, and M. J. Manfra, *Microwave-induced resistance oscillations in a back-gated GaAs quantum well*, Phys. Rev. B **95**, 235415 (2017).

[165] D. Tabrea, I. A. Dmitriev, S. I. Dorozhkin, B. P. Gorshunov, A. V. Boris, Y. Kozuka, A. Tsukazaki, M. Kawasaki, K. von Klitzing, and J. Falson, *Microwave response of interacting oxide two-dimensional electron systems*, Phys. Rev. B **102**, 115432 (2020).

[166] I. V. Andreev, V. M. Muravev, V. N. Belyanin, and I. V. Kukushkin, *Measurement of cyclotron resonance relaxation time in the two-dimensional electron system*, Appl. Phys. Lett. **105** (2014).

[167] P. Alonso-González, A. Y. Nikitin, F. Golmar, A. Centeno, A. Pesquera, S. Vélez, J. Chen, G. Navickaite, F. Koppens, A. Zurutuza, F. Casanova, L. E. Hueso, and R. Hillenbrand, *Controlling graphene plasmons with resonant metal antennas and spatial conductivity patterns*, Science **344**, 1369–1373 (2014).

[168] B. Horn-Cosfeld, M. Cerchez, T. Heinzel, L. Freise, K. Pierz, and H. W. Schumacher, *Generation of phonon-induced resistance oscillations by terahertz radiation*, Phys. Rev. B **100**, 245407 (2019).

[169] P. Alekseev and A. Alekseeva, *Transverse magnetosonic waves and viscoelastic resonance in a two-dimensional highly viscous electron fluid*, Phys. Rev. Lett. **123**, 236801 (2019).

[170] Y. Dai, R. R. Du, L. N. Pfeiffer, and K. W. West, *Observation of a cyclotron harmonic spike in microwave-induced resistances in ultraclean GaAs / AlGaAs quantum wells*, Phys. Rev. Lett. **105**, 246802 (2010).

[171] A. I. Berdyugin, S. G. Xu, F. M. D. Pellegrino, R. Krishna Kumar, A. Principi, I. Torre, M. Ben Shalom, T. Taniguchi, K. Watanabe, I. V. Grigorieva, M. Polini, A. K. Geim, and D. A. Bandurin, *Measuring Hall viscosity of graphene's electron fluid*, Science **364**, 162–165 (2019).

[172] V. A. Volkov and A. A. Zabolotnykh, *Bernstein modes and giant microwave response of a two-dimensional electron system*, Phys. Rev. B **89**, 121410(R) (2014).

[173] P. Olbrich, J. Kamann, M. König, J. Munzert, L. Tutsch, J. Eroms, D. Weiss, M.-H. Liu, L. E. Golub, E. L. Ivchenko, V. V. Popov, D. V. Fateev, K. V. Mashinsky, F. Fromm, T. Seyller, and S. D. Ganichev, *Terahertz ratchet effects in graphene with a lateral superlattice*, Phys. Rev. B **93**, 075422 (2016).

[174] S. Hubmann, V. V. Bel'kov, L. E. Golub, V. Y. Kachorovskii, M. Drienovsky, J. Eroms, D. Weiss, and S. D. Ganichev, *Giant ratchet magneto-photocurrent in graphene lateral superlattices*, Phys. Rev. Research **2**, 033186 (2020).

[175] V. Ryzhii, A. Chaplik, and R. Suris, *Absolute negative conductivity and zero-resistance states in two-dimensional electron systems: A plausible scenario*, J. of Exp. Theo. Phys. Lett. **80**, 363–366 (2004).

[176] A. T. Hatke, M. A. Zudov, L. N. Pfeiffer, and K. W. West, *Temperature dependence of microwave photoresistance in 2D electron systems*, Phys. Rev. Lett. **102**, 066804 (2009).

[177] T. Ando, *Theory of cyclotron resonance lineshape in a two-dimensional electron system*, J. Phys. Soc. Japan **38**, 989–997 (1975).

[178] I. A. Dmitriev, A. D. Mirlin, and D. G. Polyakov, *Cyclotron-resonance harmonics in the ac response of a 2D electron gas with smooth disorder*, Phys. Rev. Lett. **91**, 226802 (2003).

[179] V. I. Ryzhii, *Photoconductivity characteristics in thin filmssubjected to crossed electric and magnetic fields*, Sov. Phys. Solid State **11**, 2078 (1970).

[180] V. I. Ryzhii, *Photoconductivity of a two-dimensional electron gas in a strong magnetic field*, Sov. Phys. Semicond. **20**, 1299 (1986).

[181] A. C. Durst, S. Sachdev, N. Read, and S. M. Girvin, *Radiation-induced magnetoresistance oscillations in a 2D electron gas*, Phys. Rev. Lett. **91** (2003).

[182] M. G. Vavilov and I. L. Aleiner, *Magnetotransport in a two-dimensional electron gas at large filling factors*, Phys. Rev. B **69** (2004).

[183] M. Khodas and M. G. Vavilov, *Effect of microwave radiation on the nonlinear resistivity of a two-dimensional electron gas at large filling factors*, Phys. Rev. B **78** (2008).

[184] I. A. Dmitriev, M. G. Vavilov, I. L. Aleiner, A. D. Mirlin, and D. G. Polyakov, *Theory of microwave-induced oscillations in the magnetoconductivity of a two-dimensional electron gas*, Phys. Rev. B **71**, 115316 (2005).

[185] I. A. Dmitriev, S. I. Dorozhkin, and A. D. Mirlin, *Theory of microwave-induced photocurrent and photovoltage magneto-oscillations in a spatially nonuniform two-dimensional electron gas*, Phys. Rev. B **80**, 125418 (2009).

[186] I. A. Dmitriev, M. Khodas, A. D. Mirlin, D. G. Polyakov, and M. G. Vavilov, *Mechanisms of the microwave photoconductivity in two-dimensional electron systems with mixed disorder*, Phys. Rev. B **80**, 165327 (2009).

[187] R. L. Willett, L. N. Pfeiffer, and K. W. West, *Evidence for current-flow anomalies in the irradiated 2D electron system at small magnetic fields*, Phys. Rev. Lett. **93**, 026804 (2004).

[188] A. A. Bykov, *Microwave-induced magnetic field oscillations of the electromotive force in a two-dimensional Corbino disk at large filling factors*, JETP Lett. **87**, 233–237 (2008).

[189] S. I. Dorozhkin, I. V. Pechenezhskiy, L. N. Pfeiffer, K. W. West, V. Umansky, K. von Klitzing, and J. H. Smet, *Photocurrent and photovoltage oscillations in the two-dimensional electron system: Enhancement and suppression of built-in electric fields*, Phys. Rev. Lett. **102**, 036602 (2009).

[190] S. I. Dorozhkin, I. A. Dmitriev, and A. D. Mirlin, *Negative conductivity and anomalous screening in two-dimensional electron systems subjected to microwave radiation*, Phys. Rev. B **84**, 125448 (2011).

[191] Q. Shi, M. A. Zudov, I. A. Dmitriev, K. Baldwin, L. Pfeiffer, and K. West, *Fine structure of high-power microwave-induced resistance oscillations*, Phys. Rev. B **95**, 041403(R) (2017).

[192] M. A. Zudov, *Period and phase of microwave-induced resistance oscillations and zero-resistance states in two-dimensional electron systems*, Phys. Rev. B **69**, 041304(R) (2004).

[193] S. A. Studenikin, M. Potemski, A. Sachrajda, M. Hilke, L. N. Pfeiffer, and K. W. West, *Microwave-induced resistance oscillations on a high-mobility two-dimensional electron gas: Exact waveform, absorption/reflection and temperature damping*, Phys. Rev. B **71**, 245313 (2005).

[194] Y. Zeng, J. Li, S. Dietrich, O. Ghosh, K. Watanabe, T. Taniguchi, J. Hone, and C. Dean, *High-quality magnetotransport in graphene using the edge-free corbino geometry*, Phys. Rev. Lett. **122**, 137701 (2019).

[195] S. Studenikin, M. Byszewski, D. Maude, M. Potemski, A. Sachrajda, Z. Wasilewski, M. Hilke, L. Pfeiffer, and K. West, *The microwave induced resistance response of a high mobility 2DEG from the quasi-classical limit to the quantum Hall regime*, Phys. E: Low-Dimens. Syst. Nanostructures **34**, 73–76 (2006).

[196] S. A. Studenikin, A. S. Sachrajda, J. A. Gupta, Z. R. Wasilewski, O. M. Fedorych, M. Byszewski, D. K. Maude, M. Potemski, M. Hilke, K. W. West, and L. N. Pfeiffer, *Frequency quenching of microwave-induced resistance oscillations in a high-mobility two-dimensional electron gas*, Phys. Rev. B **76**, 165321 (2007).

[197] R. Krishna Kumar, D. A. Bandurin, F. M. D. Pellegrino, Y. Cao, A. Principi, H. Guo, G. Auton, M. Ben Shalom, L. A. Ponomarenko, G. Falkovich, K. Watanabe, T. Taniguchi, I. Grigorieva, L. S. Levitov, M. Polini, and A. Geim, *Superballistic flow of viscous electron fluid through graphene constrictions*, Nat. Phys. **13**, 1182–1185 (2017).

[198] N. C. Mamani, G. M. Gusev, T. E. Lamas, A. K. Bakarov, and O. E. Raichev, *Resonance oscillations of magnetoresistance in double quantum wells*, Phys. Rev. B **77**, 205327 (2008).

[199] A. V. Chaplik, *Energy spectrum and electron scatteringprocesses in inversion layers*, Sov. Phys. JETP **33**, 997 (1971).

[200] G. F. Giuliani and J. J. Quinn, *Lifetime of a quasiparticle in a two-dimensional electron gas*, Phys. Rev. B **26**, 4421–4428 (1982).

[201] M. Polini and G. Vignale, *The quasiparticle lifetime in a doped graphene sheet*, In No-nonsense physicist: An overview of Gabriele Giuliani's work and life; edizioni della normale ed.; quaderni selections; Polini, M., Vignale, G., Pellegrini, V., Jain, J. K., Eds. **2**, 107 (2016).

[202] A. Principi, G. Vignale, M. Carrega, and M. Polini, *Bulk and shear viscosities of the two-dimensional electron liquid in a doped graphene sheet*, Phys. Rev. B **93**, 125410 (2016).

[203] I. Dmitriev, M. Vavilov, I. Aleiner, A. Mirlin, and D. Polyakov, *Theory of the oscillatory photoconductivity of a two-dimensional electron system*, Phys. E: Low-Dimens. Syst. Nanostructures **25**, 205–211 (2004).

[204] S. Dorozhkin, A. Kapustin, V. Umansky, K. von Klitzing, and J. Smet, *Microwave-induced oscillations in magnetocapacitance: Direct evidence for nonequilibrium occupation of electronic states*, Phys. Rev. Lett. **117**, 176801 (2016).

[205] S. Wiedmann, G. M. Gusev, O. E. Raichev, A. K. Bakarov, and J. C. Portal, *Crossover between distinct mechanisms of microwave photoresistance in bilayer systems*, Phys. Rev. B **81**, 085311 (2010).

[206] A. T. Hatke, M. A. Zudov, L. N. Pfeiffer, and K. W. West, *Giant microwave photoresistivity in high-mobility quantum Hall systems*, Phys. Rev. B **83**, 121301(R) (2011).

[207] R. G. Mani, V. Narayanamurti, K. von Klitzing, J. H. Smet, W. B. Johnson, and V. Umansky, *Radiation-induced zero-resistance states in GaAs / AlGaAs heterostructures: Voltage-current characteristics and intensity dependence at the resistance minima*, Phys. Rev. B **70**, 155310 (2004).

[208] S. Studenikin, M. Potemski, P. Coleridge, A. Sachrajda, and Z. Wasilewski, *Microwave radiation induced magneto-oscillations in the longitudinal and transverse resistance of a two-dimensional electron gas*, Solid State Commun. **129**, 341–345 (2004).

[209] R. G. Mani, C. Gerl, S. Schmult, W. Wegscheider, and V. Umansky, *Nonlinear growth in the amplitude of radiation-induced magnetoresistance oscillations*, Phys. Rev. B **81**, 125320 (2010).

[210] S. Hubmann, P. Soul, G. Di Battista, M. Hild, K. Watanabe, T. Taniguchi, D. K. Efetov, and S. D. Ganichev, *Nonlinear intensity dependence of photogalvanics and photoconductance induced by terahertz laser radiation in twisted bilayer graphene close to magic angle*, Phys. Rev. Materials **6**, 024003 (2022).

[211] M. Helm, E. Gornik, A. Black, G. Allan, C. Pidgeon, K. Mitchell, and G. Weimann, *Hot electron Landau level lifetime in GaAs / GaAlAs heterostructures*, Physica B+C **134**, 323–326 (1985).

[212] G. A. Rodríguez, R. M. Hart, A. J. Sievers, F. Keilmann, Z. Schlesinger, S. L. Wright, and W. I. Wang, *Intensity-dependent cyclotron resonance in a GaAs / GaAlAs two-dimensional electron gas*, Appl. Phys. Lett. **49**, 458–460 (1986).

[213] Z. Mics, K.-J. Tielrooij, K. Parvez, S. A. Jensen, I. Ivanov, X. Feng, K. Müllen, M. Bonn, and D. Turchinovich, *Thermodynamic picture of ultrafast charge transport in graphene*, Nat. Commun. **6** (2015).

[214] E. V. Beregulin, S. D. Ganichev, K. Y. Glukh, G. M. Gusev, Z. D. Kvon, A. Y. Shik, and I. D. Yaroshetskii, *Submillimeter photoconductivity in inversion layers at a silicon surface*, Sov. Phys. JETP **48**, 247 (1988).

[215] E. V. Beregulin, S. D. Ganichev, K. Y. Glukh, G. M. Gusev, Z. D. Kvon, A. Y. Shik, and I. D. Yaroshetskii, *Rapid submillimeter photoconductivity and energy relaxation of a two-dimensional electron gas near the surface of silicon*, Sov. Phys. JETP **70**, 1138 (1990).

[216] E. M. Baskin, L. N. Magarill, and M. V. Entin, *Two-dimensional electron-impurity system in a strongmagnetic field*, Sov. Phys. JETP **48**, 365 (1978).

[217] A. V. Bobylev, F. A. Maaø, A. Hansen, and E. H. Hauge, *Two-dimensional magnetotransport according to the classical Lorentz model*, Phys. Rev. Lett. **75**, 197–200 (1995).

[218] A. D. Mirlin, D. G. Polyakov, F. Evers, and P. Wölfle, *Quasiclassical negative magnetoresistance of a 2D electron gas: Interplay of strong scatterers and smooth disorder*, Phys. Rev. Lett. **87**, 126805 (2001).

[219] D. G. Polyakov, F. Evers, and I. V. Gornyi, *Cyclotron resonance in antidot arrays*, Phys. Rev. B **65**, 125326 (2002).

[220] I. A. Dmitriev, A. D. Mirlin, and D. G. Polyakov, *Oscillatory ac conductivity and photoconductivity of a two-dimensional electron gas: Quasiclassical transport beyond the Boltzmann equation*, Phys. Rev. B **70**, 165305 (2004).

[221] Y. Beltukov and M. Dyakonov, *Microwave-induced resistance oscillations as a classical memory effect*, Phys. Rev. Lett. **116**, 176801 (2016).

[222] S. Dorozhkin, A. Kapustin, I. Dmitriev, V. Umansky, K. von Klitzing, and J. H. Smet, *Evidence for non-Markovian electron dynamics in the microwave absorption of a two-dimensional electron system*, Phys. Rev. B **96**, 155306 (2017).

[223] A. D. Chepelianskii and D. L. Shepelyansky, *Floquet theory of microwave absorption by an impurity in the two-dimensional electron gas*, Phys. Rev. B **97**, 125415 (2018).

[224] C. Girard and A. Dereux, *Near-field optics theories*, Rep. Progr. Phys. **59**, 657–699 (1996).

[225] F. Keilmann and R. Hillenbrand, *Near-field microscopy by elastic light scattering from a tip*, Philosophical Transactions of the Royal Society of London. Series A: Mathematical, Physical and Engineering Sciences **362**, edited by D. Richards and A. Zayats, 787–805 (2004).

[226] O. Keller, *Quantum theory of near-field electrodynamics*, Nano-Optics and Nanophotonics (Springer Berlin Heidelberg, 2012).

Acknowledgements

Completing this dissertation has been a journey of challenge and growth, and I am deeply grateful to the people whose support and guidance made this achievement possible.

First and foremost, I would like to express my heartfelt gratitude to Sergey, whose tireless support, insightful feedback, and scientific guidance have been immeasurable throughout my research journey and have broadened my academic horizon.

Special thanks also goes to Vanya, who provided theoretical support in many joint publications, answered my questions in countless lengthy discussions, devoted time to proofreading the manuscript, and shared many valuable suggestions.

In addition, I would like to thank the countless co-authors, especially Sergey Danilov, Leonid, Jonathan, Vasily, and Maxim for sharing their knowledge and ideas with me in many fruitful discussions, and especially Leonid and Vasily for proofreading the manuscript. I would like to thank Denis and Marina for providing excellent graphene samples. Especially Denis I would also like to thank for his interesting insights, inspiring discussions and the great time we spent together in the lab.

My appreciation also goes to the growth teams of Dominique Bougeard's group as well as the Rzhanov Institute, namely Nikolai Mikhailov, Sergey Dvoretsky, and all those involved in the growth process, for providing us with high quality AlGaAs/GaAs and HgCdTe/HgTe wafers. Special thanks to Imke for preparing and cutting the wafers and for establishing excellent contacts.

Furthermore, I would like to thank the whole working group Christian, Ivan, Marcel, Sophia, Isabella and Sebastian as well as the alumni Stefan, Max and Susi for a great and funny time, countless parties with and without occasion and for motivating me in tough times. I would also like to thank Marcel, Isabella, Sophia and Ivan for spending countless hours proofreading the manuscript and for their valuable suggestions and comments.

I would also like to thank my former bachelor and master students Katja, Philipp, Georg, Maxi and Sophia for a wonderful and funny time and for their great support in the lab. I hope I was able to teach you at least as much as you taught me.

Finally, I would like to express my heartfelt thankfulness to my family, especially my parents and my sister Vally, for their endless love, encouragement, and understanding. Their constant support and belief in my abilities, as well as their sacrifices, have been my source of strength throughout this academic journey. I will never be able to thank them enough.

Finally, I would like to thank my friends during my studies for the wonderful years and all those unnamed people who have supported and inspired me in various ways.

Thank You Very Much!

Appendices

The following figures illustrate further results and analysis of additional measurements that complement and support the data presented and discussed in the main text. For convenience, the figure sets are organized into subsections.

A SdHO-periodic Oscillations in the Photoresistance

An analysis of the SdHO-periodic oscillations in the photoresistance is presented. Fig. A.1 shows a representative example of the data for GaAs #A obtained at a frequency of $f = 0.297$ THz plotted against the absolute value of the inverse magnetic field $1/|B|$. Panels (a – d) correspond to the left-handed (σ^-), and panels (e – h) to the right-handed (σ^+) radiation helicity. The inverse magnetic field values are rescaled to the period of the oscillations at $T = 1.8$ K for clarity. It is clearly seen that the photoresistance oscillations are indeed $1/B$-periodic and feature the same period over the whole temperature range, as indicated by the equidistant gray book lines. This behavior is further supported by Fig. A.2, where the inverse magnetic field positions of the oscillation extrema are plotted as a function of the filling factor ν of the LLs for the σ^- helicity and corresponding temperatures. The positions follow a straight line through the origin given by $1/|B_\nu| = 2\pi\hbar n_e/e\nu$. Since the oscillations in the photoresistance arise from the reduction in oscillation amplitude caused by electron gas heating, they have maxima (minima) at even (odd) LL filling factors, in contrast to SdHO in the dark magnetotransport, which have minima (maxima) at even (odd) filling factors. This and the periodicity clearly confirm that the photoresistance oscillations are related to the SdHO in conventional magnetoresistance. A similar behavior is observed for all samples, including GaAs and HgTe QWs as well as graphene, under conditions where the SdHO-related heating mechanism dominates.

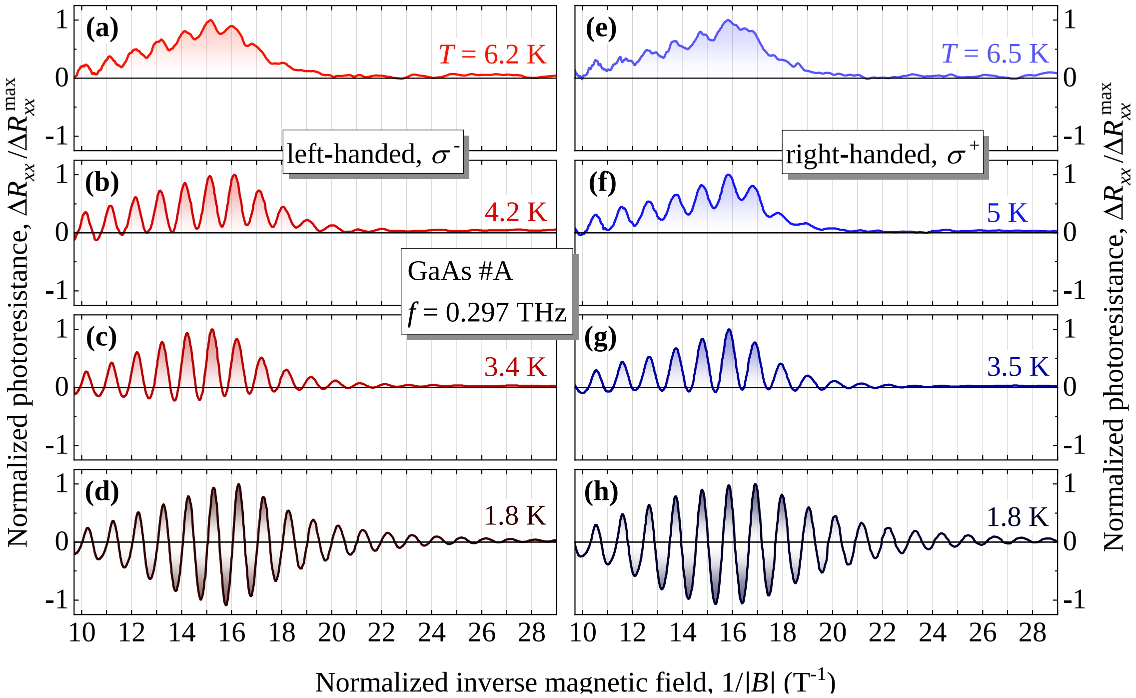

Figure A.1: **(a − d)** Normalized photoresistance obtained for GaAs #A, f = 0.297 THz and left-handed (σ^-) helicity plotted against the absolute value of the inverse magnetic field. The traces are shown for different temperatures indicated next to the corresponding curve. **(e − h)** Similar plot of photoresistance traces measured at right-handed (σ^+) helicity. For a clearer illustration of the $1/B$-periodicity, the inverse magnetic field scale has been multiplied for each temperature by a fixed difference of one period of the photoresistance oscillations at T = 1.8 K. Figure adapted from Ref. [47] and supplemental material therein.

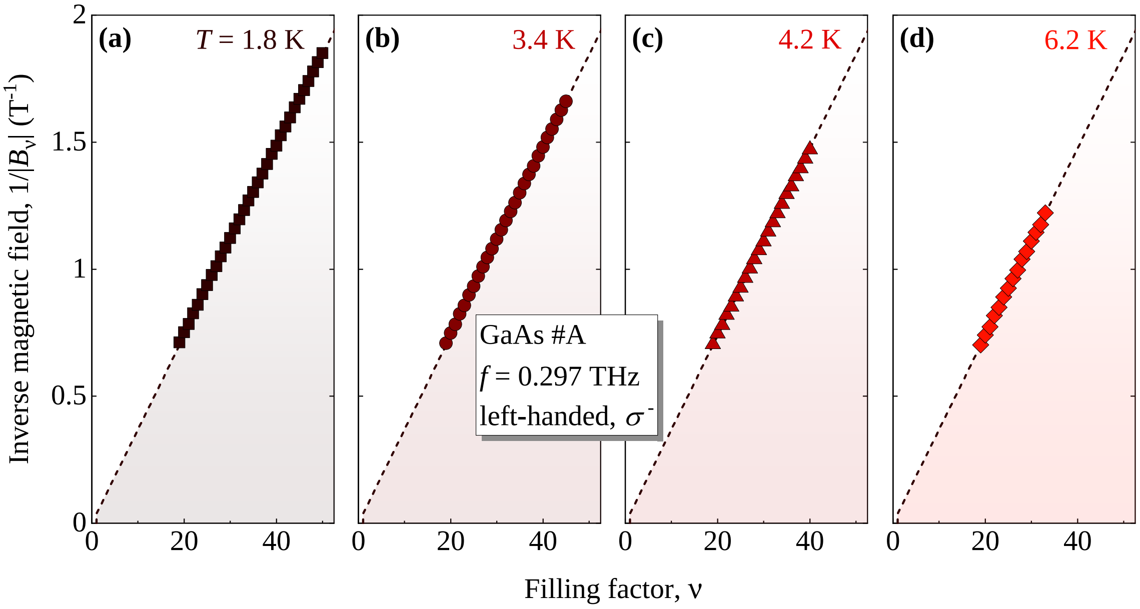

Figure A.2: **(a – d)** The inverse magnetic field positions of the oscillation extrema of the photoresistance shown in Figs. A.1(a – d) as a function of the filling factor of the LL. The panels present the data for different temperatures $T = 1.8, 3.4, 4.2$ and 6.2 K. The dashed lines denote the calculated relation according to $1/B_\nu = 2\pi\hbar n_e/e\nu$. Figure adapted from Ref. [47] and supplemental material therein.

B Temperature Dependencies of Transmittance & Photoresistance

A set of transmittance curves for different temperatures is presented in Fig. B.1 in response to $f = 0.297$ THz for σ^- [panel (a)] and σ^+ [panel (b)] radiation helicities. The power was set to $P = 10$ mW. It is evident that the shape of the CR dip changes slightly with temperature. Figures B.2 and B.3 show the temperature dependencies at $f = 0.69$ and 1.63 THz, respectively, for both radiation helicities obtained in GaAs #A and at the highest available power levels. In addition, Figs. B.4 and B.5 illustrate similar data sets recorded in GaAs #B. The overall behavior, including the significant increase in the amplitude ratio, supports the results shown in Fig. 8.2 of the main text. As an example, this is illustrated quantitatively in Fig. B.6 for GaAs #A and both frequencies in an analog manner as presented in Fig. 8.4.

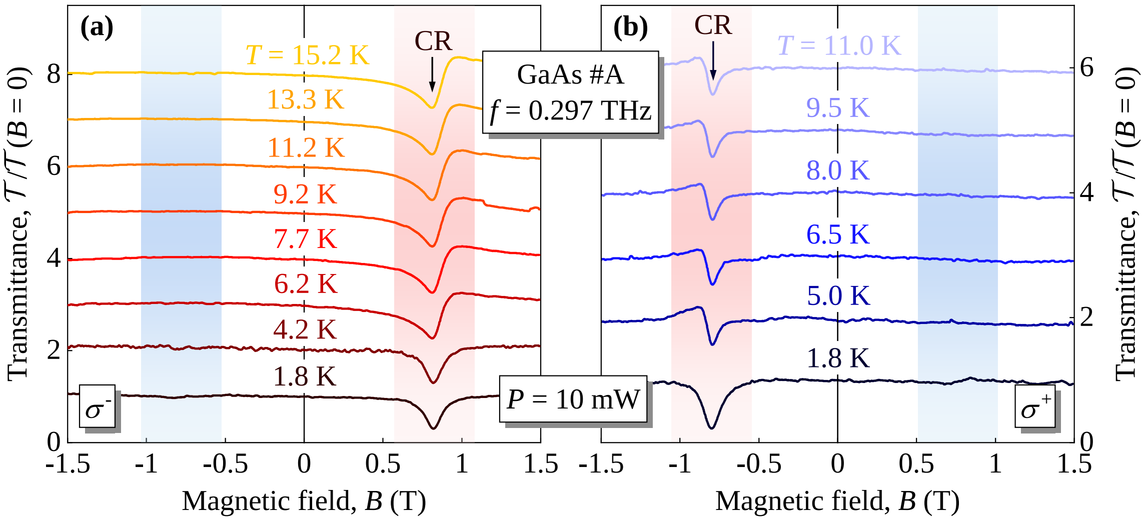

Figure B.1: **(a)** Radiation transmittance $\mathcal{T}/\mathcal{T}(B=0)$ for different temperatures, normalized to its value at $B = 0$. The set of curves was obtained under left-handed (σ^-) circular polarization. **(b)** Transmittance measured in response to right-handed (σ^+) circularly polarized radiation. The vertical arrows mark the position of the CR, and the red and blue shaded magnetic-field regions indicate the vicinity of the CRA and CRI sides. All traces were obtained in GaAs #A, $f = 0.297$ THz and $P = 10$ mW. Figure adapted from Ref. [48] and supplemental material therein.

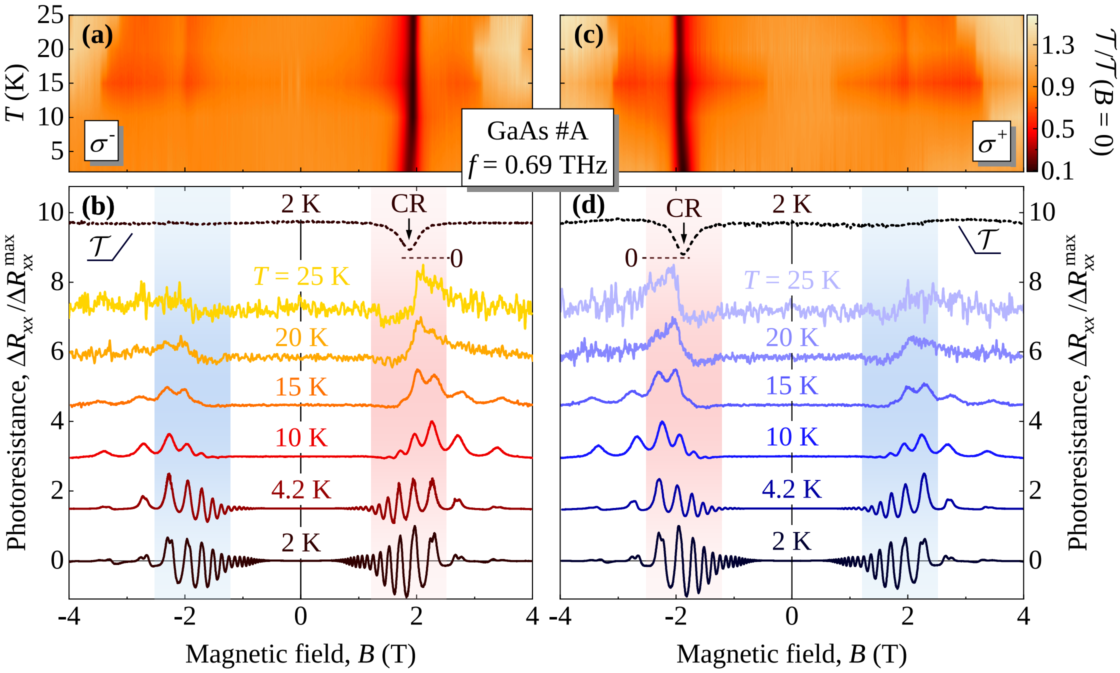

Figure B.2: **(a, c)** Temperature-contour maps of the normalized transmittance $\mathcal{T}/\mathcal{T}(B=0)$ traces measured at a frequency of $f = 0.69$ THz for left-handed (σ^-) [panel (a)] and right-handed (σ^+) [panel (c)] circularly polarized radiation. **(b, d)** Corresponding temperature dependencies of the photoresistance ΔR_{xx} for both radiation helicities. The photoresistance curves were normalized to their maximum value $\Delta R_{xx}^{\max}$. The traces are up-shifted for clarity. The dashed curve denotes the transmittance for $T = 2$ K, where zero transmittance is marked by a dashed horizontal line near the CR dip. The vertical arrow marks the position of the CR, and the red and blue shaded magnetic-field regions indicate the vicinity of the CRA and CRI sides. All results were performed in GaAs #A using the maximum available radiation power $P \approx 10$ mW at the sample. Figure adapted from Ref. [47].

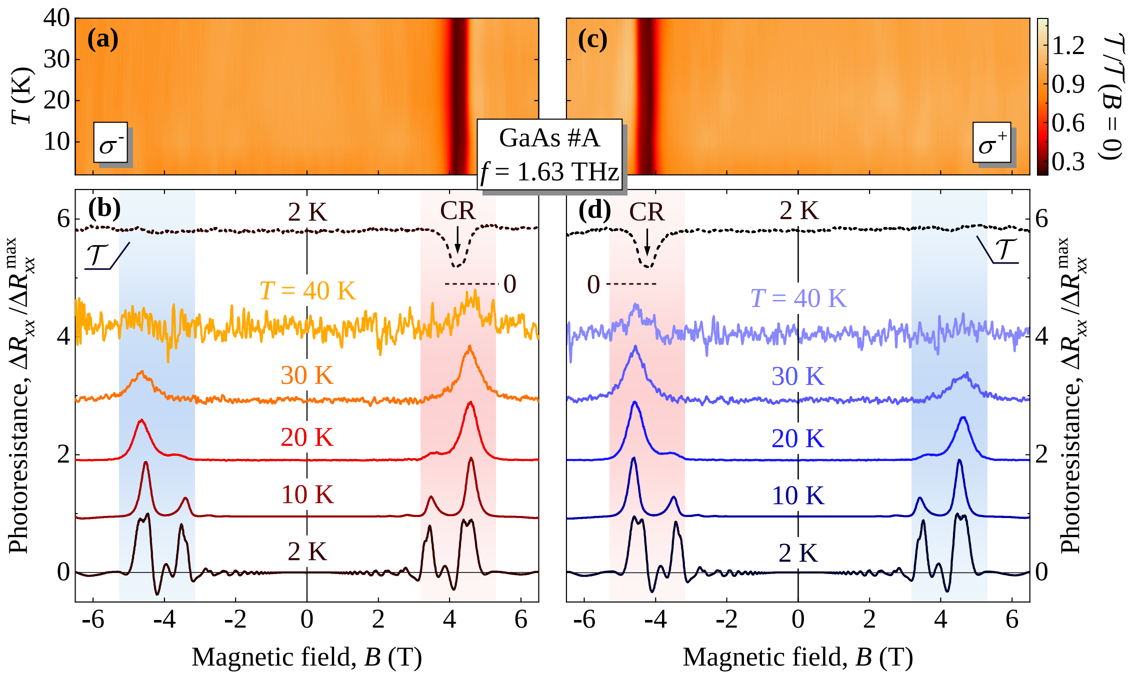

Figure B.3: **(a, c)** Temperature-contour maps of the normalized transmittance curves measured at a frequency of $f = 1.63$ THz for left-handed (σ^-) [panel (a)] and right-handed (σ^+) [panel (c)] circularly polarized radiation. **(b, d)** Corresponding temperature dependencies of the normalized photoresistance for both radiation helicities. The traces are up-shifted for clarity. The dashed trace represents the transmittance for $T = 2$ K, where zero transmittance is marked by a dashed horizontal line near the CR dip. The vertical arrow marks the position of the CR, and the red and blue shaded magnetic-field regions indicate the vicinity of the CRA and CRI sides. All results were obtained in GaAs #A using the highest possible power of $P \approx 40$ mW at the sample. Figure adapted from Ref. [47].

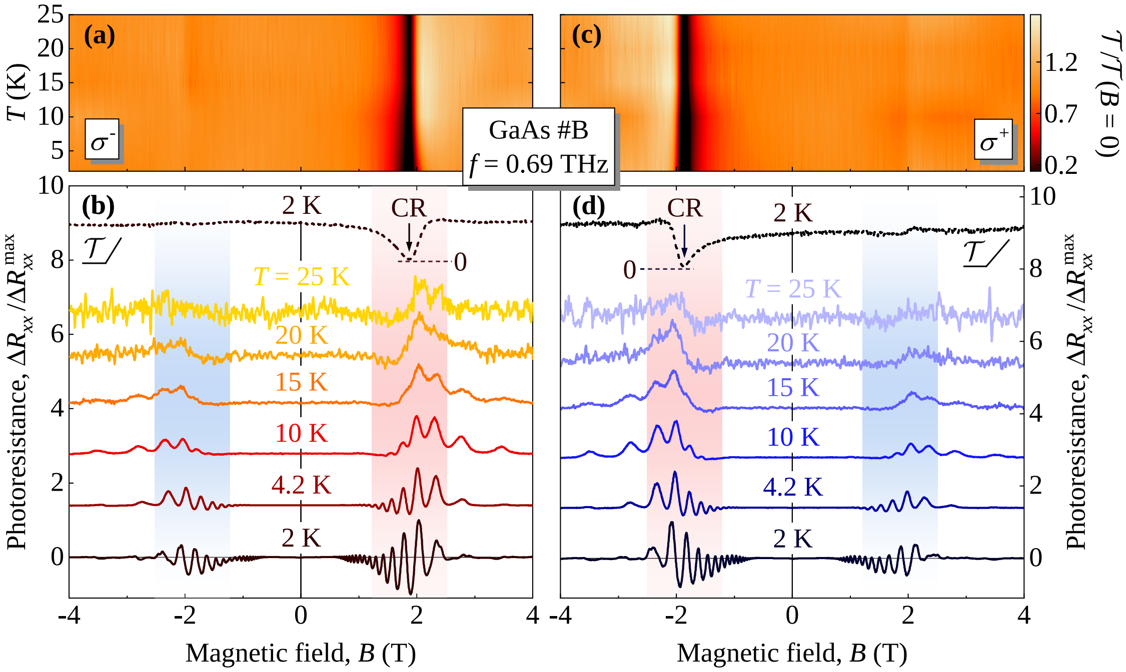

Figure B.4: **(a, c)** Temperature-contour maps of the normalized transmittance traces measured at a frequency of $f = 0.69$ THz for left-handed (σ^-) [panel (a)] and right-handed (σ^+) [panel (c)] circularly polarized radiation. **(b, d)** Corresponding temperature dependencies of the normalized photoresistance for both radiation helicities. The traces are up-shifted for clarity. The dashed trace denotes the transmittance for $T = 2$ K, where zero transmittance is marked by a dashed horizontal line near the CR dip. The vertical arrow marks the position of the CR, and the red and blue shaded magnetic-field regions indicate the vicinity of the CRA and CRI sides. All traces were obtained in GaAs #B using the highest possible power of $P \approx 10$ mW at the sample. Figure adapted from Ref. [47] and supplemental material therein.

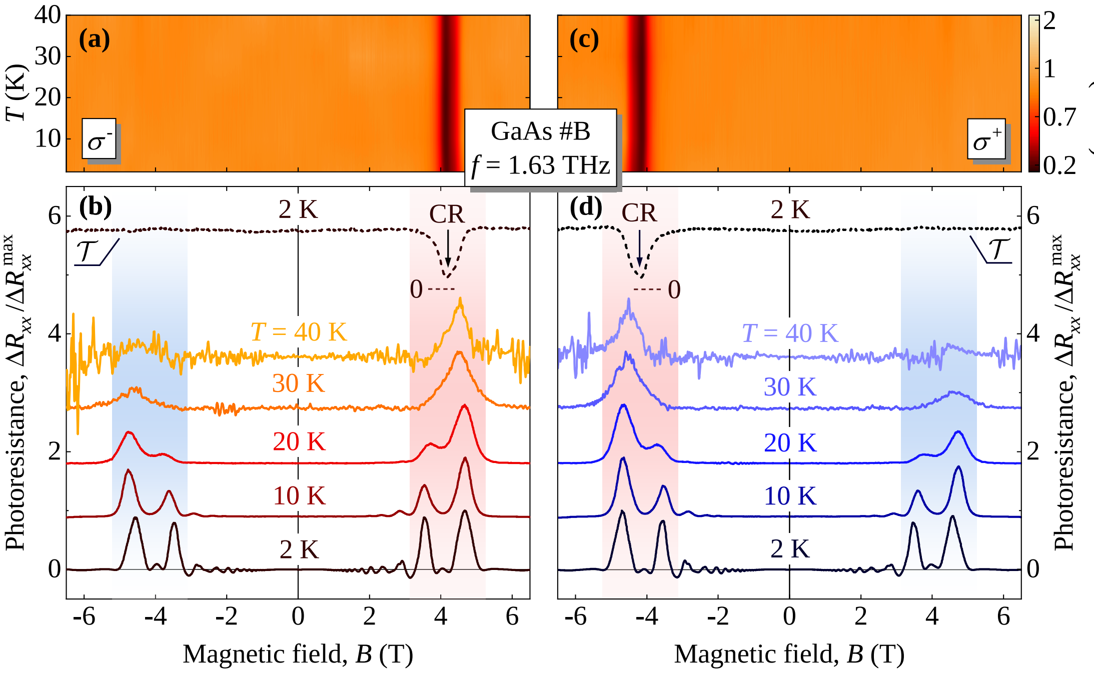

Figure B.5: (a, c) Temperature-contour maps of the normalized transmittance traces measured at a frequency of $f = 1.63$ THz for left-handed (σ^-) [panel (a)] and right-handed (σ^+) [panel (c)] circularly polarized radiation. **(b, d)** Corresponding temperature dependencies of the normalized photoresistance for both radiation helicities. The traces are up-shifted for clarity. The dashed trace represents the transmittance for $T = 2$ K, where zero transmittance is marked by a dashed horizontal line near the CR dip. The vertical arrow marks the position of the CR, and the red and blue shaded magnetic-field regions indicate the vicinity of the CRA and CRI sides. All traces were obtained in GaAs #B using the highest possible power of $P \approx 40$ mWat the sample. Figure adapted from Ref. [47] and supplemental material therein.

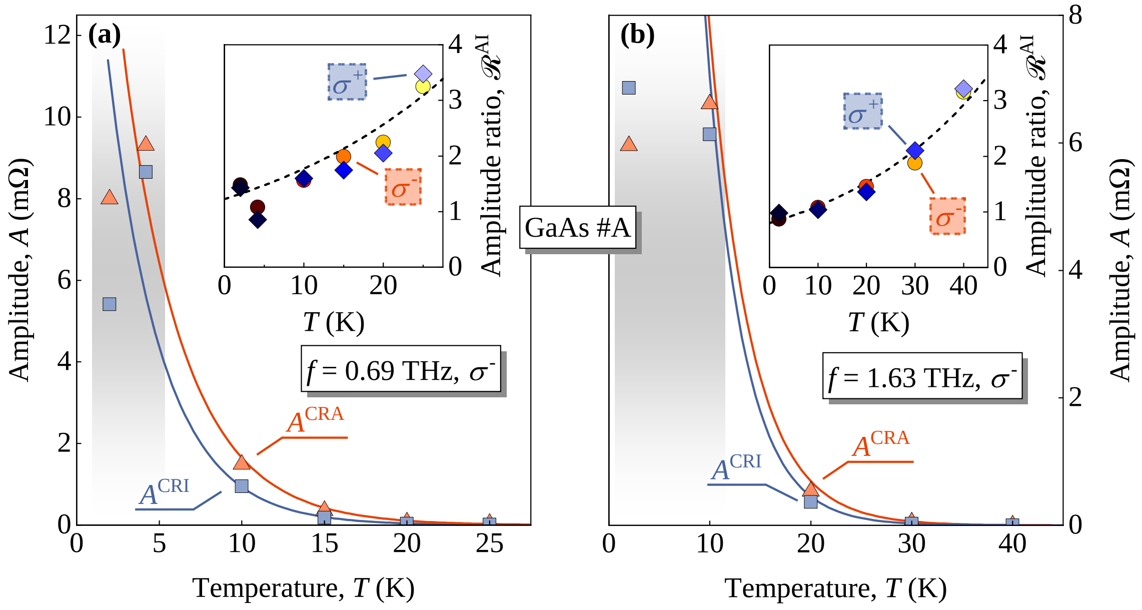

Figure B.6: (a) Temperature dependencies of the CRA and CRI amplitudes recorded in response to $f = 0.69$ THz and σ^- configuration, referring to the traces shown in Fig. B.2. The values were determined using the estimation procedure presented in Figs. 8.4(a, b). The solid colored lines are guides for the eyes following an exponential decay. The inset shows the amplitude ratios $\mathscr{R}^{\mathrm{AI}}$ calculated for both helicities. The dashed curve follows the ratio of the guidelines in the main panel. **(b)** Analogous plot to panel (a) but for the traces obtained at $f = 1.63$ THz shown in Fig. B.3. Gray shaded areas in all panels indicate the region where the SdHO-periodic oscillations dominate the photosignal. All results were obtained in GaAs #A and recorded at the highest power available at the corresponding frequency. Figure adapted from Ref. [47] and supplemental material therein.

C Power Dependencies of Transmittance & Photoresistance

Figure C.1 shows the power dependence for $f = 0.297$ THz measured in GaAs #A at $T = 1.8$ K. The data set is the σ^+ counterpart of the results shown in Fig. 8.5 in the main text. The growth of the amplitude ratio as well as the nonlinearity of the CRA photoresistance in the vicinity of the CR is accurately reproduced. This behavior is complemented by data measured at a higher frequency ($f = 0.69$ THz). The individual traces are shown in Fig. C.2, the power evolution of the shape of the photoresistance curves and the corresponding amplitude analysis are presented in Figs. C.3 and C.4, respectively. Figures C.5 and C.6 show additional power dependencies obtained at higher temperatures in the range $T = 4.2 - 10$ K. Already at $T = 4.2$ K the amplitude ratio exhibits no significant change with power reduction. For comparison, see Fig. 8.6 in the main text, where the amplitude ratios for different measurement temperatures are plotted as a function of radiation power. This constant ratio is a consequence of the absence of nonlinearity in the photoresponse. Figure C.7 supports this statement by comparing the photoresistance curves for the CRA and CRI regimes normalized to their respective radiation powers.

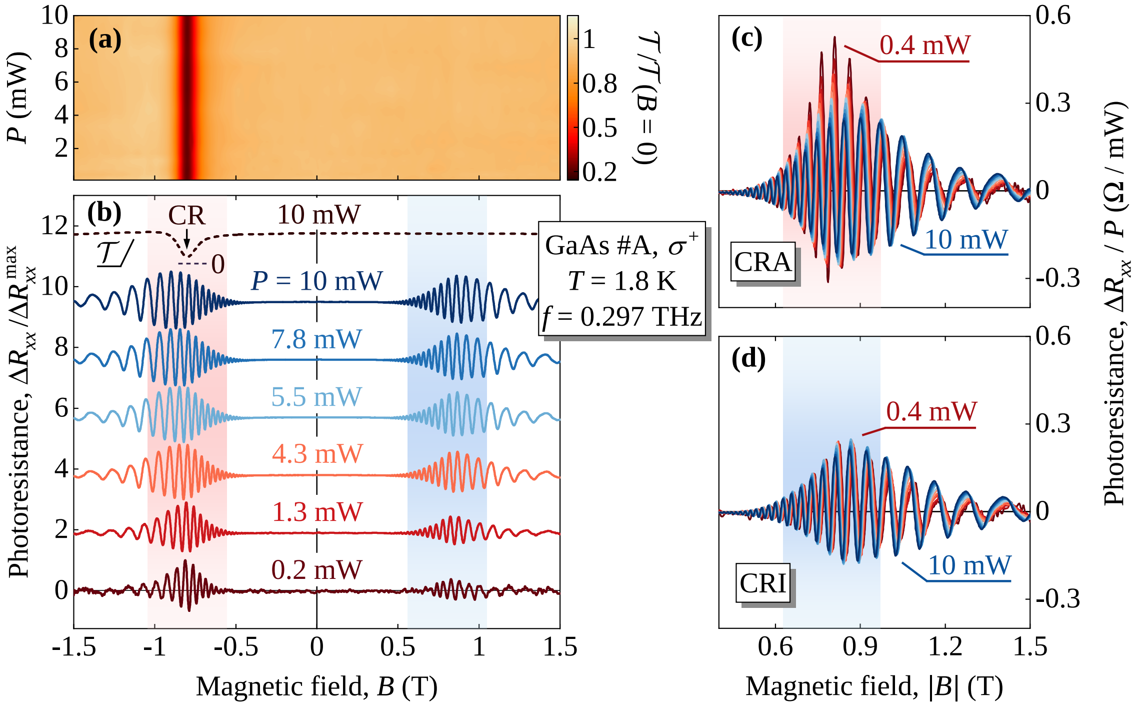

Figure C.1: Analog of Fig. 8.5 obtained for the opposite radiation helicity (σ^+). **(a)** Contour map of the normalized transmittance for different radiation powers. **(b)** The colored curves represent the corresponding normalized photoresistance traces, offset for clarity. The dashed curve denotes the transmittance for $P = 10$ mW, where zero transmittance is marked by a dashed horizontal line near the CR dip. The vertical arrow marks the position of the CR, and the red and blue shaded magnetic-field regions indicate the vicinity of the CRA and CRI sides. **(c, d)** CRA and CRI photoresistance normalized to the corresponding radiation power. The results were obtained for GaAs #A at $T = 1.8$ K in response to $f = 0.297$ THz. Figure adapted from Ref. [48] and supplemental material therein.

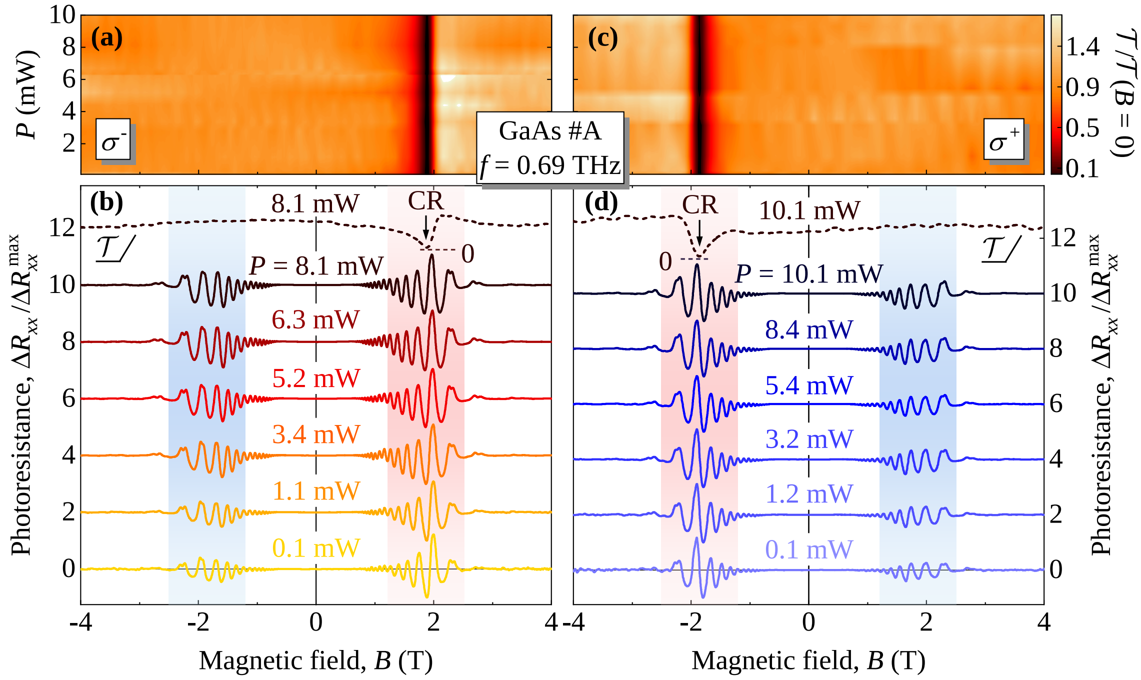

Figure C.2: **(a, c)** Power dependence contour plots of the normalized radiation transmittance recorded in response to $f = 0.69$ THz for left-handed [panel (a)] and right-handed helicity [panel (c)]. **(b, d)** Corresponding normalized photoresistance curves for various radiation powers down to fractions of milliwatt, up-shifted for clarity. The black dashed curve represents the transmittance at the highest power $P = 8.1$ and 10.1 mW in panels (b) and (d), respectively. The CR dip is denoted by a vertical arrow, and zero transmittance is indicated by a dashed horizontal line near the dip. The shaded red and blue areas mark the CRA and CRI polarities, respectively. All results were obtained at $T = 1.8$ K in GaAs #A. Figure adapted from Ref. [48] and supplemental material therein.

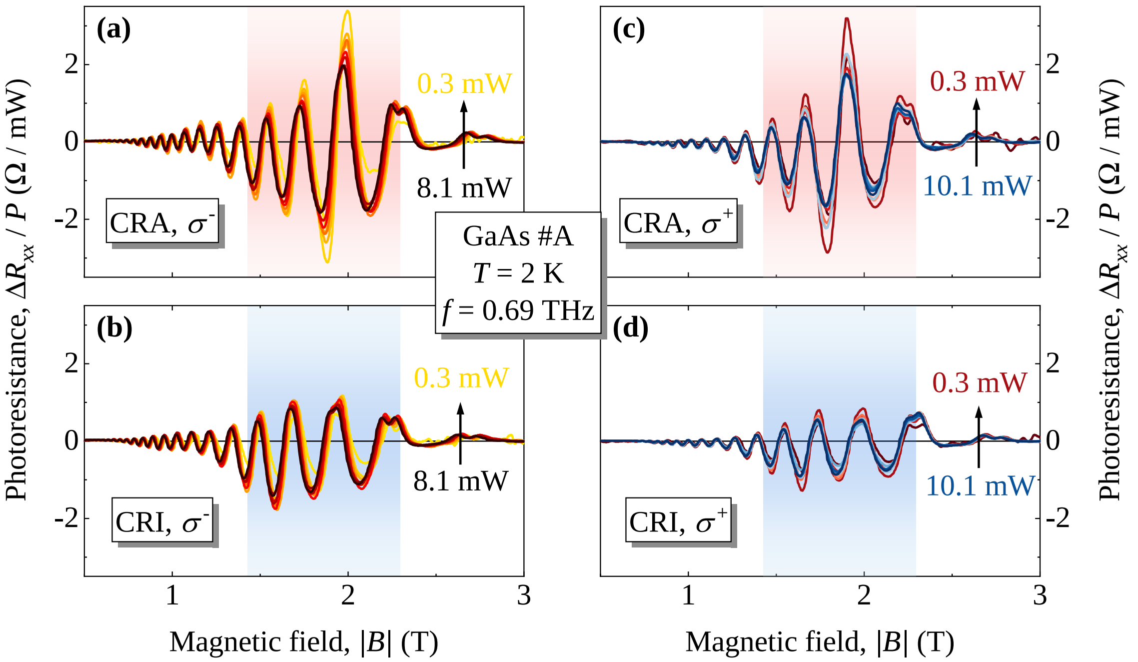

Figure C.3: Traces measured for different radiation powers in the corresponding available range, normalized to their respective powers. The CRA and CRI polarities are shown separately. The full traces are provided in Fig. C.2. Panels (a, b) and (c, d) present curves for σ^- and σ^+, respectively. The results were obtained for GaAs #A at $T = 2$ K in response to $f = 0.69$ THz. Figure adapted from Ref. [47] and supplemental material therein.

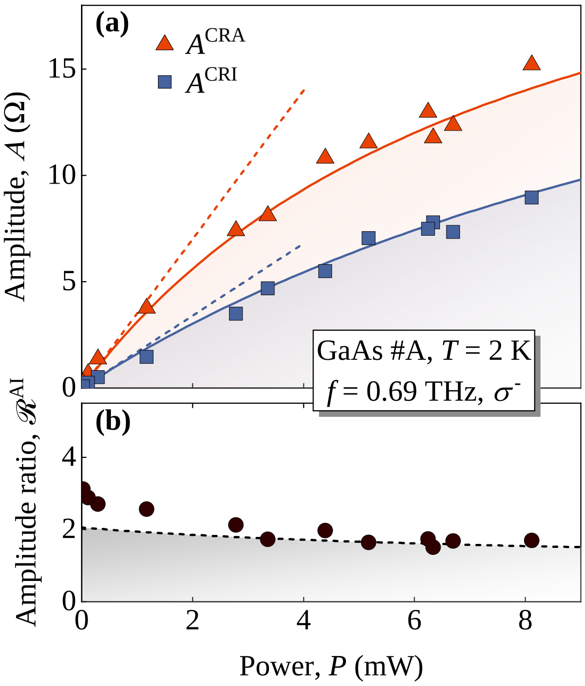

Figure C.4: (a) Power dependence of A^{CRA} (red triangles) and A^{CRI} (blue squares) for $f = 0.69$ THz and $T = 2$ K. The solid curves are fits according to Eq. (8.2) and the dashed lines represent their linear dependencies ($P_{\mathrm{s}} \to \infty$). The saturation powers used to fit the data yield $P_{\mathrm{s}}^{\mathrm{CRA}} = 8.0$ mW and $P_{\mathrm{s}}^{\mathrm{CRI}} = 16$ mW, and the corresponding scaling parameters are given by $a^{\mathrm{CRA}} = 3.5\ \Omega/\mathrm{mW}$ and $a^{\mathrm{CRI}} = 1.7\ \Omega/\mathrm{mW}$. The parameters satisfy the condition $P_{\mathrm{s}}^{\mathrm{CRA}}/P_{\mathrm{s}}^{\mathrm{CRI}} \simeq a^{\mathrm{CRI}}/a^{\mathrm{CRA}}$. **(b)** Power dependence of the corresponding amplitude ratio $\mathscr{R}^{\mathrm{AI}}$. The dashed curve denotes the ratio of the fitting curves in panel (a). All results were obtained in GaAs #A for σ^- helicity. Figure adapted from Ref. [48] and supplemental material therein.

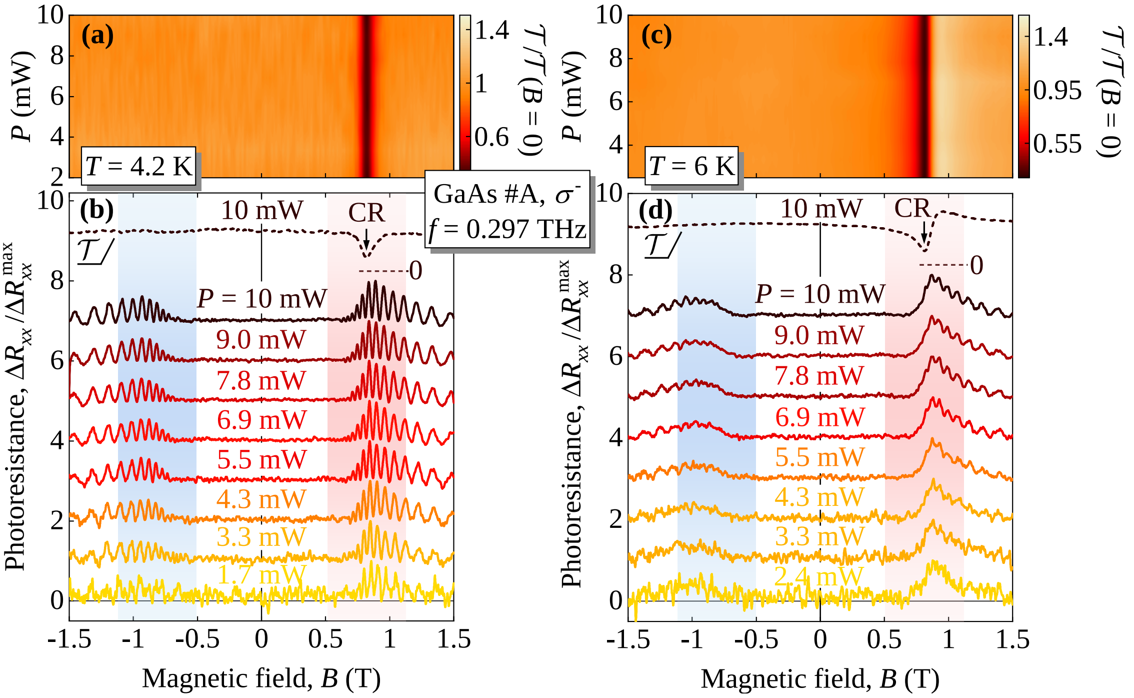

Figure C.5: **(a)** Contour map of the normalized transmittance obtained at a fixed measurement temperature $T = 4.2$ K and different radiation powers. **(b)** Power dependence of the corresponding normalized photoresistance curves at $T = 4.2$ K, up-shifted for clarity. **(c, d)** Normalized transmittance and photoresistance obtained at $T = 6$ K and different radiation powers, presented in an similar way as panels (a, b). The dashed traces in panels (b, d) show the transmittance for $P = 10$ mW, where zero transmittance is marked by dashed horizontal lines near the CR dips. The vertical arrows mark the position of the CR, and the red and blue shaded magnetic-field regions indicate the vicinity of the CRA and CRI sides. All results were measured in GaAs #A for σ^- helicity and $f = 0.297$ THz. Figure adapted from Ref. [48] and supplemental material therein.

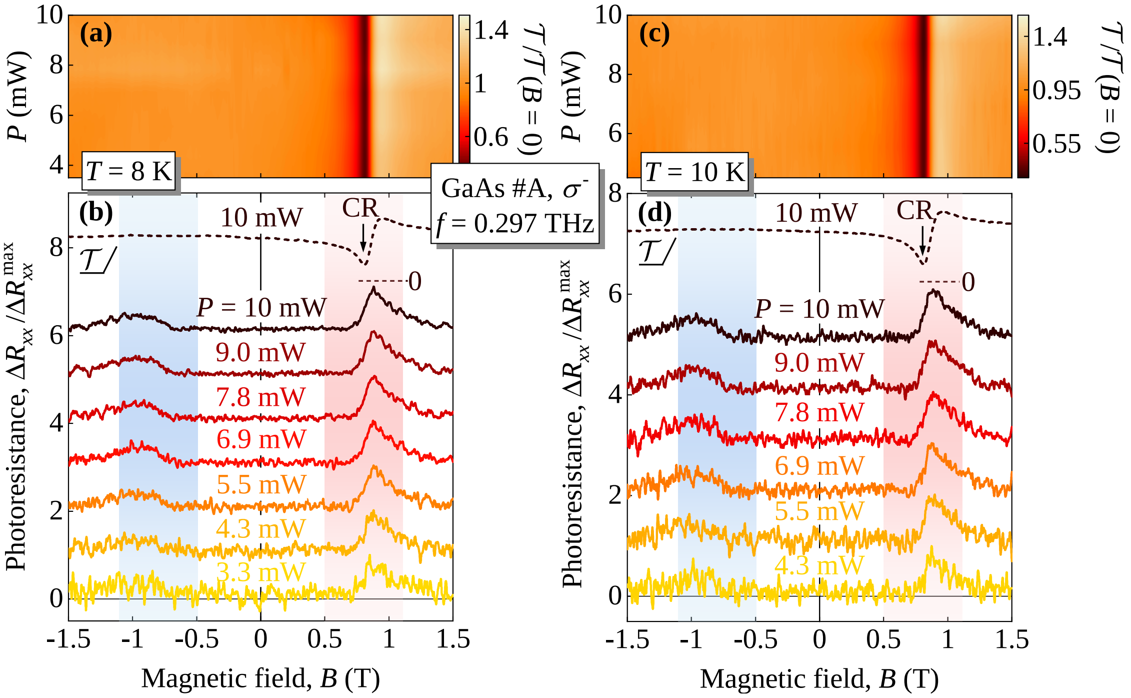

Figure C.6: **(a, c)** Power dependence of the normalized transmittance for $T = 8$ and 10 K visualized as a color map. **(b, d)** Normalized photoresistance curves for different powers and fixed temperatures, $T = 8$ and 10 K. The dashed traces denote the transmittance for $P = 10$ mW, where zero transmittance is marked by dashed horizontal lines near the CR dips. The vertical arrows mark the position of the CR, and the red and blue shaded magnetic-field regions indicate the vicinity of the CRA and CRI sides. All results were obtained in GaAs #A for σ^- helicity and $f = 0.297$ THz. Figure adapted from Ref. [48] and supplemental material therein.

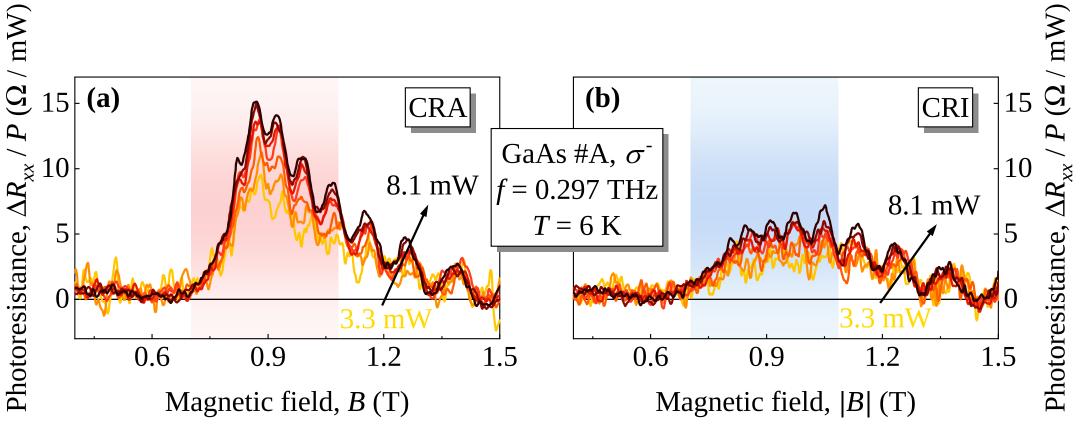

Figure C.7: **(a, b)** Photoresistance curves obtained at CRA [panel (a)] and CRI sides [panel (b)], normalized to the corresponding radiation power. The results were obtained for GaAs #A at $T = 6$ K in response to $f = 0.297$ THz. Figure adapted from Ref. [48] and supplemental material therein.

D Transmittance & Photoresistance in the MIRO Regime

Figure D.1 shows the temperature and power dependencies of the transmittance and photoresistance in the MIRO regime. The data were recorded in GaAs #C after room light illumination at a frequency of $f = 0.290$ THz and σ^+ helicity. Note that GaAs #C was grown with a different fabrication scheme than GaAs #A and #B, see Sec. 4.1 for details. The results are presented in a similar manner to Fig. 8.7 in the main text. The corresponding amplitude analysis is shown in Fig. D.2 with respect to temperature and power (analogous to Fig. 8.8 in the main text). Similar to GaAs #A in Fig. 8.7, the amplitude ratio becomes significantly larger at high T, where the photoresistance is dominated by bolometric effects. For completeness, Fig. D.1(e) presents the transmittance and photoresistance curves obtained with a BWO setup at $f = 0.324$ THz, $T = 3.7$ K, and $P \approx 0.5$ mW[12]. The photoresistance amplitude ratio is about 30. Figures D.3 and D.4 extend the temperature dependence of transmittance and MIRO photoresistance with high-frequency data ($f = 0.69$ THz). The former figure shows the results for GaAs #A and the latter figure presents the measurements for GaAs #B.

---

[12] Measurements were performed at the technical university of Vienna by Maxim Savchenko and Alexey Shuvaev in the group of Andrei Pimenov, https://www.ifp.tuwien.ac.at/spectroscopy (accessed January 1, 2024) and published in Ref. [89].

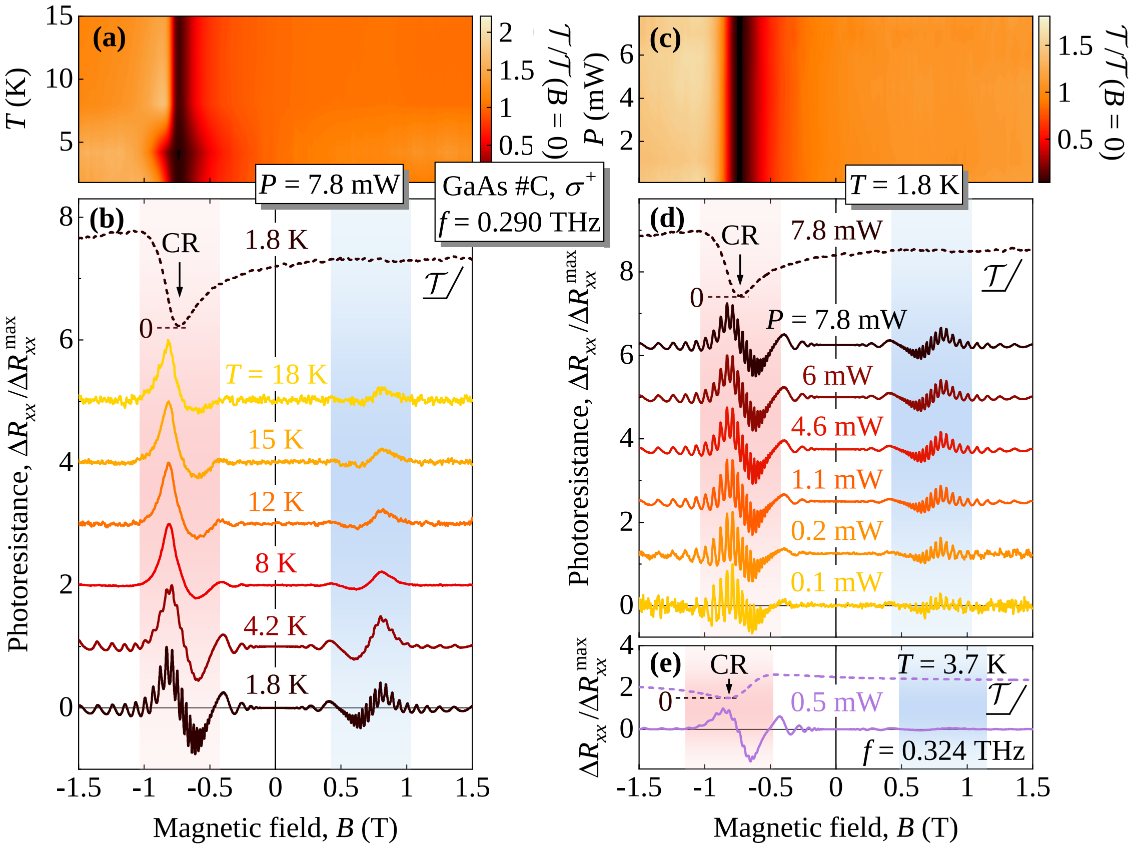

Figure D.1: **(a)** Contour maps of normalized transmittance for different temperatures and a fixed radiation power $P = 10$ mW. **(b)** Corresponding normalized photoresistance shown for different temperatures up to $T = 18$ K. **(c)** Power dependence of the normalized transmittance for a fixed temperature of $T = 1.8$ K shown as a color map. **(d)** Power dependence of the corresponding photoresistance. The traces in panels (b, d) are offset for clarity, and the dashed curves denote the transmittance for $T = 1.8$ K and $P = 7.8$ mW, where the zero values are marked by dashed horizontal lines near the CR dips. The vertical arrows mark the position of the CR, and the red and blue shaded magnetic-field regions indicate the vicinity of the CRA and CRI sides. The result in panels (a – d) were performed for $f = 0.290$ THz. **(e)** Transmittance (dashed) and photoresistance (solid) traces recorded at $T = 3.7$ K and a frequency of $f = 0.324$ THz generated by a BWO with a power of about $P \approx 0.5$ mW. The data in panels (a – d) are adapted from Ref. [48] and the traces in panel (e) were taken with authors' permission from Ref. [89]. All results were obtained in GaAs #C after room light illumination and σ^+ helicity configuration.

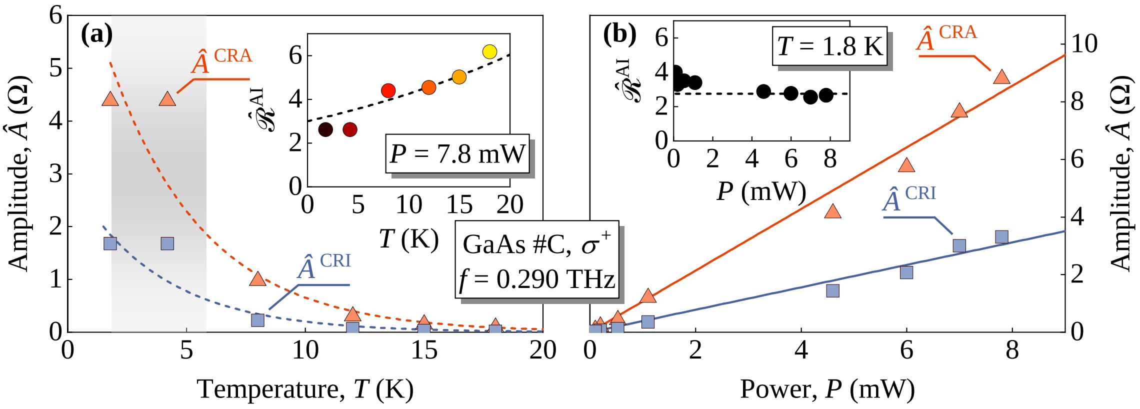

Figure D.2: **(a)** Amplitude values of MIRO, $\hat{A}^{\mathrm{CRA}}$, and $\hat{A}^{\mathrm{CRI}}$ plotted as a function of measurement temperature at $P = 7.8$ mW. The colored dashed lines represent guides for the eye following an exponential decay. The gray shaded area indicates the region where MIRO dominates the photoresponse. The inset shows the corresponding dependence of the amplitude ratios $\hat{\mathscr{R}}^{\mathrm{AI}}(\mathrm{T})$. Here the dashed curves represent guides for the eye. **(b)** Power dependence of the MIRO amplitudes recorded at $T = 1.8$ K. The solid lines denote linear fits according to $\hat{A}^{\mathrm{CRA,CRI}}(P) \propto P$. All results were obtained at $f = 0.290$ THz and σ^+ helicity in GaAs #C. The main data set is shown in Fig. D.1. Figure adapted from Ref. [48].

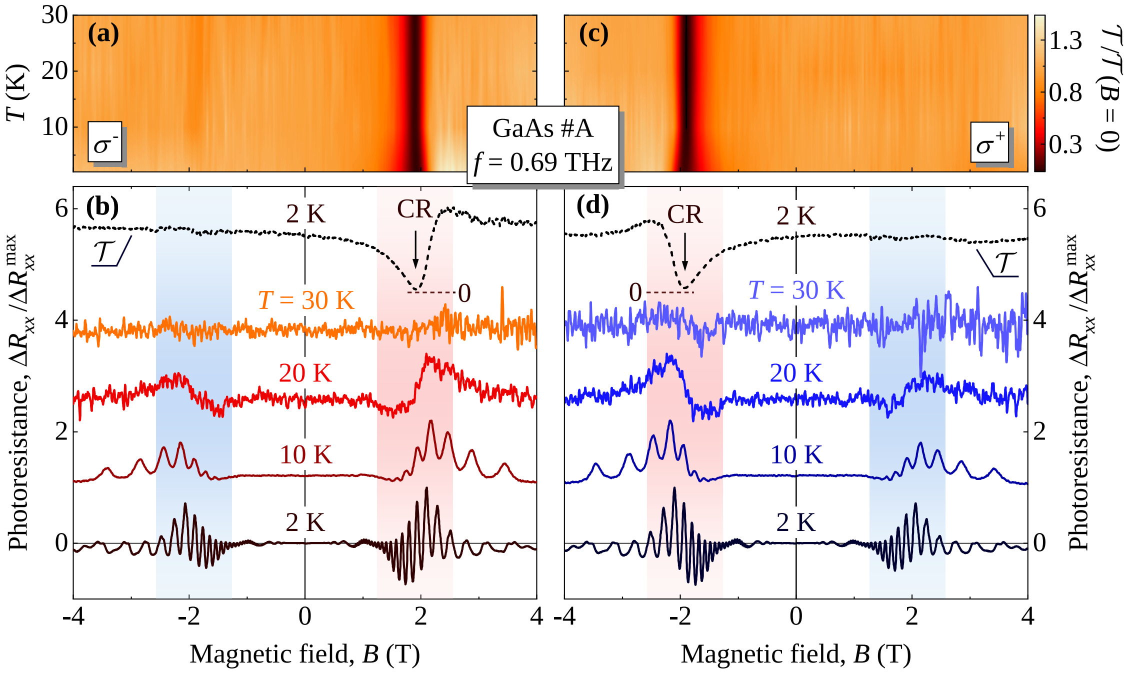

Figure D.3: **(a)** Contour map of the normalized transmittance curves at different temperatures recorded in the σ^- configuration. **(b)** Corresponding normalized photoresistance traces, offset for clarity. The dashed curve shows the transmittance for $T = 2$ K, where zero transmittance is marked by a dashed horizontal line near the CR dip. The vertical arrow marks the position of the CR, and the red and blue shaded magnetic-field regions indicate the vicinity of the CRA and CRI sides. **(c, d)** Temperature dependence of the normalized transmittance and corresponding photoresistance recorded for the opposite helicity (σ^+ configuration) and plotted similarly to panels (a, b). The sample was illuminated with ambient light prior to the measurements. All results were recorded in GaAs #A and performed for $f = 0.69$ THz at maximum available power $P = 8$ mW at the sample. Figure adapted from Ref. [47].

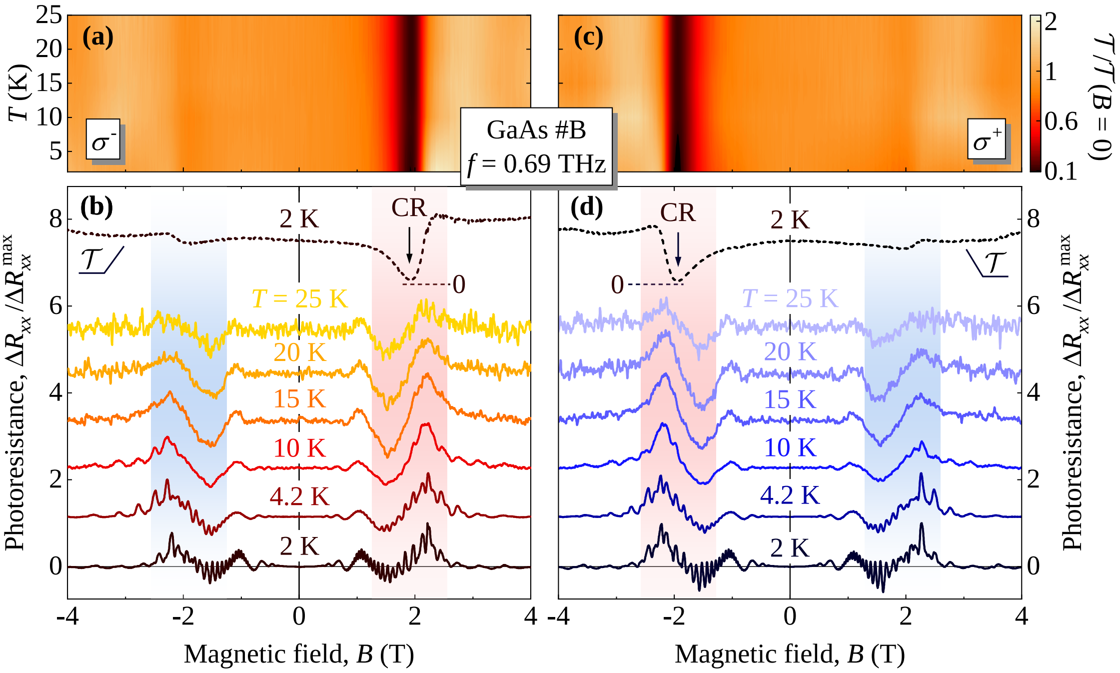

Figure D.4: **(a)** Contour map of the normalized transmittance traces at different temperatures obtained in the σ^- configuration. **(b)** Corresponding normalized photoresistance traces, offset for clarity. The dashed curve denotes the transmittance for $T = 2$ K, where zero transmittance is marked by a dashed horizontal line near the CR dip. The vertical arrow marks the position of the CR, and the red and blue shaded magnetic-field regions indicate the vicinity of the CRA and CRI sides. **(c, d)** Temperature dependence of the normalized transmittance and corresponding photoresistance recorded for the opposite helicity (σ^+ configuration) and plotted similarly to panels (a, b). The sample was exposed to ambient light prior to measurements. All traces were recorded in GaAs #B and were performed for $f = 0.69$ THz at maximum available power $P = 8$ mW at the sample. Figure adapted from Ref. [47] and supplemental material therein.

E Polarization Purity of the Circularly Polarized THz Radiation

Figure E.1(a) shows the recorded photosignal as a function of the polarizer angle. The signal was detected by a zero-bias detector equipped with a horn antenna. The radiation output of the IMPATT-diode source was σ^- polarized. The THz radiation was focused by a PTFE lens and directed to the detector by plane and parabolic mirrors, see Fig. E.1(b). The linear wire-grid polarizer in front of the detector was mounted to rotate freely, allowing the circularly polarized THz output to be converted to linearly polarized radiation of arbitrary direction. Since for a perfectly circularly polarized beam the detected photosignal should be independent of the polarizer angle, i.e., it should give constant values for each angle, this setup can be used to estimate the purity of the circular polarization provided by the source. The deviation from the mean amplitude is about 6 %, which gives a circular purity of 94 %. Note that the radiation components polarized along the wires are reflected by the polarizer. To avoid this back reflection into the source, which results in a standing wave pattern, the polarizer was tilted by about 40°. The tilt of the PTFE attenuator was also used to reduce back reflection. More details about the IMPATT-diode source can be found in Sec. 3.2.

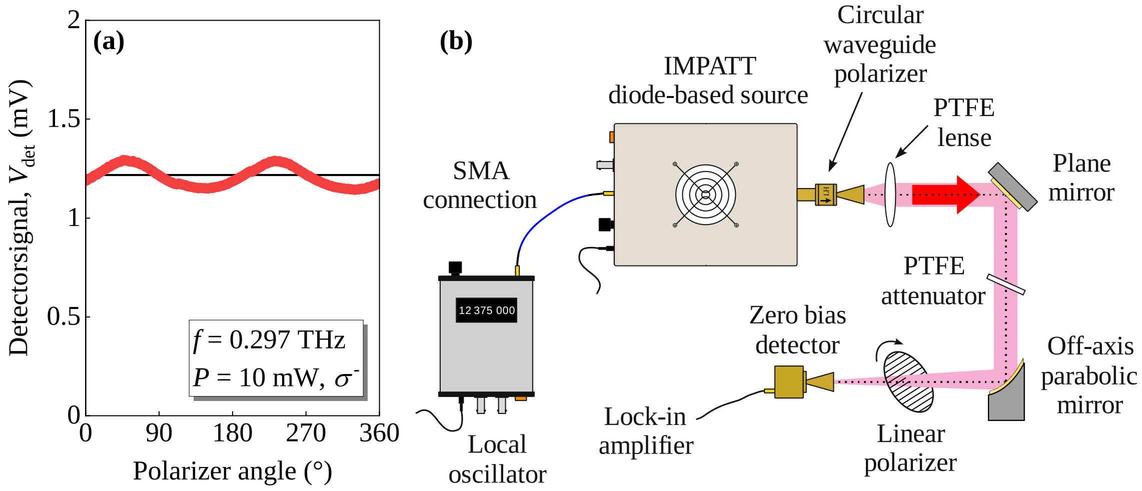

Figure E.1: **(a)** Photosignal V_{det} as a function of polarizer angle, recorded with a pyroelectric detector. **(b)** Sketch of the corresponding IMPATT diode-based quasi-optical setup. The result was obtained in response to $f = 0.297$ THz with $P = 10$ mW and σ^- configuration.